Focused and Steady-State Characteristics of Shaped Sonic Boom Signatures: Prediction and Analysis

Domenic J. Maglieri, Percy J. Bobbitt, and Steven J. Massey
Eagle Aeronautics, Inc., Hampton, Virginia

Kenneth J. Plotkin
Wyle Laboratories, Arlington, Virginia

Osama A. Kandil and Xudong Zheng
Old Dominion University, Norfolk, Virginia

June 2011

NASA STI Program . . . in Profile

Since its founding, NASA has been dedicated to the advancement of aeronautics and space science. The NASA scientific and technical information (STI) program plays a key part in helping NASA maintain this important role.

The NASA STI program operates under the auspices of the Agency Chief Information Officer. It collects, organizes, provides for archiving, and disseminates NASA's STI. The NASA STI program provides access to the NASA Aeronautics and Space Database and its public interface, the NASA Technical Report Server, thus providing one of the largest collections of aeronautical and space science STI in the world. Results are published in both non-NASA channels and by NASA in the NASA STI Report Series, which includes the following report types:

- TECHNICAL PUBLICATION. Reports of completed research or a major significant phase of research that present the results of NASA programs and include extensive data or theoretical analysis. Includes compilations of significant scientific and technical data and information deemed to be of continuing reference value. NASA counterpart of peer-reviewed formal professional papers, but having less stringent limitations on manuscript length and extent of graphic presentations.

- TECHNICAL MEMORANDUM. Scientific and technical findings that are preliminary or of specialized interest, e.g., quick release reports, working papers, and bibliographies that contain minimal annotation. Does not contain extensive analysis.

- CONTRACTOR REPORT. Scientific and technical findings by NASA-sponsored contractors and grantees.

- CONFERENCE PUBLICATION. Collected papers from scientific and technical conferences, symposia, seminars, or other meetings sponsored or co-sponsored by NASA.

- SPECIAL PUBLICATION. Scientific, technical, or historical information from NASA programs, projects, and missions, often concerned with subjects having substantial public interest.

- TECHNICAL TRANSLATION. English-language translations of foreign scientific and technical material pertinent to NASA's mission.

Specialized services also include creating custom thesauri, building customized databases, and organizing and publishing research results.

For more information about the NASA STI program, see the following:

- Access the NASA STI program home page at *http://www.sti.nasa.gov*

- E-mail your question via the Internet to help@sti.nasa.gov

- Fax your question to the NASA STI Help Desk at 443-757-5803

- Phone the NASA STI Help Desk at 443-757-5802

- Write to:
  NASA STI Help Desk
  NASA Center for AeroSpace Information
  7115 Standard Drive
  Hanover, MD 21076-1320

NASA/CR–2011-217156

Focused and Steady-State Characteristics of Shaped Sonic Boom Signatures: Prediction and Analysis

Domenic J. Maglieri, Percy J. Bobbitt, and Steven J. Massey
Eagle Aeronautics, Inc., Hampton, Virginia

Kenneth J. Plotkin
Wyle Laboratories, Arlington, Virginia

Osama A. Kandil and Xudong Zheng
Old Dominion University, Norfolk, Virginia

June 2011

TABLE OF CONTENTS

ABSTRACT

The objective of this study is to examine the effect of flight, at off-design conditions, on the propagated sonic boom pressure signatures of a small "low-boom" supersonic aircraft. The amplification, or focusing, of the low magnitude "shaped" signatures produced by maneuvers such as the accelerations from transonic to supersonic speeds, climbs, turns, pull-up and pushovers is the concern. To analyze these effects, new and/or improved theoretical tools have been developed, in addition to the use of existing methodology. Several shaped signatures are considered in the application of these tools to the study of selected maneuvers and off-design conditions. The results of these applications are reported in this paper as well as the details of the new analytical tools. Finally, the magnitude of the focused boom problem for "low boom" supersonic aircraft designs has been more accurately quantified and potential "mitigations" suggested. In general, "shaped boom" signatures, designed for cruise flight, such as asymmetric and symmetric flat-top and initial-shock ramp waveforms retain their basic shape during transition flight. Complex and asymmetric and symmetric initial shock ramp waveforms provide lower magnitude focus boom levels than N-waves or asymmetric and symmetric flat-top signatures.

STUDY STRUCTURE

The present study involved six (6) tasks that are listed below:

       Task 1 - <u>Identify Aircraft and Maneuvers</u>

       Task 2 - <u>Parametric Representation of F-function</u>

       Task 3 - <u>Sonic Boom Analysis Tool Update</u>

       Task 4 - <u>Focus Condition Study</u>

       Task 5 - <u>Improved Focal Zone Signature Analysis</u>

       Task 6 - <u>Operational Approaches for Focus Mitigation</u>

OVERVIEW

A low-boom supersonic cruise aircraft is optimized for cruise conditions. Off-design conditions will happen during climb to cruise altitude and descent. Particularly loud booms can occur under focus conditions. Focus will occur during initial transition to supersonic flight and can also occur as a result of turns, acceleration or pushover maneuvers during supersonic flight. The conditions that cause focus booms depend only on the atmosphere and the kinematics of the aircraft's trajectory. However, the signature at focus depends on the aircraft configuration and the characteristics of the shaped signature it produces entering the focus region. Focus signatures for supersonic turns during cruise conditions are expected to be similar to the cruise design shape. For the transition focus, the signature is not expected to have aged to the steady state carpet boom condition but still may contain many of the same characteristics as the carpet boom.

PCBoom4[1] currently computes the propagation of a sonic boom through the atmosphere, including the signatures at focus for arbitrary maneuvers. Focus signatures are computed by applying the Gill and Seebass[2] numeric focus solution for a step function shock to each shock in the signature entering the focal zone using Guiraud's[3] scaling criteria. This is reasonable for N-waves, where the shocks are virtually steps. Its applicability to complex minimized "shaped" signatures is questionable. A new numeric method by Auger and Coulouvrat[4] agreed with the PCBoom4[1] method for N-waves, but showed that two closely spaced shocks in a non-N-wave boom interacted and were not amplified as much as the PCBoom4[1] method predicts. Consequently, one would expect that non-N-wave signatures would also deviate from the PCBoom4[1] results.

PCBoom4[1] has been updated to include the six(6) parameter George-Seebass[5] model to facilitate the computation of the optimum design area distribution. A computer code based in part on the method of reference 4 has been produced and the focusing of a number of "shaped" signatures analyzed. In addition, methodology has been formulated for determining the effective area distributions and F-functions at off-design Mach numbers.

The objective of the present study is to examine the influence of shaped sonic boom signatures on maneuver focus booms with particular emphasis on the transition phase of flight from subsonic to supersonic speeds.

APPROACH

In order to address the study objective, six(6) tasks were defined as follows:

Task 1 - Identify aircraft and maneuvers. A low-boom aircraft configuration will be selected. A prime choice will be the supersonic business jet being studied by NASA Langley Research Center. The aircraft's flight envelope and nominal mission profile and range of in-flight maneuvers will be obtained.

Task 2 - Parametric representation of F-function. The cruise F-function for the selected aircraft will be defined such that it can be modeled by the six parameters of the George-Seebass[5] model. The parameters will be adjusted such that they are related to the cruise flight conditions of the aircraft. With the calculation of the design lift distribution and thus the volume contribution, the F-function at other conditions can be estimated with the new analysis tools developed. This task is presented in **Appendix A**: "The Calculation of Design and Off-Design Effective area Distributions and F-Function

for Minimum Boom Supersonic Cruise Aircraft" by Percy J. Bobbitt and Steven J. Massey, Eagle Aeronutics, Inc.

Task 3 - Sonic boom analysis tool update. The source input/generation routines in Wyle Laboratories Sonic Boom Prediction computer Program (PCBoom4)[1] will be updated to accept the six parameter F-function model as an input. This task is presented in **Appendix B**: "Incorporation of George Seebass Signature into PC BOOM4" by Kenneth J. Plotkin, Wyle Laboratories.

Task 4 - Focus condition study. PCBoom4[1] will be run for the following cases.
- Full Nominal Mission
- Focal Analysis For Variations of Transonic Acceleration.
- Climb, turns at cruise and descent-deceleration at end of cruise.
This task is presented in **Appendix C**: "Focus Condition Study" by Kenneth J. Plotkin, Wyle Laboratories.

Task 5 - Improved focal zone signature analysis. A new computer code similar to that of Auger and Coulouvrat[4] will be formulated and applied to a variety of signature shapes to determine their effect on the focus factor. This task is presented in **Appendix D:** "Development and Application of a Transition Flight Sonic Boom Focusing Computer Code" by Osama Kandil and Xudong Zheng, Old Dominion University.

Task 6 - Operational approaches for focus mitigation. Investigate operational methods to minimize focus booms during transition from subsonic to supersonic speeds (e.g., varying acceleration rates, climb angle and a caustic-elimination maneuver). Display sample "focus avoidance" operational charts for normal supersonic flight operations, for standard turns and descent-deceleration to subsonic speeds.

Results and discussion of each of the above six(6) tasks will be provided in the following sections of this report.

TASK 1 - IDENTIFY AIRCRAFT AND MANEUVERS

The low-boom supersonic business jet (SBJ) configuration described by Mack[6] has been selected for this study. A three-view of the configuration along with a listing of some of its characteristics including the cruise design low boom asymmetric initial-shock ramp type "shaped" signature is given in figure 1. The aircraft is a highly swept arrow-wing configuration with two aft-mounted engines. It is 132.5 feet long with a 55 foot wing span, 1560.25 square foot wing area, and has a gross takeoff weight of 99,435 pounds and an empty weight of 41,434 pounds. Design range with 10 passengers and crew of 2 is 4000 n.mi. at a design cruise Mach number of 2.0. Details of the airplane geometry, airplane flight envelope and nominal mission profile were also obtained.

The SBJ initiates transition from subsonic to supersonic speeds (0.95-1.4) at constant altitude of 32,850 feet and with an acceleration rate of about 0.2 m/sec^2. It continues to accelerate in a slight climb to M = 2 at about 41,000 feet, the start of cruise. From there it flies a constant Mach number and and at constant C_L to 60,000 feet, the end of cruise. No maneuvers (i.e., turns) are included in the design mission. At the end of cruise, the SBJ decelerates from M = 2.0 to M = 1.0 at a nearly constant altitude of about 60,000 feet in order to avoid boom focusing.

With regards to in-flight maneuvers, three will be considered in this study: (1) accelerations from sub-sonic to supersonic flight; (2) Mach 2 turns at cruise altitude; and (3) descent and deceleration at the end of cruise flight. For the transition from subsonic to supersonic flight, values of acceleration rates from 0.2 m/sec^2, through 2.5 m/sec^2 are analyzed and three flight path angles, -1°, 0°, and +3° will be examined.

TASK 2 - PARAMETRIC REPRESENTATION OF F-FUNCTION

For this task, the cruise F-function for the selected aircraft was approximated so that it could be modeled by the six parameter George-Seebass[5] model. The parameters were adjusted so that they are related to the cruise flight equivalent area distribution of the aircraft. This provided basic lift and volume contributions such that the F-function at other flight-Mach number conditions can be estimated.

In the process of developing Task 2, which is described in detail in **Appendix A**, an improvement to the Darden[7] and Mack[8] method for designing vehicles to have minimum boom shaped signatures at cruise is made through simplification of the basic equation. In addition, a simple method for calculating the lift distribution allows the effective area distribution due to volume at the design Mach number to be rapidly evaluated. A code that permits calculation of the equivalent volume at other Mach numbers using the design Mach number volume distribution plus the "lift distribution" methodology allow the total effective area distributions, and thus F-functions, for Mach numbers from the cruise value down to the normal M = 1.0 cuts (actual geometry). To demonstrate this capability the design F-function (F) and effective area (Ae) for an asymmetric flattop and initial-shock ramp configuration at M = 2.0 is shown in figure 2 along with the same quantities calculated for M = 1.4. It can be seen that although the F-functions for both M = 2.0 and M = 1.4 are quite similar. The influence of small inflections in the volume and lift distributions, and thus the effective area distribution at M = 1.4, result in significant fluctuations in the aft portions of the flattop and ramp F-functions.

TASK 3 - SONIC BOOM ANALYSIS TOOL UPDATE

As previously mentioned, the current focus signature technology implemented in PCBoom4[1] code is the Gill and Seebass[2] solution. It is applied as an incident step function to each shock in a signature entering the focal zone using Guiraud's[3] scaling criteria. This has been successful for N-waves and thus, one would believe it should be even more successful for the bow-shock of a flat-top, since that is closer to the original step solution. It is not, however, clear how successful it would be for a minimum-shock ramp signature. Auger and Coulouvrat[4] recently examined both an N-wave and a Concorde type three-shock sawtooth boom shape as input signature using a numeric code (see fig. 3). They showed that focusing of the N-wave bow-shock is well represented by Gill-Seebass[2] and Guiraud[3]. Amplification of the Concorde initial shocks are, however, considerably less than would be predicted by that method. Marchiano and Coulouvrat[9] also showed that for symmetrical multi-shock signatures, the focus factor is strongly influenced by shock spacing (see fig. 4)

The thrust of this task is to update the source input/generation routines in the PCBoom4[1] computer program to accept the six-parameter George-Seebass[5] F-function model as an input. The details of this modification are given in **Appendix B**. Parameters are in the form established by Darden[7] and George-

Seebass[5]. Input is via a parameter file read in line with the main input data file. It is processed via a subroutine, so this option is independent of future PCBoom updates.

The updated code was used to compute the aging of the cruise designed asymmetric flattop and ramp type signature developed under Task 2 "Parametric Representation of F-Functions." Results for the two shaped signatures are given in figure 5 for the steady-flight start of cruise condition of $M = 2$ at 41,000 feet. It can be seen that the George-Seebass[5] near-field F-function waveforms do age as they propagate to the ground to become the designed asymmetric flattop and initial-shock ramp signatures.

TASK 4 - FOCUS CONDITION STUDY
The updated PCBoom4[1] prediction code was used to obtain the boom signatures at ground level for a standard atmosphere with no winds and for three specified airplane operating conditions or maneuvers encountered during the nominal mission of the SBJ, (1) focal analysis for variations in acceleration rates and climb angle during transition from subsonic to supersonic speeds, (2) turns during cruise and (3) descent-deceleration to subsonic speeds. For the nominal mission, the aircraft conducts transition flight at 32,850 feet accelerating to $M = 1.4$ at a rate of about 0.2 m/sec^2, then continues climb-acceleration to $M = 2.0$ at 41,000 feet, the start of cruise. Cruise flight is conducted at $M = 2.0$ and the airplane flies at a constant lift coefficient concluding at 60,000 feet, the end of cruise. No turns are initiated during cruise flight. To preclude focus booms at the end of cruise, the aircraft decelerates at 60,000 feet to $M = 1.0$ and then descends to landing. Analysis of the sonic boom associated with transition flight are provided in Appendix C.

Transonic acceleration was initiated at 32,850 feet for acceleration rates that varied from 0.2 m/sec^2 through 2.0 m/sec^2 and for three climb angles of -1.0^o, 0°, and 3° at acceleration rates of from 0.6 m/sec^2 to 1.0 m/sec^2. Two sample cases are given in figure 6 for transition flight at a constant altitude of 32,850 feet and an acceleration rate of 0.6 m/sec^2. Predicted ground signatures for the asymmetric flat-top and initial-shock ramp designs, using PCBoom4, are shown at maximum focus and for the carpet boom. It can be seen that both focus signatures show strong initial spikes. The carpet boom signatures have essentially developed into an asymmetric flat-top and initial-shock ramp shape. It should be noted that the strong initial spikes displayed at the maximum focus are not a result of the initial spike designed into the near-field F-function but are associated with the Gill-Seebass[2] solution for an incident step function to each shock in the signature entering the focal zone using Guiraud's[3] scaling criteria.

Further examination of the influence of acceleration rate and climb angle will be presented later in this study under Task 6 "Operational Approaches for Focus Mitigation" along with focus avoidance operational charts regarding turns during cruise and descent-deceleration to subsonic speeds.

TASK 5 - IMPROVED FOCAL ZONE SIGNATURE ANALYSIS
Sonic boom focusing of N-wave type signatures has been addressed by several investigators. Lansing[10] applied acoustic theory through a graphical ray-tracing procedure to show the effects of

supersonic flight maneuvers, such as sideslip, turns, dive and linear acceleration on the ground shock patterns. Barger[11] has studied the sonic boom wave shapes and caustic lines, which are generated by a supersonic aircraft performing general turning and accelerating maneuvers, using a graphical method. Hayes[12] suggested the transition focus boom may be eliminated incorporating a push-over pull-up maneuver (vertical acceleration) to cancel out the focusing caused by the forward acceleration. The current focus signature methodology, implemented in PCBoom4[1], is to apply the Gill and Seebass[2] solution for an incident step function to each shock entering the focal zone using Guiraud's[3] scaling criteria. This method has been successful for N-waves and should be even more successful for the bow-shock of an asymmetric or symmetric flattop shaped signature since it is closer to the original step solution. It is not clear how successful it would be for an asymmetric or symmetric initial-shock ramp signature.

Rosales[13] and Tabak[14] studied the focusing and caustics of weak shock waves using the method of matched asymptotic expansions. They have concluded that the nonlinear Tricomi equation, which describes the behavior of the shock fronts near caustics, does not appear to admit the triple shock intersections, which have been observed experimentally. Coulouvrat[15] has shown that the focusing of a weak shock wave at a caustic is essentially a nonlinear phenomenon. He has shown that the nonlinear wave equation is reduced to the Kusnetsov[16] equation for the potential function so that the problem is numerically tractable.

Recently Auger and Coulouvrat[4] have presented a numerical method to simulate the focusing of sonic booms by solving the nonlinear Tricomi equation using an iterative algorithm, which is based on an unsteady version of the equation with an artificial time variable. The numerical algorithm is a modification of a pseudo spectral method. Their numerical scheme has been validated and has been applied to the focusing of the Concorde aircraft sonic boom during acceleration from Mach 1 to Mach 2. Results using their numerical method clearly demonstrate (see fig. 3) that other existing predictive methods, which serve well when the incoming signature is assumed to be an N-wave or step function cannot handle the multi-shock signature associated with Concorde transition flight. Marchiano and Coulouvrat[9] further illustrate the significance of spacing between the bow and second shock and signature symmetry on the focus boom overpressure (see fig. 4).

The utility of the Auger-Coulouvrat[4] and Marchiano-Coulouvrat[9] nonlinear analyses for the focusing of non N-wave signatures is clear. Therefore, this task was undertaken to develop a numerical code based upon the Auger-Coulouvrat[4] method for simulating shock wave focusing. A computational solver which uses a two-step pseudospectral method was developed to solve the unsteady version of the nonlinear Tricomi equation. Algorithms, coding and testing of the schemes for the numerical solution of the unsteady linear Tricomi equation in the time and frequency domain and the nonlinear Burgers' equation using shock capturing and shock fitting scheme have been programmed and checked. Details of the ODU computational solver developed under this task is given in **Appendix D** along with applications to six incoming shock wave signatures shown in figure 7 and include an N-wave, the Concorde three-shock and four low-boom shaped signatures, an asymmetric and symmetric flat-top and an asymmetric and symmetric initial shock-ramp.

The ODU developed numerical code was tested to confirm that it replicates the results obtained by Auger-Coulouvrat[4] for transition focus for an incoming N-wave signature and a Concorde type multi-shock saw-tooth signature. The results are presented in figure 8. Signatures are shown for four dimensionless distances in the region of the focus; post-focus of $Z = 1.5$ and $Z = 0.5$, at focus of Z_{max} and at pre-focus of $Z = -0.5$. Figure 8(a) is for the incoming N-wave and figure 8(b) is for the incoming Concorde type multi-shock saw-tooth waveform. Examination of the signatures of figure 8 with those presented in figure 3 indicate consistency between the ODU developed numerical code and Auger-Coulouvrat[4]. Both show that the multi-shock incoming signature results in significantly reduced amplification of the bow shock focus overpressure as compared to the incoming N-wave.

Next, the ODU numerical code was used to predict the signatures in the vicinity of the transition focus boom for four low-boom shaped cruise signatures that included the asymmetrical and symmetrical flat-top and asymmetrical and symmetrical initial-shock ramp type. Results are presented in figure 9 for both symmetrical signatures at the focus (Z_{max}) and post-focus ($Z = 1.5$), (see also **Appendix D**). Examination of figure 9 indicates that at the focus the symmetrical flat-top signature results in a bow-shock focus factor (defined herein as the ratio of the bow shock overpressure at the focus location to the bow shock overpressure of the incoming signature) of 4.2. This value, which is nearly the same as would be realized for an incoming N-wave (see fig. 8) was expected since the flat-top signature is essentially the Guiraud's step function input. The symmetrical initial-shock ramp signature, however, results in a bow shock focus factor of about two-thirds of the flat-top or N-wave. This is due to the ramp delay time assigned to the shaped signature. Similar results were realized for the cases of asymmetric initial-shock flat-top and ramp signatures (see **Appendix D**).

A summary of the focus overpressures and focus factors for both the bow and tail shocks for all six incoming signatures that were examined is given in figure 10. Figure 10(a) presents the predicted bow and tail focus overpressures resulting from the six incoming signatures having bow and tail shock overpressures values shown in figure 7 and also by the signature sketches at the top of the figure. The focus boom levels range from a maximum of about 9.6 psf for the N-wave tail shock to a minimum of about 2.2 psf for the flat-top signatures. Note also that the overpressure levels for the incoming signatures also ranged from a high of 2.56 psf for the N-wave tail shock to the lowest of 0.5 psf for the flat-top signatures.

When the maximum positive shock of all six incoming signatures is normalized to 1.0 psf, the resulting focus overpressures for bow and tail shocks is shown in figure 10(b). Here it can be seen that the highest focus level of about 8.5 psf is associated with the asymmetric flat-top signature and the lowest about 2.4 psf with the Concorde 3-shock waveform and the asymmetric and symmetric initial shock-ramp signatures at about 2.8 psf.

Focus factors for all six signatures are presented in figure 10(c) and are obtained by ratioing the maximum bow and tail focus overpressures (shown in figure 10(a)) to the maximum bow and tail overpressures of the incoming signatures (shown in fig. 7).

It can be seen from figure 10(c) that the lowest focus factors of the bow shock are associated with the Concorde type multi-shock and asymmetric and symmetric initial shock ramp signatures. Note also that the tail shock focus factors (defined herein as the ratio of the tail shock focus to the tail shock of the incoming signature) are greater than the bow shock focus factors for all the incoming signatures with a maximum of about 5.7 for the symmetric flat-top incoming signature.

Some interesting features regarding the "post focus" region refracted signatures can be illustrated with figure 11. Shown on the figure are the post-focus signatures ($Z = 1.5$) for all six incoming waveforms considered in this study. Note that for all six incoming signatures, which includes an N-wave, the Concorde three-shock, and both the asymmetrical and symmetrical flat-top and initial-shock ramp signatures remain essentially "U" shaped. In addition, the initial double shock of the Concorde incoming signature is also evident on the refracted waveform (fig. 11(b)) and the larger tail shock of the asymmetric flattop signature (see fig. 11(c)) is obvious on the refracted waveform. In fact, the refracted signature tail shock is equal to, or larger than, the refracted bow shock in all six cases. Although not included in the present report, the predicted refracted waveform for an incoming symmetrical ramp signature of 0.5 psf overpressure, 150 ms period and 30 ms rise times, is also "U" shaped.

TASK 6 - OPERATIONAL APPROACHES FOR FOCUS MITIGATION

The thrust of this task is to investigate operational methods to avoid focus booms reaching the ground during the entire supersonic portion of flight of the small supersonic business jet. Any rapid deviation of a vehicle from steady level flight conditions can produce considerable modifications in the location, number and intensity of the ground shock wave patterns. For example, focus booms may result from a supersonic climb-pushover maneuver, sideslips and turns during supersonic cruise and improper descent deceleration schedules. Questions regarding focus booms range from, can they be avoided and controlled to the size of the focus area and magnitude of the focus factor.

For military operations, all of the above mentioned maneuvers may not be unavoidable. A comprehensive study of maneuvers typical of a large SST-type airplane by Haglund and Kane[17] showed that it is possible to perform normal SST flight operations without producing focus booms except during the transonic acceleration phase of flight. Thus, for a commercially operated supersonic business jet, maneuvers such as pull-ups, pushovers, sideslips and abrupt turns at supersonic speeds would be avoided and the proper deceleration-descent schedule would be employed through the use of operational charts for focus boom avoidance such as illustrated in figure 12 taken from Wanner, et al,[18] and the work of Ribner[19] for turn maneuvers and Haglund and Kane[17] for deceleration-descent.

Transition flight from subsonic to supersonic speeds, however, cannot be avoided and thus the focus boom associated with this phase of flight can only be minimized, not eliminated. Considerable knowledge has been acquired regarding the nature, prediction and measurement of transition focus booms for N-wave design aircraft. These booms are very localized, affect relatively small regions on the ground and unlike carpet booms from steady flight, are not "dragged" along behind the aircraft. Focus factors ranging from 2 to 5 times the nominal carpet boom overpressure have been observed.

It has been demonstrated in flight tests that this transition focus region can be placed to within plus or minus 1000 feet of the desired location if the vehicle performance and atmospheric conditions are known (ref. 20). It should also be kept in mind that to have the continuously propagated shocks coalesce in an orderly fashion to create a focus boom, the atmosphere must be quiescent. Atmospheric turbulence,

especially in the lower layers, has been shown in flight tests to minimize focusing, and even appeared to eliminate it in some cases (refs. 21 and 22).

Haglund and Kane[23] have examined flight test data involving acceleration rates of 0.04 g to 0.10 g that suggests that a method to alleviate the transonic accelerating caustic is to accelerate rather slowly. They concluded, however, that based upon current prediction methods at that time, there was no method available for calculating the variation of caustic intensity with acceleration magnitude even though the limited experimental data did suggest a pronounced effect on caustic intensity. Recently, Auger and Coulouvrat[4] concluded that acceleration rate and altitude have very little influence on ground track focusing (see Table 1, P_a^{-max} column) for the range of accelerations and Mach numbers that they examined.

Another obvious method of reducing the intensity of the focus boom during transition flight is to climb while accelerating. Such a maneuver increases the Mach number and altitude at which the focus boom is generated and increases the length of the ray path along which the focus travels resulting in a decrease of the pressure level of the incoming carpet boom signature. In a number of past studies regarding supersonic vehicle concepts, the transition phase of flight usually dictated engine size in terms of engine thrust. Transonic climb-accelerations were usually limited to less than one-degree due to engine thrust limitations. In the present study, transition flight was examined for the four incoming signatures including an N-wave, double peaked N-wave, flat top and ramp for climb angles of -1°, 0° (level flight) and $+3^o$ and for acceleration rates that varied from 0.6 m/sec^2 through 1.0 m/sec^2. The effect of acceleration rate, flight path angle and altitude on boom focussing is shown in figures 13 and 14, respectively, text and figures from a data set in **Appendix C**. The aircraft initiates transition flight at 32,850 feet altitude at an accelerate rate of 0.6 m/sec^2 for climb angles of -1°, 0°, (level flight) and $+3.0^o$. As such, the focus for the -1 and +3 degree profiles occur at altitudes other than 32,850 feet.

As stated in **Appendix C**, each figure has two parts. Part "a" shows the bow-shock overpressure as a function of acceleration for level flight, three-degree climb, and one degree dive. The results are shown as curves for each flight path angle. Part "b" shows the bow shock overpressure as a function of altitude. Results in that part are shown as points, without regard to acceleration rate of flight path angle.

Note that in Part "a" of each figure, the bow-shock overpressures for level flight and one degree dive do not vary substantially with acceleration while the bow-shock overpressures for the three degree climb increases with increasing acceleration. The trend for the three degree climb is not, however, an acceleration effect. It is an altitude effect: for lower acceleration rates the aircraft reaches higher altitudes before the focus occurs. Part "b" of each figure shows that the strongest parameter is altitude. There is some variation in the cluster of results around each altitude, but the biggest effect is that amplitudes are smaller at higher altitudes.

In 1971, Hayes[12] suggested the transition focus boom may be eliminated incorporating a push-over pull-up maneuver (vertical acceleration) to cancel out the focusing caused by the forward acceleration. Haglund and Kane[23] examined the maneuver and concluded that the maneuver as

envisioned by Hayes[12] should be reversed, that the maneuver should be a pull-up followed by a push-over in order to eliminate the caustic at the ground. In their study they described the mechanism of caustic elimination and gave an indication of its feasibility for commercial SST operation. They identified several problems which included the excessive thrust required to perform the transition maneuver for a commercial SST and noted that the caustic elimination maneuver they examined was not optimized for maneuver thrust margin. They noted that the most crucial problem is the "suddenness" of the pull-up and pushover maneuver that must be initiated to terminate focusing. This must be accomplished just before threshold (cut-off) Mach number is reached, which can vary from 1.0 to over 1.3 depending upon the atmospheric conditions between the airplane and the ground. They concluded that more study is required to assess the feasibility of the maneuver.

Since SBJ's may incorporate a greater level of excess thrust, and given that significant advancements have been made on flight control-operational systems and rapid access to meteorological information, it was decided to re-examine the Hayes[12] caustic-elimination maneuver using PCBoom4[1]. The results of this effort, described in **Appendix C**, offer little encouragement that such a maneuver is realistic for commercial operations and for the same reasons cited previously.

Some thought has been given to incorporating a slow and mild roll-oscillation maneuver during transition flight to disburse/diffuse/smear the focus boom over a wider swath to each side of the ground track. It is recommended that considerably more thought and effort go into examining such maneuvers.

CONCLUDING REMARKS

A study has been undertaken to determine the influence of shaped sonic boom signatures from a small supersonic business jet on maneuver focus booms with particular emphasis on the transition phase of flight from subsonic to supersonic speeds. Six incoming boom waveforms were utilized in the study including an N-wave, a saw-tooth three-shock signature, an asymmetric flat-top and initial-shock ramp signatures and a symmetrical flat-top and minimum-shock ramp signatures. Aircraft maneuvers included variations of transition rates of accelerations, climb-to-cruise, turns at cruise and descent-deceleration to subsonic speed. Focus booms were predicted using the sonic boom prediction computer program, PCBoom4[1], which was updated for this study to accept the six-parameter Seebass/George[5] F-function model as an input (see **Appendix B)** and now allows inclusion of non-N-wave shaped signatures.

In addition, a numerical code has been developed by ODU (see **Appendix D**) with the objective of simulating the transition focus boom results of the Auger-Coulouvrat[4] numeric method for an incoming N-wave and three-shock sawtooth signatures. Comparison of the two numeric methods show that similar results were obtained with the ODU code with respect to the nature of the signatures in the pre-, post-, and focus-regions and the resulting magnitudes of the focus boom. Lower values are observed for the non N-wave Concorde sawtooth type input signature. The ODU code was then applied to the asymmetrical and symmetrical flat-top and initial-shock ramp "shaped" signatures to investigate the nonlinear focusing associated with these four incoming shaped signatures. Both the symmetric and asymmetric flat-top signatures, as expected, exhibited similar focus factor of an incoming N-wave. For the cases of symmetrical and asymmetrical initial-shock ramp signatures, a bow shape focus-factor of about two-thirds of that of an N-wave or flat-top were observed. In all cases, the tail shock focus-factor was always

greater. In the post focus region all six of the incoming signatures considered show that the refracted waveforms are still "U" shape. Although not included in the present report, the predicted refracted waveform for an incoming symmetrical ramp signature of 0.5 psf overpressure, 150 ms period and 30 ms rise times, is also "U" shaped.

The various sections of **Appendix A** collectively provide a method of determining F-function and area distributions, at off design Mach numbers, for configurations that have optimum flat-top and ramp-type signatures, as well as other shapes, at the design Mach number. When these methods were applied, at lower off-design Mach numbers, it was found that the overall character of the off-design signature is similar to that at the design cruise Mach numbers. Many have thought that at these low off-design Mach numbers that the signature would degenerate to N-waves but that is not the case. This would seem to have positive implications for reducing the magnitude of focussed booms at low Mach numbers. Also, in **Appendix A**, an equation is developed that allows one to determine the actual maximum cross-sectional area (normal cuts) from the volume contribution (fuselage) to maximum effective cross-sectional area at the design Mach number. In other words, a simple way is provided to determine if an optimum design has enough volume in the cabin for people.

A number of operational approaches for focus mitigation were also examined with regards to the operation of small supersonic business jets (see **Appendix C**). It is obvious that with the exception of transition flight, such a vehicle can and should operate in such a manner as to completely avoid generating focus booms throughout its flight profile. Minimization, and even elimination, of transition focus booms have been examined in the past and re-examined in this study using PCBoom4[1]. It is found that the focus boom can be minimized by initiating transition at higher altitudes and increasing climb angle. Acceleration rates have been found to have little influence. A revisiting of the Hayes[12] caustic-eliminating maneuver involving a pushover-pull-up maneuver is still considered impractical based upon current aircraft performance capabilities. There may be a possibility of minimizing the focus during transition by means of a maneuver involving a mild oscillating roll.

REFERENCES

1. Plotkin, K. J.; and Grandi, F.: Computer Models for Sonic Boom Analysis: PCBoom4, CABoom, BooMap, CORBoom. Wyle Rept. WR 02-11, June 2002.
2. Gill, P. M. and Seebass, A. R.: Nonlinear Acoustic Behavior at a Caustic: An Approximate Analytical Solution. Aeroacoustics: Fan, STOL, and Boundary Layer Noise; Sonic Boom; Aeroacoustic Instrumentation, Henry T. Nagamatsu, ed., American Inst. of Aeronautics and Astronautics, c. 1975, pp. 353-386 (also AIAA Paper 73-1037, 1973).
3. Guiraud, J. P.: Acoustique Geoemtrique, Bruit Balistique Des Avions Supersoniques et Focalization. J. Mech., vol. 4, no. 2, June 1965, pp. 215-267.
4. Auger T. and Coulouvrat, F.: Numerical Simulation of Sonic Boom Focusing. AIAA Jour. Vol. 40, No. 9, Sept. 2002, pp. 1726-1734.
5. George, A. R., and Seebass, A. R.: Sonic Boom Minimization Including Both Front and Rear Shocks. AIAA Journal, 9(10), pp, 2091-2093. Oct. 1971.
6. Mack, Robert J.: A Supersonic Business-Jet Concept Designed for Low Sonic Boom. NASA TM-2003-212435, Oct. 2003

7. Darden, Christine A.:Sonic Boom Minimization with Nose-Bluntness Relaxation. NASA TP 1348, 1979.
8. Mack, R. J. and Darden, C. M.: A Wind-Tunnel Investigation of the Validity of a Sonic Boom Minimization Concept. NASA TP-1421, 1979.
9. Marchiano, R. and Coulouvrat, F.: Numerical Simulation of Shock Wave Focusing at Fold Caustics with Application to Sonic Boom. J. Acoust. Soc. Am. 114(4), Pt. 1, Oct. 2003, pp. 1758-1771.
10. Lansing, D. L.: Application of Acoustic Theory to Prediction of Sonic-Boom Ground Patterns from Maneuvering Aircraft. NASA TN-D-1860. Oct. 1964.
11. Barger, R. L.: Sonic-Boom Wave-Front Shapes and Curvatures Associated With Maneuvering Flight. NASA TP 1511, Dec. 1979.
12. Hayes, Wallace D.: Sonic boom. Annual Review of Fluid Mechanics. Vol. III, M. Van Dyke et al, Eds. Annual Review, Inc. (Palo Alto, CA), 1971, pp. 269-290.
13. Rosales, R. R. and Tabak, E. G.: Caustics of Weak Shock Waves. Phys. of Flds., Vol. 10, 1998, pp. 206-222, Jan. 1998.
14. Tabak, E. G.; and Rosales, R. R.: Focusing of Weak Shock Waves and the von Neumann Paradox of Oblique Shock Reflection. Phys. of Flds., Vol. 6, May 1994, pp. 1874-1892.
15. Coulouvrat, F.: Focusing of Weak Acoustic Shock Waves at a Caustic Cusp. Wave Motion. Vol. 32, 2000, pp. 233-245.
16. Kuznetsov, V. P.: Equations of Nonlinear Acoustics. Soviet Physical Acoustics. Vol. 16, 1970, pp. 467-470.
17. Haglund, G. T. and Kane, E. J.: Effect of SST Operational Maneuvers on Sonic Boom. J. Aircraft, Aug. 1972, pp. 563-568.
18. Wanner, J.C.L.; Vallee, J.; Vivier, C.; and Thery, C.: Theoretical and Experimental Studies of the Focus of Sonic Boom. Proceedings of the Second Sonic Boom Symposium (1970), J. Acous. Soc. Am., Vol. 52, No. 1, 1972, pp. 52-71.
19. Ribner, H. S.: Supersonic Turns Without Superbooms. UTIAS Technical Note No. 174, also AFOSR-TR-0239, Jan. 1972.
20. Downing, J. M.; Zamot, N.; Moss, C.; Morin, D.; Wolski, E.; Chung, S.; Plotkin, K.; and Maglieri D. J.: Measurement of Controlled Focused Sonic Booms From Maneuvering Aircraft. J. Acoust. Soc. Am., 104(1), 112-121, July 1998.
21. Maglieri, D. J.; Hilton, D. A.; and McLeod, N. J.: Further Experiments of Atmospheric Retraction and Aircraft Accelerations on Sonic Boom Ground Pressure Patterns. NASA TN-D-3520, July 1966.
22. Downing, Micah; Zamot, Noel; Moss, Chris; Moran, Daniel; Wolski, E.; Chung, Sukhway; Plotkin, Kenneth; and Maglieri, Domenic J.: USAF Flight Investigation of Focused Sonic Booms. Project "Have Bears," NASA CP-3335, pp. 259-277, July, 1996.
23. Haglund, George T. and Kane, Edward J.: Analysis of Sonic Boom Measurements Near Shock Wave Extremities for Flight Near Mach 1.0 and For Airplane Accelerations. NASA CR 2417, July 1974.

Table 1: Influence of acceleration rate and altitude on focusing during transition flight in standard atmosphere. Concorde sawtooth type incoming signature (from ref. 4).

Acceleration $m \cdot s^{-2}$	Mach	μ	$\overline{P}_a^{max}$	P_0,Pa	p^{max},Pa	$\bar{z}(\overline{P}_a^{max})$	Boundary-layer thickness, m
				11.500 m			
0.2	1.161	0.0751	2.9047	51.5933	149.8631	0.1026	500.3414
0.4	1.1742	0.0746	2.8053	51.9724	145.7982	0.1037	484.4704
0.6	1.1881	0.0772	2.8635	52.0731	149.1113	0.1043	479.8086
0.8	1.2018	0.0793	2.8794	51.8124	149.1886	0.1009	479.1981
1.0	1.2149	0.0799	2.9219	52.9147	154.6115	0.1037	462.7679
				12.000 m			
0.2	1.1611	0.0689	2.8343	49.4604	140.1856	0.0980	489.1740
0.4	1.1745	0.0738	2.9534	48.8129	144.1640	0.1020	498.4926
0.6	1.1887	0.0750	2.8371	49.2570	139.7470	0.1032	487.3308
0.8	1.2026	0.0764	2.7920	49.9749	139.5299	0.1066	474.4114
1.0	1.2160	0.0773	2.8671	50.4399	144.6162	0.1026	465.8065
				12.500 m			
0.2	1.1611	0.0728	2.9222	46.1063	134.7318	0.0992	523.8691
0.4	1.1747	0.0725	2.9063	47.4471	137.8955	0.1009	494.0023
0.6	1.1892	0.0759	2.9127	46.8411	136.4341	0.1026	501.0383
0.8	1.2034	0.7490	2.7785	47.0229	130.6531	0.0997	488.0990
1.0	1.2172	0.0730	2.8975	47.9370	138.8975	0.9970	465.1803

Symbols:

μ = measurements of nonlinear effects relative to diffraction

$\overline{P}_a^{max}$ = maximum amplitude of dimensionless acoustic pressure

p_0 = ambient pressure at rest

$\bar{z}$ = dimensionless distance to the caustic
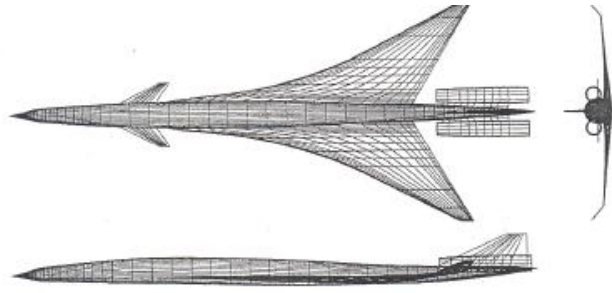
(a) Three-view of low boom SBJ concept.

Length	132.5 ft.
Span	55 ft.
Wing Area	1560.25 ft.^{2}
TOGW	99,435 lbs.
OEW	41,434 lbs.
Range	4000 n. mi.
Cruise Mach	2.0

(b) Airplane characteristics.
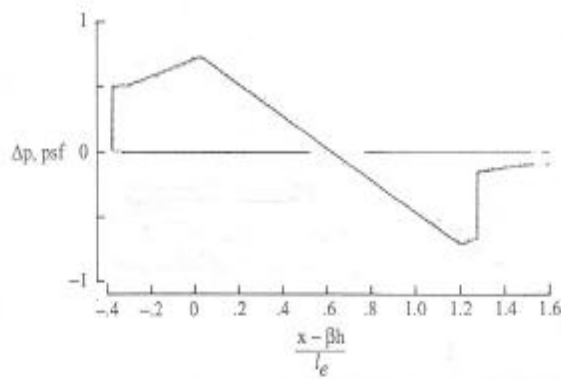
(c) Design ground signature.

Figure 1. - Low boom supersonic business jet concept selected for study (from ref. 6).
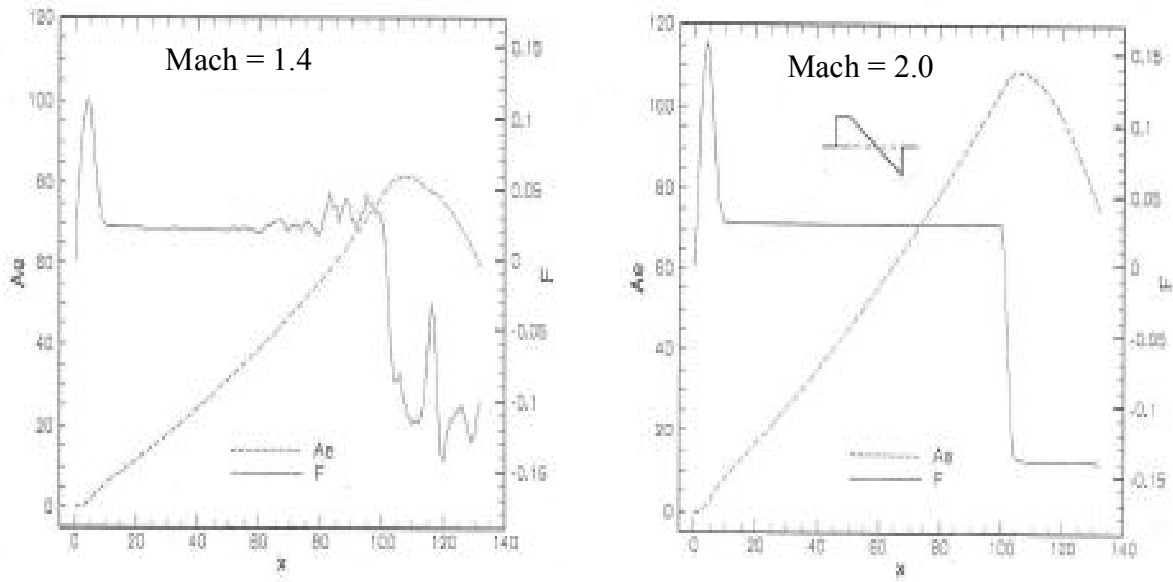
(a) Asymmetric flat-top configuration.
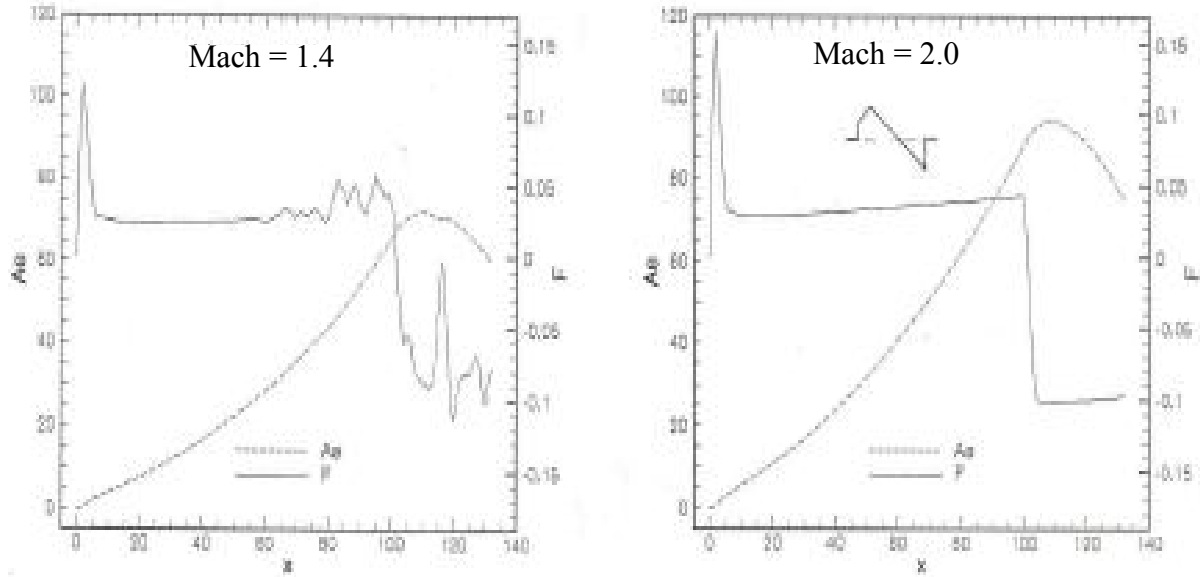
(b) Asymmetric initial-shock ramp configuration.

Figure 2. - Comparison of F-functions and equivalent area distributions for two
configurations at M = 1.4 and M = 2.0
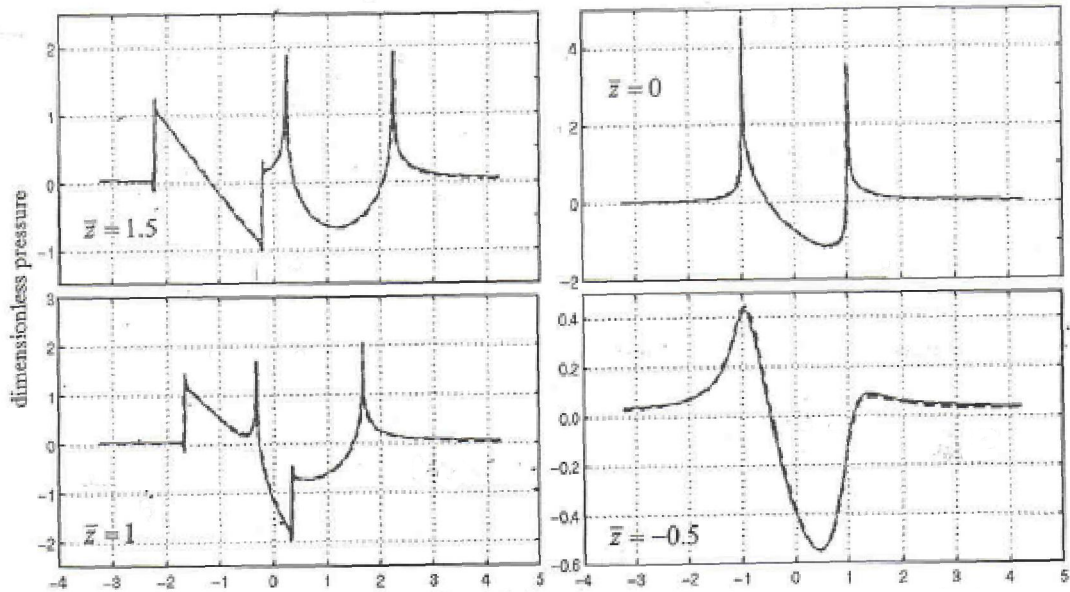
dimensionless phase variable

Comparison between analytical (---) and numerical (—) solutions in the linear case at $\bar{z}$ = 1.5, 1, 0 (caustic), and -0.5 (shadow) for incoming N-wave..
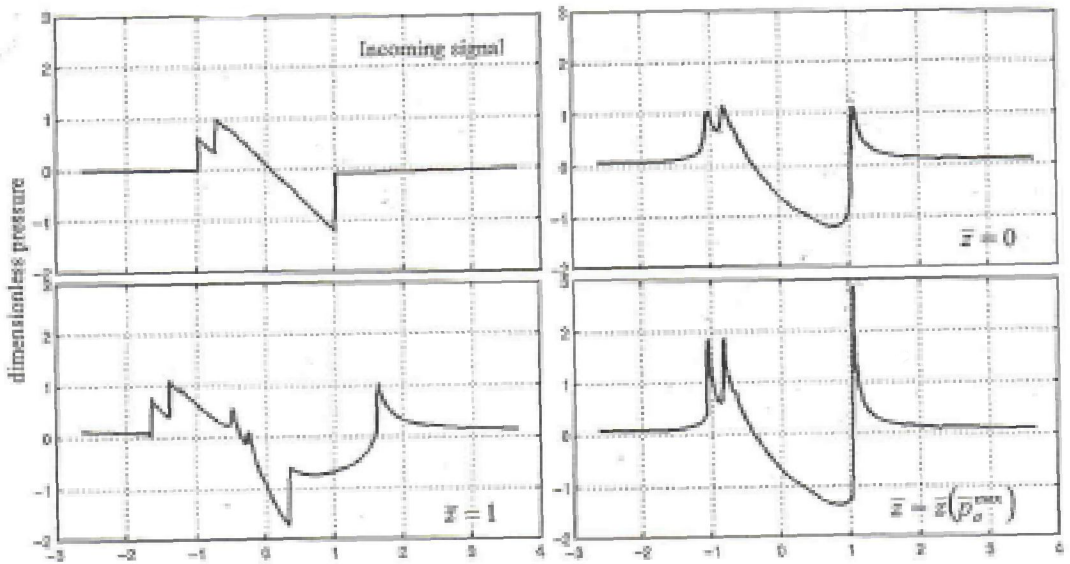
dimensionless phase variable

Numerical simulation of Concorde sonic boom ground track focusing due to constant acceleration (0.6 ms^{-2}) and horizontal flight (altitude 12 km) in standard atmosphere: incoming signal and dimensionless simulations at three different distances.

Figure 3. - Influence of incoming sonic boom signature on focus boom during transition flight (from ref. 4).

τ (dimensionless time)
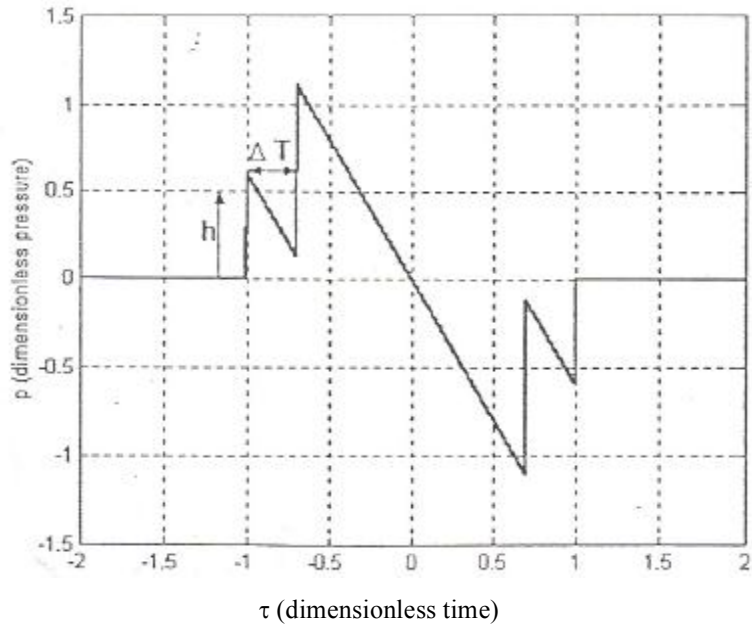
"Optimized" signal where the nose and leading edge shocks have not yet merged.
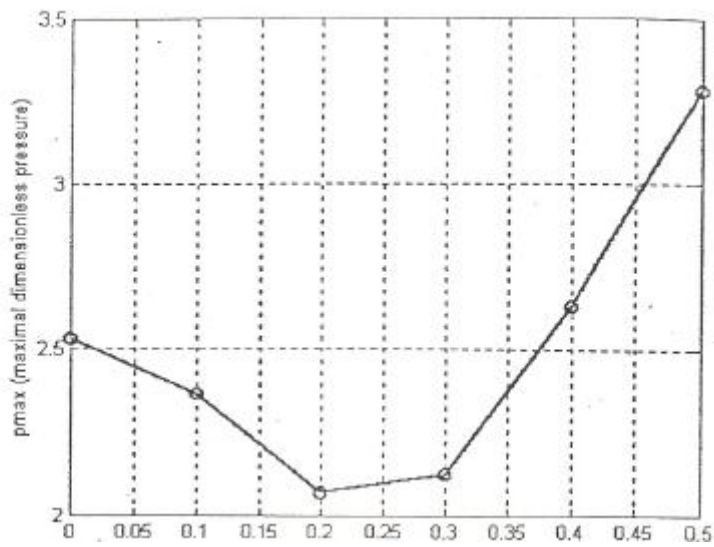
Interval between the two shocks, ΔT (dimensionless time).

Maximal overpressure as a function of the time interval between the nose and the leading edge shocks.

Figure 4. - Effect of shock-spacing on focus boom overpressure for a symmetrical multi-sonic boom incoming signature during transition flights (from ref. 9).

Asymmetric flat-top   Asymmetric initial-shock ramp
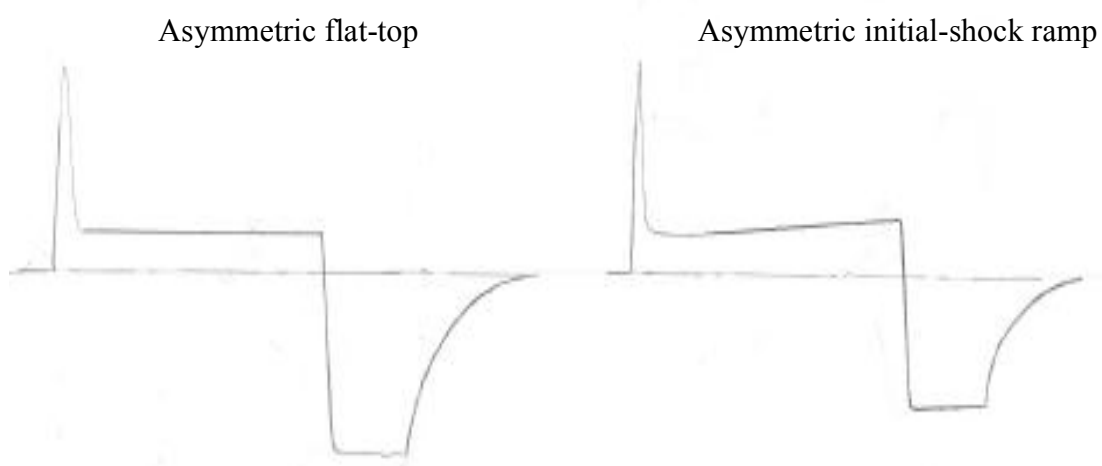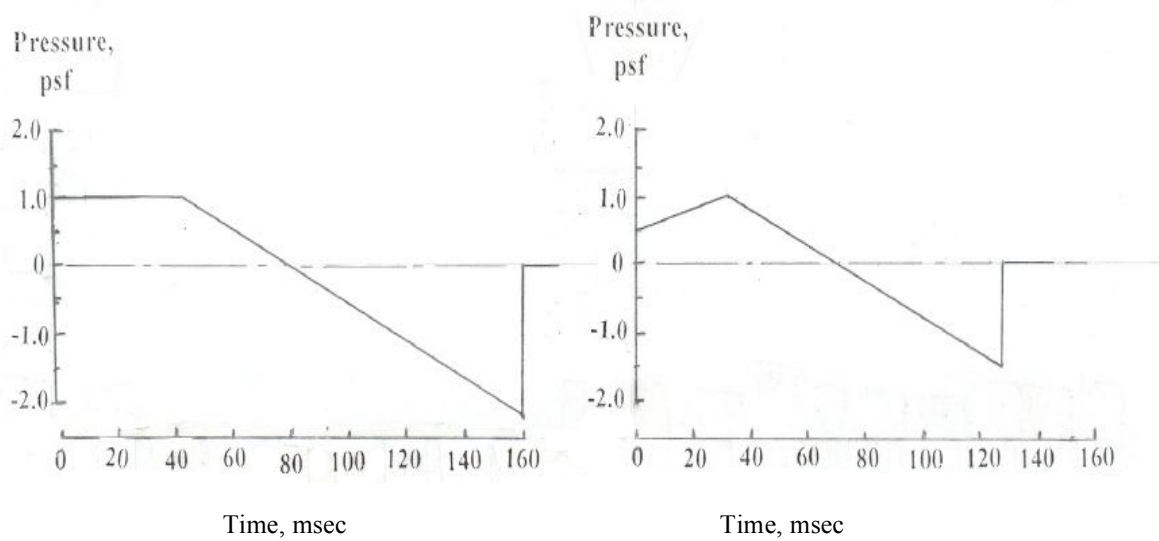
(a) F-functions.

(b) Ground signatures

Figure 5. - Aging of F-functions for two shaped configurations using PCBoom4 for
M = 2.0 and 41,000 ft. altitude.

19

Focus

Time, milliseconds

Time, milliseconds

Carpet

(a) Asymmetric flat-top

(b)   Asymmetric initial-shock ramp
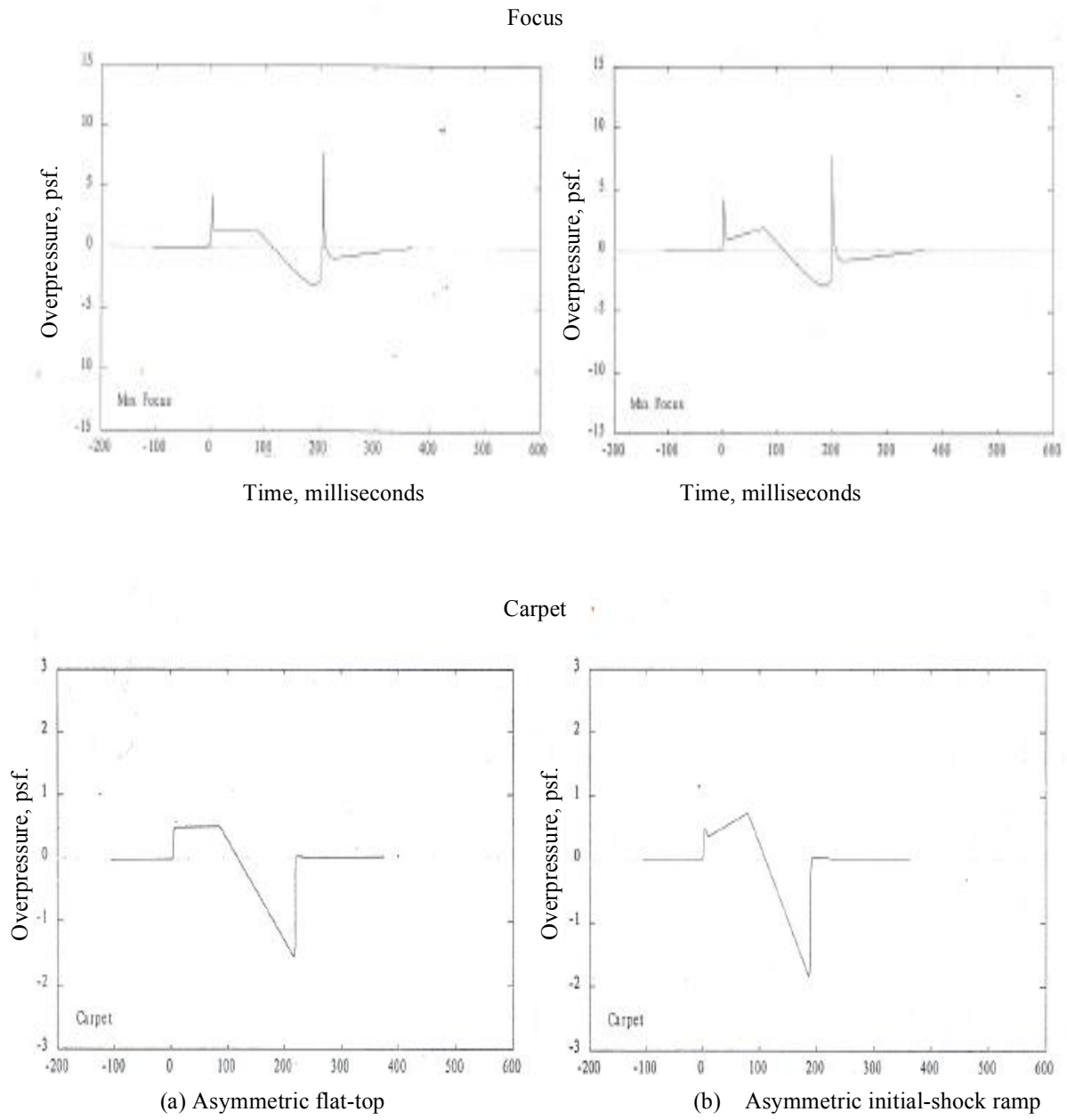
Figure 6. - Predicted focus and carpet boom signatures during transition flight using
PCBoom4. Level flight at 32,850 ft. altitude and an acceleration rate of 0.6 m/sec^2.
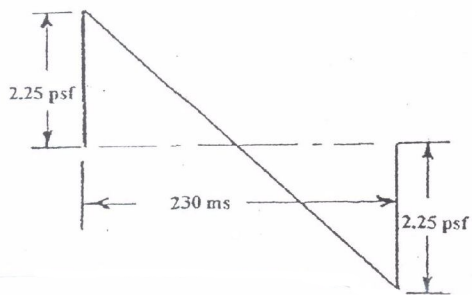
Symmetric N-wave.
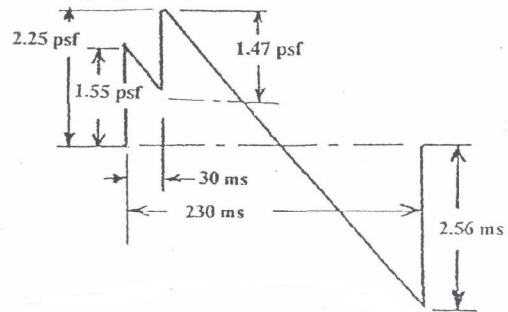
Concorde three shock.
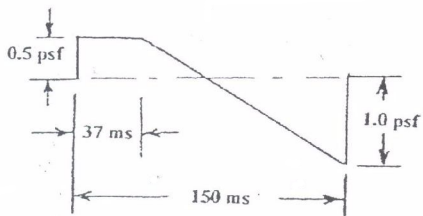
Asymmetric flat-top.
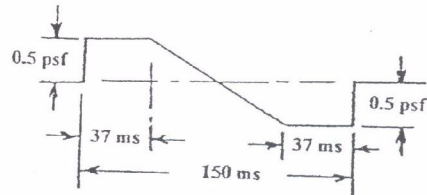
Symmetric ramp.
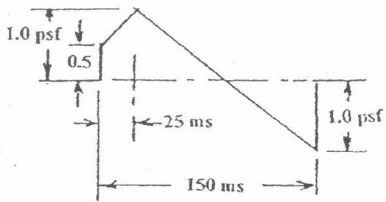
Asymmetric initial shock ramp.
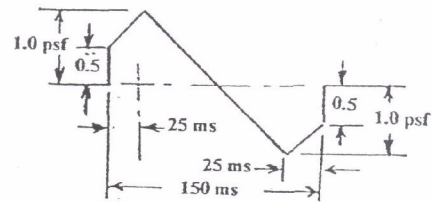
Symmetric initial shock ramp.

Figure 7. - Descriptions of six incoming signatures examined using
Old Dominion numerical code.
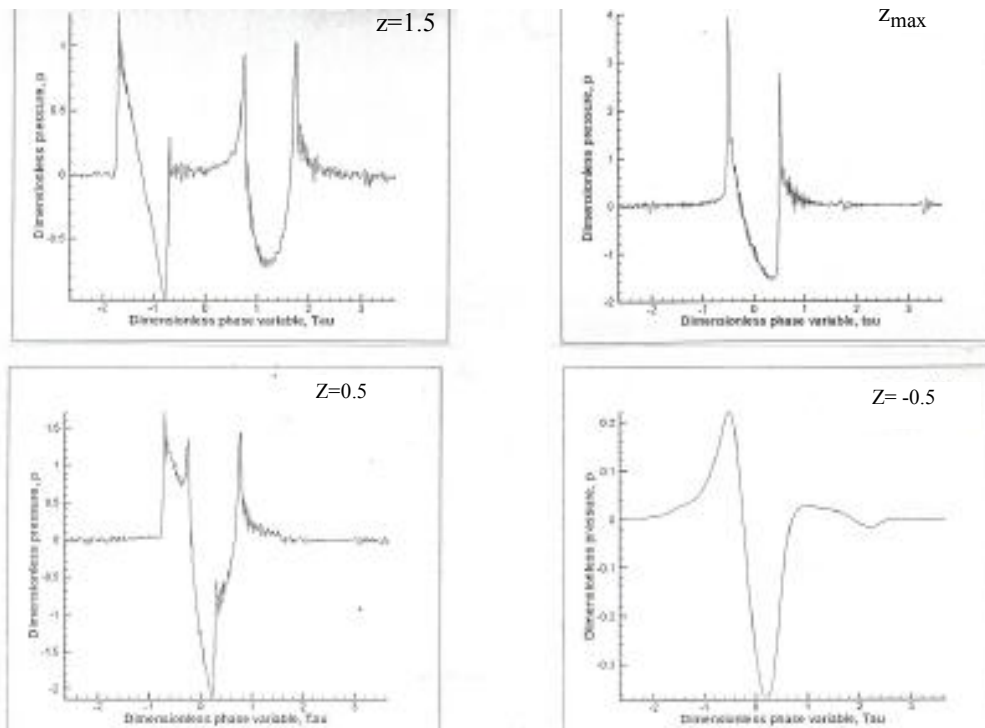
(a) N-wave incoming signature.
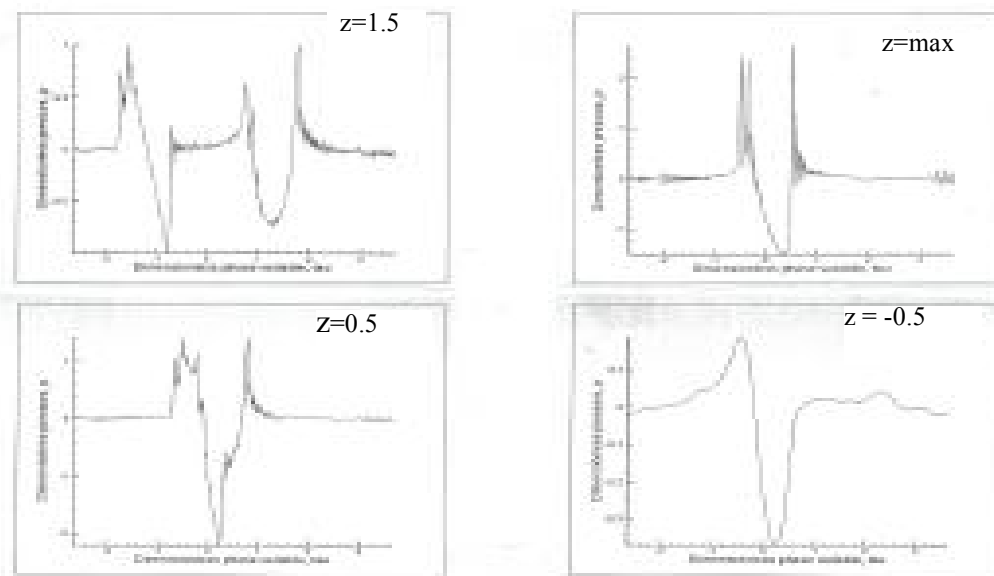
(b) Concorde three-shock saw-tooth incoming signature.

Figure 8. - Predicted signatures for level transition flight for an N-wave and Concorde 3-shock incoming signatures using Old Dominion University numerical code.
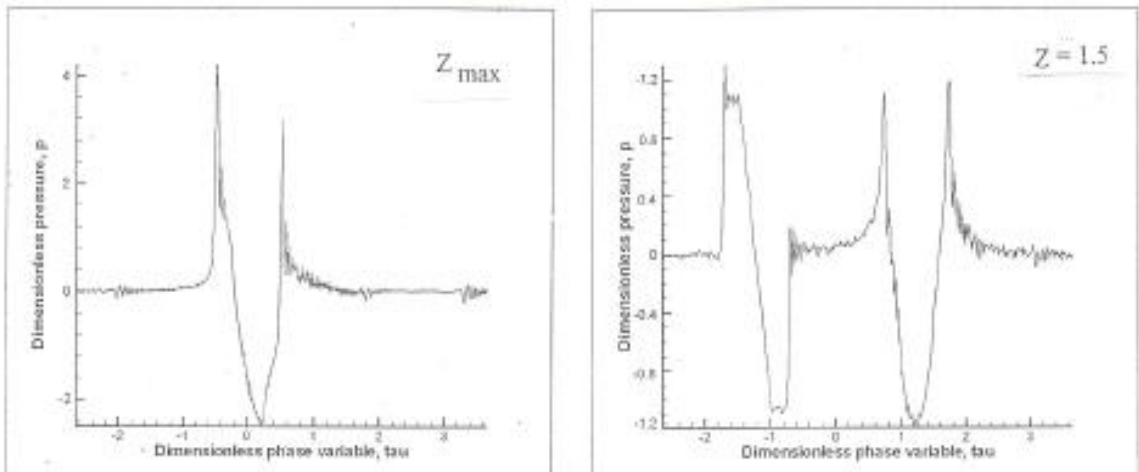
(a) Symmetrical flat-top incoming signature.
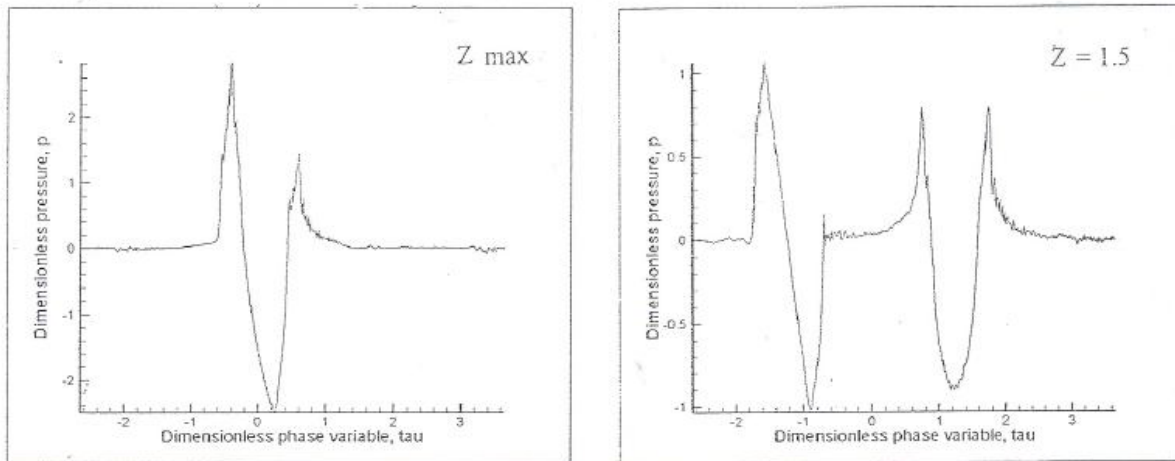
(b) Symmetrical initial-shock ramp incoming signature.

Figure 9. - Predicted signatures at maximum focus and post-focus during transition
using the Old Dominion University (ODU) code.

(a) For incoming signature overpressures.

(b) With overpressures normalized to a maximum positive shock of 1.0.

(c) Focus overpressures in (a) divided by incoming signature values.
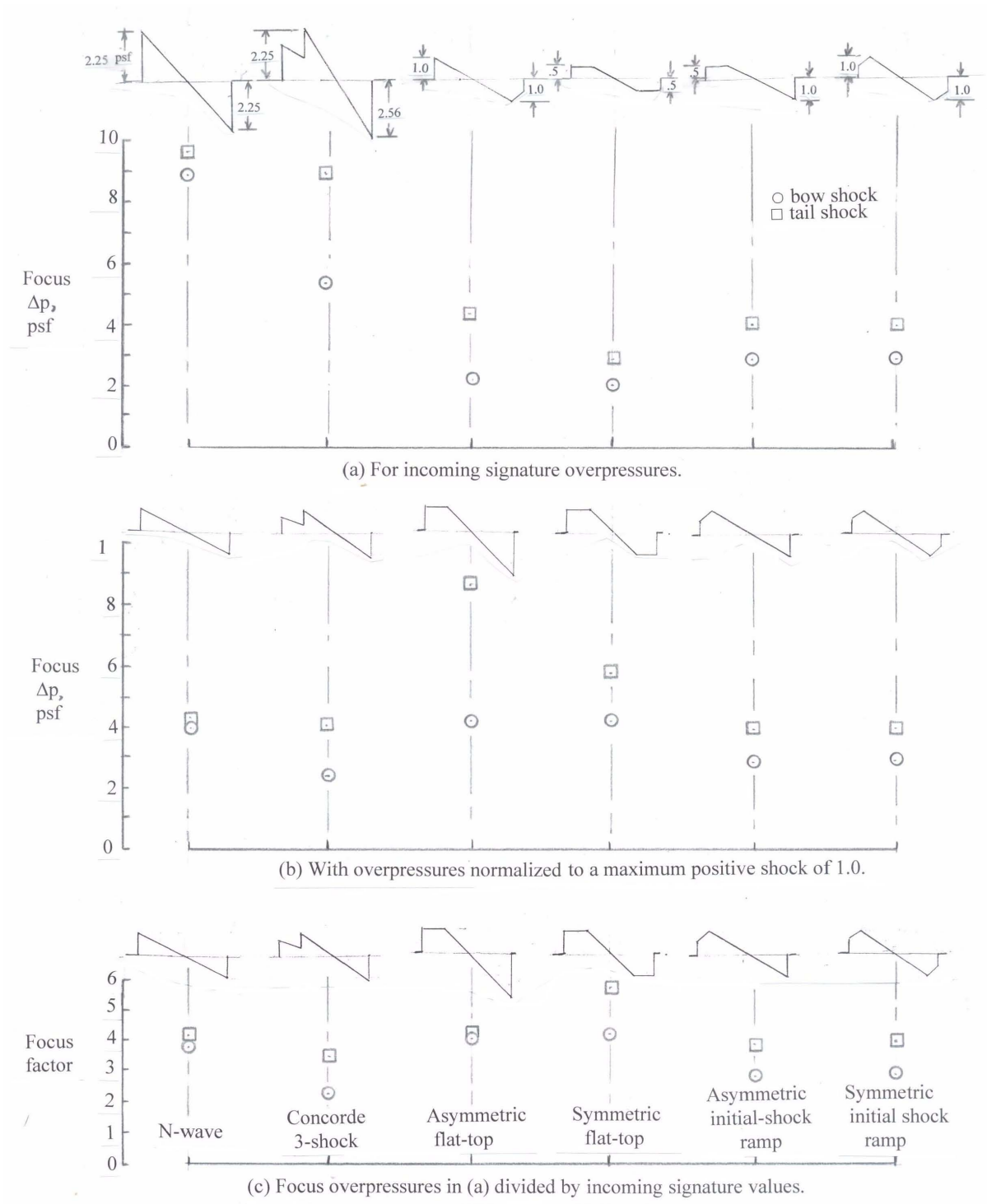
Figure 10. - Summary of predicted bow and tail shock focus overpressures and focus factor associated with six sonic boom signatures. Horizontal flight at 12 km altitude and constant acceleration rate of 0.6 ms.
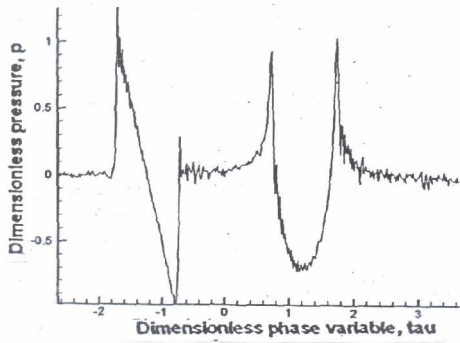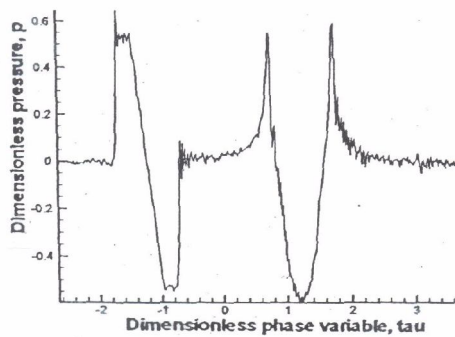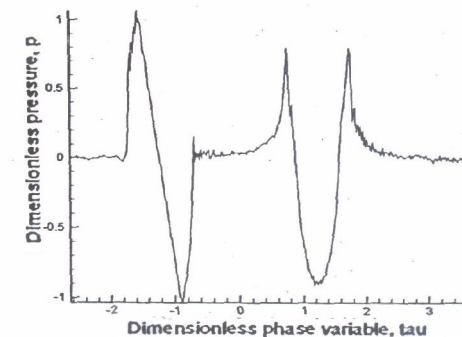
(a) N-wave.
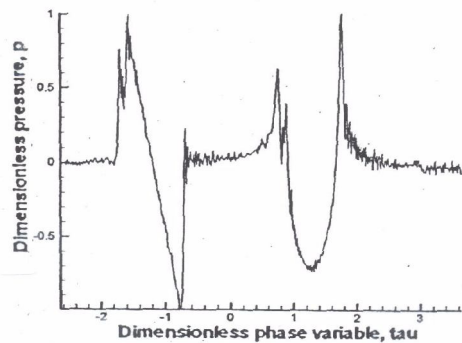
(b) Concorde 3-shock.
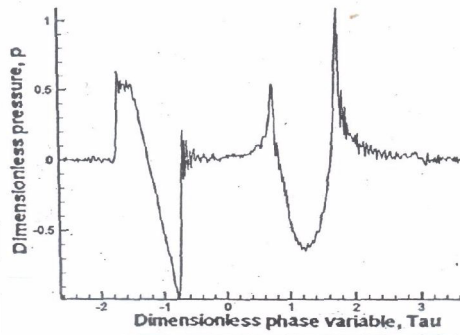
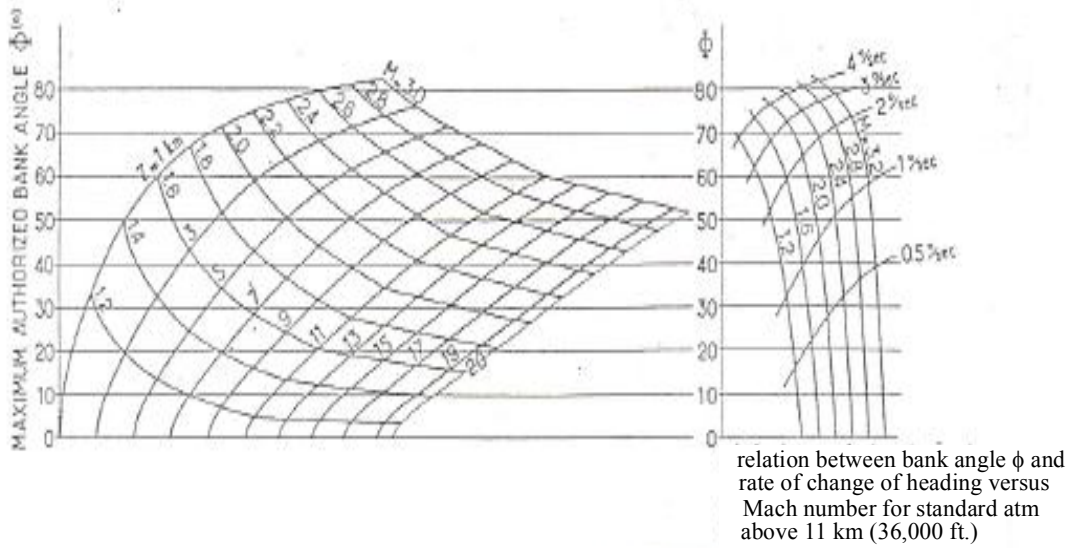(c) Asymmetric flat-top.
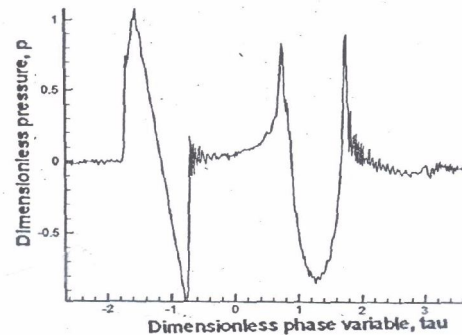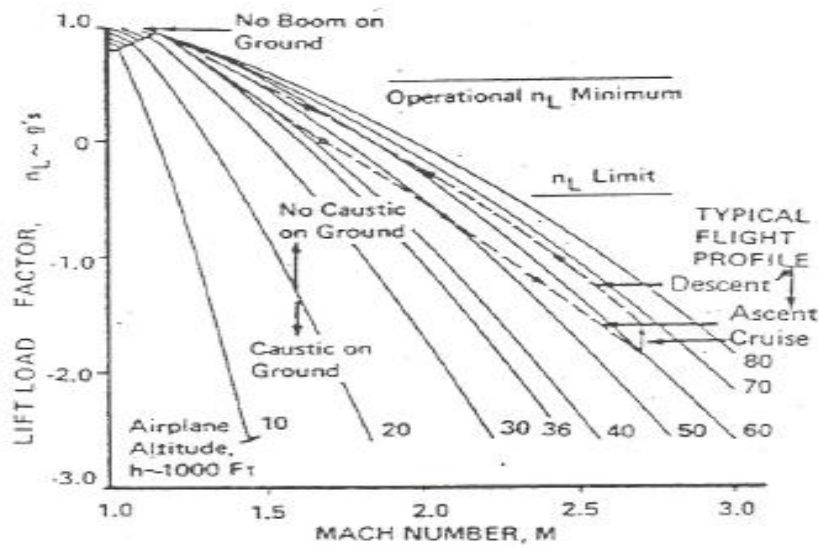
(d) Asymmetric initial-shock ramp.

(e) Symmetric flat-top.

(f) Symmetric initial-shock ramp.

Figure 11. - Pressure variation for various incoming signatures in the post-focus region (Z=1.5) and nf = 20,000 steps.

relation between bank angle ϕ and rate of change of heading versus Mach number for standard atm above 11 km (36,000 ft.)
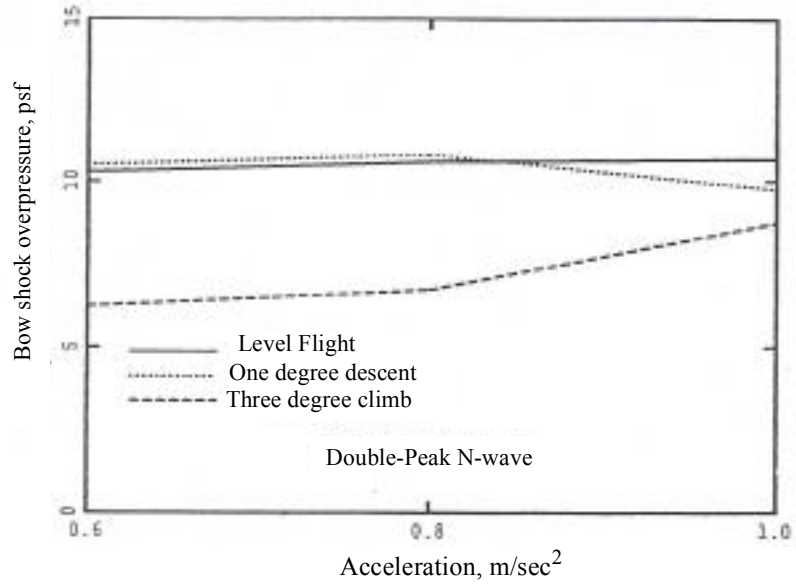
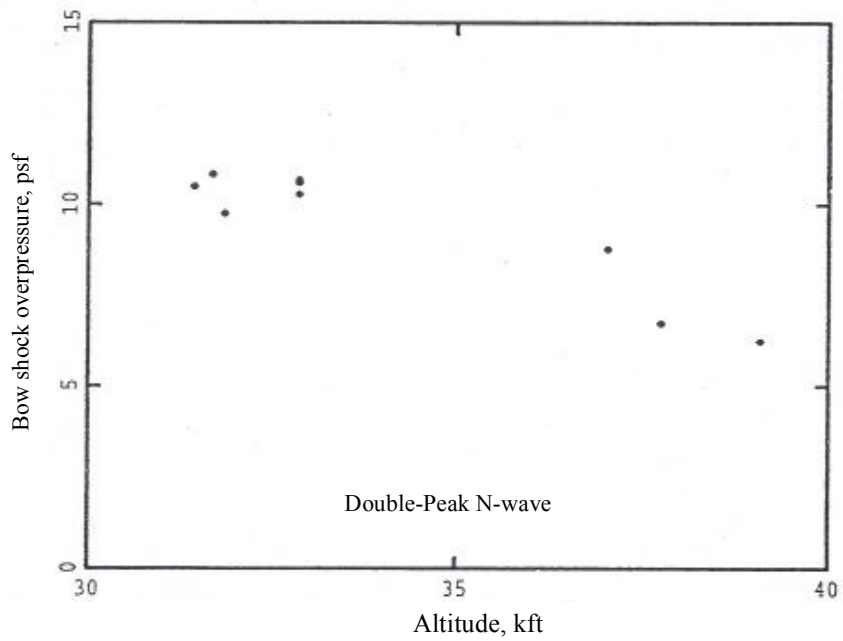(a) Maximum authorized bank angle in order to avoid focus during turn maneuvers (ref. 18).

(b) Pushover requirements for caustic formation on the ground (ref. 17).

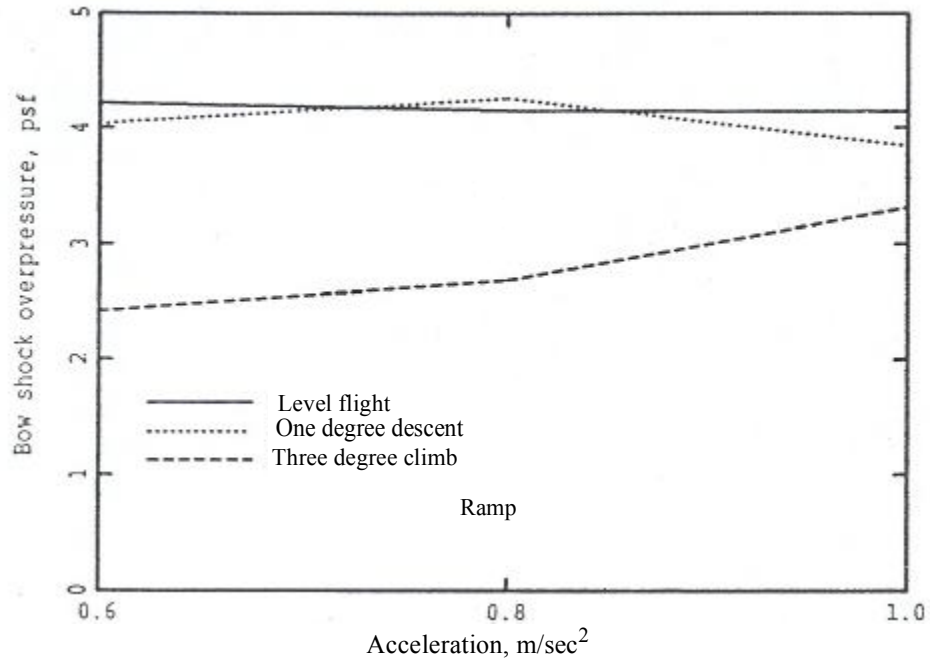Figure 12. - Examples of focus boom avoidance operational charts.

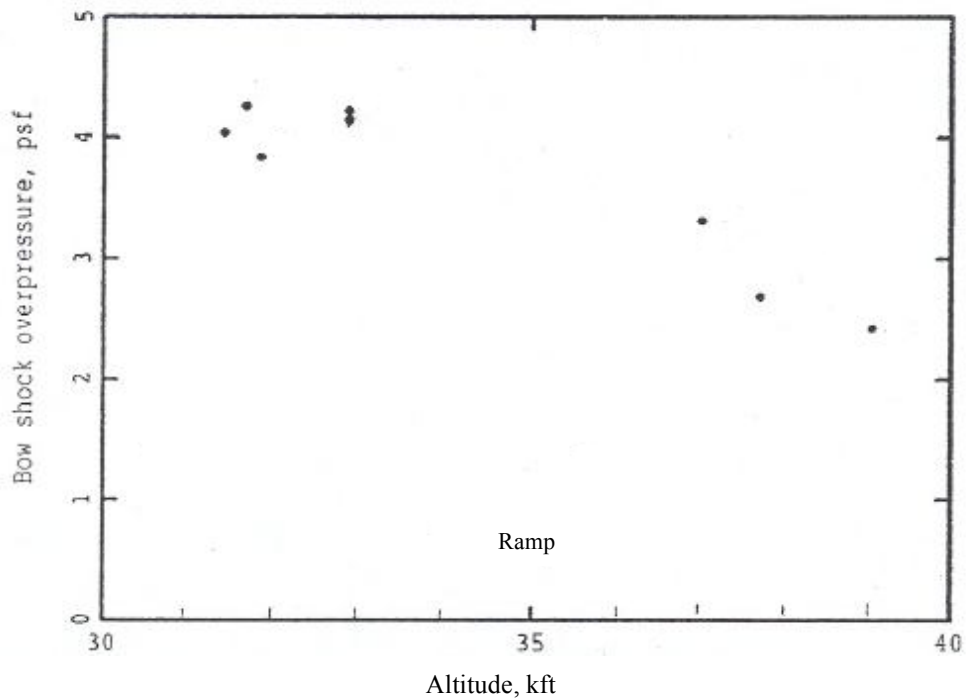(a) Effect of acceleration on overpressure for three flight path angles.

(b) Effect of altitude on overpressure.

Figure 13. - Effect of acceleration, flight path angle and altitude on overpressure for a double peak N-wave signature.

(a) Effect of acceleration on overpressure for three flight path angles.

(b) Effect of altitude on overpressure

Figure 14. - Effect of acceleration, flight path angle and altitude on overpressure
for a ramp signature.

Appendix A

**The Calculation of Design and Off-Design Effective Area
Distributions and F-Function for Minimum Boom Supersonic-Cruise Aircraft**

by Percy J. Bobbitt and Steven J. Massey
Eagle Aeronautics, Inc.

The aerodynamic design of low-boom supersonic cruise aircraft can be carried out in a number of ways. An aircraft's lines can be laid out using "common sense" principals with the knowledge that a long slender, lightly loaded design is more likely to have a lower boom than a heavily loaded design with a "modestly" swept wing. It is also known that being slender is not a guarantee of a low boom. The "right" longitudinal distribution of the combined volume and lift is critical, independent of how it is achieved. Different levels of technology can also be used singularly or in combination. The whole job can be done using Euler and Navier Stokes CFD codes coupled with the appropriate grid software and optimization schemes. It can also be done using a combination of CFD and "Mach-plane-cut" technology where the overall effective volume (Mach cuts) and lift distributions are driven toward a theoretically defined optimum distribution. The latter being one that yields a flat-top, ramp-type, or a combination of these two, sonic booms with low initial and tail shock strengths. It also should be one permitting a realistic diameter fuselage and lift distribution necessary for the anticipated start-of-cruise-weight. The simple equation

$$W = \frac{2q_\infty}{\beta} A_{e,\iota}$$

allows one to estimate the effective area due to lift at the design point at the downstream end of the configuration. Since W = lift, the angle of attack required to produce the necessary lift can also be determined from a variation of lift with angle of attack. The latter can be obtained using a CFD code or, in preliminary design, linear methodology. In Section B of this appendix, a linear method for determining the longitudinal accumulation of lift for highly swept wings is described.

The optimum total effective area distribution required for a "starting point", when the first-cut configuration lay-out and weight estimates have been made, can be calculated using Darden's equations and program contained in reference 1 of Section A of this appendix. An F-function and associated total effective area distribution must be defined iteratively to insure that once the effective area distribution due to lift has been determined and subtracted from the total optimum area distribution that the volume distribution remaining is sufficient for both the wing and fuselage.

It must be remembered that the optimum design is at the design Mach number and the combined wing and fuselage volume contribution is a result of taking Mach-plane cuts at that Mach number and/or from the use of methodology like that of Darden in Reference 1 of Section A. If the Mach-plane cuts of a pre-defined fuselage and wing, plus the effective area distribution due to lift do not match the optimum, then modifications must be made or the optimum redefined.

Another and simpler approach is to leave the fuselage lines undefined initially and determined them by successively redefining the optimum and subtracting out the lift distribution until a realistic volume distribution is achieved. This latter step, however, requires that the design-Mach effective area distribution can somehow be used to determine the normal or Mach 1.0 cuts (the actual geometry). In section C a method is presented to accomplish this.

Once volume and lift distributions are achieved that are adequate (realistic) and conform to the optimum, then the effective distributions of volume and lift, and hence total effective area, for other Mach numbers can be determined. These effective area distributions can be used in turn to determine the F-function for these off design Mach numbers.

The equations for these tasks are defined in subsequent sections where in some cases existing methodology is refined and in others new derivations are offered.

There are five subsequent sections that treat the following subjects:
    A. Effective Area Distribution and Design Parameters for a Supersonic Executive Jet.
    B. Effective Area Distribution due to Lift for a Slender Wing With Subsonic Leading Edges.
    C. Determination of Basic (M = 1) Axisymmetric Geometry From the Design Effective Volume Distribution.
    D. Method of Determining F-Function at Off-Design Mach Numbers.
    E. Effective Area and F-Function Distribution for Executive Jet at Off-Design Mach Numbers.

Section E uses the methodology of Sections A, B. C. and D to calculate the total A_e and the associated F functions for Mach numbers of 1.2, 1.3, 1.4, 1.5, 1.6, 1.8, and 2.0.

There is no attempt in this appendix to design an optimum, low boom aircraft. However, the quantities used in the F-function analyses do yield an aircraft of usable dimensions. The various sections, collectively, provide a method of determining the F-function and area distributions, at off design Mach numbers, for configurations that have optimum flat-top and ramp-type signatures, as well as other shapes, at the design Mach number. When these methods were applied, at lower off design Mach numbers, they showed that the "optimum" configurations still maintained their basic flat-top and ramp-type F-function signature shapes. This capability could be useful in determining the acceleration focused booms of configurations which have flat-top or ramp-type F-function signatures at the design Mach number

Finally, a simple equation is developed in Section C that allows one to determine the actual maximum cross-sectional area (normal cuts) from the maximum effective cross-sectional area at the design Mach number.

A. Effective area Distribution and Design Parameters for a Supersonic Executive Jet

The definition of an optimum flat-top or ramp signature begins with the effective area-distribution equation of Darden (ref. 1).

$$
\begin{aligned}
A_e(x) = \ & \frac{32}{15}\frac{H}{y_f}x^{5/2} + 1\left(x - \frac{y_f}{2}\right)\frac{8}{15}\left(x - \frac{y_f}{2}\right)^{3/2}\left[\left(\frac{3y_f}{2} + 2x\right)\left(\frac{1}{y_f}\right)(2C - 4H)\right. \\
& + 5(2H - C)\Bigg] + 1(x - y_f)4(x - y_f)^{3/2}\left[\left(\frac{2C}{y_f}\right)\left(-\frac{2}{15}\right)(3y_f + 2x) + \frac{2}{3}C\right. \\
& + \frac{4}{15}\left(\frac{H}{y_f}\right)(3y_f + 2x) - \frac{4}{3}H + \frac{2}{15}B(3y_f + 2x) - \frac{2}{3}By_f + \frac{2}{3}C\Bigg] \\
& - 1(x - \lambda)\frac{8}{3}(x - \lambda)^{3/2}(C + D)
\end{aligned}
$$

(A1)

(Note in subsequent equations the y coordinate in equation (A1) has been changed to x.)

where $1(x - \bar{x})$ is the Heaviside unit step function. Equation (A1) derives from the integral equation for $A_e(r)$ based on the F-function defined initially by Seebass and George in reference 2 and further developed by Darden in reference 1. This integral equation is given below.

$$
A_e(x) = A\int_o^x F(\xi)(1 - \xi)^{1/2}d\xi
$$

(A2)

with the F-function defined as

|		
$F_x = 2xH/x_f$	$0 \le x \le x_f/2$	(A3a)
$F_x = C(2x/x_f - 1) - H(2x/x_f - 2)$	$x_f/2 < x < x_f$	(A3b)
$F_x = B(x - x_f) + C$	$x_f < x < \gamma$	(A3c)
$F_x = B(x - x_f) - D$	$\gamma < x < l$	(A3d)

A typical form of the resulting area distribution A_e is seen in figure A1 from reference 1. A discussion of the original formulation of the F-function and associated code is given in **Appendix B.**

The equation above can be simplified to

$$
A_e(x) = \frac{32}{15}\frac{Hx^{5/2}}{x_f} - 1\left(x - \frac{x_f}{2}\right)\frac{16}{15}\left(x - \frac{x_f}{2}\right)^{5/2}\left(\frac{2H - C}{x_f/2}\right)
$$

(A4)

$$
+ 1(x - x_r)\frac{16}{15}(x - x_f)^{5/2}\left(\frac{2H - 2C}{x_f} + B\right) - 1(x - \lambda)\frac{8}{3}(x - \lambda)^{3/2}(C + D)
$$

which, because of its compactness, enables better insight into the effect of the various parameters on the distribution A_e and the value at x = l. The latter is particularly important since the distribution of A_e due to lift (a component of the total A_e) is usually known and its maximum value which is at the wing trailing edge is maintained downstream (see sketch).

Sketch Showing Effective Area Breakdown.
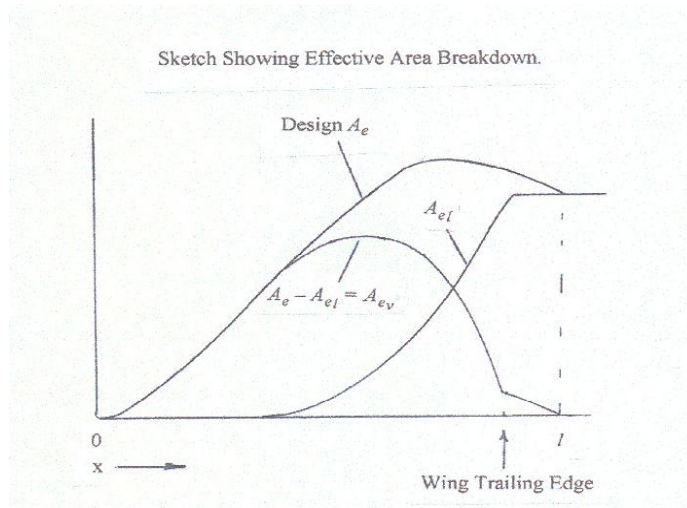
Another aspect of the compact form of A_e is that it shows that the area on the compression side of the signature, controlled by the first three terms, varies as the five halves power of x.

Thus the maximum of the effective volume contribution ($A_{e,v} = A_e - A_{e,l}$) as well as the length of the configuration can be controlled. This is aided by the following equation which relates the maximum cross-sectional area of the basic configuration to the maximum effective volume at the design Mach number (derived in Section C entitled *"Determination of Basic (M=1) Axisymmetric Geometry from the Design Effective Volume Distribution"*).

$$(A_{e_v})_{M=1} = \frac{(A_{e_v}) Design Mach}{M} \qquad (A5)$$

This equation can also be used to insure that the basic configuration has the required size. Note that A_{e_v} includes all configuration components.

To illustrate the use of these equations, the optimum A_e distribution, yielding a flat-top sonic boom, for a supersonic executive jet at $M = 2.0$ is plotted in figure A2 along with the associated F-function. The F-function parameters that yield the effective area distribution of figure A2 are given in the table A1 below. See figure A1 for the relationship of the parameters H, x_f, λ, C, D, B, and l to the F-function.

Table A1. - Values of quantities required to define F-function for flat-top signature case.

F-Function Parameters
H = 0.2
y_f = 8
C = 0.03
D = 0.13969
B = 0
λ = 102
l = 132

F-function at x = 132 and beyond	
x	F
132	0.130
134	0.130
135	0.109
136	0.0945
137	0.0845
138	0.07716
139	0.07143
140	0.06682
141	0.06300
142	0.05976

The weight of this aircraft at the start of cruise is 90,500 pounds and the start-of-cruise altitude is 41,000 feet. A plot of the propagated flat-top pressure signature on the ground (sonic boom) for this aircraft is shown in figure A3.

A similar analysis was carried out for an aircraft with the ramp-type signature where the F-function had the following input parameters and values listed in table A2.

Table A2. - Values of quantities required to define F-function for first ramp signature case.

F-Function Parameters
H = 0.2
y_f = 4
C = 0.02
D = 0.128076312
B = 0.00022
λ = 102
l = 132

F-Function at x = 132 and beyond	
x	F
132	0.142
134	0.142
135	0.11406
136	0.9878
137	0.08835
138	0.08065
139	0.07467
140	0.06985
141	0.06585
142	0.06247

The weight, altitude and Mach number are the same as the "flat-top" case. A plot of the total A_e and the associated F-function for the ramp case is given in figure A4. The propagated signature on the ground, yielded by the above F-function, is shown in figure A5. The maximum A_e for this case is approximately 95. When the effective area due to lift is subtracted, the remaining area distribution due to volume was determined, using equation (A5), to be too small for a realistic executive aircraft. When using an optimum area distribution, such as that provided by equation (A4), this is one of the checks that must be made. Consequently, a "second" ramp type configuration and F-function were defined with the following higher B, C, and D Values.

B = 0.00025
C = 0.025
D = 0.181196935

With respect to the first ramp-signature case the value of D was adjusted to yield a more negative value of F at x = 132 of -0.15. A plot of the A_e and associated F- function for the second ramp-signature case is given in figure A6. Note that the maximum A_e value has increased to 110 which is comparable to the flat- top signature case (Figure A2). The propagated signature on the ground for this case is shown in figure A7. It is evident from figure A7, with the increase in volume over the first ramp-case, that the initial shock strength, the maximum pressure, and the trailing shock strength have all increased. However, the initial shock strength is still substantially lower than that of the flat top (Figure A3).

Reference 1: Darden, Christine A.: Sonic Boom Minimization with Noise Blunted Relaxation. NASA TP-1348, 1979.
Reference 2: Seebass R.; and George, A. R.: Sonic Boom Minimization, Jour. Acous. Soc. of America, Vol. 51, No. 2 (Part 3), 1972
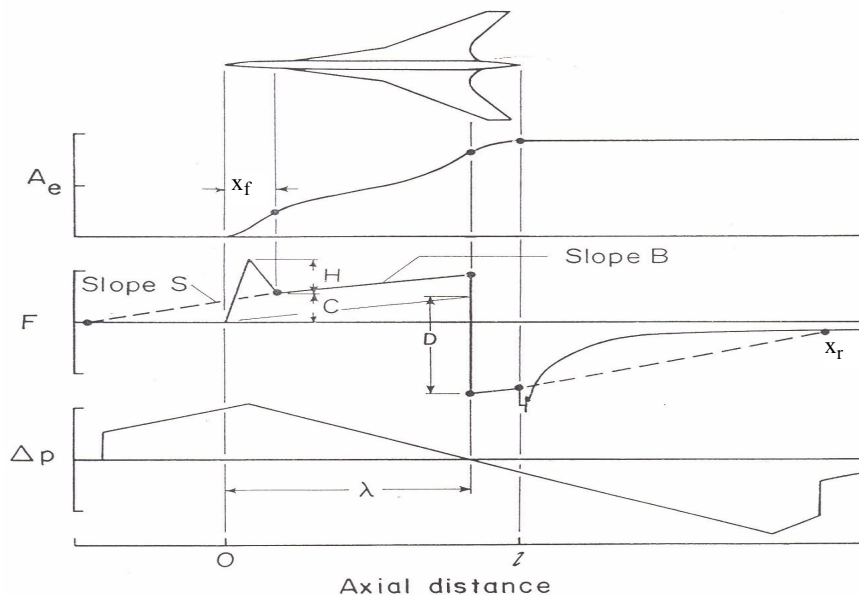

Figure A1. - Illustration of the theoretical concepts of near-field sonic boom (ref. 1).
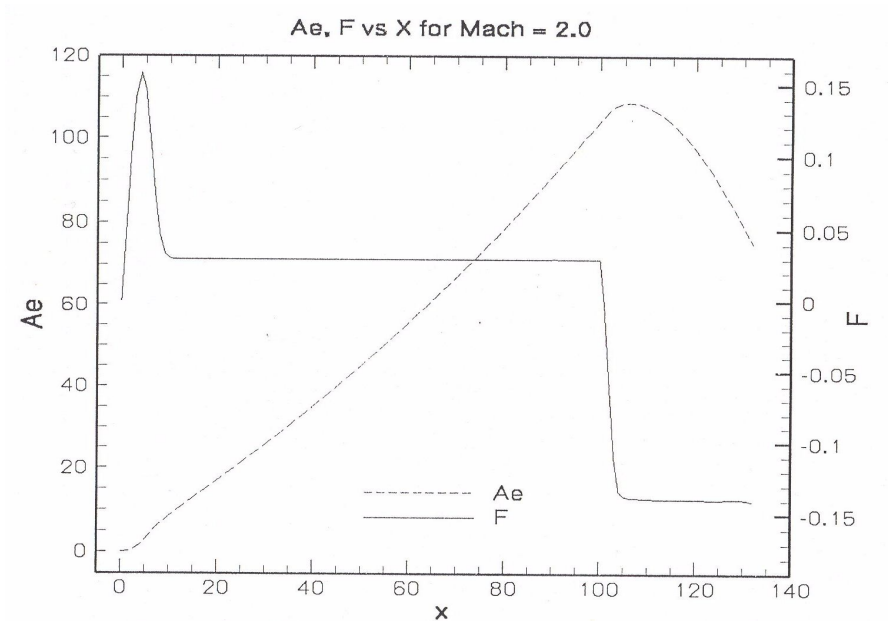
Figure A2. - Variation of the total effective area (A_e) and the associated F-function with x for the flat-top configuration for the parameters of Table A1. M = 2.0, W =90,500 lbs., h = 41,000 feet.
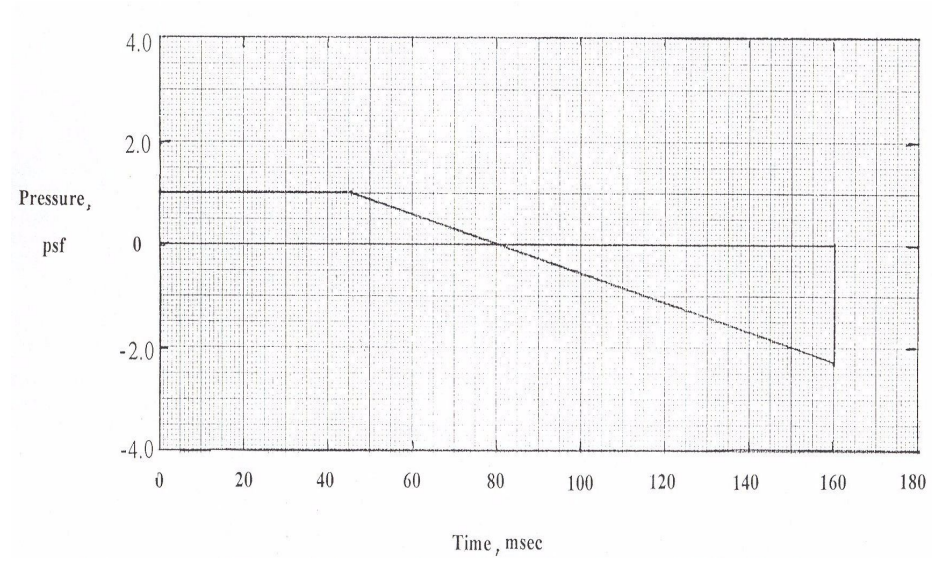

Figure A3. - Flat-top pressure signature on the ground for a supersonic executive jet for the start of cruise conditions and optimum F-function. M = 2.0, W =90,500 lbs., h = 41,000 feet.
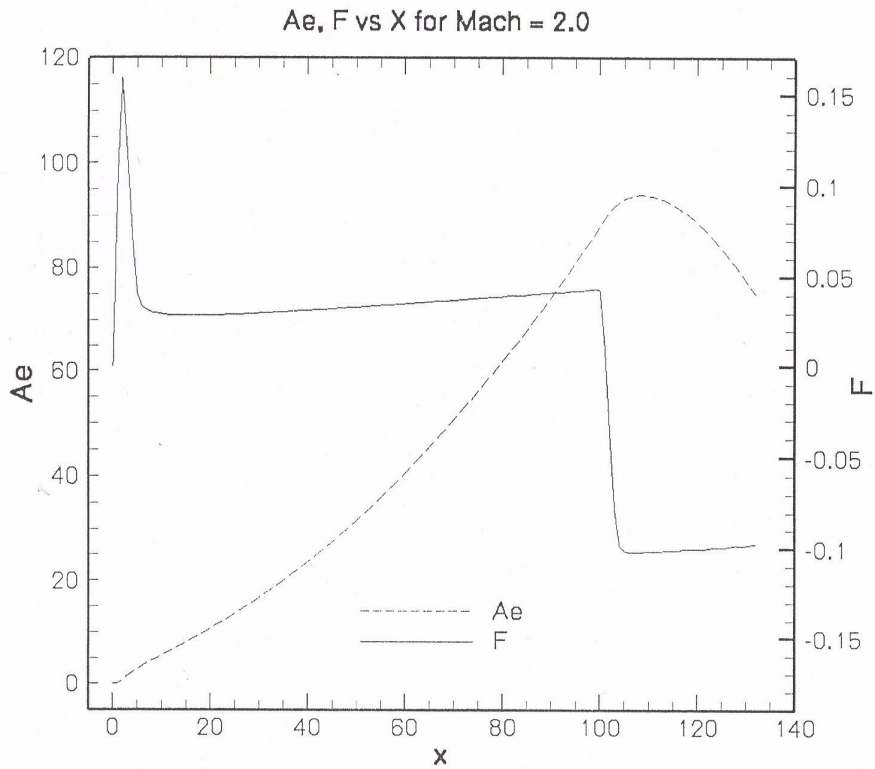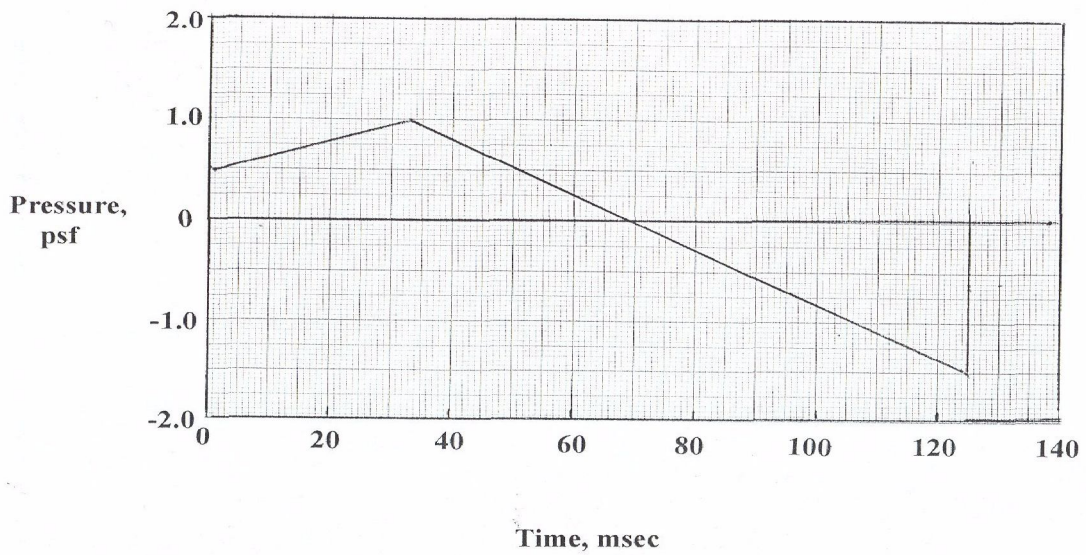
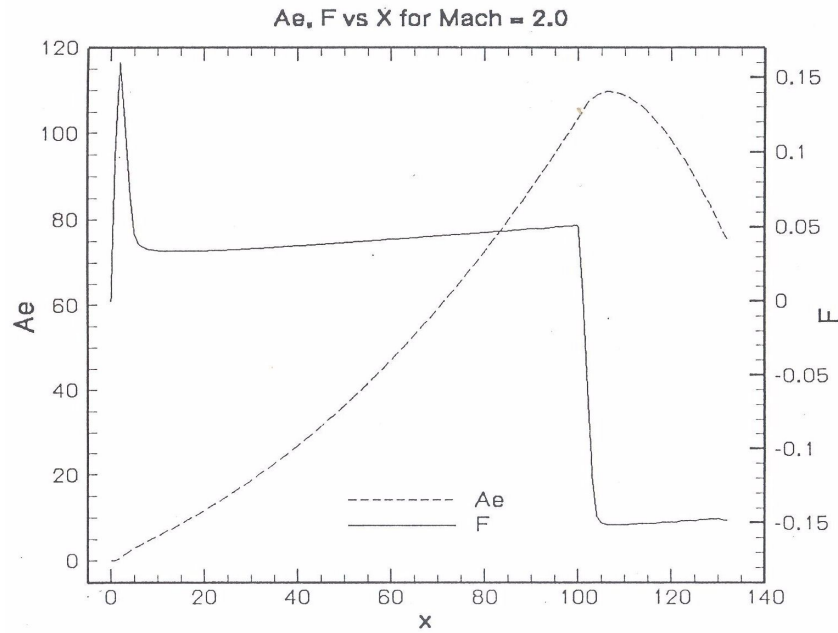Figure A4. - Variation of the total effective area (A_e) and associated ramp F-function with x for the parameters of Table A2. M = 2.0, W = 90,500 lbs., and h = 41,000 ft.
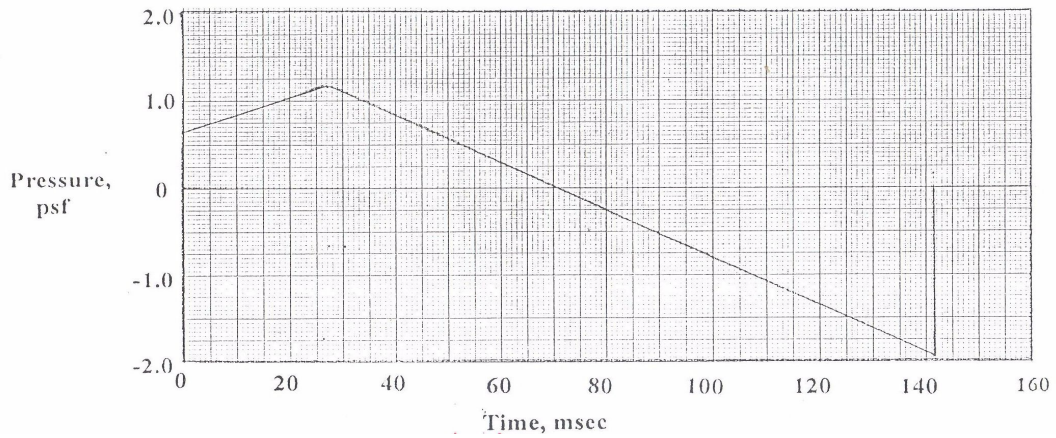

Figure A5. - Ramp-type signature on the ground for a supersonic executive jet for the start of cruise conditions and optimum F-function. M = 2.0, W = 90,500 lbs., and h = 41,000 feet.

Figure A6. - Variation of the total effective area (A_e) and associated F-function with x
for the second ramp-type signature. M = 2., W = 90,500 lbs, and h = 41,000 ft.

Figure A7. - "Second" ramp-type signature on the ground for a supersonic executive jet for the start of cruise
conditions and optimum f-function. M = 2.0, W =90,500 lbs., h = 41,000 feet.

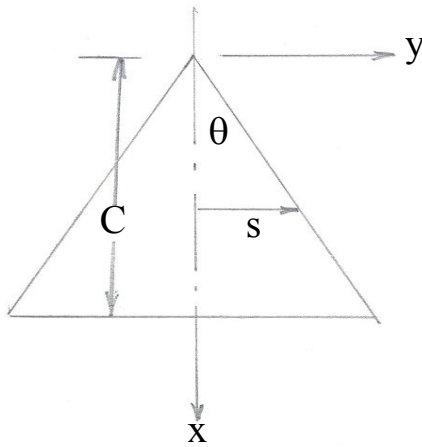## B. Effective Area Distribution Due to Lift for a Slender Wing With Subsonic Leading Edges.

The lifting pressure on a triangular wing with subsonic leading edges is from C. E. Brown in NACA TN 1183 (1946).

$$\frac{\Delta p}{q_\infty} = \frac{4\alpha c^2}{(c^2 - h^2)^{1/2} E(1 - \beta^2 c^2)}$$ (B1)

where

$$c = \frac{s}{x} = \tan\theta$$

$$h = \frac{y}{x}$$

and E $(1-\beta^2 c^2)$ is an elliptic integral of the second kind and plotted in figure B1. A convenient curve fit to the variation of $E(1-\beta^2 c^2)$ with βc is

$$E(1 - \beta^2 c^2) = 1 + 0.2452\,\beta c + 0.3496(\beta c)^2$$

The total lift in coefficient form, on the wing is given by

$$C_L = \frac{1}{S}\int_o^C \int_{-x\tan\theta}^{x\tan\theta} \frac{\Delta P}{q_\infty} dx dy$$ (B2)

or

$$C_L = \frac{4\alpha\tan\theta}{C^2 E(1-\beta^2 c^2)} \int\limits_{o}^{C} \int\limits_{-x\tan\theta}^{x\tan\theta} \frac{x\,dx\,dy}{\sqrt{x^2\tan\theta^2 - y^2}} \qquad (B3)$$

with $S = C\tan\theta$ and C is the wing chord.

Carrying out the integration yields

$$C_L = \frac{2\pi\alpha\tan\theta}{E(1-\beta^2 c^2)} \qquad (B4)$$

However, if one is interested in the accumulation of lift force itself as required for the equivalent effective area distribution due to lift, then one requires the variation of lift with longitudinal distance, i.e.,

$$L(x) = \frac{4\alpha\tan\theta^2\pi x}{E(1-\beta^2 c^2)} q_\infty \qquad o \le x \le C \qquad (B5)$$

where the apex is at x = 0. The equivalent effective area due to lift required for determining the F-function is given by

$$A_{e,\,l} = \frac{\beta}{2q_\infty} \int\limits_{o}^{x} L(x)\,dx \qquad (B6)$$

with L(x) given by equation (5).

Carrying out the integration yields

$$A_{e,\,l} = \frac{\beta\alpha\pi\tan\theta^2 x^2}{E(1-\beta^2 c^2)} \qquad (B7)$$

If instead of a triangular wing a cranked delta or a swept wing with a "segmented" leading edge is selected, such as in the bottom of figure B2., then equations for L(x) and $A_{e,\,l}$ must account for this segmentation. Note that the wing at the bottom of figure B2 is an approximation, i.e., a three segment leading edge, of the wing with the smoothly varying leading edge sweep at the top of figure B2. An approximate method is utilized which assumes that this pressure distribution is conical downstream of each segment with a virtual apex on the root chord, i.e, at x_6 and x_7 in figure B3. Furthermore, in the present calculations the wing tip is assumed to go to a point (see fig. B3). While this yields a trivial increase in area for the wing under consideration it allows a simplification of the methodology.

With the aforementioned assumption the following equations are obtained for the effective area distribution due to lift

.

$$A_{e,l} = \frac{\pi\alpha\beta\tan\theta^2(x-x_1)^2}{E(\beta c_1)} \qquad x_1 \le x \le x_2 \tag{B8}$$

$$A_{e,l} = \pi\alpha\beta\left[\frac{(x_2-x_1)^2\tan\theta^2}{E(Bc_1)}\right] +$$
$$\frac{(x-x_2)(x+x_2-2x_6)\tan^2\theta_2}{E(\beta c_2)} \qquad x_2 \le x \le x_3 \tag{B9}$$

$$A_{e,l} = \pi\alpha\beta\left[\frac{(x_2-x_1)^2\tan^2\theta_1}{E(\beta c_{1(2)})} + \right.$$

$$\frac{(x_3-x_2)(x_3+x_2-2x_6)\tan^2\theta_2}{E(\beta c_2)}$$

$$\left. +\frac{(x-x_3)(x+x_3-2x_7)\tan^2\theta_3}{E(\beta c_3)}\right] \qquad x_3 \le x \le x_5 \tag{B10}$$

where $E(\beta c_n)$ is the "short form" for $E(1-\beta^2 c_n^2)$.

Equation 10 includes the lift in the trailing edge notch from x_4 to x_5. Consequently, it must be subtracted by use of the following equation.

$$A_{e,l} = -2\alpha\beta\frac{\tan^2\theta_3}{E(\beta c_3)}\left\{ (x-x_7)^2\sin^{-1}\frac{(x-x_7-c_1)k_1}{x-x_7} + \right.$$

$$c_1k_1\left[\frac{\sqrt{-(x-x_7)^2(k_1^2-1)+2(x-x_7)c_1k_1^2-c_1^2k_1^2}}{(k_1^2-1)}\right.$$

$$\left.-\frac{c_1k_1^2}{(k_1^2-1)^{3/2}}\sin^{-1}\frac{[(x-x_7)(k_1^2-1)-c_1k_1^2]}{c_1k_1}\right.$$

$$-\frac{c_1}{(k_1{}^2-1)}-\frac{c_1 k_1{}^2}{(k_1{}^2-1)^{3/2}}\sin^{-1}\frac{1}{k_1}\Biggr]\Biggr\} \quad x_4 \le x \le x_5 \tag{B11}$$

where $c_1 = x_4 - x_7$ and $k_1 = \dfrac{\tan\theta_4}{\tan\theta_3}$.

The angle of attack in equations (B8) to (B11) is unknown so the calculation is made of $\dfrac{A_{e,l}}{\alpha}$

and the angle of attack determined from the values of $\dfrac{A_{e,l}}{\alpha}$ at x_5, using the following equations

$$\frac{2q_\infty}{\beta}\left(\frac{A_{e,l}}{\alpha}\right)_{x=x_5}\alpha = \left(\frac{L(x_5)}{\alpha}\right)_{x=x_5}\alpha = W$$

so

$$\alpha = \frac{W}{\dfrac{2q_\infty}{\beta}\left(\dfrac{A_{e,l}}{\alpha}\right)_{x=x_5}} \tag{B12}$$

The value of $\left(\dfrac{A_{e,l}}{\alpha}\right)_{x=x_5}$ is determined from the sum of equations (B10) and (B11) at $x = x_5$.

The wing lift calculations do not include the fuselage. However, there is some compensation that occurs that make the longitudinal distribution of lift calculated using the wing-alone equations still reasonably accurate. When the wing span is small with respect to fuselage diameter, the body acts like an infinite reflection plane and the wing lift distribution is essentially like that of the wing alone (see tip of figure B4).

When the wing span is large relative to the fuselage diameter, more lift is lost on the wing near the fuselage relative to the large body case, however, the lift on the body is higher, as illustrated in figure B4 and the longitudinal distribution of lift is not much different from the wing alone. The level of the distribution is dictated by the angle-of-attack which is adjusted to make the total lift equal to the weight of the aircraft. Consequently, the longitudinal distribution of lift calculated for the wing alone, for both large and small body diameters, is a reasonable approximation of that for the wing on a fuselage even though the spanwise details may vary.

Figure B5 gives the variation of the Mach 2.0 effective area due to lift with longitudinal distance. At $x_2 = 65$ where there is an abrupt change in slope of the leading edge, there is a corresponding change in slope of the variation of $A_{e,l}$ with x. The equations for the F-function, however, assume a continuously varying $A_{e,l}$. Thus, it is convenient to "fillet" this discontinuity in slope of the $A_e l$ variation, as illustrated in figure B6. This implies that there is also a small geometrical fillet

employed in the area of the change in slope of the leading edge. A similar change occurs at x_3 but it is much less severe.
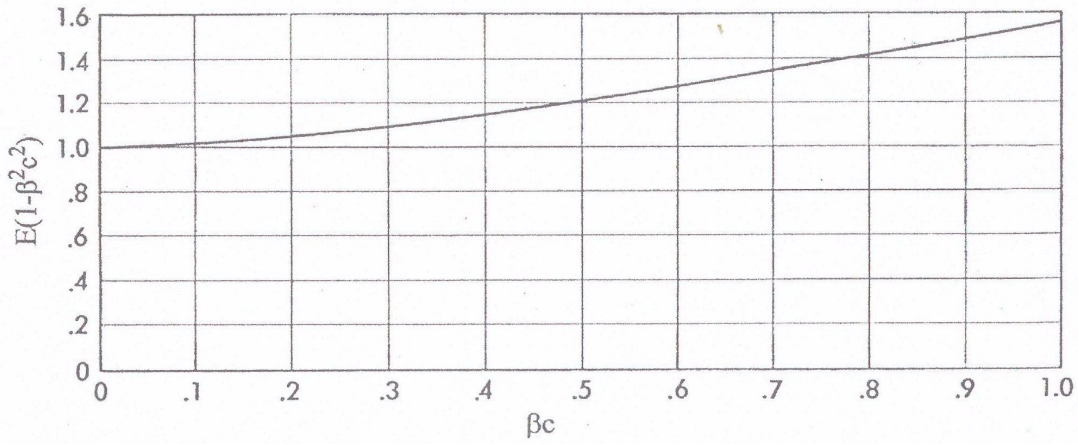

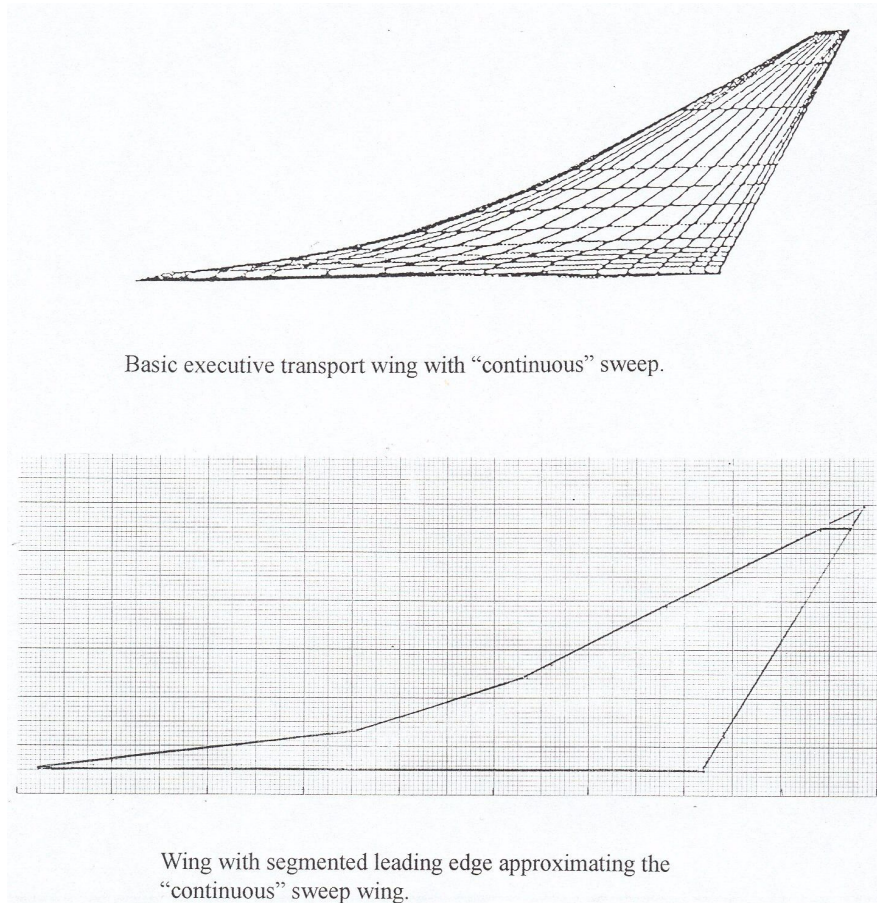Figure B1. -The value of the function of $(1 - \beta^2 c^2)$ versus βc.

Basic executive transport wing with "continuous" sweep.

Wing with segmented leading edge approximating the "continuous" sweep wing.

Figure B2. - Supersonic executive transport wing with continuously varying sweep and its "approximation" with a "segmented" leading edge.
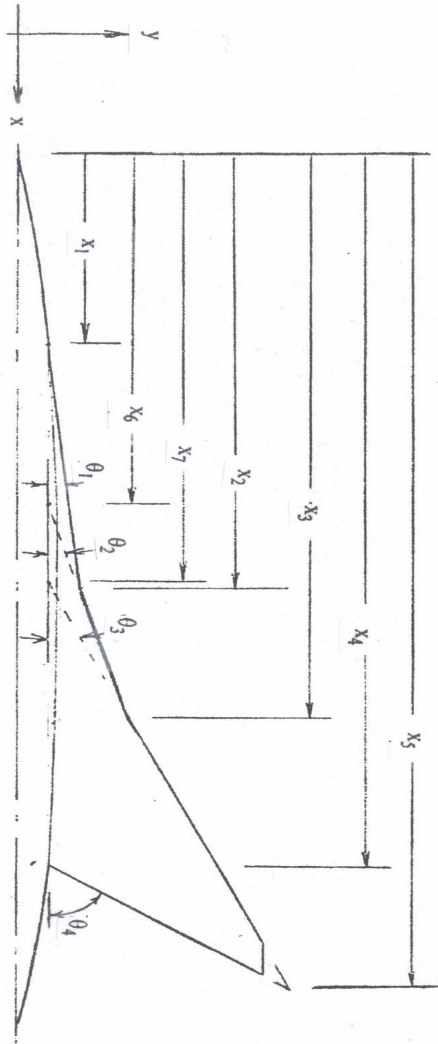
Table of Dimensions and Angles	
$x_1 = 32.5$	$\theta_1 = 6^o$
$x_2 = 65.0$	$\theta_2 = 17^o$
$x_3 = 83.5$	$\theta_3 = 27^o$
$x_4 = 102.0$	$\theta_4 = 59.17^o$
$x_5 = 118.5$	
$x_6 = 52.5$	
$x_7 = 64.225$	

Figure B3. - Schematic of wing/body defining symbols, angles and dimensions.
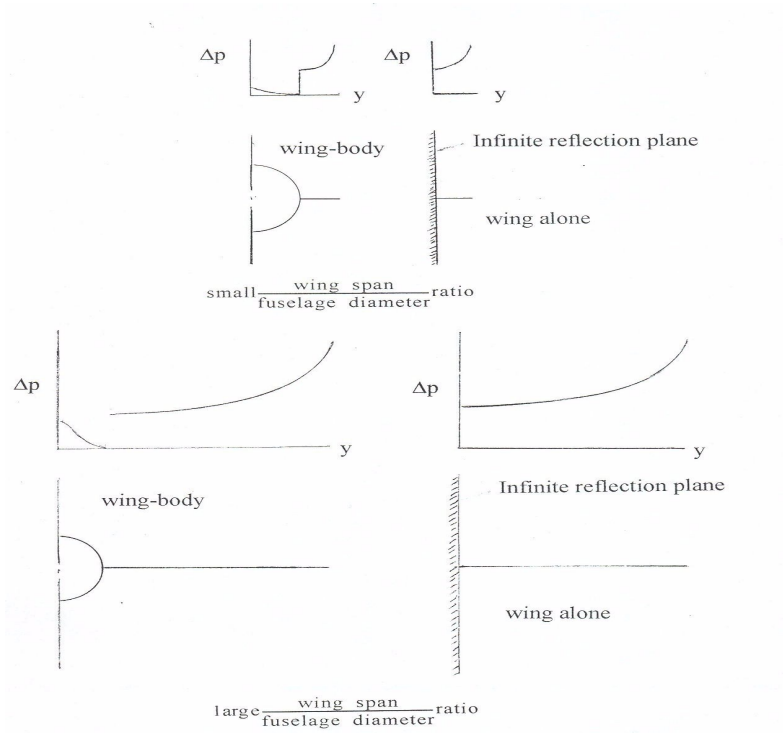
Figure B4.- Schematic comparing pressures for wing alone and wing body for small and large bodies.
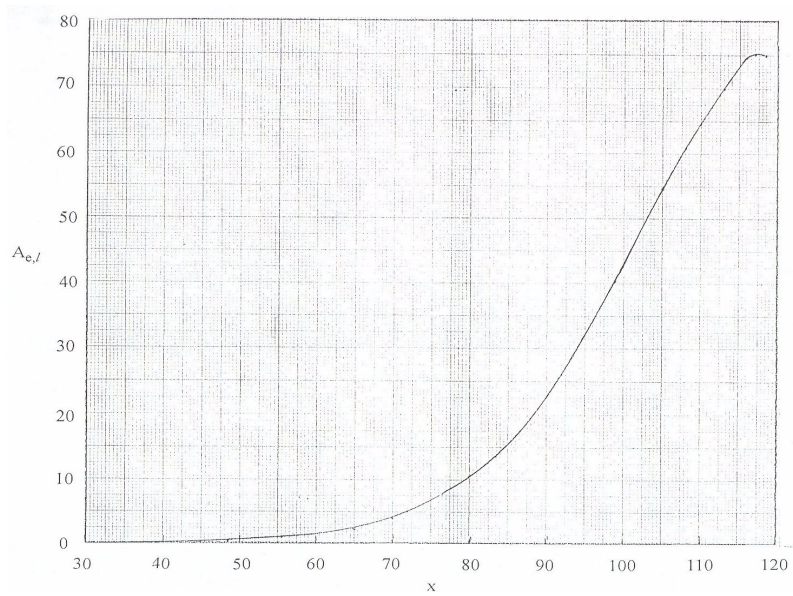Δp in the figure is P_{upper}-P_{lower}.

Figure B5. - Variation of effective area due to lift with longitudinal distance for M = 2.0.
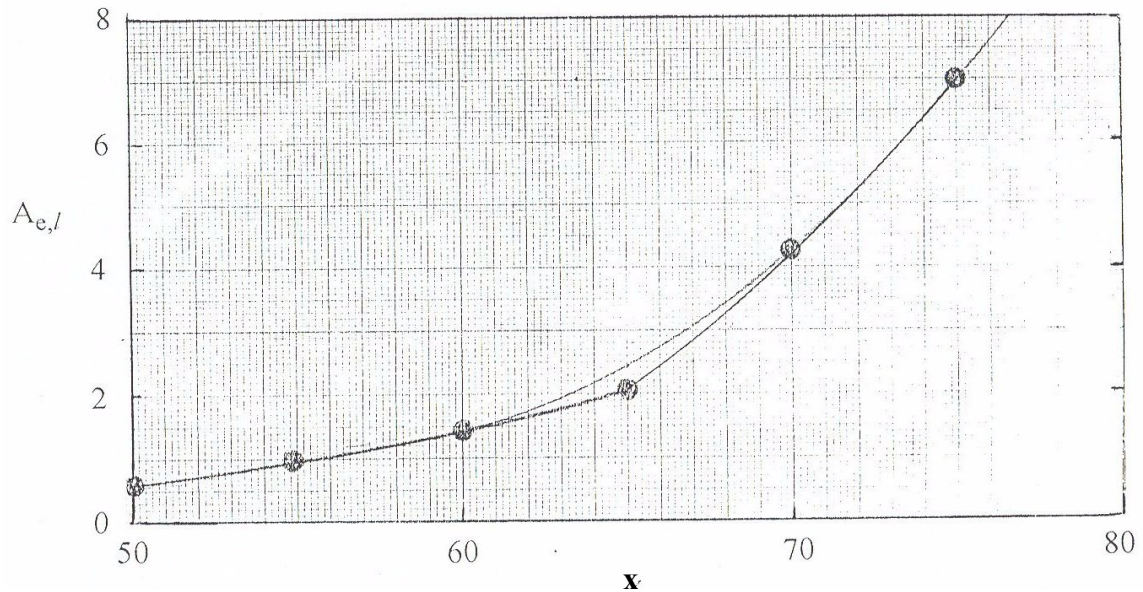W = 90,500 lbs, h = 41,000 feet.

Figure B6. - Plot showing the "filleting" of the slope discontinuity in the variation of A_e with x

Section C. Determination of Basic (M = 1) Axisymmetric Geometry From the Design Effective Volume Distribution.

Assume that over a small streamwise distance the geometry of a section of the effective circular body can be approximated by a linear frustum
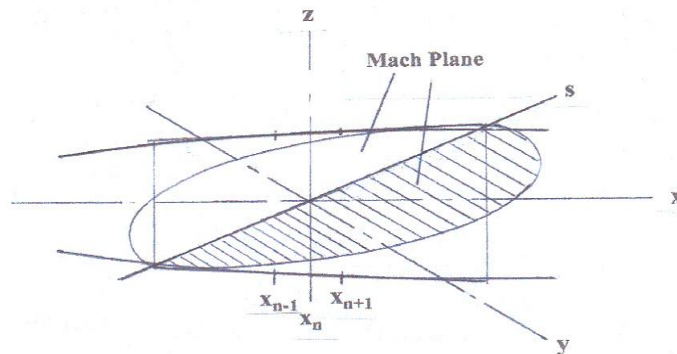
With this local linear approximation of r(x) we obtain

$$r_n(x) = A_n + B_n(x - x_n) \tag{C1}$$

$$A_n = \frac{r_{n+1}(x_n - x_{n-1}) + r_{n-1}(x_{n+1} - x_n)}{x_{n+1} - x_{n-1}}$$ (C2)

$$B_n = \frac{r_{n+1} - r_{n-1}}{x_{n+1} - x_{n-1}}$$ (C3)

Note that A is the difference approximation of r_n and B of $\frac{dr_n}{dx}$. With the cross-section of the body defined by

$$y^2 + z^2 = r^2(x)$$ (C4)

and with the Mach plane cutting the body defined by

$$z = \frac{(x - x_n)}{\beta}$$

$$and \quad \beta = \sqrt{M^2 - 1}$$

the equation for the boundary of the area cut by the Mach plane is

$$y^2 = [A_n + B_n(x - x_n)]^2 - \frac{(x - x_n)^2}{\beta^2}$$ (C5)

Solving for y we obtain

$$y = \pm\left[A_n^2 + 2A_n B_n (x - x_n) + \left(B_n^2 - \frac{1}{\beta^2} \right)(x - x_n)^2 \right]^{1/2}$$ (C6)

Defining $x - x_n = \bar{x}$ and factoring equation (C6), we get

A-18

$$y = \left[A_n - \left(\frac{1}{\beta} - B_n\right)\bar{x} \right]\left[A_n + \left(\frac{1}{\beta} + B_n\right)\bar{x} \right] \tag{C7}$$

which indicates that y goes to zero at $\quad \bar{x} = -\dfrac{A}{\dfrac{1}{\beta} + B} \quad and \quad \dfrac{A}{\dfrac{1}{\beta} - B}$.

The cross-sectional area of the ellipse cut by the Mach plane is

$$A_e = 2\int y\,ds$$

where the integration over the half plane (see crossed-hatched area in sketch) is doubled.

With ds = $\dfrac{Md\bar{x}}{\beta}$. The A_e equation becomes

$$A_e = \frac{2M}{\beta} \int_{-\frac{A_n}{\frac{1}{\beta} + B_n}}^{\frac{A_n}{\frac{1}{\beta} - B_n}} y\,d\bar{x} \tag{C8}$$

where y is given by equation (C6).

Carrying out the integration of equation (C8) yields, after a lot of simplification

$$A_e = \frac{\pi M A_n^{\,2}}{(1 - \beta^2 B_n^{\,2})^{3/2}} \tag{C9}$$

We note that $A_n \approx r_n$ and $B_n \approx \dfrac{d_{r_n}}{dx}$ so that equation (C9) can also be written

$$A_e = \frac{\pi M r_n^2}{\left[1 - \beta^2 \left(\frac{d_{rn}}{dx}\right)^2\right]^{3/2}} \tag{C10}$$

where r_n is the unknown radius of the basic body of revolution, i.e., the Mach = 1.0, or normal cut. The variation of A_e with x for the design Mach number is known.

For any x location, the value of r_{n+1}, required in equations (C2) and (C3), is not known. However, we can solve for r_{n+1} using equation (C9) where we know r_{n-1}, i.e., at x = 0.

With n = 2 we find $x_{n-1} = x_1 = 0$ and $r_{n-1} = r_1 = 0$ (see sketch). and $x_{n+1} = x_3$ and $r_{n+1} = r_3$.

Apex of body showing numbering scheme used in equations.
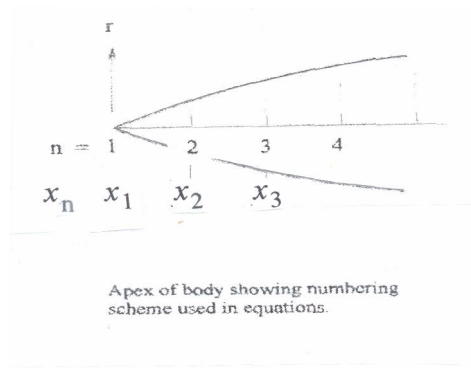
Equation (C2) for A_2 (i.e. is for n = 2) becomes

$$A_2 = \frac{r_1(x_3 - x_2) + r_3(x_2 - x_1)}{x_3 - x_1} \tag{C11}$$

and equation (C3) for B_2

$$B_2 = \frac{r_3 - r_1}{x_3 - x_1} \tag{C12}$$

With $x_1 = r_1 = 0$, equations (C11) and (C12) for A_2 and B_2 reduce to

$$A_2 = \frac{r_3 x_2}{x_3} \tag{C13}$$

and

$$B_2 = \frac{r_3}{x_3} \tag{C14}$$

Substituting A_2 and B_2 from equations (C13) and (C14) into equation (C19) yields

$$A_{e_2} = \frac{\pi\left(\dfrac{r_3 x_2}{x_3}\right)^2 M}{\left[1 - \beta^2\left(\dfrac{r_3}{x_3}\right)^2\right]^{3/2}} \tag{C15}$$

Equation (C15) can be solved directly or iteratively for r_3, however, a more exact solution is possible by taking advantage of the fact that A_e varies as $x^{5/2}$, from $x = 0$ to $x = y_f/2$. Consequently, one would expect the basic area distribution (Mach = 1.0 cuts) to have the same type of dependency.

If we assume

$$r_n = K_n x^{5/4} \tag{C16}$$

and

$$\frac{d_{rn}}{dx} = \frac{5}{4} K_n x^{1/4} \tag{C17}$$

Then equation (C10) becomes

$$A_{en} = \frac{\pi M K_n^2 x^{5/2}}{\left[1 - \left(\dfrac{5}{4}\beta x^{1/4}\right)^2 K_n^2\right]^{3/2}} \tag{C18}$$

By defining

$$k_1 = A_{en}/\pi M x^{5/2} \tag{C19}$$

and

$$k_2 = \left(\frac{5}{4}\beta x^{1/4}\right)^2 \tag{C20}$$

then the solution of equation (C8) for K_n can be written as

$$K_n = \left(\frac{P}{3}\right)^{3/2}\left\{2\sin\left[30° + \frac{1}{3}\cos^{-1}\left(1 - \frac{27}{2P^3 k_2}\right)\right] - 1\right\}^{3/2} \tag{C21}$$

with $P = 1/k_1^{2/3} k_2$

Substituting K_n back into equation (C16) yields the value for r_n. Equations (C16) and (C21) should be useful for x values up to $\approx x_f/2$ i.e., for $x_f = 8$, x values up to 4.0.

Beyond this point one must revert to solving equation (C9) for r_{n+1} using an iterative technique where successive guesses for r_{n+1} are made until equation (C9) is satisfied. Actually, since the calculation of r_{n+1} is a "bootstrap" calculation with each step depending on the last, it is more accurate to use a slightly different form of equation (C9), i.e.,

$$\sqrt{\frac{A_e}{\pi M}} = \frac{A_n}{(1 - \beta^2 B_n^2)^{3/4}} \tag{C22}$$

Equation (C2) and (C3) are required for A_n and B_n while for unequal Δx values, the following equation for B_n is preferable to equation (C3).

$$B_n = \frac{(r_{n+1} - r_n)(x_n - x_{n-1})^2 + (r_n - r_{n-1})(x_{n+1} - x_n)^2}{(x_{n+1} - x_{n-1})(x_{n+1} - x_n)(x_n - x_{n-1})} \tag{C23}$$

It has been found that the iterative "bootstrap" calculation (starting at x = 0) for r_{n+1} beyond the maximum value of r_{n+1} tends to become unstable. Consequently, the calculation for r_{n+1} beyond the maximum value is made starting at x = *1* and working back to the maximum value of r_{n+1}. In this case, it is assumed that the variation of A_e with x near x = *1 is* linear thus the value of

$r_{n_{max-2}}$ required to start the calculation is determined in an iterative fashion from

$$A_{e_{v,n_{max-1}}} = \frac{\pi\left(\dfrac{r_{n_{max-2}} - x_{n_{max-1}}}{x_{n_{max-2}}}\right)^2 M}{\left[1 - \beta^2\left(\dfrac{r_{n_{max-2}}}{x_{n_{max-1}}}\right)^2\right]^{3/2}} \tag{C24}$$

which is a simple variation of equation (C15).

Once the basic (M = 1.0 cuts) body of revolution is determined one can determine the effective area distribution for other Mach numbers by simply substituting the appropriate Mach number and basic body r values in equation (C9) with A_n and B_n given by equations (C2) and (C23).

Finally, it should be noted that when r_n is a maximum and $\dfrac{d_{r_n}}{dx} = 0$ that equation (C10) reduced to

$$A_{e_{v,n}} = \pi r^2{}_n M$$

or

$$\frac{\text{Maximum effective cross sectional area at design Mach}}{M} = \frac{\text{Max cross sectional area at M = 1.0}}{}$$

D. Method of Determining F-function at Off-Design Mach Numbers

The basic F function is determined by

$$F(x) = \frac{1}{2\pi} \int_o^x \frac{A_e''(\xi)}{(x-\xi)^{1/2}} d\xi \tag{D1}$$

Integration of equation (D1) in this section is done primarily using a simple numerical scheme, however, the first three x stations i.e., with x_m equal to x_1 to x_3, take advantage of the functional character of A_e and are done analytically.

Consistent with the first term of equation (A1) of Section A, it is assumed that

$$A_e = k5^{5/2} \qquad \text{(D2)}$$

thus

$$A_e'' = \frac{15}{4}k\xi^{1/2} \qquad \text{(D3)}$$

Substituting this equation for A_e'' in equation (D1) and integrating yields

$$F(x) = \frac{15}{16}kx \qquad \text{(D4)}$$

in non-dimensional form, equation (D4) becomes

$$\bar{F}(\bar{x}) = \frac{15}{16}\bar{k}\bar{x} \qquad \text{(D5)}$$

where

$$\bar{F}(\bar{x}) = \frac{F(x)}{\sqrt{l}} \qquad \text{(D6)}$$

$$\bar{x} = \frac{x}{l}$$

$$\bar{k} = k\sqrt{l}$$

Note that in equation (D4) k has the units of $1/(\sqrt{l})$.

Equation (D5) will be used for the first three intervals of $\bar{F}(\bar{x}_m)$ and the length of each interval is specified as 0.01. The actual center points of each interval are then $\bar{x}_1 = 0.005,\ \bar{x}_2 = 0.015$ and $\bar{x}_3 = 0.025$ with m = 1, 2, 3 and the normalized overall length being 1.0.

Thus,

$$\bar{F}(\bar{x}_1) = 0.0046875\bar{k} \qquad\qquad \bar{x} = 0.005$$

$$\bar{F}(\bar{x}_2) = 0.0140625\bar{k} \qquad\qquad \bar{x} = 0.015 \tag{D7}$$

$$\bar{F}(\bar{x}_1) = 0.0234375\bar{k} \qquad\qquad \bar{x} = 0.025$$

and the value of $\bar{F}(\bar{x})$ at $\bar{x} = 0.03$ for use in the subsequent $\bar{F}(\bar{x})$ equation for values of $\bar{x} > 0.03$ is

$$\bar{F}(\bar{x}) = 0.028125\bar{k}$$

It is important to note that choosing that choosing $\bar{x}_3 = 0.03$ implies that $\bar{x}_f$ is 0.06 (see equations (A3) in Section A) so that an $\bar{x}$ of 0.03 covers the initial half of the spike from 0 to $\bar{x}_f/2$ at the start of the F-function distribution (see fig. A1). Furthermore, this $\bar{x}_f$ value of 0.06 was chosen because higher values of $\bar{x}_f$ do not yield any additional drag benefit (see fig. 8 of ref. 1). Obviously other values of $\bar{x}_f$ can be used but the interval from 0 to $\bar{x}_f/2$ should be divided into equal segments.

To determine values of $\bar{F}(\bar{x})$ beyond values of 3 the equation for $F(x)$ (in non-dimensional form) has been integrated by parts to yield

$$\bar{F}(\bar{x}) = \frac{1}{n}\left\{ \bar{A}_e^{''}(\bar{x}+0.005)\sqrt{\bar{x}_m + 0.005 - (\bar{x}_3 + 0.005)} + \int_{\bar{x}_3 + 0.005}^{\bar{x}_m} \bar{A}_e^{''}(\bar{\xi})\sqrt{\bar{x}_m - \bar{\xi}}\,d\bar{\xi} \right\} \tag{D9}$$

$$4 \le m \le m_{max}$$

The integration in equation (D7) is carried out numerically so that equation (D7) can be recast, with $\bar{x}_3 = 0.025$ as

$$\bar{F}(\bar{x}) = \frac{1}{\pi}\left\{ \bar{A}_e^{''}(0.03)\sqrt{\bar{x}_m - \bar{x}_3} + \sum_{n=4}^{m} \bar{A}_e^{''}(\bar{\xi}_n)\sqrt{\bar{x}_m - \bar{\xi}_n}\Delta\bar{\xi} + \pi\frac{15}{16}\bar{k}(0.03) \right\} \tag{D10}$$

$$x \le n \le m$$
$$4 \le m \le m_{max}$$

or with $\bar{A}_e(0.03)$ from equation (D3)

$$\bar{F}(\bar{x}) = \frac{1}{\pi}\left\{ 0.64952\bar{k}\sqrt{\bar{x}_m - \bar{x}_3} + \sum_{n=4}^{m}\bar{A}_e''(\bar{\xi}_n)\sqrt{\bar{x}_m - \bar{\xi}_n}\Delta\bar{\xi} + 0.028125\bar{k}\pi \right\} \tag{D11}$$

$$4 \le n \le m$$
$$4 \le m \le m_{max}$$

Values of $\bar{A}_e'''(\bar{\xi}_n)$ for $4 < n < n_{max}$ -1 are determined from

$$\bar{A}_e'''(\bar{\xi}_n) = \frac{\bar{A}_e(\bar{\xi}_{n+2}) - 2\bar{A}_e(\bar{\xi}_{n+1}) + 2\bar{A}_e(\bar{\xi}_{n-1}) - \bar{A}_e(\bar{\xi}_{n-2}) - \bar{A}_e(\bar{\xi}_{n-3})}{2(\Delta x)^3} \tag{D12}$$

For $\bar{A}_e'''(\bar{\xi}_n)$ for $n = n_{max}$ - 1 and $n = n_{max}$ use

$$\bar{A}_e'''(\bar{\xi}_n) = \frac{\bar{A}_e(\bar{\xi}_n) - 3\bar{A}_e(\bar{\xi}_{n-1}) + 3\bar{A}_e(\bar{\xi}_{n-2}) - \bar{A}_e(\bar{\xi}_{n-3})}{(\Delta x)^3} \tag{D13}$$

The numerical integration has the following features:

- Numerical integration scheme uses values of A_e''' at points $x_4, x_5, x_6...x_n$, etc. at middle of $\Delta\xi$ increments (see sketch below)
- Points are equally spaced $\Delta\xi$ apart
- Equations for of A_e''' result from cubic spline curve fits
- Values of A_{e_n}''' for n_{max} and n_{max} - 1 are evaluated by a different equation.
- Integration for each station m starts at n = 4 and ends at n=m
- Contribution of integral from x = 0 to 0.03 added as a separate term.
- $m_{max} = n_{max}$ at $\bar{x} = \bar{\xi} = 0.995$.
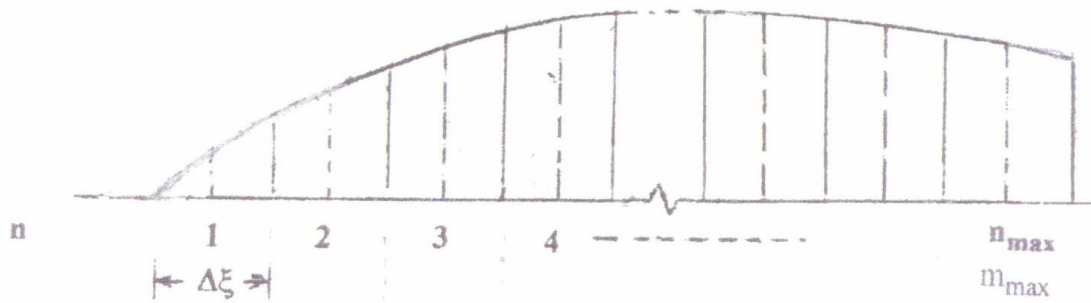
Positioning of F-Function Integral

While the integration above was for ξ and x increments of 0.01 in regions where there is large curvature, higher resolution may be required. $A'''_e(\bar{\xi}_n)$ calculations, using equations (D12) and (D13) should be made using smaller increments than 0.01 to make this determination. Inadequate resolution can result in unrealistic spikes in the F-function that often are mistaken for shocks.

E. Effective Area and F-Function Distribution for Executive Jet at Off Design Mach Numbers.

The analytical equations of the previous section have been utilized to determine the basic geometry (M = 1 Mach cuts) of the flat-top and ramp configurations whose F-functions and associated effective area distributions (A_e) were described in Section A. Using the equations of Section C, the basic geometry (M = 1.0 normal cuts) and effective volume distributions for Mach numbers of 1.2, 1.3, 1.4, 1.5, 1.6, 1.8 and 2.0 were obtained. To these were added the effective lift distribution determined using the equations of Section B. The sum of these two effective area distributions are then used in the F-function equations of Section D. The flight conditions and associated parameters used for, and determined from, the lift calculations are given in Table E1.

Results for the flat top configuration will be examined first. Figure E1 shows the variation with x of the equivalent area and its lift and volume components for the M = 2.0 flat-top configuration. Figure E2 shows the radius of the basic (M = 1 normal cuts) axisymmetric body determined from the Mach 2.0 volume distribution. Is also shows the associated area distribution. Included in these distributions are the contributions of both the wing and fuselage. The effective volume and lift distribution and associated totals for Mach numbers of 1.2 to 1.8 are given in figures E3a through E3f. The total A_e distribution for these Mach numbers have been substituted in the equations of Section D to determine the F-function for the same array of Mach numbers. Plots of these F-functions are given in figures E4a through E4g for Mach 1.2 through 2.0. It is interesting to note that the character of the F-functions for all of the Mach numbers is similar from x = 0 to around x = 60. Beyond x = 60 the signatures become irregular and around x = 100 change sign from positive to negative. Beyond x $\approx$ 100 they are also irregular (oscillatory). There are several reasons for these "bumps and dips". One is the inflections in the basic body caused by inflections in the M = 2 effective volume distribution which, in turn, was caused by the M = 2 lift distribution and its inflections when it was subtracted from the total to obtain the volume component. Included in these inflections are those due to the peak lift, the end of lift (at x $\approx$ 118) and the breaks in leading edge slope.

These inflections in the effective body at the off design Mach numbers do not line up with those in the lift distribution calculated for those same Mach numbers when the two components are added. Since the F-function is dependent on the third derivative of the total A_e curve, it is not possible to look at the plots of A_e and see all of the "bumps and dips." It is clear, however, that the overall character of the off-design F-functions for the flat-top design is similar to that at the design Mach numbers. Many have thought that at these low off design Mach numbers that the signature would degenerate to N-waves, but that is not the case. This would seem to have positive implications for reducing the magnitude of the transition focus booms at low Mach numbers.

The F-function for the flat-top design was slightly modified to produce a ramp signature on the ground.   The parameters used for the design are given in Section A. Of particular interest is the value of C which was reduced from 0.03 for the flat top signature to 0.02 with the thought that the resulting increase in slope of the F-function from y_f to λ would move the maximum volume fur-ther toward the rear. Unfortunately, the resulting reduction in the magnitude of the F-function for x_f to λ had the effect of reducing its magnitude of A_e over the whole length. Figure E5, which gives the total A_e and its lift and volume components for the ramp design, shows this effect when compared to figure E1 for a flat-top. When the basic volume distribution (M = 1 normal cuts) is calculated from the M = 2 effective volume distribution, it shows (see figure E6) that it is really too small to be a viable concept.

As noted in Section A, a "second" ramp type A_e and associated ground signature were "designed" to make the volume component comparable to that of the flat-top configuration. Figure E7 shows variation of A_e with x (see also figure A6) as well as the effective lift and volume components for this second ramp type configuration at M = 2.0. It is clear that if one compares this effective vol-ume distribution to that of the flat-top configuration (figure E1) it is nearly the same in magnitude. Consequently, the actual geometries are also similar as evidenced by comparing figures E8 and E2.

The off-design lift and volume components, for Mach numbers from 1.2 to 1.8, for the "second" ramp-type configuration are given in figure E9a to E9f. F-function distributions for the off- design conditions for M from Mach numbers 1.2 through 2.0 are given in Figures E10a to E10g.

Table E1. - Flight and Lift-Coefficient Parameters

M	h	w	q_∞	α, deg.	C_L	$C_{L,\alpha}$ per deg.
1.2	32850	94300	556.00	2.924	0.1087	0.0372
1.3	32850	93750	652.55	2.5767	0.0921	0.0357
1.4	32850	93270	756.81	2.2974	0.0790	0.0344
1.5	32850	92900	868.79	2.055	0.0685	0.0333
1.6	32850	92570	980.51	1.891	0.0605	0.0320
1.8	37230	91593	1015.25	1.90836	0.0578	0.0303
2.0	41000	90500	1045.60	1.9518	0.0555	0.0284
S_{ref} = 1560.25 ft^2						

A_e Total, Volume and Lift versus X for Mach 2.0
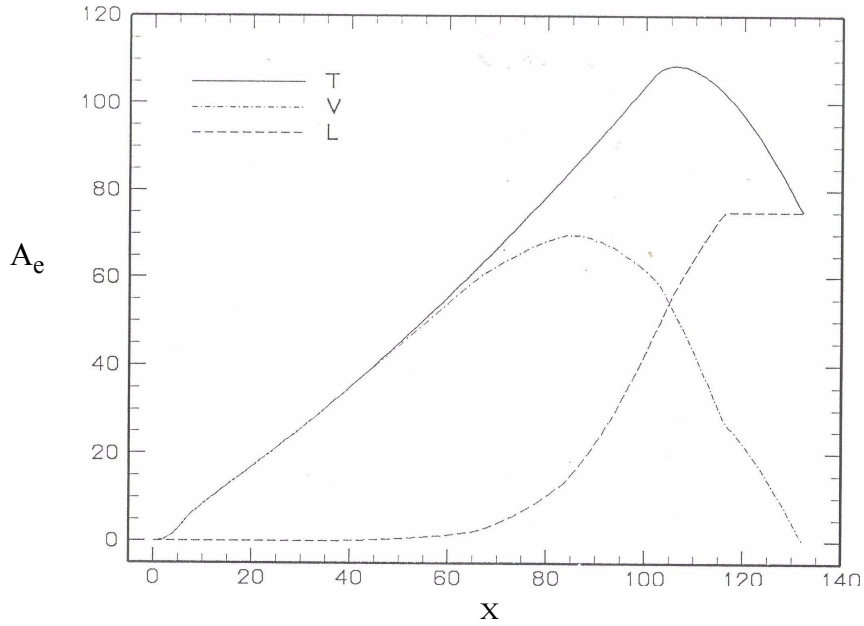

Figure E1. - Variation of A_e and its lift and volume components for the
flat-top configuration M = 2.0, W = 90,500 lbs. and h = 41,000 feet
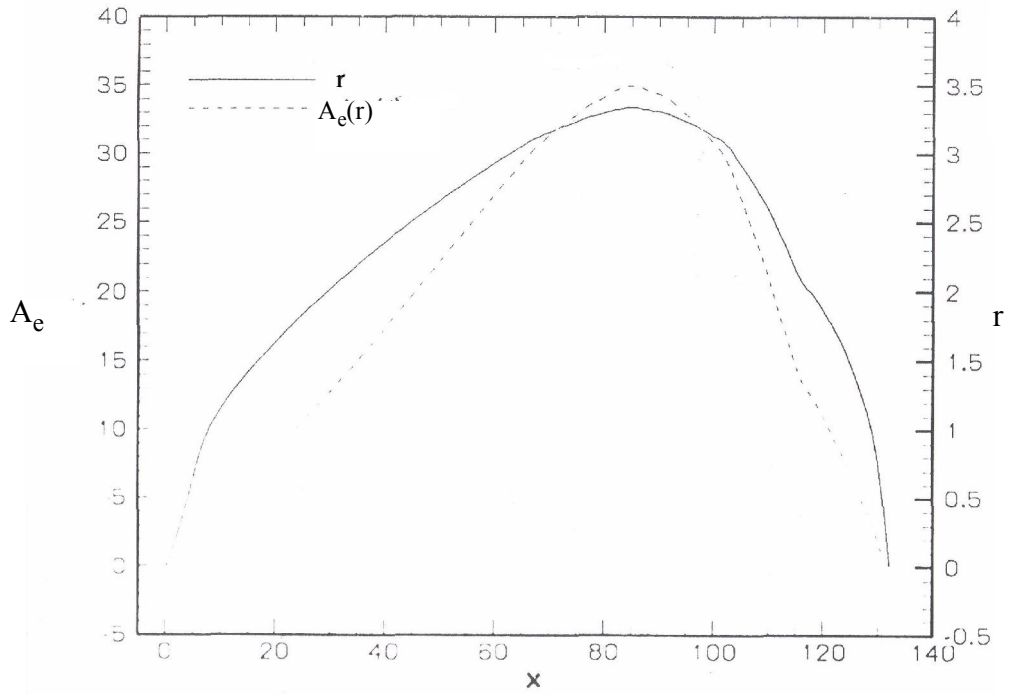
A_e r versus X for Mach = 1.0 Body

Figure E2. - Variation of the basic body (M = 1) radius and area with x
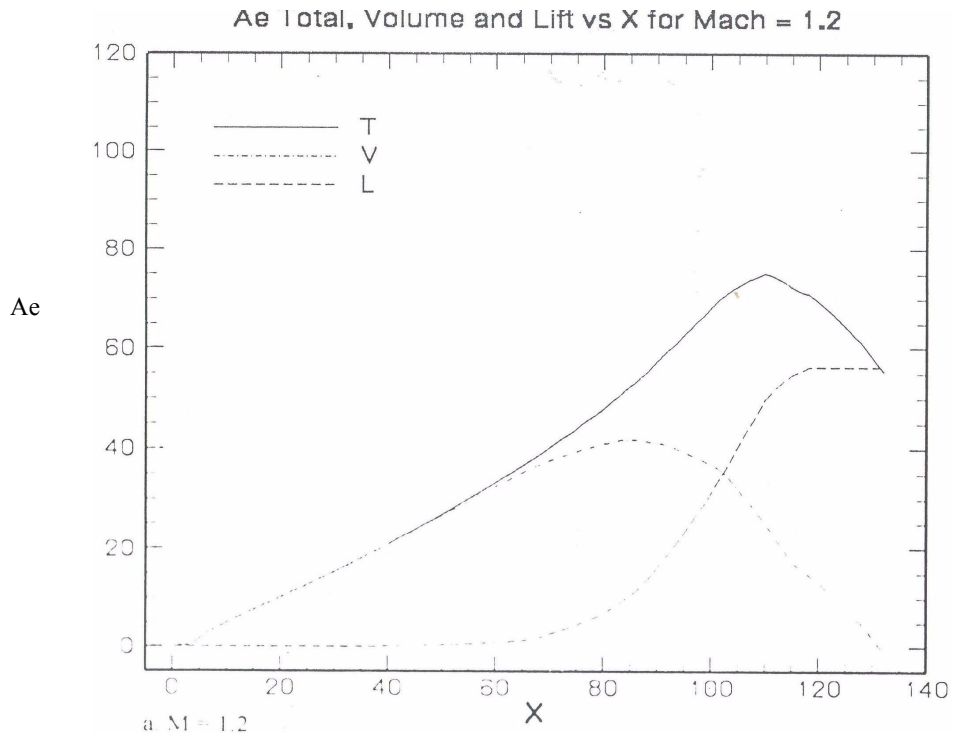for the flat-top configuration.

Ae Total, Volume and Lift vs X for Mach = 1.2

a. M = 1.2

Figure E3. - Variations of the total effective area and its lift and volume components with x for a range of off design Mach numbers from 1.2 to 1.8 for the flat-top configuration.

Ae Total, Volume and Lift vs X for Mach = 1.3

b. M = 1.3

Figure E3. - Continued.

Ae Total, Volume and Lift vs X for Mach = 1.4

c. M = 1.4

Figure E3. - Continued.

Ae Total Volume and Lift vs x for Mach = 1.5

d M 1 5
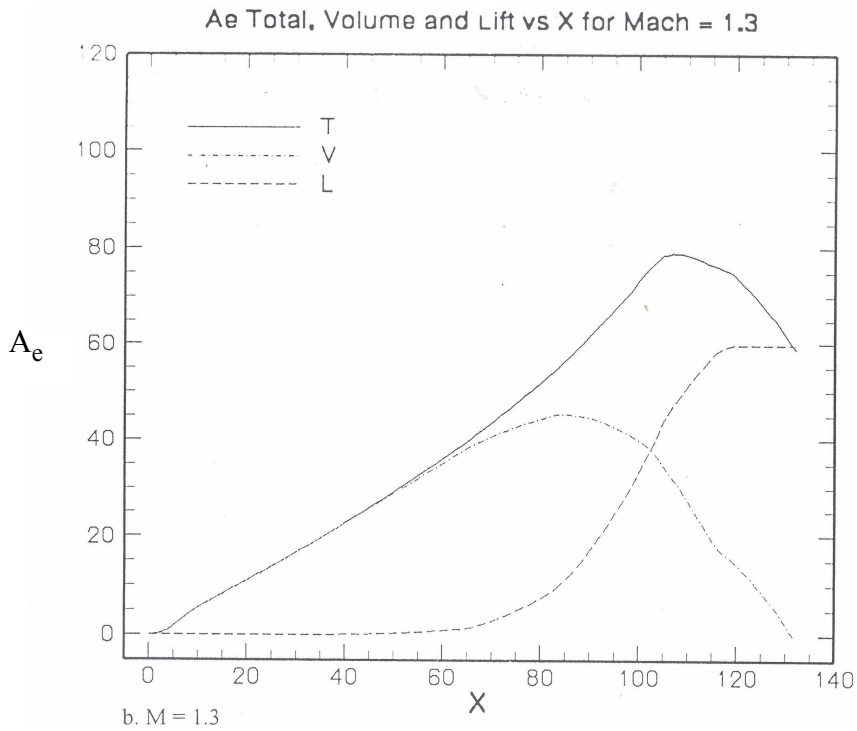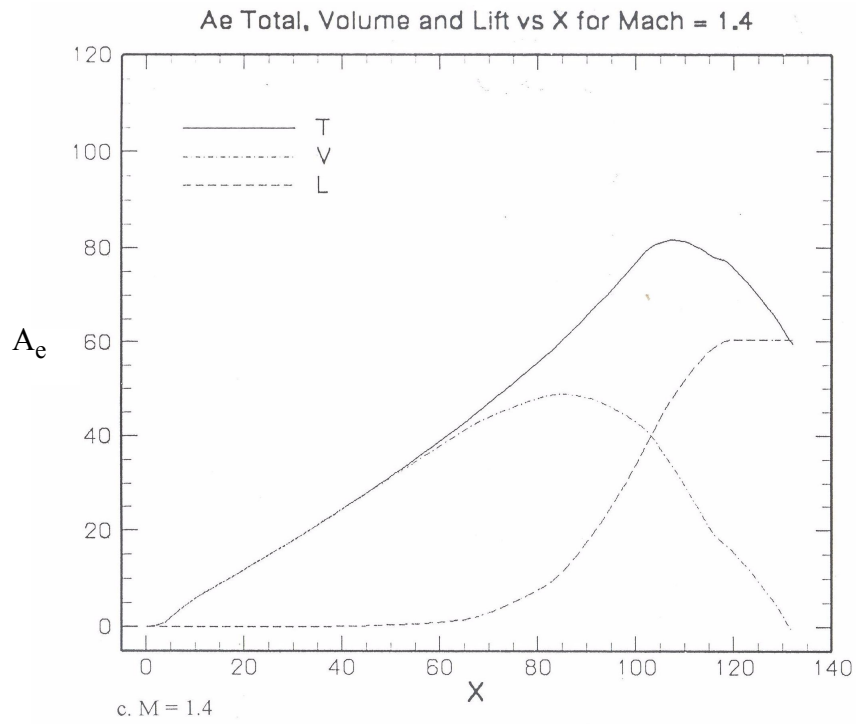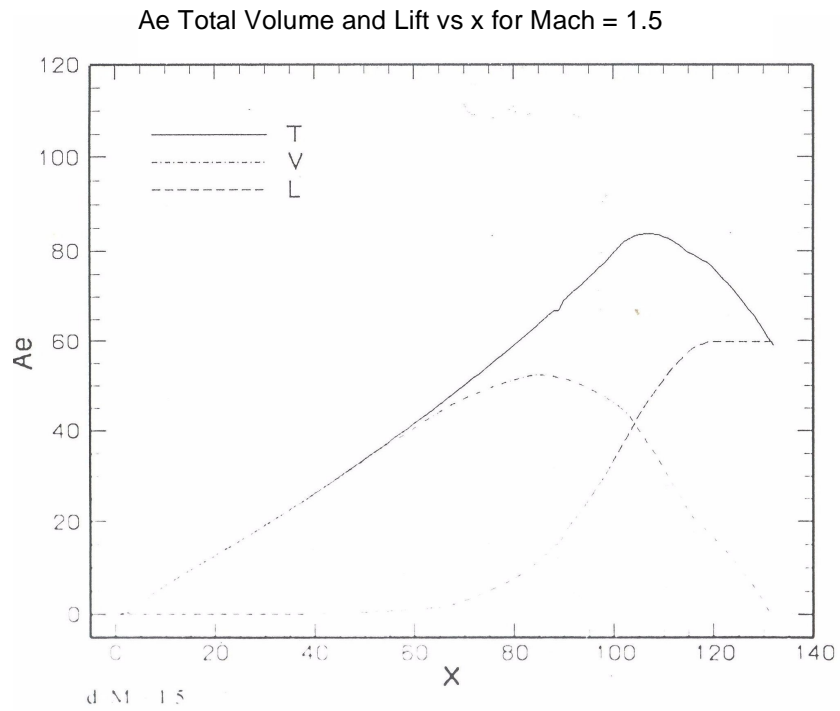
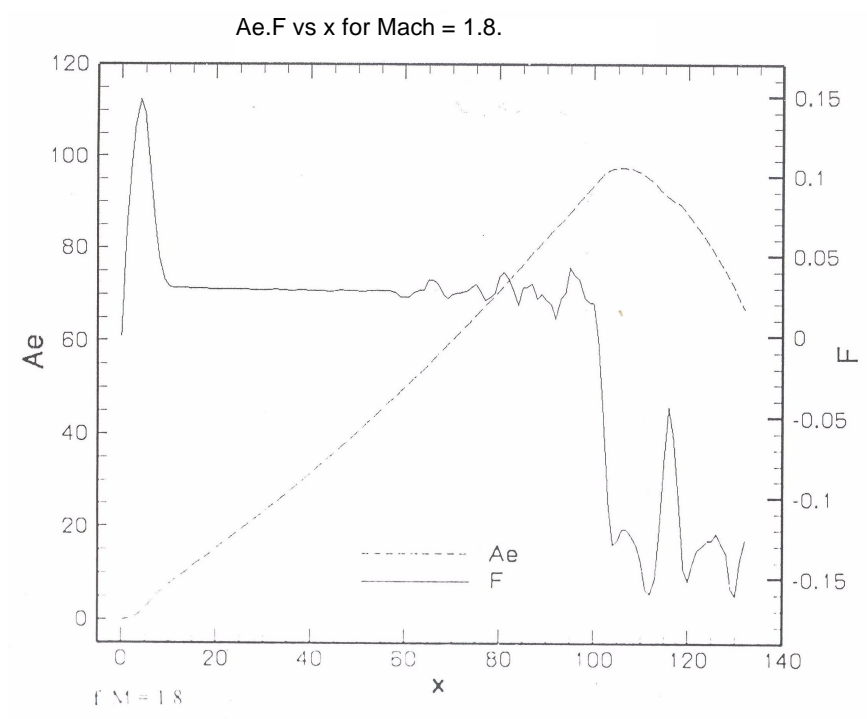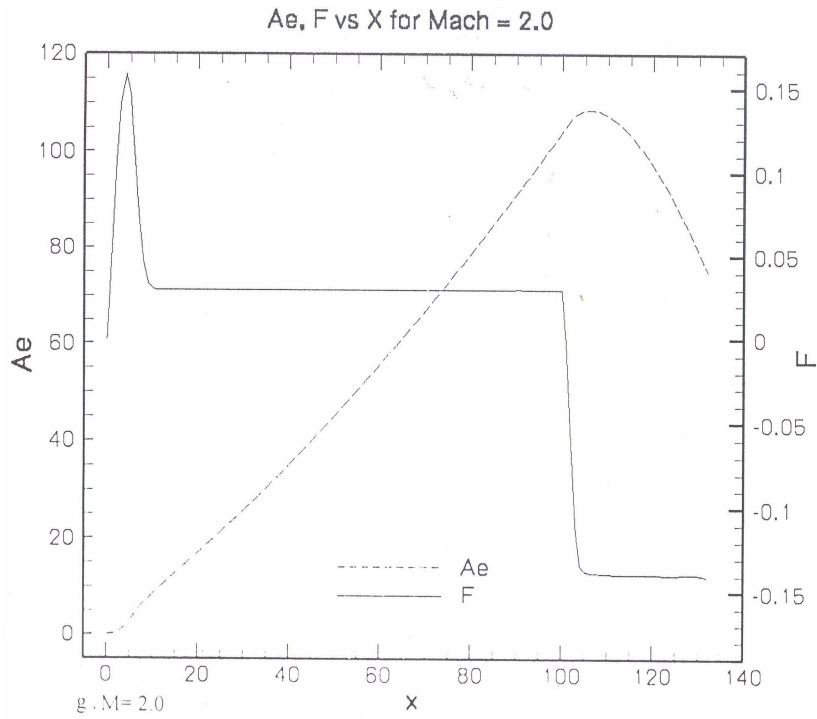Figure E3. - Continued.
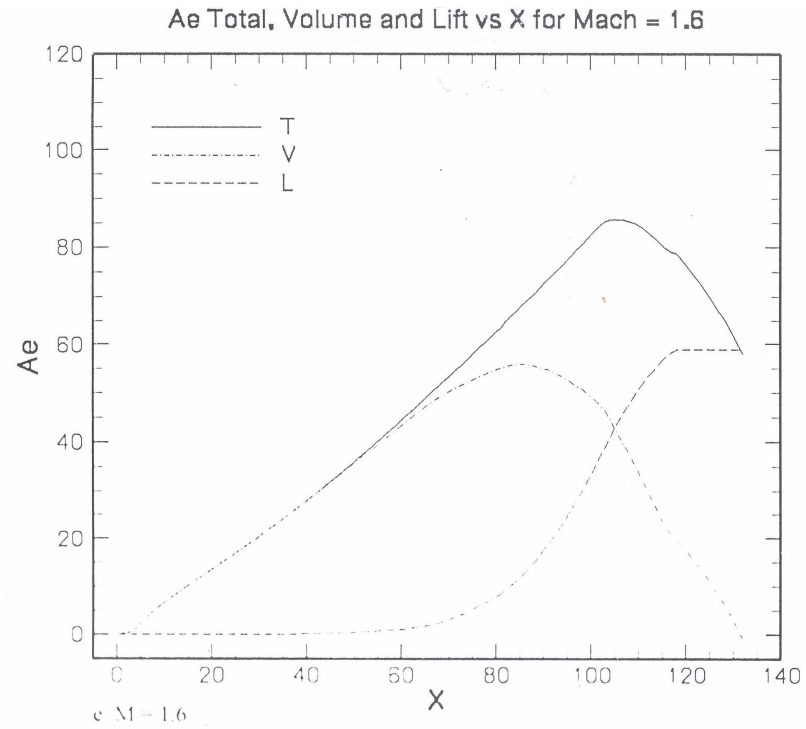
Figure E3. - Continued.
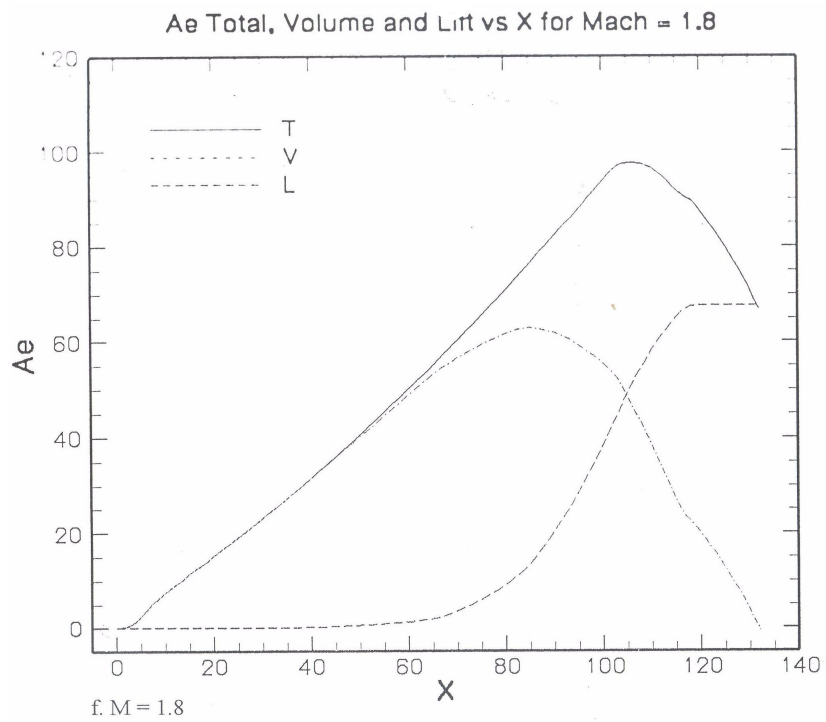
Figure E3. - Concluded.
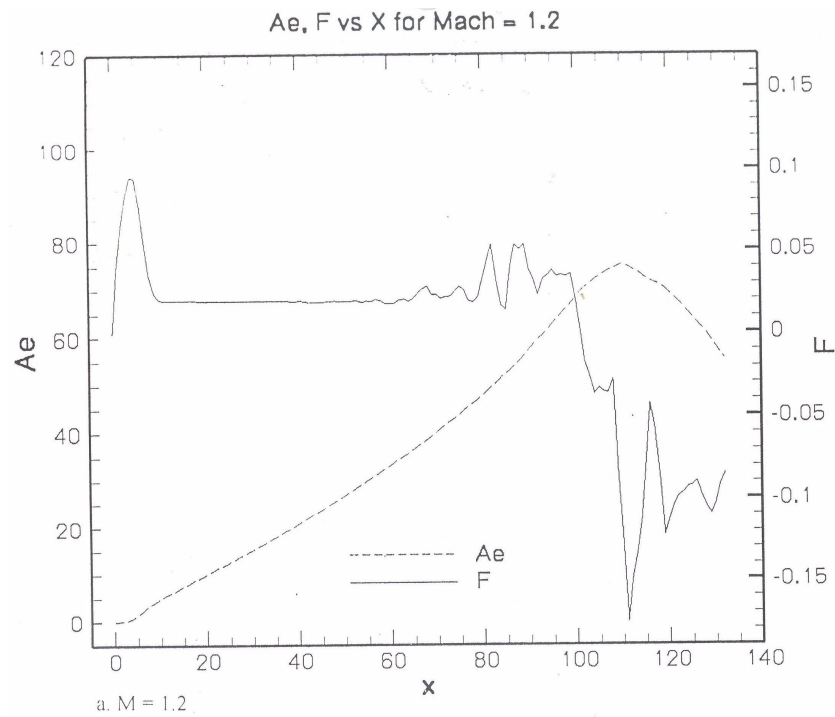
Figure E4. - Variations of the total effective area (A_e) distributions with x and the resulting F-functions for Mach numbers from 1.2 to 2.0 for the flat-top configuration.
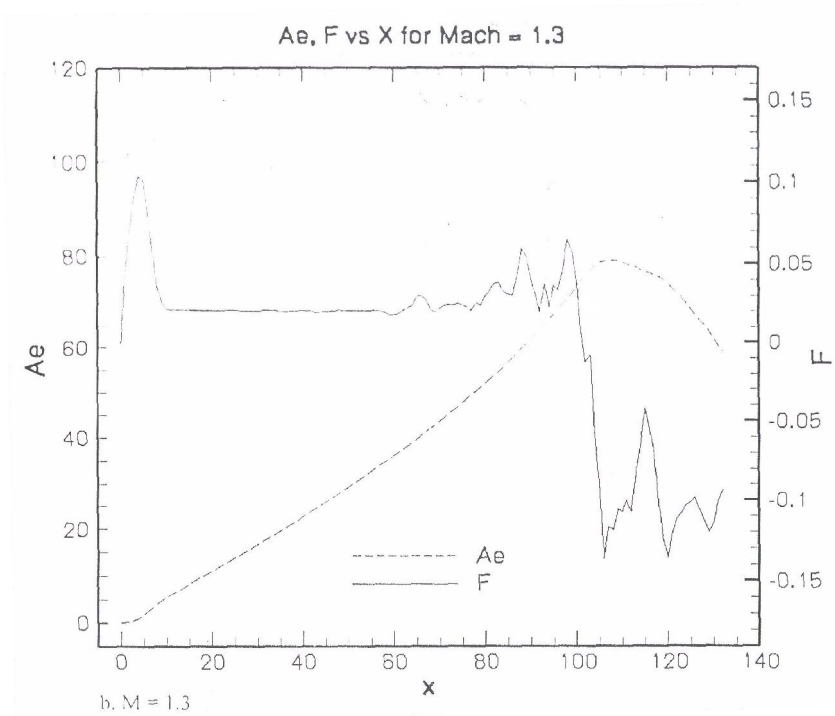
Figure E4. - Continued.
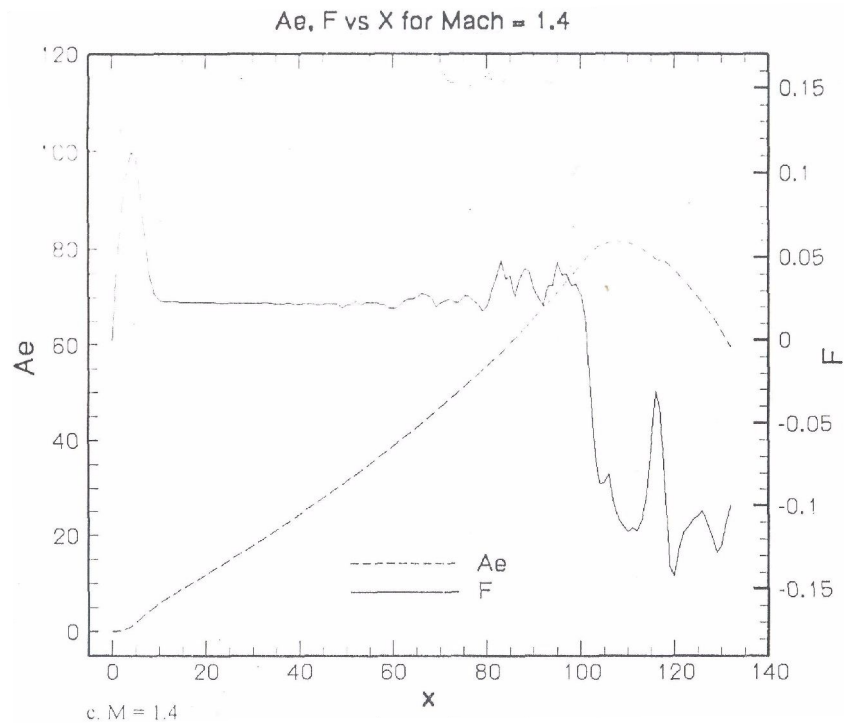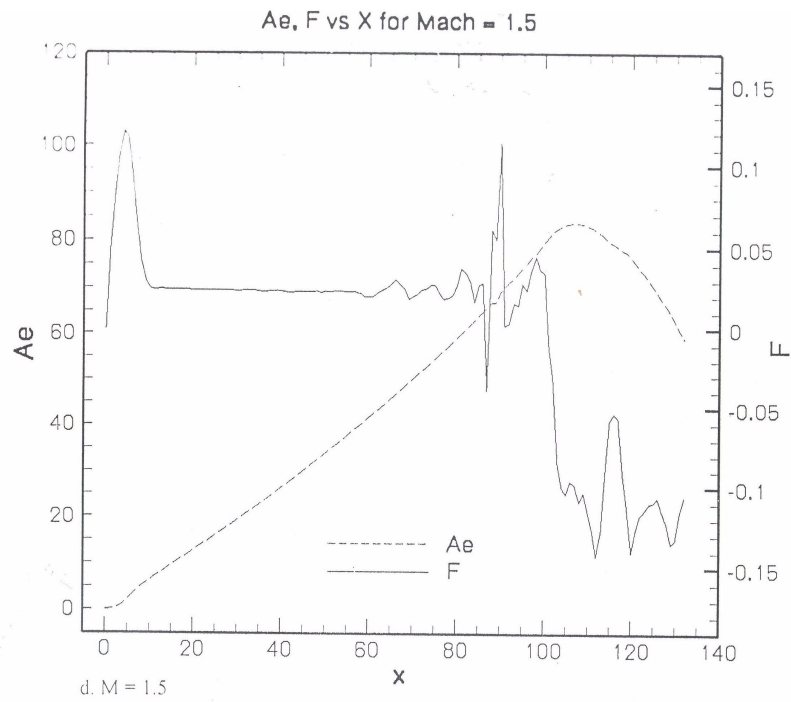
Figure E4. - Continued.

Figure E4. - Continued.

Figure E4. - Continued.

Figure E4. - Continued.

Ae, F vs X for Mach = 2.0

g . M= 2.0

Figure E4. -Concluded.

Ae Total, Volume and Lift vs x for Mach 2.0.
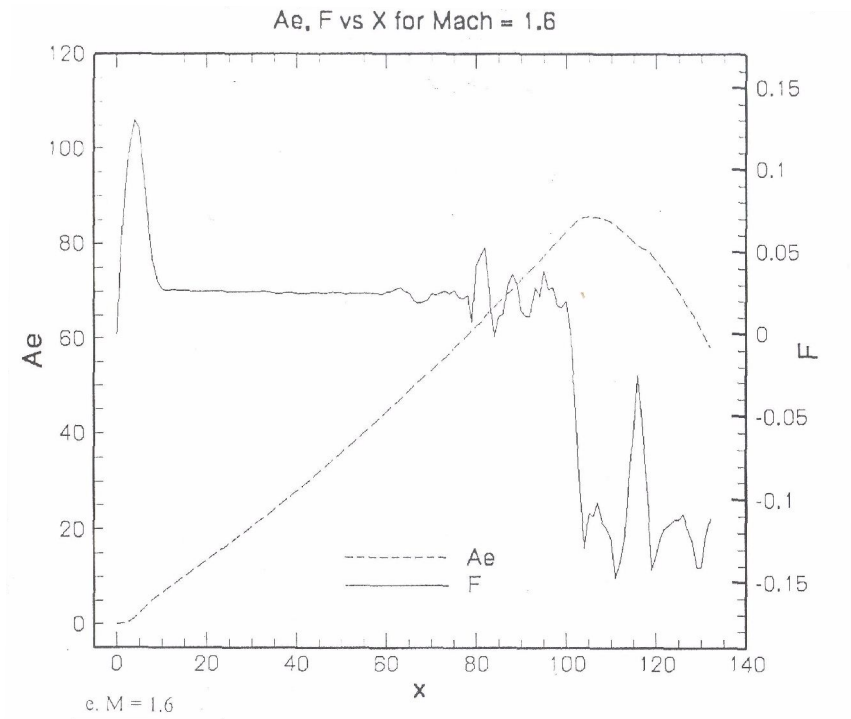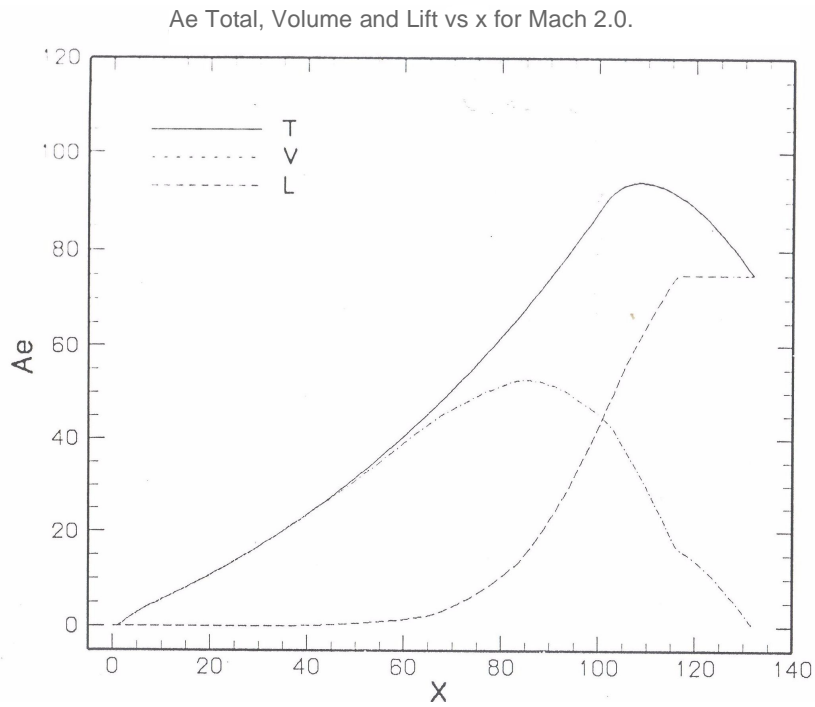
Figure E5. - Variations of the total effective area distribution and its lift and volume components, with x for the ramp configuration at the design Mach number of 2.0
W = 90,500 lbs. and h = 41,000 ft.

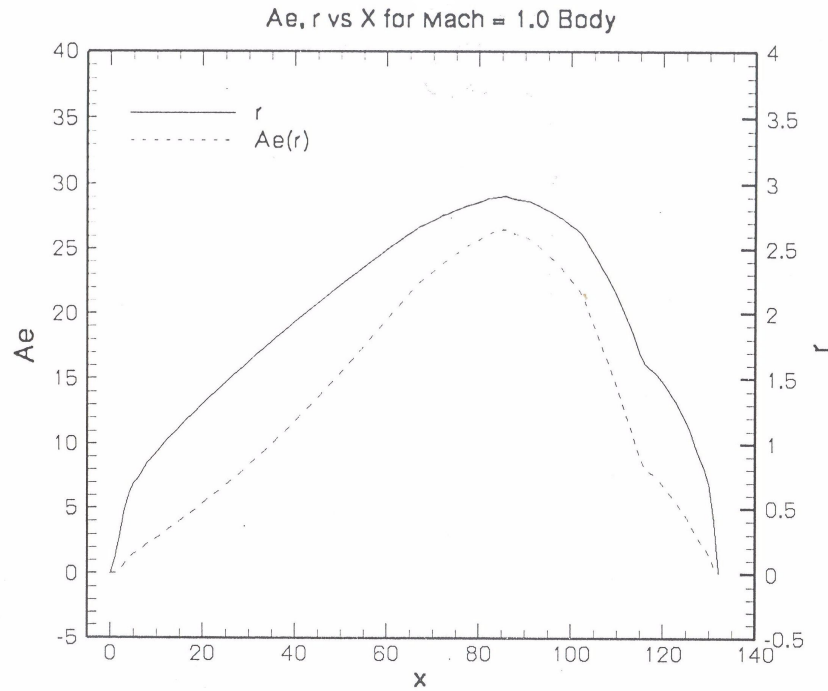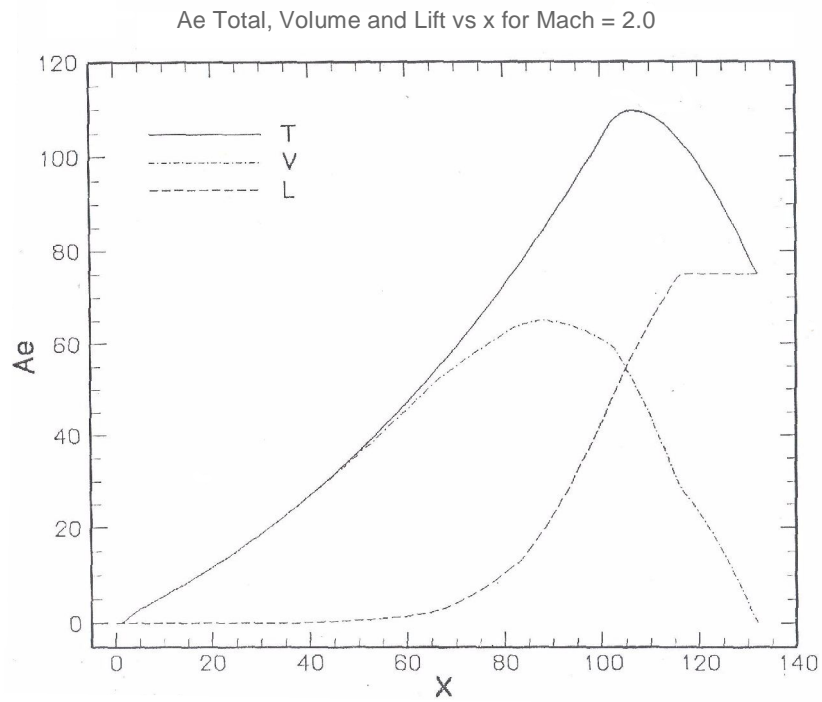Figure E6. - Variation of the basic body (M = 1 cuts) radius and area with x for the ramp configuration.

Figure E7. - Variation of A_e and its lift and volume components for the second ramp-type configuration, M = 2.0, W = 90,500 lbs. and h = 41,000 ft.
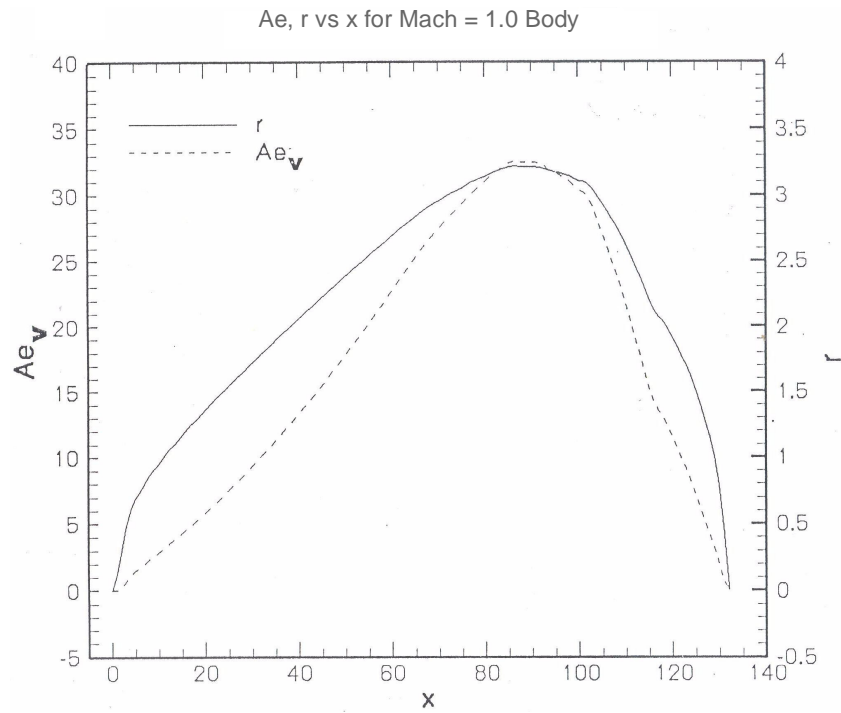
Figure E8. - Variation of the basic-body (M = 1) radius and area with x for the second ramp-type configuration.
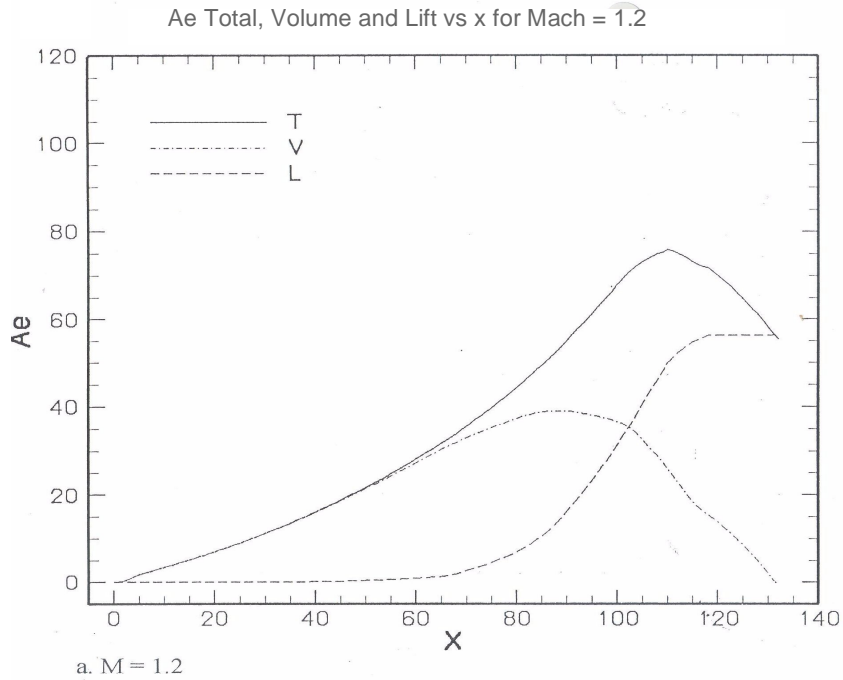

a. M = 1.2

Figure E9. - Variations of the total effective area and its lift and volume components with x for a range of design Mach numbers from 1.2 to 1.8 for the second ramp-type configuration.

Ae total, Volume and Lift vs x for Mach = 1.3

b. M = 1.3

Figure E9. - Continued.

Ae Total, Volume and Lift vs X for Mach = 1.4
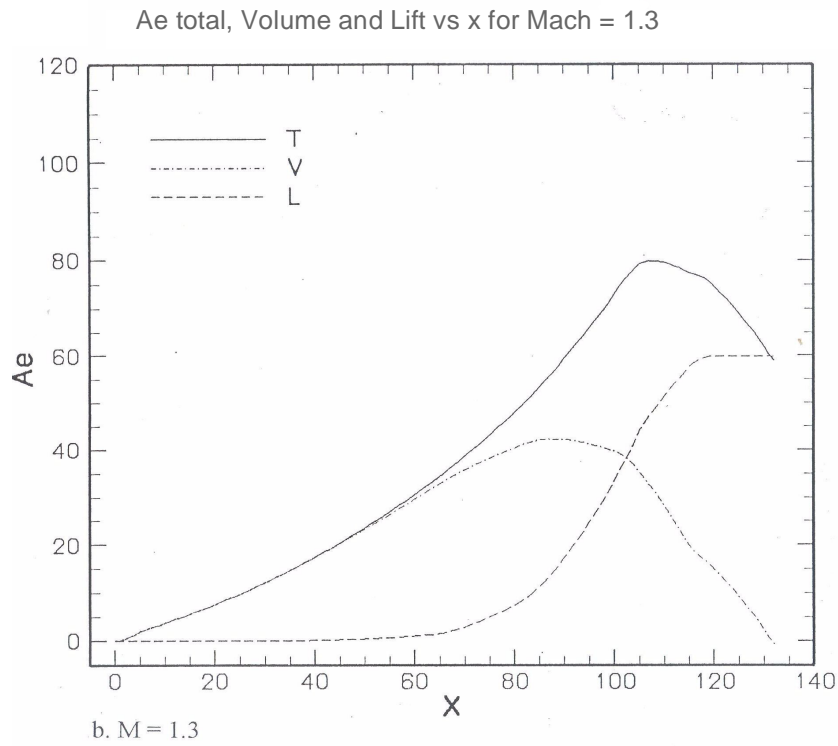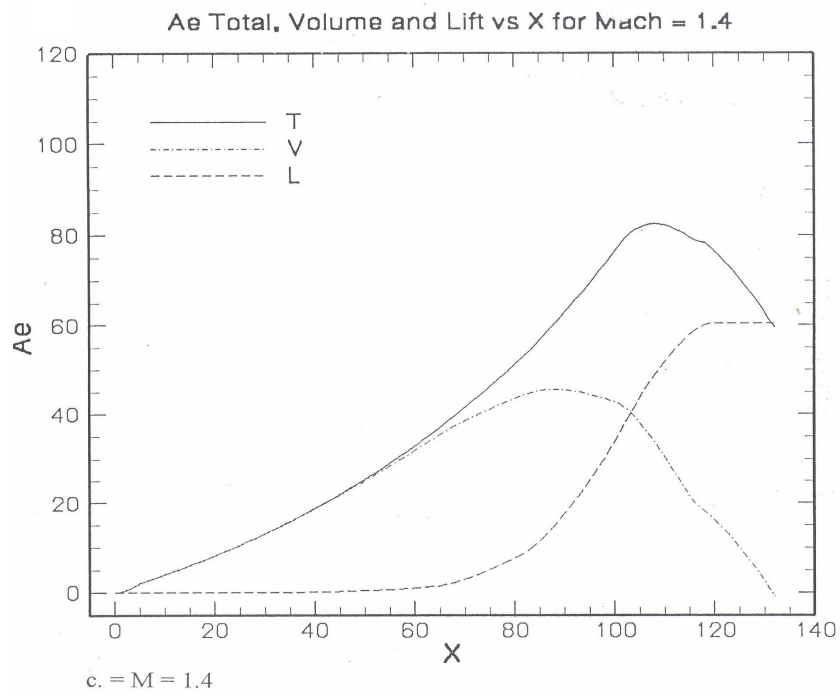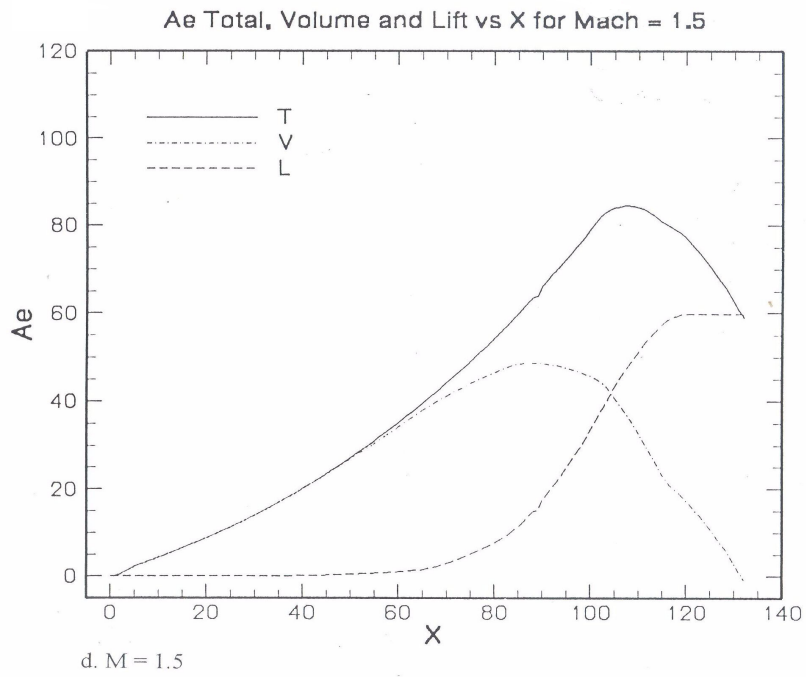

c. = M = 1.4

Figure E9. - Continued.

Figure E9. - Continued.

Figure E9. - Continued.
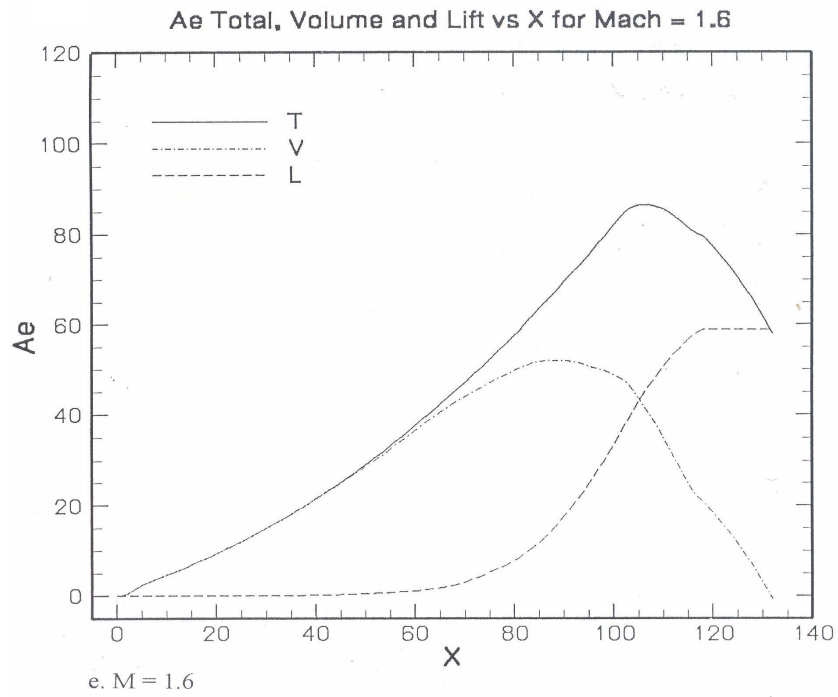
f. M = 1.8
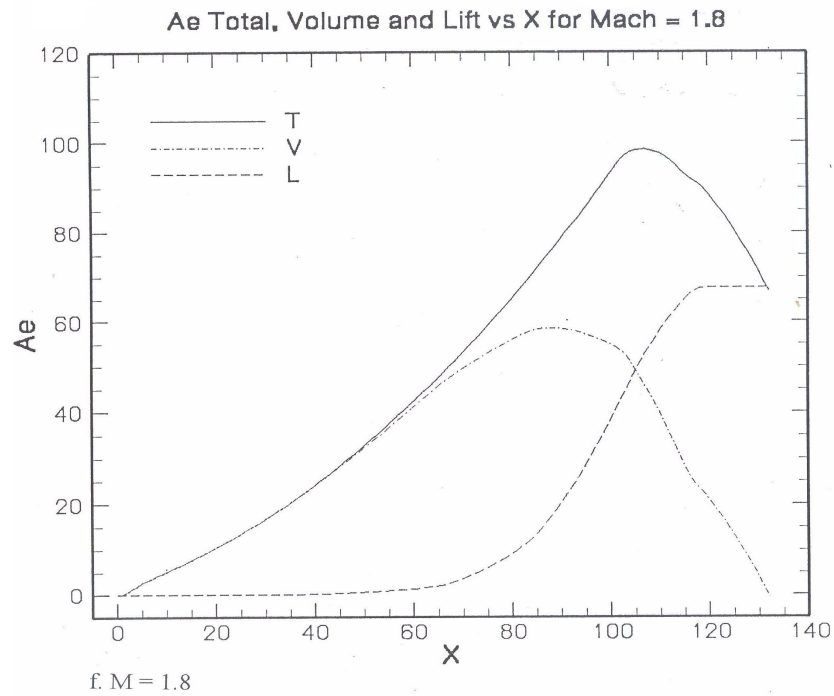
Figure E9. - Concluded.

a. M = 1.2
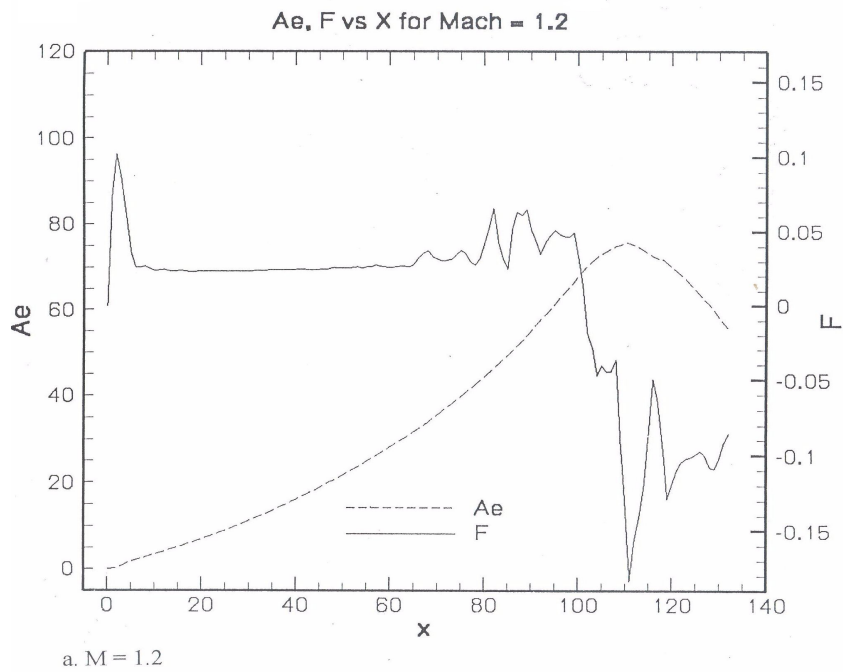
Figure E10. - Variations of the total effective area (A_e) distributions with x and the
resulting F-functions for Mach numbers from 1.2 to 2.0 for the "second" ramp-type configuration.

Ae, F vs X for Mach = 1.3

b. M = 1.3

Figure E10. - Continued.

Ae, F vs X for Mach = 1.4

c.   M = 1.4

Figure E10. - Continued.

d. M = 1.5

Figure E10. - Continued.

e. M = 1.6
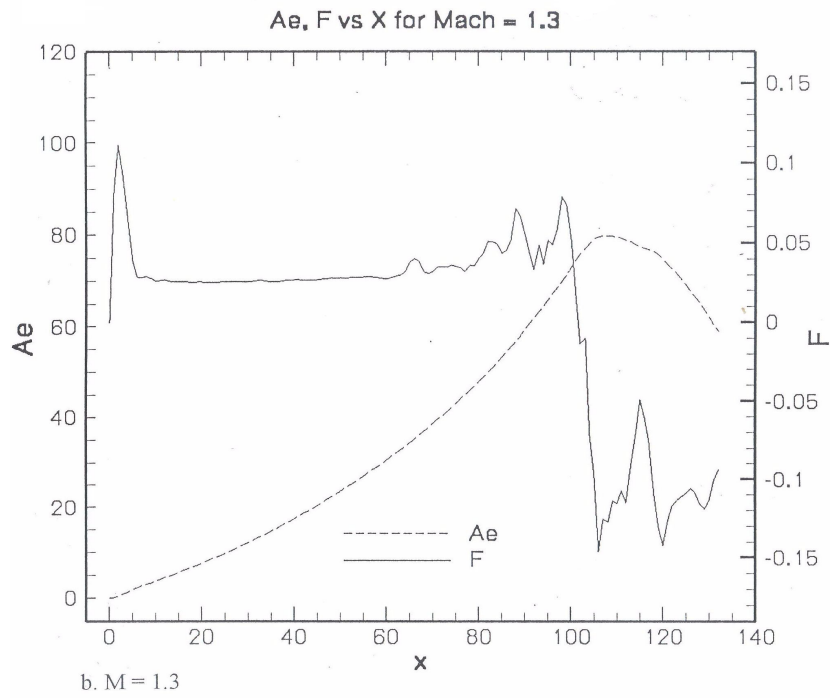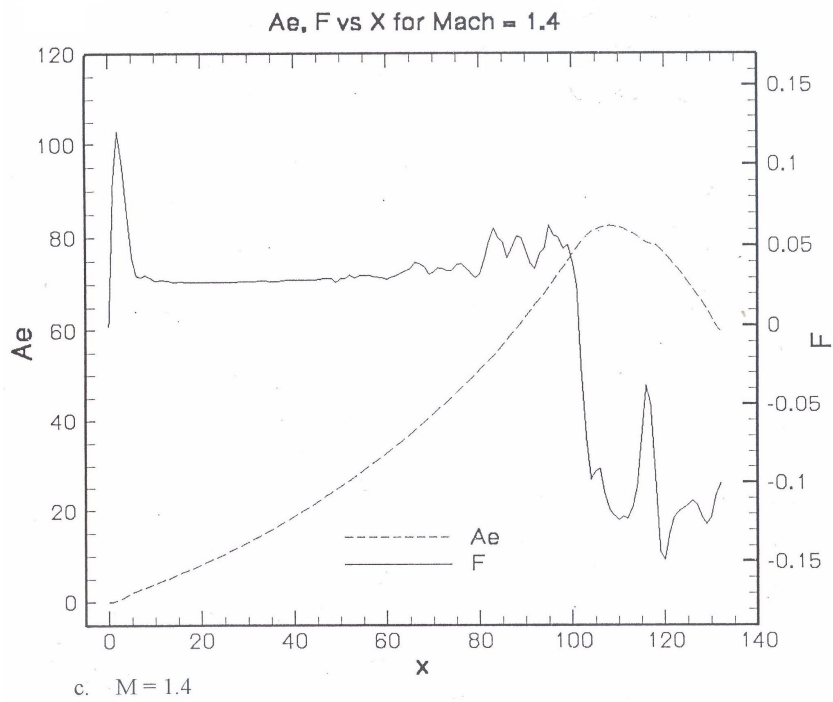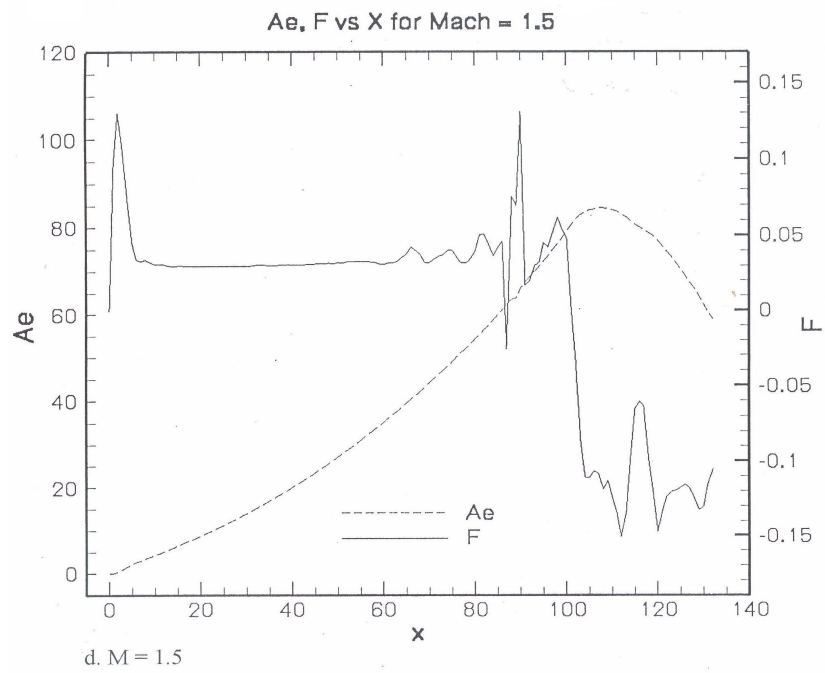
Figure E10. - Continued.

f. M = 1.8

Figure E10. - Continued.

g . M = 2.0

Figure E10. - Concluded.

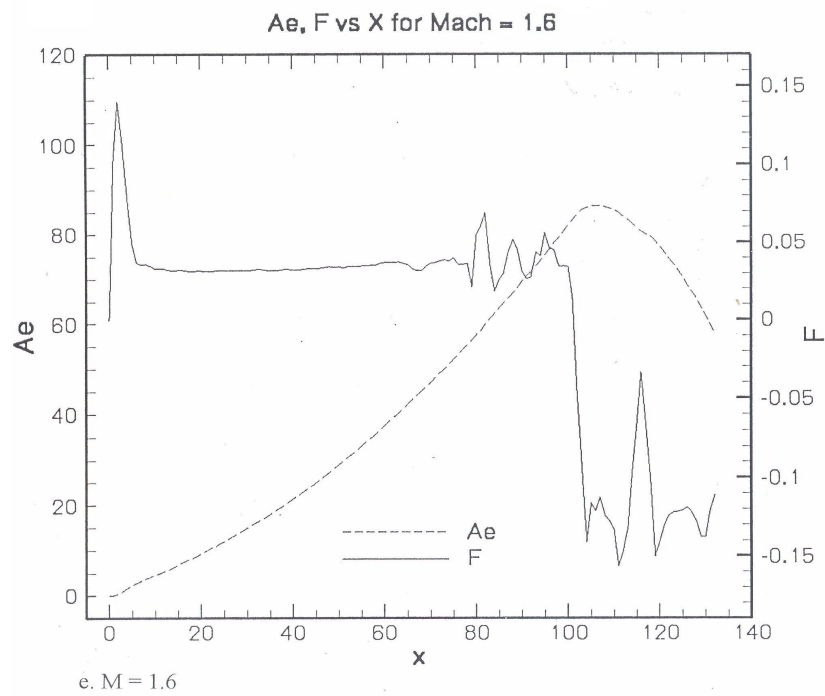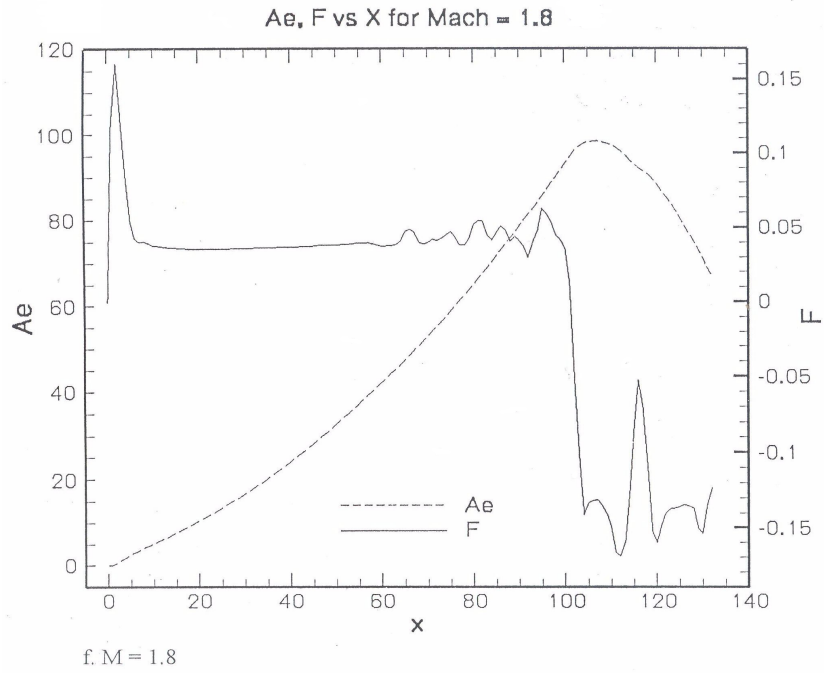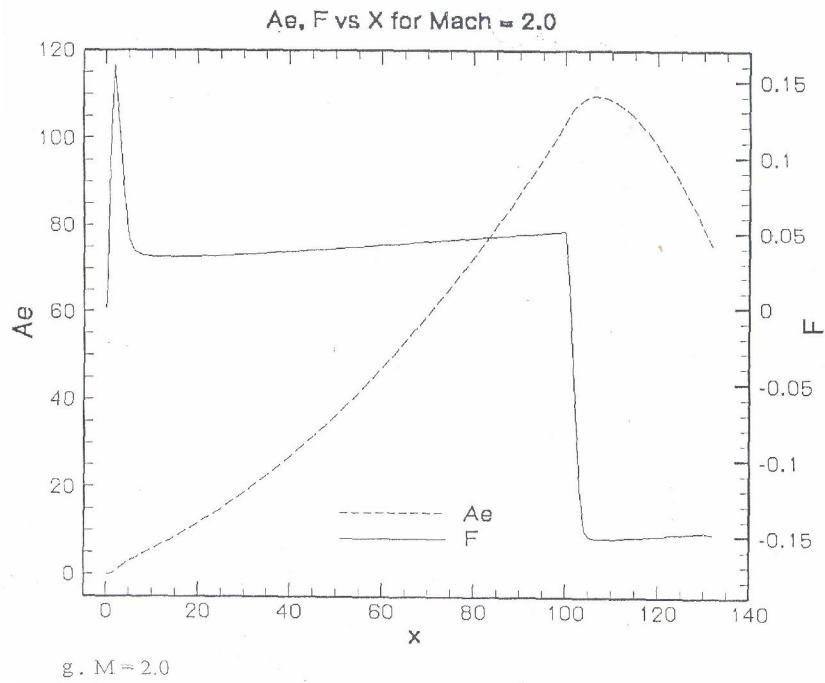**Appendix B**

Incorporaton of George-Seebass Signature into PCBOOM4

By Kenneth J. Plotkin, Wyle Laboratories

George and Seebass[1,2] define a parameterized F-function, sketched in Figure 1, that evolves into an optimal minimized flat-top or minimum-shock sonic boom signature. The F-function up to aircraft length l is given by

$$F(y) = A\delta(y) + By + C, \quad 0 \le y \le \lambda$$
$$= By - D, \qquad\qquad \lambda \le y \le l \quad (1)$$

The signature is defined by six parameters:

- A – the area of the initial nose spike
- B – the slope of the compression or (if zero) plateau regions
- C – F-intercept of the compression/plateau forward of λ
- D – F-intercept of the compression/plateau aft of λ
- λ – position of transition from forward positive to rear negative regions
- l – vehicle length

For practical design applications, the nose delta function is generally represented as a triangle, as sketched in Figure 1, with length y_f and height H, such that $A = 2H/y_f$ The quantity y_f is important in defining the initial shape of the aircraft nose, and is a key nose bluntness parameter in Darden's minimization studies[3,4] (also see Appendix A).

The signature for $y > l$ is defined, in closed form, by Equation (3) of Reference 1. This is based on the assumption of a constant area wake, and is also contained in References 5 and 6.

The slope B is the same for both the forward and aft compression/plateau regions, and is selected such that the compression at the ground will be inaudible. There is a maximum value of B, which we denote here as B_{max}, for which the compression regions will steepen to vertical at the design point. The actual slope B must be less than this, and the parameter η is used to define the actual slope: $B = \eta B_{max}$. The relation between η and the audibility of the boom is not linear, so there is no particular criterion value for η. It is, however, a useful parameter because the minimization analysis developed in References 1

and 2 rely on limits involving B_{max}. B_{max} is related in a simple way to the age parameter at the ground for the design condition.
 Figure 1, which replicates Figure 3 of Reference 2, includes dashed lines that appear to be extensions of the slope B. Those dashed lines are used as construction references in the design point area balancing, and are always at slope B_{max}. The slope-B compressions in Figure 1 happen to be drawn at $\eta = 1$. Reference 3 contains a similar sketch, but with B at a value corresponding to $\eta < 1$. The quantity we denote B_{max} is denoted s in Reference 1.

The quantity t shown in Figure 1 is the point where the tail wave intersects the B_{max} slope after l. It is not an independent parameter, but is derived from the quantities defined above. Similarly, use of nose length H and y_f instead of delta-function factor does not add another parameter, since $A = Hy_f/2$ and optimization requires that y_f is small enough that the results are equivalent to those computed for a true delta function.

B.2. PCBoom4

PCBoom4[7] is a sonic boom program that has its roots in the NASA program originally written by Thomas[8] in 1972. It has a number of extensions, including calculation of focus signatures, automatic calculation of footprints from complete maneuvers and missions, default F-functions for current supersonic aircraft, effects of rocket exhaust plumes, multiple atmosphere input formats, multiple F-function input formats, and a modern graphical user interface. Executables run on a 32-bit Windows PC.

Application of the George-Seebass form of the F-function is via an F-function signature input file in the normal stream of input data.

The main GUI interface to PCBoom4 is directed toward designers and planners dealing with conventional N-wave aircraft, and operates the boom calculation in "simple" mode. F-function input is not accessible through the GUI, but can be accessed in full mode from the command line. The GUI is reviewed here as background for general operation of the program. The GUI also provides a convenient method of generating trajectories. The GUI can be used to generate trajectories that can be used in command-line full mode runs.

The openly released version of PCBoom4 consists of the following programs:

PCB4win.exe - the main GUI
Maneuve.exe - maneuver generator
FOBoomw.exe - boom calculation program (Version 4.0)
PCBFootw.exe - post processor: organizes footprints and signatures
Wcon.exe - contour and signature display program

These programs, together with samples, help files, and an electronic copy of Reference 7, are in the PCB40 directory of the supplied PCBoom archive. That directory is the current, publicly available, version of PCBoom4.

Operation of the program though the main GUI (PCB4win) is described in Reference 7. A PCB4win user will set up a case via various dialogs and menus. If a trajectory is to be created, PCB4win will invoke MANEUVE, which allows definition of trajectories via dialogs and menus. Once a case is set and the run is ordered, PCB4win will cause FOBoomw and PCBFootw to run. Those two programs are pure command-line batch-mode executables, with no Windows API functions. After they run, PCB4win will invoke Wcon, which interactively displays footprints and signatures. Wcon can output footprints and signatures to a printer, as cgm (computer graphics metafile) graphic files, or as ASCII tables. Signatures may be viewed (and output) as time series or in spectral form. Wcon can generate and display signatures that have penetrated below the surface of a body of water.

PCB4win operates FOBoomw by writing a file, type ".DAT", that is the input to FOBoomw. PCBfootw operates on a file output from FOBoomw, and Wcon operates on files written by PCBFootw. Because of its intended use by planners (not researchers), PCB4win accesses only a fraction of FOBoomw's capabilities. Full capability may be accessed by manually writing the DAT file, then running PCBooomw, PCBfootw and Wcon from the command line:

foboomw case.dat m
pcbfootw case.out n
wcon case.qwk

where "case.dat" is the manually-created DAT file and m, n are options that control the outputs of pcboomw and pcbfootw. Options and summary use instructions may be obtained by running each of those programs with no arguments. If wcon is run with no arguments, it will prompt for a ".QWK" file to display - there are no options.

Note that these programs are manually run from a Windows command prompt. While the Windows command prompt looks very much like the old MS-DOS command prompt, and has versions of almost all the MS-DOS utilities, it is a 32 bit environment, and not actually MS-DOS. Some versions of Windows include a true 16 bit MS-DOS mode. This software will not run under MS-DOS, nor under Windows 3.x.

B.3. PCBoom4 Version 4.11

Directory PCB411 of the supplied archive contains the following, all limited distribution:

FOBoomw.exe - foboomw Version 4.11. This has George-Seebass six-parameter F-function input, plus support for "u28" evolution files, described below.
PCBfootw.exe - a slightly updated version of pcbfootw
Sigw.exe - a viewer for "u28" files, described below
INFILE.TXT - a full description of all possible inputs in the FOBoomw ".DAT" file.
Samples and supporting files

The updated (limited distribution) versions of FOBoomw and PCBFootw can be put into the installation directory for PCBoom 4.0, replacing the older versions. File INFILE.TXT describes all possible inputs to PCBoom 4.11.   Three sample DAT files are included. These illustrate the use of direct F-function input vs George-Seebass six parameter input, and single-point steady flight analysis versus full maneuver analysis. It is recommended that these be used as templates for preparing other cases.

The sample cases are:

- Ramp04.dat - a single point case using a directly specified F-function
- Ramp04g.dat - a single point case using George-Seebass F-function
- Ramp04a.dat - a full maneuver case (transonic acceleration) using a George-Seebass F-function

These three input files are presented in Figures 2, 3 and 4. Text that follows a ";" is not part of the data, but a comment to the right of numeric inputs. Referring to Figure 2, the lines in a DAT file are:

1. Title
2. Ambient pressure at the ground and local value of g. If 0 or a negative value is entered for pressure, then data are to be read from a file named in the next line. Several file formats are allowed, and defined in INFILE.TXT and WR 02-11. 0. 0. in this case means an ".ATT" format file.
3. The name of the ".ATT" atmosphere file.
4. Number of output altitudes. Descending order, all below the aircraft flight altitude minus the starting radius.
5. The output altitudes
6. Parameters organizing focal zone analysis relative to the ground. 0 0 0 directs the program to use default values, which is generally the best choice.
7. Ground reflection factor. 1.9 is traditional.
8. R/L for starting signature. Ray tracing will begin R/L aircraft lengths from the flight path. Use a value appropriate to how the starting signature was obtained.
9. Signature input mode. 2 denotes F-function at one Mach number and azimuth.

10. Number of points in signature, if it is in-line in the DAT file. 0 means it is in a separate file

11. Name of the starting signature file. This is a table of F vs x, and is presented in Figure 5.

12. Aircraft length (feet), weight (kilopounds), Mach number at which F-function is defined, and ambient pressure at which F-function is defined. This function was defined at Mach 2, and at 41000 feet where the ambient pressure is 377.16 psf.

13. Shape factor curve to be used when scaling to other Mach numbers and pressures. Shape factor curves are taken from Carlson (ref. 9). There are curves for several categories of military aircraft, for the Space Shuttle, and for commercial SST's. The number 7 is the curve for commercial SSTs.

14. Numeric parameters. See WR 02-11 and INFILE.TXT for their meaning. Otherwise leave them alone.

15. Number of azimuthal (phi) values at which to compute the boom. In this case, one.

16. The phi value. In this case, 0 degrees, straight down.

17. Comment line with names of trajectory parameters. This line has been truncated to fit the page. See WR 02-11 and INFILE.TXT for a full definition.

18. Trajectory data. In this case, there is only one point, at a steady condition of Mach 2.0, 41000 feet.

19. End-of-file marker.

Sample file ramp04g.dat, shown in Figure 3, is identical to ramp04.dat except that it specifies signature ramp04.gsf, a George-Seebass form.

Sample file ramp04a.dat, shown in Figure 4, is identical to ramp04g.dat except for the final few lines. Line 15, instead of having a positive value, has 0. That means that, at each time step, the program is to compute booms across the carpet from cutoff to cutoff. Line 16 contains a value of 5, indicating this is to be done at 5-degree increments.

Line 17 of ramp04a.dat contains "file" (left justified, lower case) followed by the name of a trajectory file. The format of lines in the trajectory file is identical to that which may appear in-line as in ramp04.dat and ramp04g.dat. There is no "END" line in this DAT file. When trajectory input is from a separate file, the END marker is in the trajectory file. The trajectory file is defined field-by-field in INFILE.TXT. A file may be used that has been generated from the PCB4win GUI or by running MANEUVE directly. It may also be generated manually in a text editor.

Figure 5 shows a directly specified F-function file. The first line is a title. The second is the number of x, F pairs. A table of values follows this.

Figure 6 shows a George-Seebass six parameter F-function file. The lines in this file are:
1. Keyword "seeb". This must be lower case, left justified.

2. Title line.
3-9. The six parameters, as defined earlier. The text to the right is informational, and not read. Note that there are seven values: H and y_f represent A, and logically count as one.

B.4. Running PCBoom4 Version 4.11

As noted in A.1, boom calculations can be run from the command line via the sequence

foboomw case.dat m
pcbfootw case.out n
wcon case.qwk

This sequence, with m = 1 and n = 5, is appropriate for cases such as the sample DAT file in Figure 4, where the last few lines specify computing boom at azimuths across the width of carpet and there is a trajectory file with at least two time steps where the boom will reach the ground. The result is a plot of the footprint, displayed via WCON. Signatures at any point in the footprint are accessed interactively from the WCON interface.

Note that the boom for a full footprint case will be strictly correct only at one point: the flight condition and azimuth at which the F-function is defined. The F-function at other points is adjusted via simple scaling rules that are applicable to N-wave booms but may not be appropriate for complex shaped booms.

An original function of the Thomas program[8] was to examine the evolution of a shaped signature as it propagated to the ground at one flight condition. That mode is available by using a single-point DAT file such as shown in Figures 2 and 3, and invoking from the command line:

Foboom case.dat m
sigw case.u28

where m = 3. Setting m = 3 specifies that foboomw will generate file case.u28 that includes the signatures at the output altitudes shown in line 5 of Figures 2 and 3. This output is at zero azimuth and time = 0, so the trajectory data in the DAT file (the final five lines in Figure 2) must specify those values. There can be up to 49 output altitudes.

The u28 file is ASCII, and is self-explanatory. Program sigw displays the signatures in stacked format. If there are more than will fit on the screen, cursor up/down scrolls the display. ESC ends the program. F11 will generate a PCX file of the current screen. The PCX file has a name of the form casen.pcx, where "n" is a sequential letter from a through z. The program tests for existing casen.pcx files, and uses the next unused letter. Up to 26 PCX files of a given case name can be generated before old ones are overwritten.

References

1. George. A.R., and Seebass, R, "Sonic Boom Minimization Including Both Front and Rear Shocks", AIAA Journal. 9 (10), 2091-2093, October 1971.

2. Seebass, A.R., and George, A.R., "Sonic-Boom Minimization," J. Acoust. Soc. Am., Vol 51, No 2 (Part 3), 686-694, 1972.

3. Darden, C.M., "Minimization of Sonic-Boom Parameters in Real and Isothermal Atmospheres," NASA TN D-7842, March 1975.

4. Darden. C.M., "Sonic Boom Minimization With Nose Bluntness Relaxation", NASA TP 1348, 1979.

5. Jones, L.B., "Lower Bounds for Sonic Bangs", J.Roy.Aeron.Soc., 65, 1-4, 1961. An ad hoc analysis of the same problem was given by Carlson, H.W., "The Lower Bound of Attainable Sonic-Boom Overpressure and Design Methods of Approaching This Limit", NASA TN D-1494, October 1962.

6. Petty, J.S., "Lower Bounds for Sonic Boom Considering the Negative Overpressure Region," Journal of Aircraft, Vol 7, No 4, 375-377, July-Aug 1970.

7. Plotkin, K.J., and Grandi, F., "Computer Models for Sonic Boom Analysis: PCBoom4, CABoom, BooMap, CORBoom," Wyle Report WR 02-11, June 2002.

8. Thomas, C.L., "Extrapolation of Sonic Boom Pressure Signatures by the Waveform Parameter Method," NASA TN D-6832, June 1972.

9. Carlson, Harry W.: Simplified Sonic Boom Prediction. NASA TP 1122, March 1978.
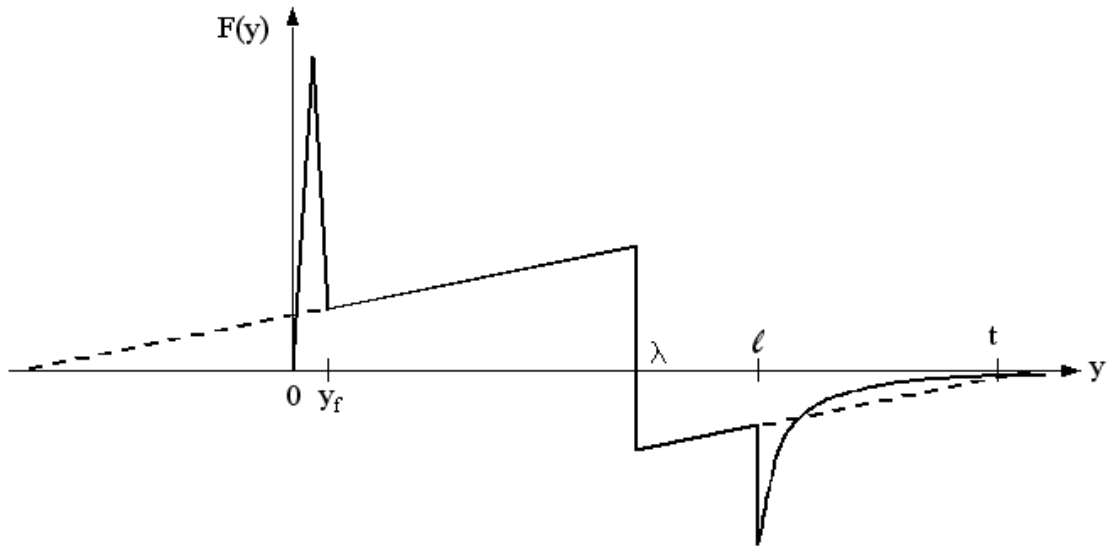
Figure 1. George-Seebass six-parameter F-function

```
Mach 2.0, 41000 ft ramp, SIG input
    0.   0.                     ;0 0 means read atmosphere from file
usstd.att
    7                           ;7 output altitudes, including ground
 30000. 25000.  20000.  15000.  10000.   5000.      0.
 0. 0. 0.                       ;See infile.txt - usually keep this as 0 0 0
 1.9                            ;Reflection coefficient
 1.00                           ;roverl
 2                              ;2=F-function
 0                              ;0 indicates read signature from file
ramp04.sig
100.    100.   2.0  377.16      ;al, weight, Mach, ref pressure
7                               ;Shape factor curve
 .5  500.   .5                  ;dphi, dstraj, tstep
 1                              ;One phi value
 0.                             ;The phi value
 keyword       tstart      xplane      yplane      fltalt       mach ...
```

Figure 2. Sample input file ramp04.dat

```
Mach 2.0, 41000 ft ramp, GSF input
    0.    0.                      ;0 0 means read atmosphere from file
usstd.att
   7                             ;7 output altitudes, including ground
 30000. 25000.  20000.  15000.  10000.   5000.      0.
 0. 0. 0.                        ;See infile.txt - usually keep this as 0 0 0
 1.9                             ;Reflection coefficient
 1.00                            ;roverl
 2                               ;2=F-function
 0                               ;0 indicates read signature from file
ramp04.gsf
100.   100.   2.0  377.16        ;al, weight, Mach, ref pressure
7                                ;Shape factor curve
 .5  500.  .5                    ;dphi, dstraj, tstep
 1                               ;One phi value
 0.                              ;The phi value
 keyword        tstart      xplane      yplane      fltalt      mach ...
                0.00        0.00        3.00        41000.   .200D+01 ...
```

Figure 3. Sample input file ramp04g.dat

```
 Transonic acceleration, ramp04.gsf source
     0.    0.                     ;0 0 means read atmosphere from file
  usstd.att
    7                            ;7 output altitudes, including ground
  30000. 25000.  20000.  15000.  10000.   5000.      0.
  0. 0. 0.                       ;See infile.txt - usually keep this as 0 0 0
  1.9                            ;Reflection coefficient
  1.00                           ;roverl
  2                              ;2=F-function
  0                              ;0 indicates read signature from file
 ramp04.gsf
 100.   100.   2.0  377.16       ;al, weight, Mach, ref pressure
 7                               ;Shape factor curve
  .5  500.  .5                   ;dphi, dstraj, tstep
  0                              ;All phis from cutoff to cutoff
  5.                             ;5 degree increments

 file 06-00.trj
```

Figure 4. Sample input file ramp04a.dat

```
Mach 2.0, 41000 ft ramp November 04, Yf = 4
    16
     0.000    0.000000
     2.000    0.200000
     4.000    0.020880
   102.000    0.042440
   102.200   -0.132960
   132.000   -0.126360
   133.000   -0.135000
   134.000   -0.135000
   135.000   -0.109000
   136.000   -0.094500
   137.000   -0.084500
   138.000   -0.077160
   139.000   -0.071430
   140.000   -0.066820
```

Figure 5. Sample F-function file ramp04.sig

```
seeb
Mach 2.0, 41000 ft ramp November 04, Yf = 4
0.2             H - height of spike
4.0             yf - duration of spike
0.02            C - height of start of ramp
0.1554          D - constant defining start of negative part
0.00022         B - slope of isentropic compression
102.0           lamda - length of positive portion
132.0           l - length to rear spike
```

Figure 6. Sample George-Seebass six parameter F-function file ramp04.gsf

Appendix C

FOCUS CONDITION STUDY
by
Kenneth J. Plotkin
Wyle Laboratories

A number of possible airplane maneuvers and off-design conditions were examined using PCBoom4 to assess the potential for generating focus booms at the ground. These included the following:

  - Full nominal mission
  - Focal analysis for variations of transonic acceleration
  - Climb, turns at cruise and descent-deceleration at end of cruise.

This analysis yields focus signatures via the current PCBoom4 method. Data generated includes the pre-focus signature entering the focal zone, plus ray and caustic curvatures.   The PCBoom4[1] method consists of using Guiraud's[2] scaling law to apply the Gill-Seebass[3] step focus solution to each shock in the pre-focus signature.

The SSBJ initiates transition from subsonic to supersonic speeds (Mach 0.95 through Mach 1.4) at constant altitude of 32,850 feet and with an acceleration rate of about 0.2 m/sec^2. It continues to accelerate in a slight climb to $M = 2$ at about 41,000 feet, the start of cruise. From there it flies a constant Mach and at constant C_L to 60,000 feet, the end of cruise. No maneuvers (i.e., turns) are included. At end of cruise, the SSBJ decelerates from $M = 2.0$ to $M = 1.0$ at a nearly constant altitude of about 60,000 feet in order to avoid boom focusing.

Three types of maneuvers were considered in this study:
  1. Acceleration from subsonic to supersonic flight.
  2. Mach 2 turns at cruise altitude.
  3. Descent and deceleration at the end of cruise.

At Mach 2, the turn rate necessary to cause a focus is well above that which would be acceptable in a passenger aircraft, so Maneuver 2 did not cause focusing. Similarly, a focus-generating push-over at the start of descent would be beyond the envelope of a passenger aircraft. In principle, there is a caustic associated with the final deceleration to subsonic speeds - this is the boundary of the limiting rays. This final deceleration caustic, however, slopes upward. Upward-curving rays forming the caustic would intercept the ground before they reached the a geometric focus point on the caustic. Thus, there is no ground focus for final deceleration.   Maneuver 3 is, therefore, not a focus condition, either from start of descent or final transition to subsonic speed.

Initial acceleration, Maneuver 1, is thus the only focusing maneuver. Values of acceleration from 0.2 m/sec^2 through 2.0 m/sec^2 were analyzed. In addition to the nominal case of level acceleration at 32,850 feet, descent and climb at - 1 degree and +3 degrees, respectively, were also examined.

The -1 and +3 degree profiles begin at Mach 1 at 32,850 feet, so that focus for these cases occur at altitudes other than 32,850 feet.

Results of the focus analysis are shown in figure 1 through figure 4 for the flat-top, ramp, N-wave and double-peak N-wave, respectively. Each figure has two parts. Part "a" shows the peak focus overpressure as a function of acceleration for level flight, three-degree climb, and one-degree dive. The results are shown as curves for each flight path angle. Part "b" shows the peak focus pressure as a function of altitude. Results in part "b" are shown as points, without regard to acceleration rate or flight path angle. Acceleration rate and flight path angle are not significant factors for focus amplification:

- In Part "a" of each figure, the peak pressures for level flight, and one degree dive vary very little, if at all, with acceleration.

- Peak focus pressure for the three-degree climb increases with increasing acceleration. This trend is not, however, an acceleration effect. It is an altitude effect. At lower acceleration rates, the aircraft reaches higher altitudes before the focus occurs.

Part "b" of each figure shows the dependence on altitude: amplitudes are smaller at higher altitudes. There is some variation in the cluster of results around each altitude, but those variation are comparable to those associated with the numeric quality of the focus calculation.

Quality of Focus Prediction

The focus results presented in this **Appendix C** contain irregularities: there is not always a smooth transition from one condition to another. This is due to numeric issues in implementation of focus theory. PCBoom4[1] calculates the focused signatures by applying the Gill-Seebass[3] step function solution to each shock in an incoming signature, scaling according to Guiraud's similitude[2]. The code, which numerically integrates along rays in finite steps, must determine the edge of the focal zone. The edge it finds is not necessarily exactly at the focal zone boundary: it is usually slightly outside of it. That kind of irregularity, together with numeric precision in obtaining ray/caustic curvature, is considered to be the cause of most of the irregularities.

Recommendations for Software Update:

The focus process in PCBoom4[1] other than the numeric issues noted above, is rigorously correct for a flat-top signature, and has proven to be acceptable for N-wave signatures. In normal application of PCBoom4[1] to practical aircraft maneuver situations, the numeric issues have not been a problem. One might consider improving PCBoom4's implementation so as to yield smooth results in research applications such as the current study. Before embarking on such a development, however, it is prudent to consider the age of the focus technology in PCBoom4[1] (the Gill-Seebass[3] numeric solution is over 30 years old) and the assumption that a single shock solution can be independently applied to complex signatures.

Auger and Coulouvrat[4] have recently published a new numeric solution for a focused boom - the first since Gill and Seebass[3]. This solution, applicable to complex booms, shows that the PCBoom4[1] procedure is not applicable to a double-shock boom where the shocks are close enough to interact. The interaction causes the focus factor to be less than that predicted by the simple PCBoom4[1] superposition. Kandil and Zheng have replicated Auger and Coulouvrat's result (see **Appendix D** of this report) confirming that a complex multiple-shock boom will have a smaller focus factor than an N-wave or flat-top.

The focus pushover events in the Shaped Sonic Boom Experiment[5] (SSBE) demonstrated that focus booms from a shaped aircraft do not occur at the shape design condition. In the case of SSBE, the pushover maneuver, while at the design Mach number, involved a much lower lift coefficient than the design condition. Transonic acceleration - the one unavoidable focus maneuver - occurs at a Mach number much lower than cruise design. This opens the possibility of a dual-mode signature, where the signature at the focus condition is sufficiently complex that its focus factor is reduced. However, the findings of **Appendix A** of this report shows that shaped signatures designed for cruise flight retained their basic shape during transition flight.

Analysis of focal signatures for a mission requires incorporation of the modern numeric focus calculation into PCBoom4[1]. PCBoom4[1] calculates the signature entering the focal zone, plus the ray and caustic curvatures. These provide the boundary conditions for the program prepared by Kandil and Zheng. PCBoom4[1] currently outputs data necessary for H. K. Cheng's[6] wavy surface underwater boom propagation program, so the infrastructure is currently in place to link PCBoom4[1] to a more sophisticated analysis model. It would be straightforward to perform that kind of linkage from PCBoom4[1] to the Kandil-Zheng numeric focus software.

Focus Avoidance Maneuvers:

In 1971, Hayes[7] suggested the transition focus boom may be eliminated incorporating pushover pull-up maneuver (vertical acceleration) to cancel out the focusing caused by the forward acceleration. Haglund and Kane[8] examined the maneuver based on a physically realistic principle: acceleration caused rays to converge, while pitch-up caused them to diverge, and they concluded that the maneuver, as envisioned by Hayes, should be reversed, and that the maneuver should be a pull-up followed by a pushover in order to eliminate the caustic at the ground. In their study they described the mechanism of caustic elimination and noted that the pull-up portion of the maneuver would require thrust in excess of that available in a commercial SST. They also pointed out that the suddenness of the pushover needed to be defined. The concept of a sudden pushover is fatal to this concept. The pushover has two physically realistic problems. First, any maneuver that approximates a discontinuity is likely to be unacceptable for a passenger carrying aircraft. Second, and even more definitive, is that at some point the boom will reach the ground. There will be a region where there is no boom at the ground and a region where there is. The division between those regions, from the ground upward, will be an envelope of rays -- a caustic. That follows from the continuity of rays, and is inevitable when an aircraft transitions from subsonic speeds to boom-generating supersonic speeds. A transient maneuver to eliminate the caustic is topologically impossible.

The analysis presented in this report, particularly part "b" of Figure 1 through Figure 4, shows that increased altitude reduces the magnitude of the focus boom. The recent Auger-Coulouvrat focus solution has shown that complex boom signatures are amplified less than simple N-waves that had been considered in the past. These two effects provide a physically realistic path to alleviate focus issues from a future supersonic business jet.

References:

1. Plotkin, K. J., and Grandi, F.: Computer Models for Sonic Boom Analysis: PCBoom4, CABoom, BooMap, CORBoom, Wyle Report WR 02-11, June 2002.
2. Guiraud, J. P.: Acoustique Geometrique, Bruit Ballistique des Avions Supersonique et Focalization." J. Mecanique, 4, 215-267, 1965.
3. Gill, Peter M; and Seebass, A. Richard: Nonlinear Acoustic Behavior at a Caustic: An Approximate Analytical Solution. Aeroacoustics: Fan, STOL, and Boundary Layer Noise; Sonic Boom; Aeroacoustic Instrumentation; Henry T. Nagamatsu, ed., American Inst. of Aeronautics and Astronautics, c. 1975, pp. 353-386. (Also AIAA Paper 73-1037, 1973.)
4. Auger, J.; and Coulouvrat, F.: Numerical Simulation of Sonic Boom Focusing,: AIAA Journal, Vol. 40, No. 9, Sept. 2002, pp. 1726-1734.
5. Plotkin, K.; Martin, R.; Maglieri, D.; Haering, E.; and Murray, J.: Pushover Focus Booms from the Shaped Sonic Boom Demonstrator. AIAA Paper 2005-0011, 2005.
6. Cheng, H. K.; Lee, C. J.; Hafez, M. M.; and Guo, W. H.: Sonic Boom Propagation and its Submarine Impact. A Study of Theoretical and Computational Issues. AIAA Paper 96-0755 (1996).
7. Hayes, W. D.: Sonic Boom: in Annual Review of Fluid Mechanics, Vol. III, M. Van Dyke, et al, eds. Annual Reviews, Inc., Palo Alto, CA 1971, pp. 269-290.
8. Haglund, G. T.; and Kane, E. J.: Analysis of Sonic Boom Measurements Near Shock Wave Extremities for Flight Near Mach 1.0 and for Airplane Accelerations. NASA CR 2417, July 1974.
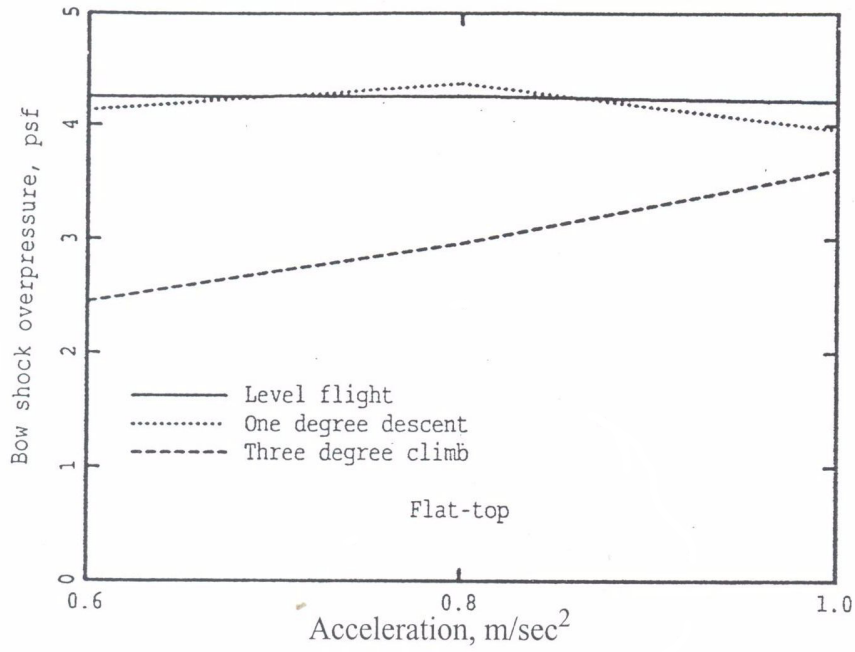
a. Effect of acceleration on overpressure for three flight path angles.
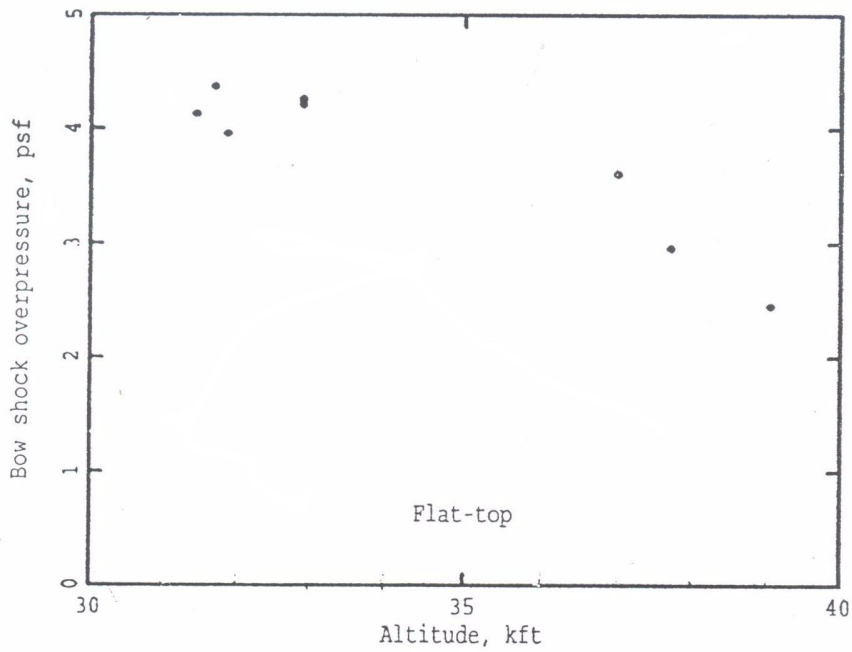
b. Effect of altitude on overpressure.

Figure 1. - Effect of acceleration, flight path angle and altitude on overpressure for a flat-top signature.
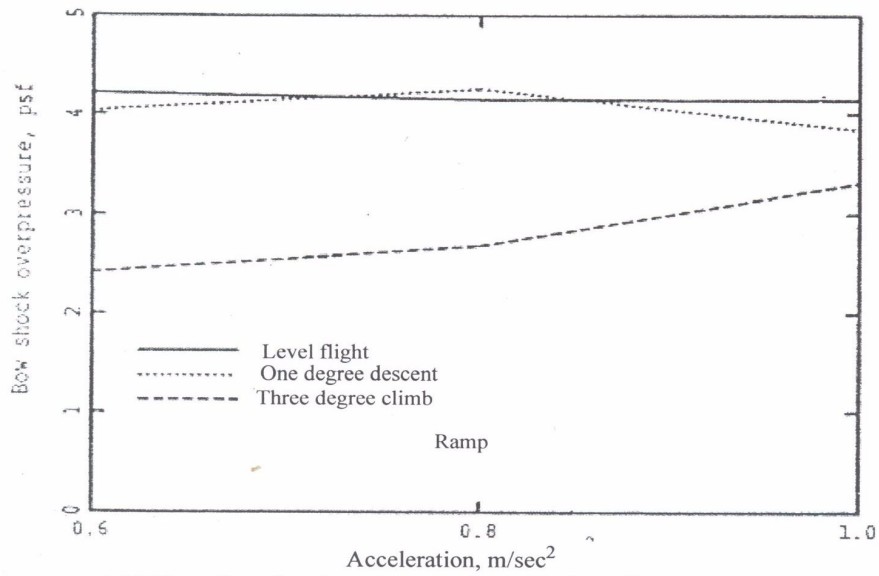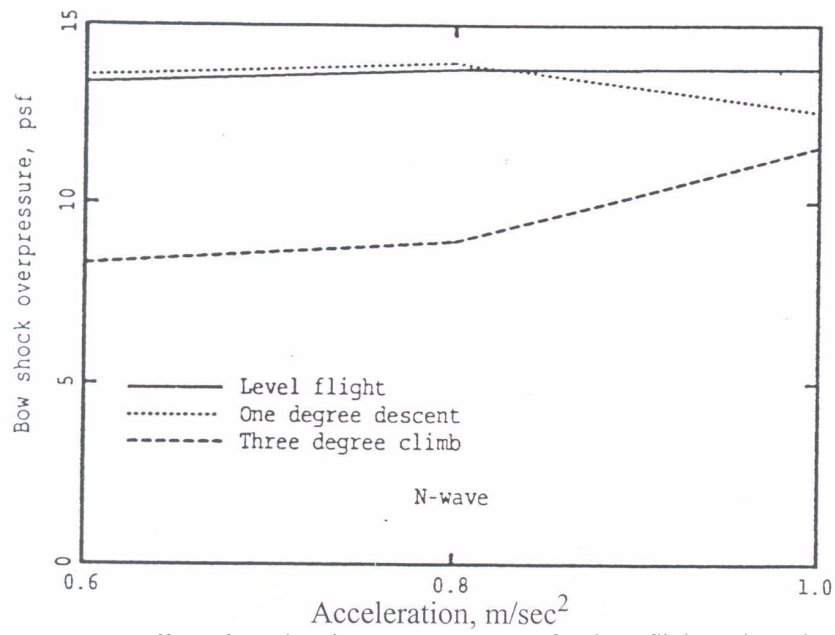
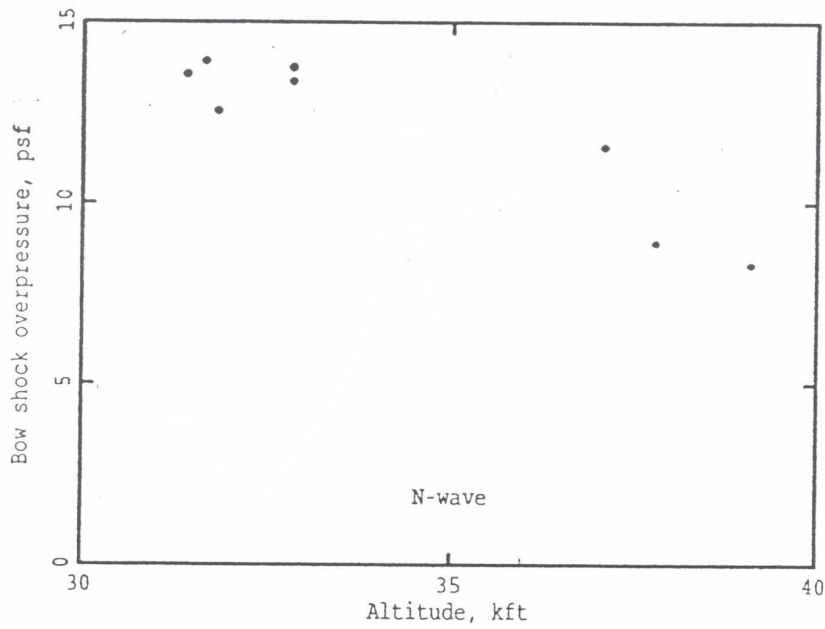(a) Effect of acceleration on overpressure for three flight path angles.
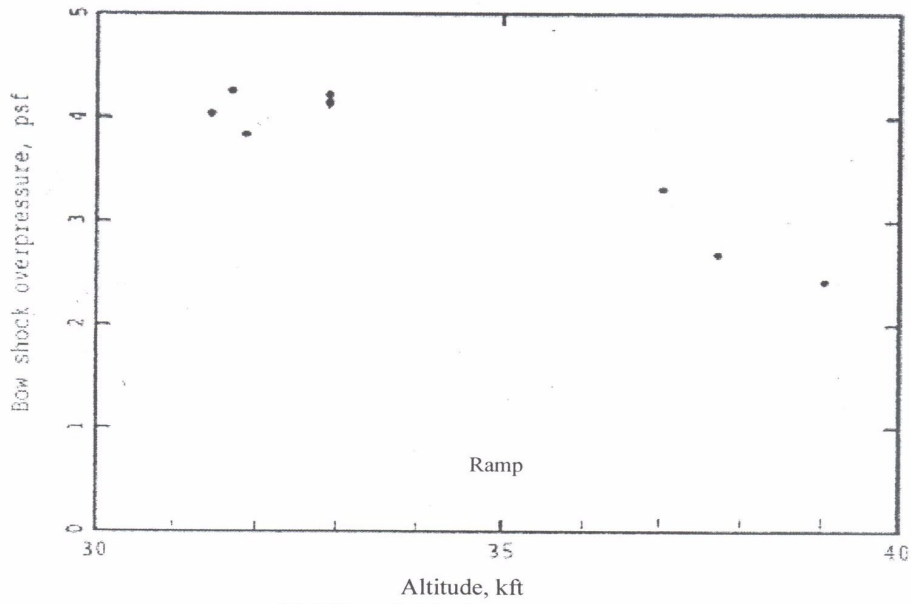
(b) Effect of altitude on overpressure

Figure 2. - Effect of acceleration flight path angle and altitude on overpressure for a ramp signature.
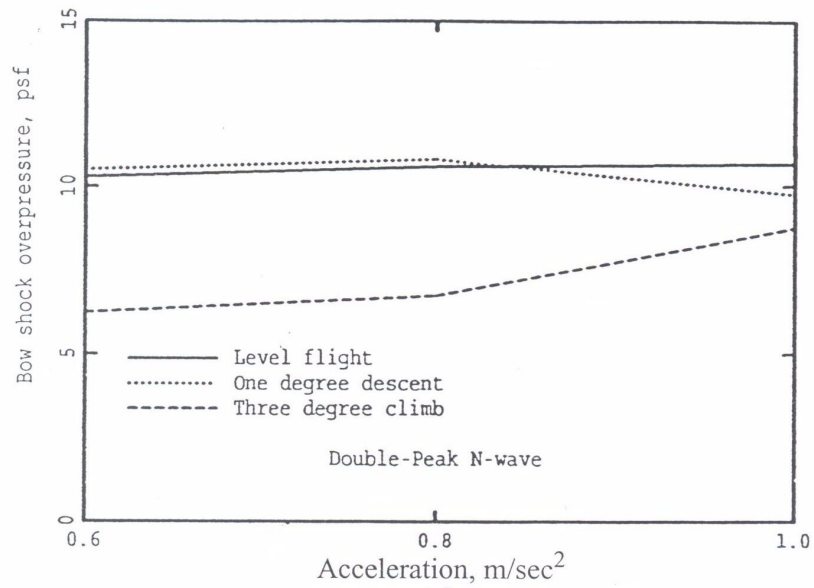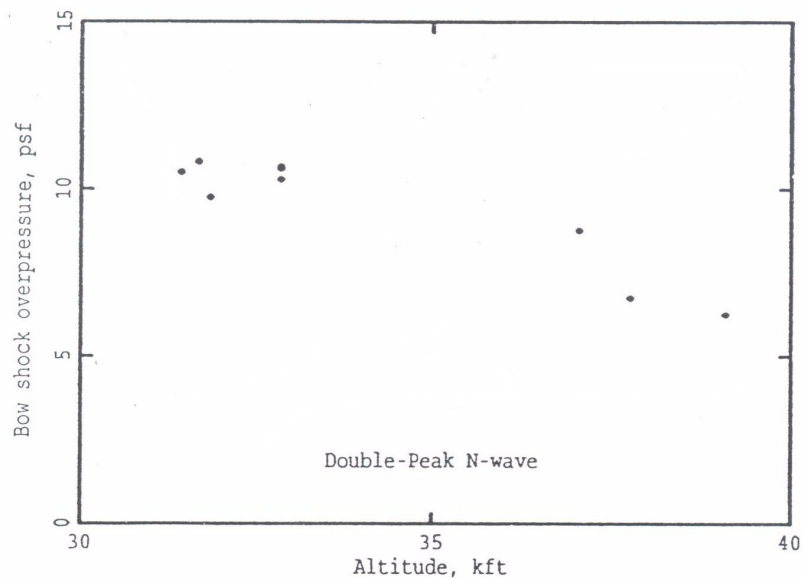
a. Effect of acceleration on overpressure for three flight path angles.

b. Effect of altitude on overpressure.

Figure 3. - Effect of acceleration, flight path angle and altitude on
overpressure for an N-wave signature.

a. Effect of acceleration on overpressure for three flight path angles.

b. Effect of altitude on overpressure.

Figure 4. - Effect of acceleration, flight path angle and altitude on overpressure for double-peak N-wave signature.

Appendix D

Development and Application
Of a Transition Flight Sonic Boom Focusing Computer Code

Osama Kandil and
Xudong Zheng
Aerospace Engineering Department, Old Dominion University
Norfolk, VA 23529

I. Overview and Summary:

The sonic-boom focusing problem has been shown to be governed by the nonlinear Tricomi equation. The Tricomi equation changes its character from a hyperbolic partial differential equation (PDE) (in illumination zone) to an elliptic PDE (in the shadow zone). At the caustic surface between the illumination zone and shadow zone, the equation is parabolic. The computational solution of this equation can be obtained by marching in pseudo time. This is achieved by adding a pseudo time term to the equation, marching in pseudo time, and reducing the pseudo-time term to a very small value (a standard CFD approach). Since the equation is a hyperbolic/elliptic type equation, the pseudo time term converts the equation to a parabolic equation in time, which allows the time marching.

The solution to this equation can be obtained, as will be shown as consisting of two parts: a part corresponding to a linear unsteady Tricomi equation, and another part as the nonlinear unsteady Burgers equation. The solution of the unsteady linear Tricomi equation is followed by the solution of the nonlinear unsteady Burgers equation to obtain the solution of the total nonlinear equation.

At any time step, the linear unsteady Tricomi equation is solved either in frequency domain using a fast Fourier transform (FFT) and its inverse, or in time domain using a finite-difference scheme. This is followed by solving the nonlinear unsteady Burgers equation either by using a finite-difference scheme or by using a closed form analytical solution. At each time step, the total computational cycle is iterated between the linear Tricomi equation and the nonlinear Burgers equation until convergence. Next, the time step is advanced and the computational cycle is repeated.

The boundary conditions for the rectangular computational domain are taken as zero pressure on the left and right boundaries and on the lower boundary as well. On the upper boundary, the incoming wave is specified as an N wave, a Concorde aircraft incoming wave or any other specified incoming wave.

In the next sections, the numerical solution algorithms, flow charts and samples of test cases are presented. The computer programs developed for each part of the splitted nonlinear Tricomi equation are integrated in one program, which includes all the options to solve the sonic boom-focusing problem under consideration. The solutions for a N incoming wave, a Concorde aircraft incoming wave, a flat-top case and a ramp-top case are presented. The solutions conclusively show the capability to predict the sonic boom focusing (superboom).

II. Background

The most intense sonic boom is the focused sonic boom due to aircraft transonic acceleration from Mach 1 to cruise speed. It leads to amplification of ground pressures up to two or three times the carpet boom shock strength. Therefore, accurate prediction of focused sonic booms around the caustic at ground level is very important. Sonic boom focusing has been also known as sonic superboom.

Weak shock waves arise in sonic boom of supersonic aircraft. Focusing of shock waves occurs at surfaces called caustics. The simplest caustic surface cases are the smooth caustic case and the cusp caustic case. Caustics are regions of wave amplification and geometrical ones. Shock wave focusing is fundamentally a nonlinear process. Here the emphasis is directed to the smooth caustic surface case.

Analysis of weak shock focusing at a smooth caustic surface has been introduced in 1965 by Guiraud [1]. He developed a theory, which includes both diffraction and nonlinear effects up to first order, which leads to the nonlinear Tricomi equation. This result was confirmed by Hayes [2], Hunter [3], and Rosales and Tabak [4,5].

Auger and Coulouvrat [6] have presented an algorithm to solve the nonlinear Tricomi equation, which was expressed in terms of the dimensionless acoustic pressure. Recently, Marchiano and Coulouvrat [7] have solved the nonlinear Tricomi equation in terms of the potential field instead of the pressure field. The nonlinear effects were treated using an "exact" solver that removed the artificial numerical dissipation and avoided instability conditions. The latter scheme was 40 times faster than the former one and convergence of the maximum peak amplitude with mesh refinement was reached.

III. Numerical Algorithms for Solution of the Non-Linear Tricomi Equation for Sonic Boom Focusing

III. a. Unsteady Nonlinear Tricomi Equation and Boundary Conditions:

The steady nonlinear Tricomi equation is modified as an unsteady equation by adding a pseudo unsteady term $\partial^2 \phi / \partial \tau \partial t$, which will tend to zero when the pseudo time marching scheme reaches the steady solution of $\phi(t \to \infty, \tau, z)$. The modified equation is given by

$$\frac{\partial^2 \phi}{\partial \tau \partial t} = \frac{\partial^2 \phi}{\partial z^2} - z \frac{\partial^2 \phi}{\partial^2 \tau} + \frac{\mu}{2} \frac{\partial}{\partial \tau} \left[(\frac{\partial \phi}{\partial \tau})^2 \right] \tag{1}$$

Where

ϕ = Acoustical potential

t = pseudo time variable

τ = dimensionless phase variable = $[t - x\,(1 - z / R_{sec}) / c_0] / T_{ac}$

x = dimensionless axial variable along the tangent to the caustic surface at the origin O

z = dimensionless normal distance to the caustic from O = $[2/(c_0^2\,T_{ac}^2\,R_{cau})]^{1/3}\,z^*$
  = z^* / δ

δ = $1/[2/(c_0^2\,T_{ac}^2\,R_{cau})]^{1/3}$ = characteristic thickness of diffraction boundary layer around the caustic

z^* = normal distance to the caustic from O

R_{sec} = radius of curvature of the intersection of the caustic surface with the Oxz plane

R_{cau} = relative radius = $1/(1/R_{sec} - 1/R_{ray})$

R_{ray} = radius of curvature of the projection in the plane (Oxz) of the ray tangent to the caustic

c_0 = ambient speed of sound at stagnation conditions

T_{ac} = characteristic duration of incoming signal near point O

μ = $2\,\beta\,M_{ac}\,[R_{cau}/(2\,c_0\,T_{ac})]^{2/3}$ = measurement of nonlinear effects relative to diffraction effects

β = $(1+\gamma)/2$ = nonlinearity parameter

M_{ac} = $P_{ac}/\rho_0\,c_0^2$ = acoustical Mach number

P_{ac} = signal maximum overpressure

ρ_0 = ambient stagnation density

The unsteady nonlinear Tricomi equation in terms of the acoustical potential is a hyperbolic/elliptic equation.

The boundary conditions to be satisfied are:

1. no disturbance before or after acoustic waved has passed

$$\phi\,(z, \tau \rightarrow \pm\infty) = 0 \qquad\qquad (2)$$
or for a periodic signal with period T

$$\phi\,(z, \tau + T) = \phi\,(z, \tau)$$

2. away from the caustic surface in the shadow zone the acoustic pressure decreases exponentially:

$$\phi\,(z\to-\infty,\tau)\to0 \tag{3}$$

3. a radiation condition is imposed (away from the caustic on the illuminated side the field matches the geometrical acoustic approximation)

$$z^{\frac{1}{4}}\frac{\partial\phi}{\partial\tau}+z^{-\frac{1}{4}}\frac{\partial\phi}{\partial z}\to2F(\tau+\frac{2}{3}z^{\frac{3}{2}}) \tag{4}$$

III. b. Numerical Solution of the Unsteady Nonlinear Tricomi Equation:

The unsteady nonlinear equation is split into two simpler equations. The first one includes the linear diffraction effects and the second one includes the nonlinear effects. Thus, the equation is split into the following two equations

$$\frac{\partial^2\phi}{\partial\tau\,\partial t}=\frac{\partial^2\phi}{\partial z^2}-z\,\frac{\partial^2\phi}{\partial^2\tau} \tag{5}$$

and

$$\frac{\partial\phi}{\partial t}=\frac{\mu}{2}\left(\frac{\partial\phi}{\partial\tau}\right)^2 \tag{6}$$

The first, Eq. (5), is the unsteady linear Tricomi equation, and the second, Eq. (6) is the inviscid nonlinear Burgers' equation.

Equation (5) can be solved in time-domain integration[8] or in frequency-domain integration [6]. Equation (6) can be solved using a shock-capturing finite-differencing scheme [9] or by an exact shock fitting scheme [10]. The integrated code includes the four sub-programs to solve equation (5) and equation (6). To solve for the nonlinear Tricomi equation, one can choose one from the two sub-programs of equation (5) which is followed by one from the two sub-programs of equation (6). The solution is obtained by iterating between the chosen sub-programs at each time step for each altitude z until convergence.

In the next sections, the algorithms for the four sub-programs are developed, the flow charts are presented, and the codes have been developed and tested.

III. c. Numerical Solution of the Linear Unsteady Tricomi Equation in Time Domain:

The linear unsteady Tricomi equation is solved using the ADI Scheme.

$$\frac{\partial^2\phi}{\partial\tau\partial t}=\frac{\partial^2\phi}{\partial z^2}-z\frac{\partial^2\phi}{\partial\tau^2}$$

$$\tag{7}$$

The details of the algorithm are given below.

Computational Algorithm:

1. Step (1): Sweep in Z direction. The difference scheme is given by

$$\frac{(\frac{\partial \phi}{\partial \tau})_{i,j}^{n+\frac{1}{2}} - (\frac{\partial \phi}{\partial \tau})_{i,j}^{n}}{\frac{\Delta t}{2}} = \frac{(\phi_{i+1,j}^{n+\frac{1}{2}} - 2\phi_{i,j}^{n+\frac{1}{2}} + \phi_{i-1,j}^{n+\frac{1}{2}})}{(\Delta z)^2} - z_{i,j} \frac{(\phi_{i,j+1}^{n} - 2\phi_{i,j}^{n} + \phi_{i,j-1}^{n})}{(\Delta \tau)^2}$$

Where $\frac{\partial \phi}{\partial \tau}$ uses up-wind differencing given by

$$(\frac{\partial \phi}{\partial \tau})_{i,j} = \frac{\phi_{i,j} - \phi_{i,j-1}}{\Delta \tau}$$

The recurrence form of the equation is given by

$$\frac{1}{(\Delta z)^2}\phi_{i+1,j}^{n+\frac{1}{2}} - 2(\frac{1}{(\Delta z)^2} + \frac{1}{\Delta \tau \Delta t})\phi_{i,j}^{n+\frac{1}{2}} + \frac{1}{(\Delta z)^2}\phi_{i-1,j}^{n+\frac{1}{2}} = 2\frac{-\phi_{i,j-1}^{n+\frac{1}{2}} - \phi_{i,j}^{n} + \phi_{i,j-1}^{n}}{\Delta \tau \Delta t} + z_{i,j}\frac{(\phi_{i,j+1}^{n} - 2\phi_{i,j}^{n} + \phi_{i,j-1}^{n})}{(\Delta \tau)^2}$$

Next, SLOR is applied

$$\phi_{i,j}^{n+\frac{1}{2}} = \phi_{i,j}^{n} + \omega(\phi_{i,j}^{n+\frac{1}{2}} - \phi_{i,j}^{n})$$

and the equation becomes

$$\phi_{i,j}^{n+\frac{1}{2}} = (1-\omega)\phi_{i,j}^{n} + \frac{\omega}{-2(\frac{1}{(\Delta z)^2} + \frac{1}{\Delta \tau \Delta t})}(2\frac{-\phi_{i,j-1}^{n+\frac{1}{2}} - \phi_{i,j}^{n} + \phi_{i,j-1}^{n}}{\Delta \tau \Delta t} + z_{i,j}\frac{(\phi_{i,j+1}^{n} - 2\phi_{i,j}^{n} + \phi_{i,j-1}^{n})}{(\Delta \tau)^2} - \frac{1}{(\Delta z)^2}\phi_{i+1,j}^{n+\frac{1}{2}}$$

$$-\frac{1}{(\Delta z)^2}\phi_{i-1,j}^{n+\frac{1}{2}})$$

The recurrence form of the z-sweep difference equation is given by

$$\frac{\omega}{(\Delta z)^2}\phi_{i+1,j}^{n+\frac{1}{2}} - 2(\frac{1}{(\Delta z)^2} + \frac{1}{\Delta \tau \Delta t})\phi_{i,j}^{n+\frac{1}{2}} + \frac{\omega}{(\Delta z)^2}\phi_{i-1,j}^{n+\frac{1}{2}} = 2\omega\frac{-\phi_{i,j-1}^{n+\frac{1}{2}} - \phi_{i,j}^{n} + \phi_{i,j-1}^{n}}{\Delta \tau \Delta t} + z_{i,j}\omega\frac{(\phi_{i,j+1}^{n} - 2\phi_{i,j}^{n} + \phi_{i,j-1}^{n})}{(\Delta \tau)^2}$$

$$-2(1-\omega)(\frac{1}{(\Delta z)^2} + \frac{1}{\Delta \tau \Delta t})\phi_{i,j}^{n}$$

Let $\frac{\omega}{(\Delta z)^2} = A_i$, $-2(\frac{1}{(\Delta z)^2} + \frac{1}{\Delta \tau \Delta t}) = B_i$, $\frac{\omega}{(\Delta z)^2} = C_i$,

$$2\omega \frac{-\phi_{i,j-1}^{n+\frac{1}{2}} - \phi_{i,j}^{n} + \phi_{i,j-1}^{n}}{\Delta\tau\Delta t} + z_{i,j}\omega\frac{(\phi_{i,j+1}^{n} - 2\phi_{i,j}^{n} + \phi_{i,j-1}^{n})}{(\Delta\tau)^2} - 2(1-\omega)(\frac{1}{(\Delta z)^2} + \frac{1}{\Delta\tau\Delta t})\phi_{i,j}^{n} = D_i$$

So the equation is written in the matrix form as

$$A_i\phi_{i+1,j}^{n+\frac{1}{2}} + B_i\phi_{i,j}^{n+\frac{1}{2}} + C_i\phi_{i-1,j}^{n+\frac{1}{2}} = D_i$$

which is given by

$$
\begin{bmatrix}
B_1 & A_1 & \cdots & \cdots & \cdots & \cdots & \cdots \\
C_2 & B_2 & A_2 & & & & \vdots \\
0 & C_3 & B_3 & A_3 & & & \vdots \\
& & & \ddots & & & \vdots \\
& & & & & & \vdots \\
& & & C_{i\max-2} & B_{i\max-2} & A_{i\max-2} & \\
& & & & C_{i\max-1} & B_{i\max-1} &
\end{bmatrix}
\begin{Bmatrix}
\phi_{1,j}^{n+\frac{1}{2}} \\
\phi_{2,j}^{n+\frac{1}{2}} \\
\vdots \\
\vdots \\
\vdots \\
\vdots \\
\phi_{i\max-1,j}^{n+\frac{1}{2}}
\end{Bmatrix}
=
\begin{Bmatrix}
D_1 - C_1\phi_{0,j}^{n+\frac{1}{2}} \\
D_2 \\
\vdots \\
\vdots \\
\vdots \\
D_{i\max-2} \\
D_{i\max-1} - A_{i\max-1}\phi_{i\max,j}^{n+\frac{1}{2}}
\end{Bmatrix}
\tag{8}
$$

These equations are solved using the Thomas algorithm.

2. Step (2): Sweep in τ direction. The difference equation is given by

$$\frac{(\frac{\partial\phi}{\partial\tau})_{i,j}^{n+1} - (\frac{\partial\phi}{\partial\tau})_{i,j}^{n+\frac{1}{2}}}{\frac{\Delta t}{2}} = \frac{(\phi_{i+1,j}^{n+\frac{1}{2}} - 2\phi_{i,j}^{n+\frac{1}{2}} + \phi_{i-1,j}^{n+\frac{1}{2}})}{(\Delta z)^2} - z_{i,j}\frac{(\phi_{i,j+1}^{n+1} - 2\phi_{i,j}^{n+1} + \phi_{i,j-1}^{n+1})}{(\Delta\tau)^2}$$

Where $\frac{\partial\phi}{\partial\tau}$ uses forward differencing given by

$$(\frac{\partial\phi}{\partial\tau})_{i,j} = \frac{\phi_{i,j+1} - \phi_{i,j}}{\Delta\tau}$$

The recurrence form is given by

$$(\frac{2}{\Delta\tau\Delta t} + \frac{z_{i,j}}{(\Delta z)^2})\phi_{i,j+1}^{n+1} - 2(\frac{z_{i,j}}{(\Delta z)^2} + \frac{1}{\Delta\tau\Delta t})\phi_{i,j}^{n+1} + \frac{z_{i,j}}{(\Delta z)^2}\phi_{i,j-1}^{n+1} = 2\frac{-\phi_{i,j+1}^{n+\frac{1}{2}} + \phi_{i,j}^{n+\frac{1}{2}}}{\Delta\tau\Delta t} + \frac{(\phi_{i+1,j}^{n+\frac{1}{2}} - 2\phi_{i,j}^{n+\frac{1}{2}} + \phi_{i-1,j}^{n+\frac{1}{2}})}{(\Delta z)^2}$$

Next, SLOR is applied

$$\phi_{i,j}^{n+\frac{1}{2}} = \phi_{i,j}^{n} + \omega(\phi_{i,j}^{n+\frac{1}{2}} - \phi_{i,j}^{n})$$

And the equation becomes

$$\phi_{i,j}^{n+1} = (1-\omega)\phi_{i,j}^{n+\frac{1}{2}} + \frac{\omega}{-2\left(\dfrac{z_{i,j}}{(\Delta z)^2} + \dfrac{1}{\Delta\tau\Delta t}\right)}\left(2\frac{-\phi_{i,j+1}^{n+\frac{1}{2}} + \phi_{i,j}^{n+\frac{1}{2}}}{\Delta\tau\Delta t} + \frac{(\phi_{i+1,j}^{n+\frac{1}{2}} - 2\phi_{i,j}^{n+\frac{1}{2}} + \phi_{i-1,j}^{n+\frac{1}{2}})}{(\Delta z)^2} - \left(\frac{2}{\Delta\tau\Delta t} + \frac{z_{i,j}}{(\Delta z)^2}\right)\phi_{i,j+1}^{n+1}\right.$$

$$\left. - \frac{z_{i,j}}{(\Delta z)^2}\phi_{i,j-1}^{n+1}\right)$$

The recurrence form of the equation in the τ sweep is given by

$$\omega\left(\frac{2}{\Delta\tau\Delta t} + \frac{z_{i,j}}{(\Delta z)^2}\right)\phi_{i,j+1}^{n+1} - 2\left(\frac{z_{i,j}}{(\Delta z)^2} + \frac{1}{\Delta\tau\Delta t}\right)\phi_{i,j}^{n+1} + \omega\frac{z_{i,j}}{(\Delta z)^2}\phi_{i,j-1}^{n+1} = 2\omega\frac{-\phi_{i,j+1}^{n+\frac{1}{2}} + \phi_{i,j}^{n+\frac{1}{2}}}{\Delta\tau\Delta t} + \omega\frac{(\phi_{i+1,j}^{n+\frac{1}{2}} - 2\phi_{i,j}^{n+\frac{1}{2}} + \phi_{i-1,j}^{n+\frac{1}{2}})}{(\Delta z)^2}$$

$$ - 2(1-\omega)\left(\frac{z_{i,j}}{(\Delta z)^2} + \frac{1}{\Delta\tau\Delta t}\right)\phi_{i,j}^{n+\frac{1}{2}}$$

Where $A_j = \omega\left(\dfrac{2}{\Delta\tau\Delta t} + \dfrac{z_{i,j}}{(\Delta z)^2}\right)$, $B_j = -2\left(\dfrac{z_{i,j}}{(\Delta z)^2} + \dfrac{1}{\Delta\tau\Delta t}\right)$, $C_j = \omega\dfrac{z_{i,j}}{(\Delta z)^2}$

$$D_j = 2\omega\frac{-\phi_{i,j+1}^{n+\frac{1}{2}} + \phi_{i,j}^{n+\frac{1}{2}}}{\Delta\tau\Delta t} + \omega\frac{(\phi_{i+1,j}^{n+\frac{1}{2}} - 2\phi_{i,j}^{n+\frac{1}{2}} + \phi_{i-1,j}^{n+\frac{1}{2}})}{(\Delta z)^2} - 2(1-\omega)\left(\frac{z_{i,j}}{(\Delta z)^2} + \frac{1}{\Delta\tau\Delta t}\right)\phi_{i,j}^{n+\frac{1}{2}}$$

So the equation is written in the matrix form as

$$A_j\phi_{i,j+1}^{n+1} + B_j\phi_{i,j}^{n+1} + C_j\phi_{i,j-1}^{n+1} = D_j$$

which is given by

$$\begin{bmatrix} B_1 & A_1 & \cdots & \cdots & & \cdots & & \cdots \\ C_2 & B_2 & A_2 & & & & & \vdots \\ 0 & C_3 & B_3 & A_3 & & & & \vdots \\ & & & \ddots & & & & \vdots \\ & & & & & & & \vdots \\ & & & & & & & \vdots \\ & & & & C_{j\max-2} & B_{j\max-2} & A_{j\max-2} & \vdots \\ & & & & & C_{j\max-1} & B_{j\max-1} \end{bmatrix}\begin{Bmatrix} \phi_{i,1}^{n+1} \\ \phi_{i,2}^{n+1} \\ \vdots \\ \vdots \\ \vdots \\ \vdots \\ \vdots \\ \phi_{i,j\max-1}^{n+1} \end{Bmatrix} = \begin{Bmatrix} D_1 - C_1\phi_{i,0}^{n+1} \\ D_2 \\ \vdots \\ \vdots \\ \vdots \\ \vdots \\ D_{j\max-2} \\ D_{j\max-1} - A_{j\max-1}\phi_{i,j\max}^{n+1} \end{Bmatrix} \qquad (8)$$

These equations are also solved using the Thomas algorithm.

3. The boundary conditions are given by

(1) $\phi(z,\tau \to \pm\infty) = 0$

$\quad \phi_{i,j\max} = 0$ (9)

(2) $\phi(z \to -\infty,\tau) = 0$

$$\phi_{i\min, j} = 0 \tag{10}$$

$$(3) \ z^{\frac{1}{4}} \frac{\partial \phi}{\partial \tau} + z^{-\frac{1}{4}} \frac{\partial \phi}{\partial z} \xrightarrow[z \to +\infty]{} 2F(\tau + \frac{2}{3} z^{\frac{3}{2}})$$

$$\text{Or } (z^{\frac{1}{4}})_{i\max, j} \frac{\phi_{i\max, j} - \phi_{i\max, j-1}}{\Delta \tau} + (z^{-\frac{1}{4}})_{i\max, j} \frac{\phi_{i\max, j} - \phi_{i\max-1, j}}{\Delta z} \to 2F(\tau + \frac{2}{3} z^{\frac{3}{2}})_{i\max, j} \tag{11}$$

The flow chart of the program for the unsteady linear Tricomi equation is given in Fig 1.

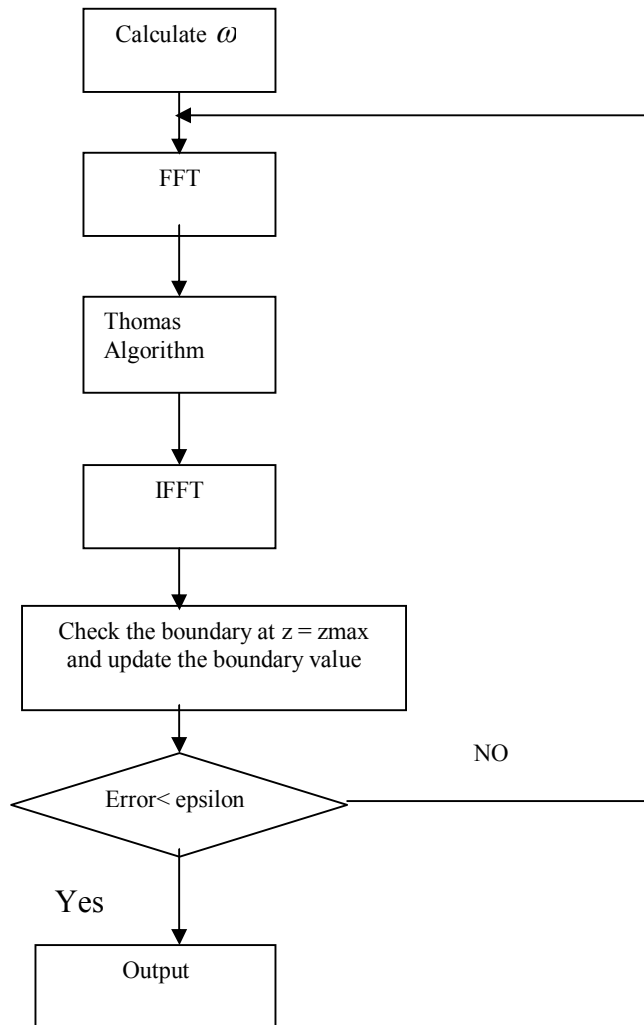## Program for Linear Unsteady Tricomi Equation in Time Domain
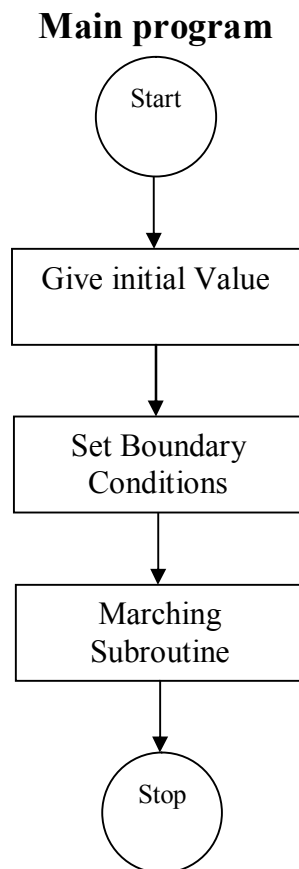
Main program

Marching Subroutine
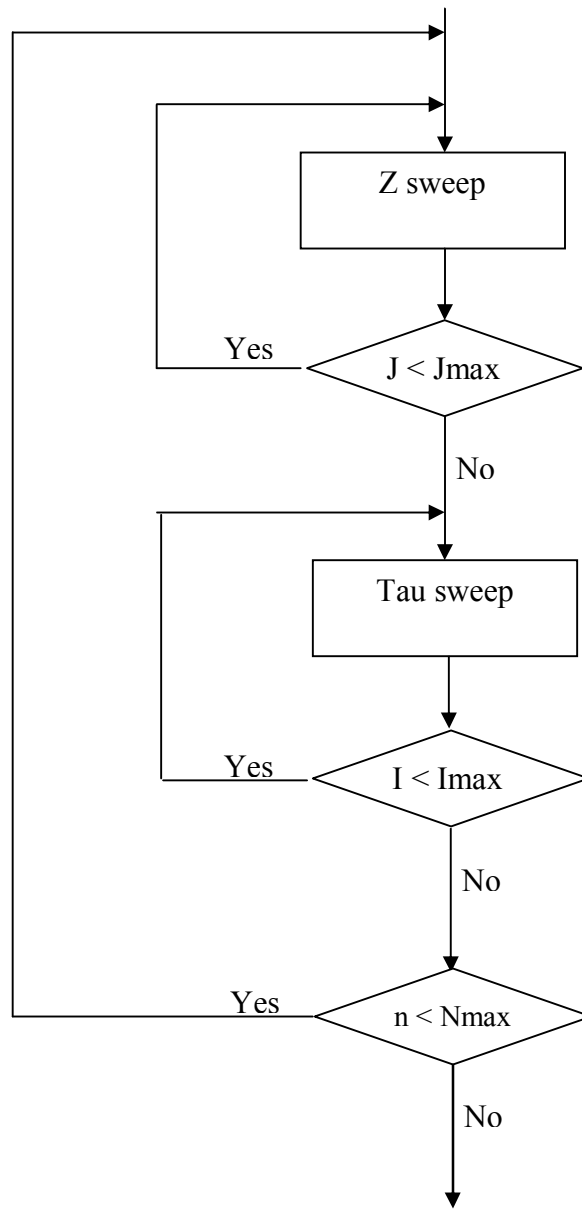
Figure 1. Flow chart of the Program for the unsteady linear Tricomi equation in time domain.

III. d. Numerical Solution of the Unsteady Linear Tricomi Equation in Frequency Domain:

In this scheme the solution is obtained in the frequency domain using a fast Fourier transform (FFT) algorithm and an inverse fast Fourier transform (IFFT).

Starting with the unsteady linear Tricomi equation,

$$\frac{\partial^2 \phi}{\partial \tau \, \partial t} = \frac{\partial^2 \phi}{\partial z^2} - z \frac{\partial^2 \phi}{\partial^2 \tau}$$ (12)

the solution is expressed as

$$\phi = \tilde{\varphi} \, e^{i\omega\tau}$$ (13)

and the equation reduces to

$$i\,\omega \frac{\partial \tilde{\varphi}}{\partial t} = \frac{\partial^2 \tilde{\varphi}}{\partial z^2} - z\omega^2 \, \tilde{\varphi}$$ (14)

For each frequency ω^n, the derivatives with respect to z are approximated with a second-order central differencing and the time derivative is obtained using a first-order forward differencing. The equation is solved using an alternating implicit scheme (ADI).

ADI scheme

$$i\omega_j^n \frac{\tilde{\varphi}_j^{n+\frac{1}{2}} - \tilde{\varphi}_j^n}{\frac{\Delta t}{2}} = \frac{\tilde{\varphi}_{j+1}^{n+\frac{1}{2}} - 2\tilde{\varphi}_j^{n+\frac{1}{2}} + \tilde{\varphi}_{j-1}^{n+\frac{1}{2}}}{(\Delta z)^2} + z_j (\omega_j^n)^2 \tilde{\varphi}_j^n$$

Boundary Conditions:

$$\tilde{\varphi}_{j\,\max} = 0$$

Once $\tilde{\varphi}_j^{n+\frac{1}{2}}$ is obtained, an inverse FFT is applied to obtain

$$\phi_j^{n+\frac{1}{2}} = \text{FFT}^{-1} \left[\tilde{\varphi}_j^{n+\frac{1}{2}} \right]$$

This result is used in the nonlinear Burgers' equation (step II.e or II.f) to obtain ϕ_j^{n+1}

FFT and IFFT for p (ω)

The continuous form of the Fourier transform is

$$p(\omega) = \int_{-\infty}^{+\infty} p(t) e^{-i\omega t} dt$$ (15)

If the continuous $p(t)$ is discretized, then $p(t) \rightarrow p(n\Delta t) \equiv p(n)$, which in turn gives us:
$\omega t \rightarrow 2\pi \Delta f n \Delta t$, but since $\Delta f = \frac{1}{(N\Delta t)}$ then

$$\omega t \rightarrow \frac{2\pi nk}{N}$$

What we have now is equivalent to a discrete time signal $p(n)$. Substituting into the continuous form of the Fourier transform gives

$$p(k\Delta\omega) = \sum_{n=0}^{N-1} p(n)e^{-i\frac{2\pi nk}{N}}$$ (16)

In the equation above, the integral form has been replaced by a summation. As N (the number of samples) increases the result goes to infinity, so to eliminate this from happening the equation is multiplied by $1/N$.

$$p(k) = \frac{1}{N}\sum_{n=0}^{N-1} p(n)W_N^{nk}$$ (17)

where $W_N^{nk} = e^{-i\frac{2\pi nk}{N}}$ (18)

The FFT is a fairly easy algorithm to implement, and it is shown step by step in the list below:

1. Pad input sequence of N samples with zero's until the number of samples is the nearest power of two.
2. Reverse the input sequence.
3. Compute (N / 2) *two* sample DFT's from the shuffled inputs.
4. Compute (N / 4) *four* sample DFT's from the two sample DFT's.
5. Compute (N / 2) *eight* sample DFT's from the four sample DFT's.
6. Until the all the samples combine into one N-sample DFT

Notice here that one is working with p instead of ϕ. However, once p is acquired, then ϕ can be found. The flow chart for the unsteady linear Tricomi equation in frequency domain is given in Fig. 2.

Program for Linear Unsteady Tricomi Equation in Frequency Domain

Calculate ω

FFT

Thomas Algorithm

IFFT

Check the boundary at z = zmax and update the boundary value

Error< epsilon

NO

Yes

Output

Figure 2. Flow chart of the Program for the linear unsteady Tricomi equation in frequency domain.

Computational Test

The computational test is that of the fast Fourier transform (FFT) and the inverse fast Fourier transform (IFFT) using a square signal. Figure 3 shows the results after FFT, the IFFT is used back for the time domain, which produces Fig. 4. It is observed that the IFFT produces the same signal as that of the original square signal.
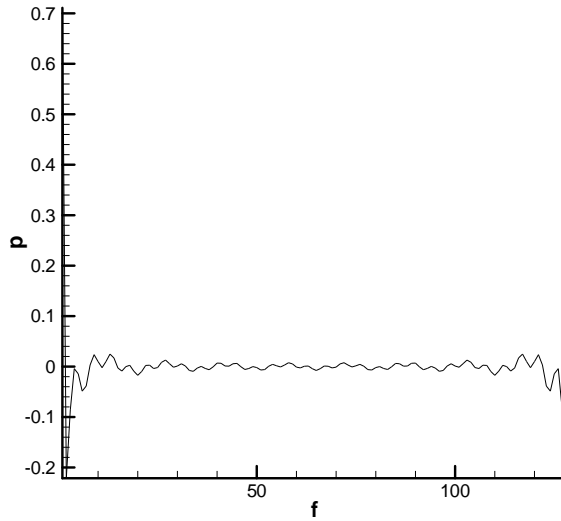
Figure 3. FFT in the frequency domain
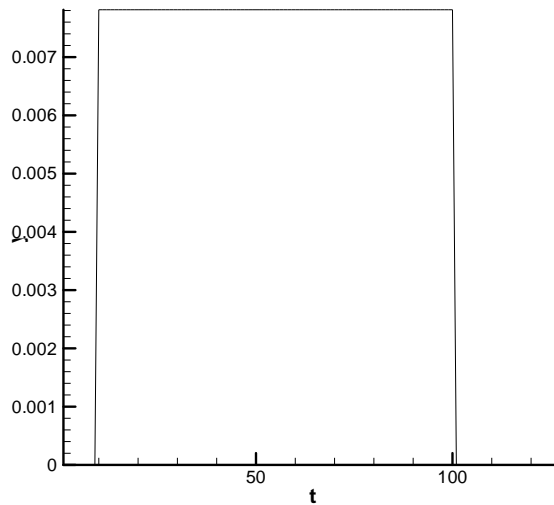
Figure 4. IFFT in the time domain

III. e. Numerical Solution of the Nonlinear Burgers Equation using shock Capturing Scheme and Application:

The computational algorithm of the nonlinear Burgers is given below. Two schemes are developed; the first is a First-order scheme and the second is a second-order scheme. This is followed by a computational application of the two schemes.

$$\frac{\partial \varphi}{\partial t} + \frac{\partial}{\partial \tau}(-\frac{\mu}{2}\varphi^2) = 0 \tag{19}$$

Computational Algorithm:

1. First-Order Scheme

$$\varphi_i^{n+1} = \varphi_i^n - f_{i+1/2} + f_{i-1/2} \tag{20}$$

Where the superscript gives the time-step number. Quantities lacking a superscript are evaluated at the time-step n. The numerical fluxes are

$$f_{i+1/2} = \begin{cases} \dfrac{\delta t}{\delta x}\phi_i & w_{i+1/2} \geq 0 \\[2mm] \dfrac{\delta t}{\delta x}\phi_{i+1} & w_{i+1/2} < 0 \end{cases} \tag{21}$$

where $\phi_i = (-\dfrac{\mu}{2}\varphi^2)_i$

The direction variable w is in principle the characteristic speed. However it is convenient to define w as a quantity with the same sign as the characteristic speed. Namely,

$$w_{i+1/2} \equiv (\phi_{i+1} - \phi_i)(\varphi_{i+1} - \varphi_i) \tag{22}$$

2. Expansion Shock Correction

According the second law of thermodynamics, the expansion shock is forbidden. This means that a shock discontinuity in an expansion of the flow must cease to be a shock by unsteepening at a rate determined by the expansion. To eliminate expansion shocks, replace a single flux as follows:

$$f_{i+1/2} \rightarrow \frac{1}{2}(f_{i+3/2} + f_{i-1/2} - \frac{\delta t}{\delta \tau}(\varphi_{i+1} - \varphi_i)(u_{i+1} - u_i)) \tag{23}$$

3. Higher-Order Scheme

A stable second-order upwind scheme involving the point i and two points to the left or right (depending on the sign of the characteristic) may be defined as follows:

a. Predictor step defines fluxes at time level $n+1/2$ according to the following. We use the first-order fluxes including the expansion correction to define

$$\phi_i^{n+1/2} = \phi_i^n - \frac{1}{2}u_i(f_{i+1/2} - f_{i-1/2}) \tag{24}$$

b. Corrector step uses second-order up-wind differences on $\phi^{n+1/2}$, In flux conservative form, they are defined as:

$$F_{i+1/2} = \frac{\delta t}{\delta \tau} \times \begin{cases} \dfrac{3}{2}\phi_i^{n+1/2} - \dfrac{1}{2}\phi_{i-1}^{n+1/2} & w_{i+1/2} \geq 0 \\[2mm] \dfrac{3}{2}\phi_{i+1}^{n+1/2} - \dfrac{1}{2}\phi_{i+2}^{n+1/2} & w_{i+1/2} < 0 \end{cases} \tag{25}$$

$$\varphi_i^{n+1} = \varphi_i^n - F_{i+1/2} + F_{i-1/2} \tag{26}$$

4. Hybrid Scheme

We construct the provisional quantities

$$\varphi_i^* = \varphi_i^n - f_{i+1/2} + f_{i-1/2} \tag{27}$$

$$\delta f_{i+1/2} = F_{i+1/2} - f_{i+1/2} \tag{28}$$

The quantities φ^* represent a first-order update in which monotonicity has been preserved. The second-order scheme above does not preserve monotonicity so we must filter the flux-corrections by using a local algorithm called a flux-limiter. This filter, which forbids the enhancement of extrema, is the heart of the FCT technique.

$$\delta f_{i+1/2} \rightarrow Sgn(\delta f_{i+1/2}) \max\{0, \min[\left|\delta f_{i+1/2}\right|, Sgn(\delta f_{i+1/2})(\varphi_{i+2}^* - \varphi_{i+1}^*), Sgn(\delta f_{i+1/2})(\varphi_i^* - \varphi_{i-1}^*)]\} \tag{29}$$

The hybrid scheme is now completed as follows

$$\varphi_i^{n+1} = \varphi_i^* - \delta f_{i+1/2} + \delta f_{i-1/2} \tag{30}$$

In summary, φ^n, u^n and ϕ^n are taken to be known and φ^{n+1} is obtained by execution of the following steps in order: Eqs. (22), (21), (23), (24), (25), and (23) with F for f, and Eqs. (27)-(30)

Computational Application:

In the nonlinear Burgers' Equation

$$\frac{\partial \varphi}{\partial t} + \frac{\partial}{\partial \tau}(-\frac{\mu}{2}\varphi^2) = 0$$

let $-\mu$ as the speed of sound, a, and solve for resulting equation

$$\frac{\partial \varphi}{\partial t} + \frac{\partial}{\partial \tau}(\frac{a}{2}\varphi^2) = 0$$

Where a = 340.

Next, let the initial conditions be

$$\varphi_0(\tau) = \max(0, bx(\tau_0 - \tau)); \quad \tau \geq 0$$
$$\varphi_0(-\tau) = -\varphi_0(\tau); \quad \tau < 0$$

Where b = 3 and $\tau_0 = 120$ (see Fig. 5 for the initial function shape).

A grid of 302 points is used with periodic boundary conditions. Keeping $\left|u\right|_{max} \frac{\delta t}{\delta \tau} = \frac{1}{4}$ and $\delta \tau = \frac{\tau_0}{40}$, we get the solutions given below for the first-order scheme (first column, Figs 6.b-6.d) and the second-order scheme (second column Figs. 6.e- 6.g).
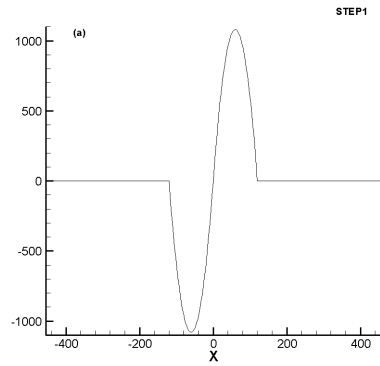
Figure 5. Initial function shape to be solved with the first-order and second-order schemes
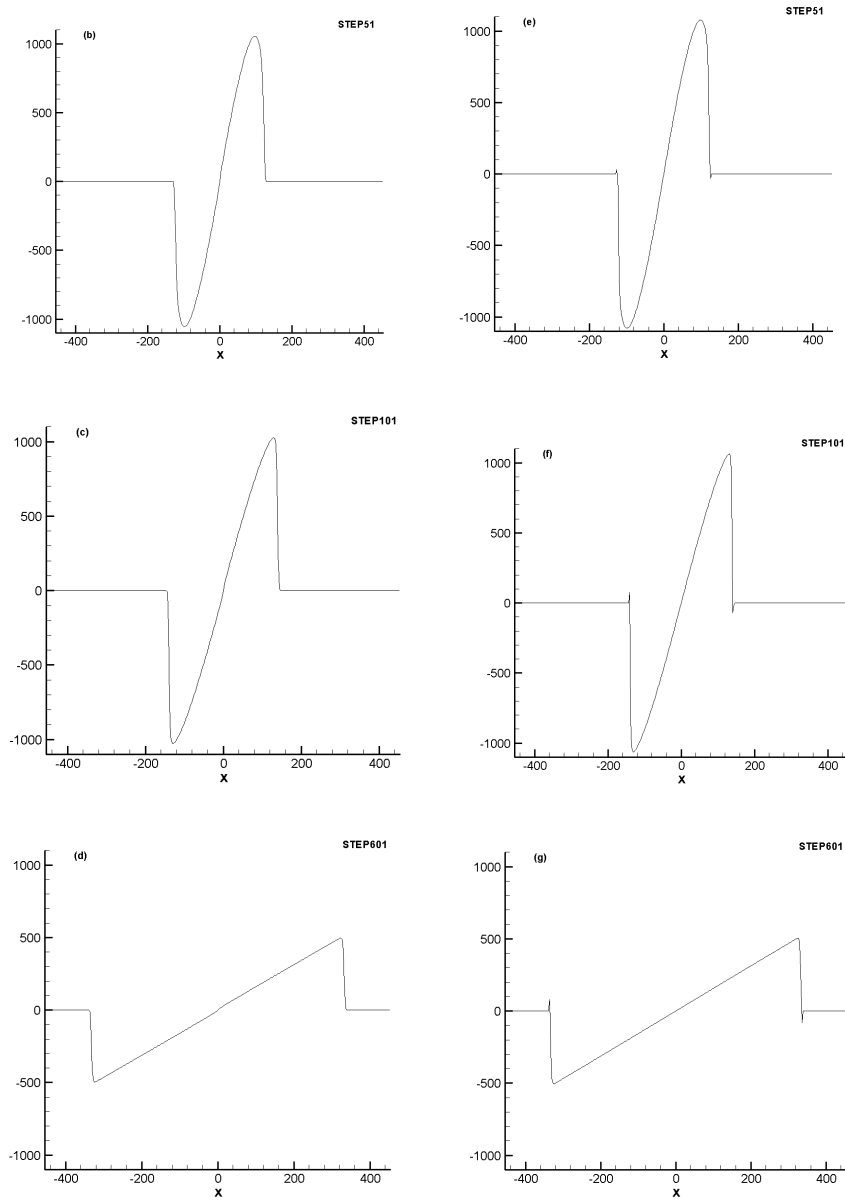
Figure 6. Symmetric N-wave shock development using first-order scheme (Figs. 6.b-6.d) and Second-order scheme (Figs. 6.e-6.g)

The solutions are in good agreement with each other and with the results of Ref. 8. The flux limiter should be adjusted to eliminate the little overshoot and undershoot in the second-order solution.

III. f. Analytical Solution of the Nonlinear Burgers Equation using shock Fitting Scheme:

$$\frac{\partial \varphi}{\partial t} + \frac{\partial}{\partial \tau}(-\frac{\mu}{2}\varphi^2) = 0 \tag{31}$$

Let $u(\varphi) = -\mu\varphi$, According to the method of characteristics, Eq. (31) demands constancy of $u = -\varphi$ along the trajectory

$$\tau_t = u(\varphi) \tag{32}$$

So the value of φ at (τ, t) may be found by following the trajectory backward to the initial condition; that is,

$$\varphi(\tau, t) = \varphi_0(\tau - tu(\varphi)) \tag{33}$$

This equation will be valid before the shock is formed. After the shock formation, φ becomes multi-valued in τ and, thus, physically meaningless. The actual signal contains one or more shock waves, and a proper treatment of the shocks eliminates the multivaluedness. A shock wave moves faster than the acoustic propagation speed in front of it and slower than the propagation speed behind it. Thereby, parts of the signal are propagated into the shock and this phenomenon permits the remaining part of the signal to be single-valued.

In order to do this, we introduce the function $\zeta(\tau, t)$ (for the specific t, we drop the notation and write simply $\zeta(\tau)$), defined as follows:

$$\zeta(\tau) = \int_{-\infty} \varphi(\tau_0)d\tau(\tau_0) = \int_{-\infty} \varphi \frac{d\tau}{d\tau_0}d\tau_0 \tag{34}$$

Where

$$\tau_0 = \tau - tu(\varphi) = \tau - t(-\mu\varphi) \tag{35}$$

is the initial coordinate of signal.

The derivative with respect of τ_0 is taken to get

$$\frac{d\tau}{d\tau_0} = 1 + t(-\mu)\frac{d\varphi}{d\tau_0} \tag{36}$$

Substituting Eq. (36) into Eq. 3(4), we obtain

$$\zeta(\tau) = \int_{-\infty} \varphi(\tau_0) d\tau_0 + \frac{1}{2}(-\mu)t\varphi(\tau_0)^2 \qquad (37)$$

According to Eq. (35), one can write

$$\varphi(\tau_0) = \frac{\tau - \tau_0}{t(-\mu)}$$

Substituting this result into Eq. (37), we get

$$\zeta(\tau) = \int_{-\infty} \varphi(\tau_0) d\tau_0 + \frac{(\tau - \tau_0)^2}{2(-\mu)t} \qquad (38)$$

Now the function $\zeta(\tau)$ is obtained (see fig. 7), and the single-valued function $\sup \zeta(\tau)$ can be identified.

Then $\varphi(\tau,t)$ only keeps the segments of τ which appear in $\sup \zeta(\tau)$
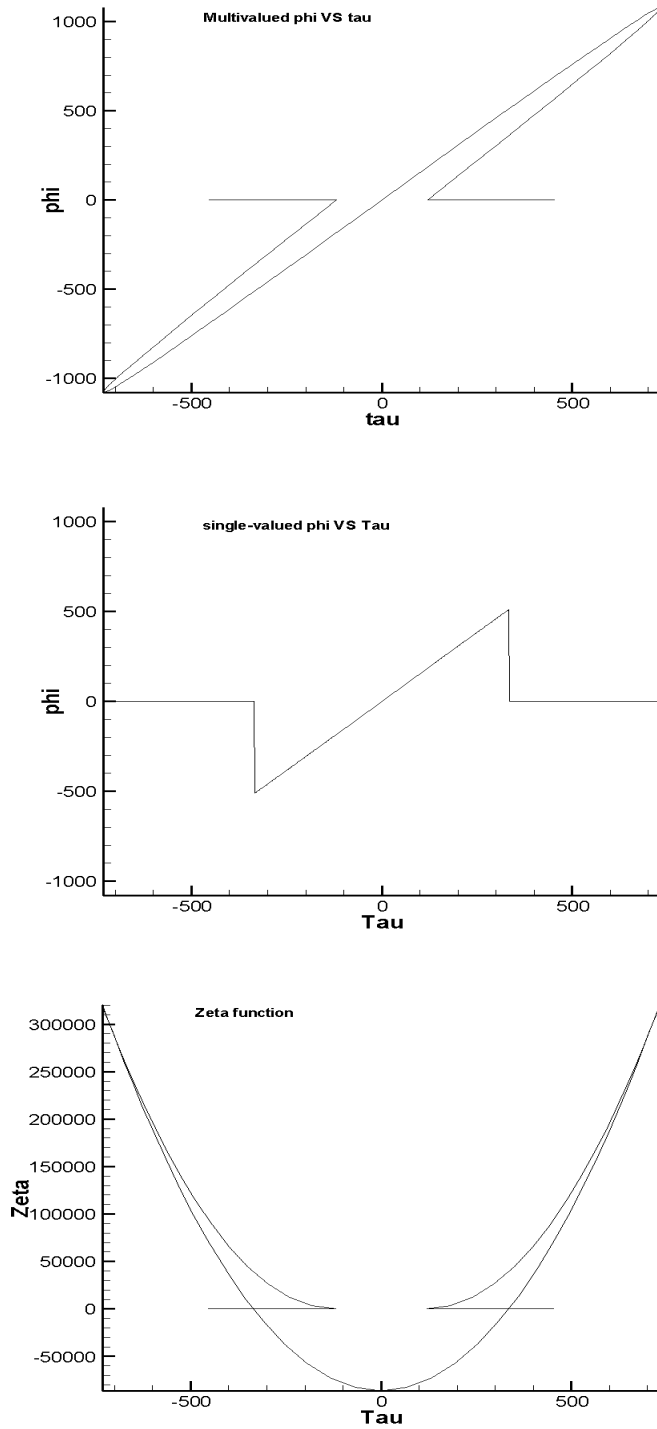
Figure 7. Distortion of signal.

Computational Application:

In order to compare the results of the shock capturing scheme of the previous section, Sec. III.e. , we use the same application case of the previous Section in the current analytical solution of the nonlinear Burgers' equation.

Starting with the nonlinear Burgers' equation

$$\overline{\frac{\partial \varphi}{\partial t}} + \overline{\frac{\partial}{\partial \tau}}(-\overline{\frac{\mu}{2}}\varphi^2) = 0$$

We let $-\mu$ as a, speed of sound, and solve the equation in the form

$$\overline{\frac{\partial \varphi}{\partial t}} + \overline{\frac{\partial}{\partial \tau}}(\overline{\frac{a}{2}}\varphi^2) = 0$$

Where a = 340.

Next, we let the initial condition be

$$\varphi_0(\tau) = \max(0, bx(\tau_0 - \tau)); \quad \tau \geq 0$$
$$\varphi_0(-\tau) = -\varphi_0(\tau); \quad \tau < 0$$

Where b = 3 $\quad \tau_0 = 120$

The analytical solution produces the following results.
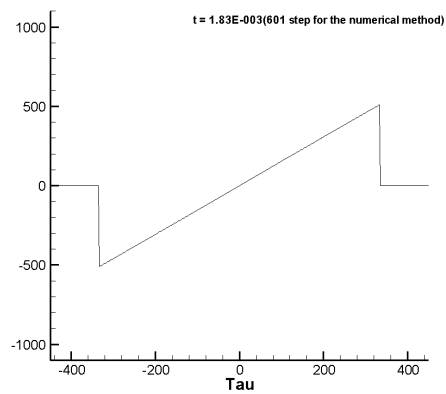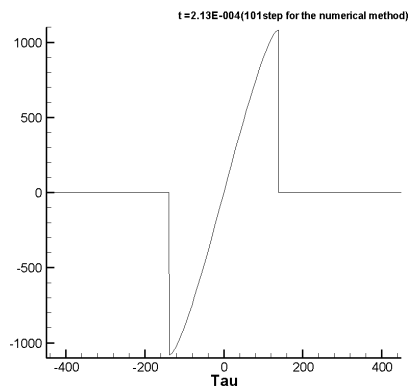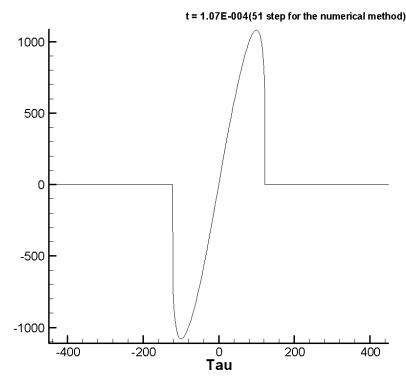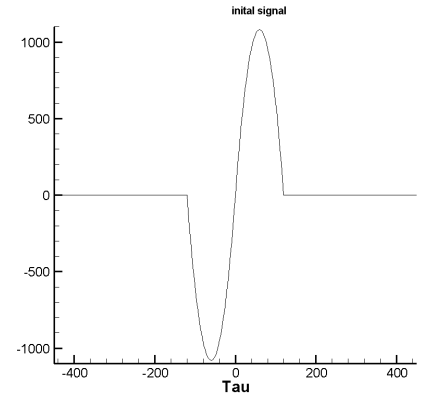
Figure 8. Analytical solution

It is obviously clear that the analytical solution given by Fig 8 above is exactly the same as the numerical solution obtained in Sec. III.e., Figs. 6.b and 6.g. This application validates the numerical solution of the nonlinear Burgers equation.

III. g. Integrated Computer Program:

The integrated computer program consists of four main sub-programs and a Driver main program. Two of sub-program are for the two schemes to solve the linear Tricomi equation, and the other two sub-programs are for the two schemes to solve the nonlinear Burgers equation.

The two schemes to solve the linear Tricomi equation use either the frequency-domain scheme or the time-domain scheme. The other two schemes are developed to solve the nonlinear Burgers equation using either a finite-difference scheme or a closed-form analytical scheme.

To choose a combination of two sub-programs to solve for the nonlinear Tricomi equation, we introduced an input flag called "Mode" in the Driver main program. Depending of the value chosen for Mode from the list below, the driver will direct the solution to different combinations of two of the sub-programs, as given below:

1. Mode 00 is for frequency domain and for numerical Burgers equation
2. Mode 01 is for frequency domain and for closed form Burgers equation
3. Mode 10 is for time domain and for numerical Burgers' equation
4. Mode 11 is for time domain and for Closed Form Burgers' equation

IV   Validation of Computer Code:

Here, the numerical scheme and code given below is tested for validation. The test cases are those of Ref. 6, with an incoming N-wave or an incoming Concorde aircraft case. Another four tests are solved, which include two flat-top and two ramp-top cases. The computational domain, boundary conditions, illumination and shadow zones, caustic surface and incoming and outgoing waves are shown in Fig. 9. The illumination zone is governed by a hyperbolic Tricomi equation, and the shadow zone is governed by an elliptic Tricomi equation. At the caustic surface, the equation is parabolic. Since the outgoing wave is unknown, the incoming wave is specified only. The incoming wave could be an N-wave, a wave corresponding to a Concorde aircraft, or any other incoming wave such as those shown on figure 10.
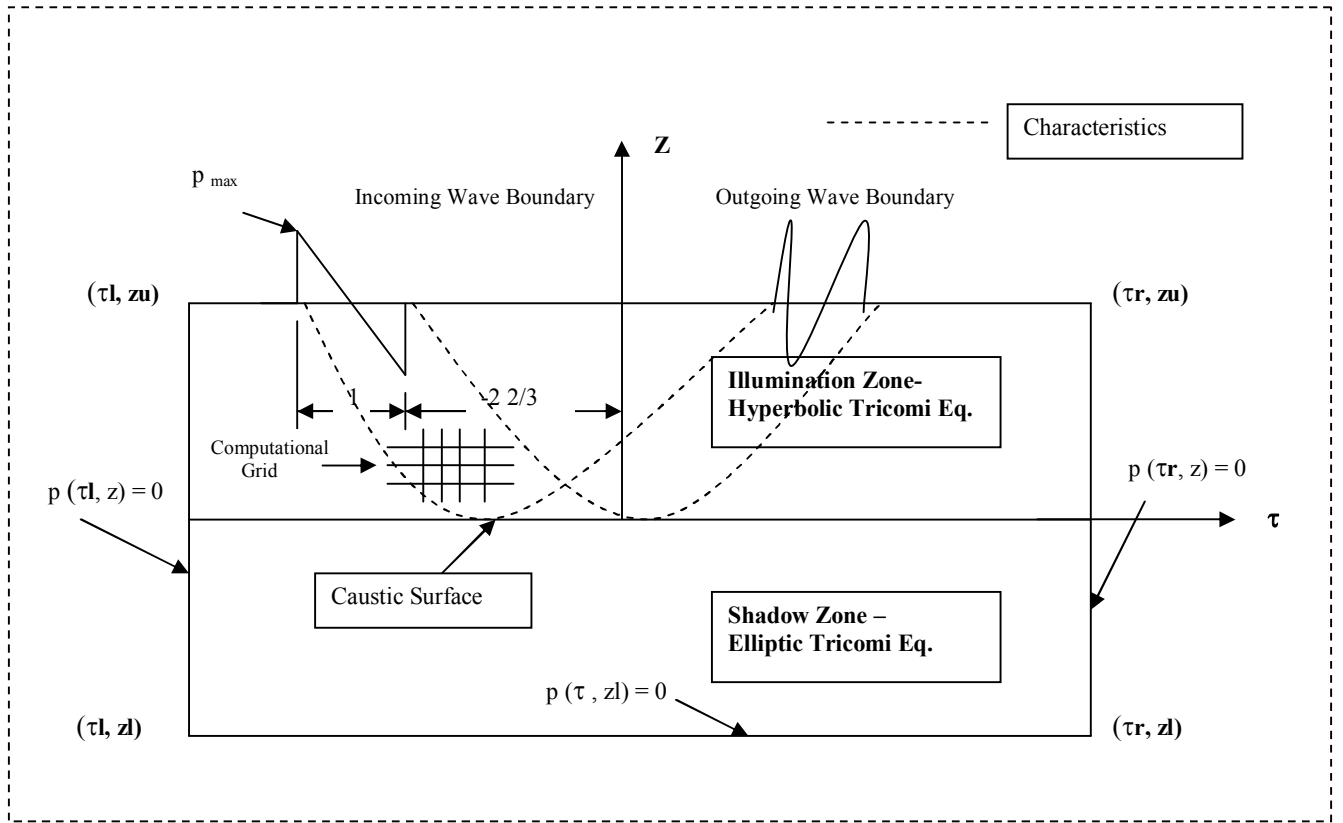
Figure 9. Computational domain, boundary conditions, illumination and shadow zones, caustic surface and incoming and outgoing waves

Incoming Sonic Boom Signatures

N-Wave
(10-1)

2.25 psf

230 ms

2.25 psf

Concorde
(10-2)

2.25 psf

1.55 psf

1.47 psf

30 ms

230 ms

2.56 ms

Flat-top 1
(10-3)

0.5 psf

37 ms

150 ms

1.0 psf

Ramp-top 1
(10-4)

1.0 psf

0.5

25 ms

150 ms

1.0 psf

Flat-top 2
(10-5)

0.5 psf

37 ms

37 ms

150 ms

0.5 psf

Ramp-top 2
(10-6)

1.0 psf

0.5

25 ms

25 ms

150 ms

0.5

1.0 psf
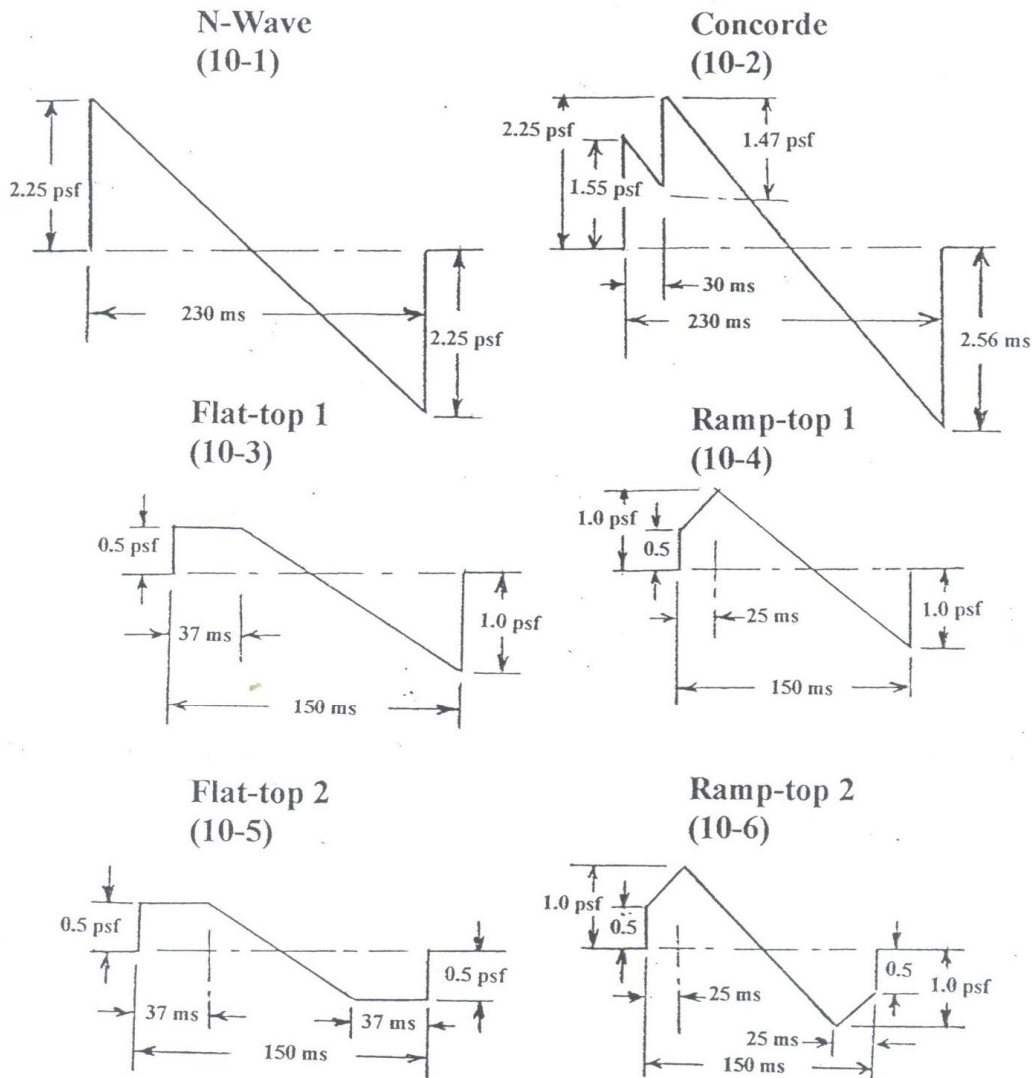
Figure 10. Different shapes of incoming sonic boom signatures.

Solution for an Incoming N-wave (Fig.10-1 Case):

Computational domain and grid:

We choose a rectangular domain with $z \in [-2.,2.]$ and $\tau \in [-2.67, 3.67]$ dimensionless units, and the number of grid points in the Z direction is 1000 and in the τ direction is 2048 points when using the time-domain scheme, or frequencies when using the frequency-domain scheme. It should be noticed that the higher the frequencies are or the points in τ the better the solutions are.

The F- function of Eq. (11) on the upper boundary z = 2.0 is used as an incoming N-wave (see Fig 10.1)., which extends from τ = -1.386 to $\tau = -2.836$ (duration of 1) with p_{max} = 1.0 and p_{min} = -1 (τ and p are dimensionless).   With these dimensionless pressure and duration, p = 1 is equivalent to 2.25 psf and τ = 1 is equivalent to 230 ms. The dimensionless time step for the

pseudo time integration is taken as 0.001. The case has been run for 20,000 time steps until the total error of the pseudo unsteady time term was reduced to 10^{-7}.

Results and Discussion:

Figure 11 shows the pressure contours of the incoming wave as it progresses in the domain toward the caustic surface at $z = 0$ and outgoing wave as it originates from the caustic surface. In Fig. 12, it is noticed that the predicted wave at the caustic surface shows pressure peaks of 2.8, 1.8 and -1.35 (equivalent to 6.3 psf, 4.05 psf and –3.04 psf, respectively). These results conclusively show that the superboom response from the dimensionless pressure peaks of ± 1 is predicted. It is also consistent with the results of Ref. 6. Figure 13 shows p_{max} of 3.9 which is equivalent to 8.775 at $Z = 0.0845$. Figures 14 and 15 show the interaction of the incoming wave with the outgoing wave at $z = 0.5$ and 1.5. The figure shows the growth of the pressure peaks as it proceeds toward the caustic surface. Figure 16 shows the pressure wave in the shadow zone, which is fading away.

The small-amplitude high-frequency waves shown on the pressure curves are due to the frequency domain resolution. It can be removed using an additive numerical dissipation in the computational scheme. However, care must be used since too much numerical dissipation can wipe out small shocks.
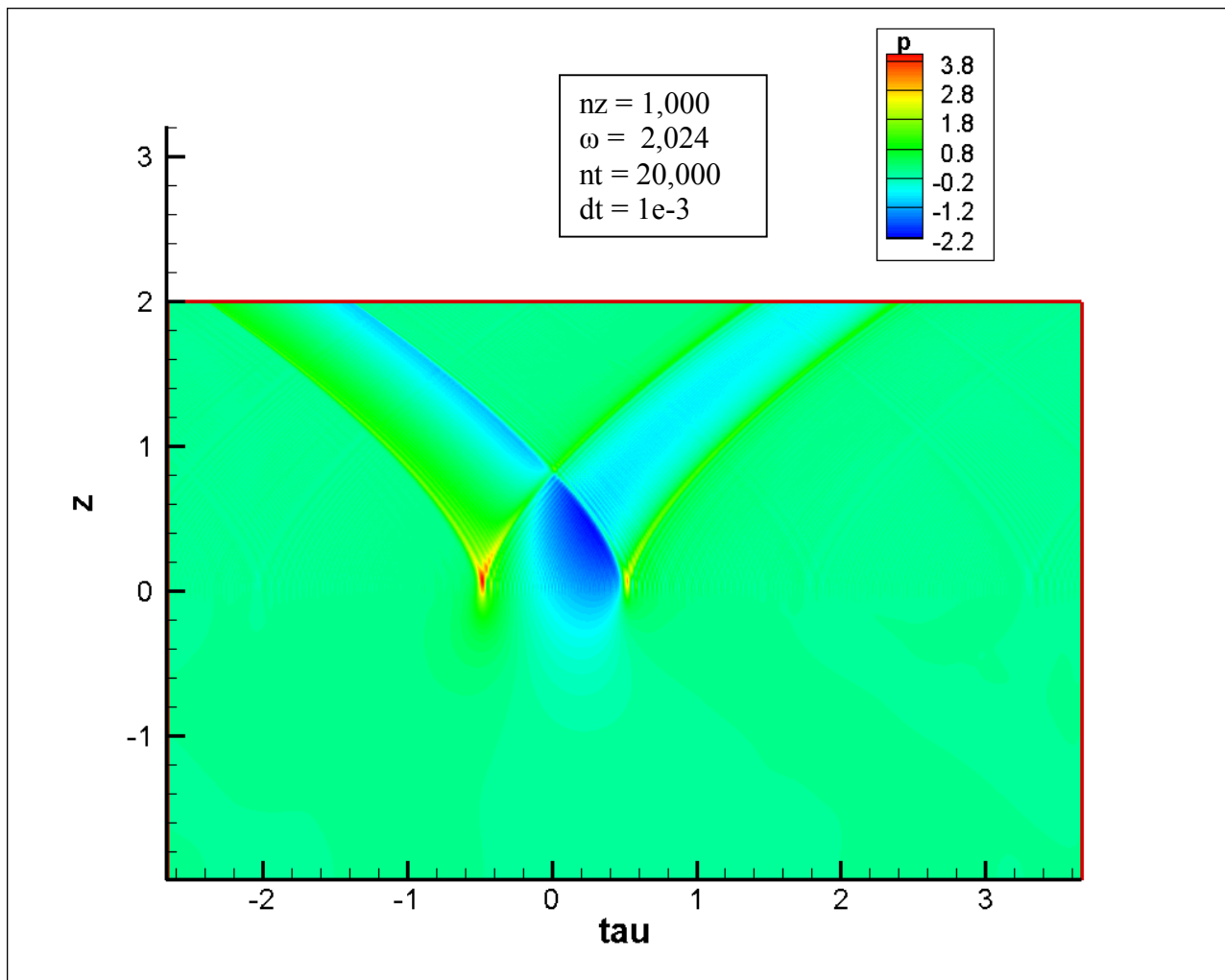
Figure 11. Pressure contours for an incoming N-wave at (fig. 10-1 case) nt = 20,000 time steps. The outgoing wave is clearly predicted.
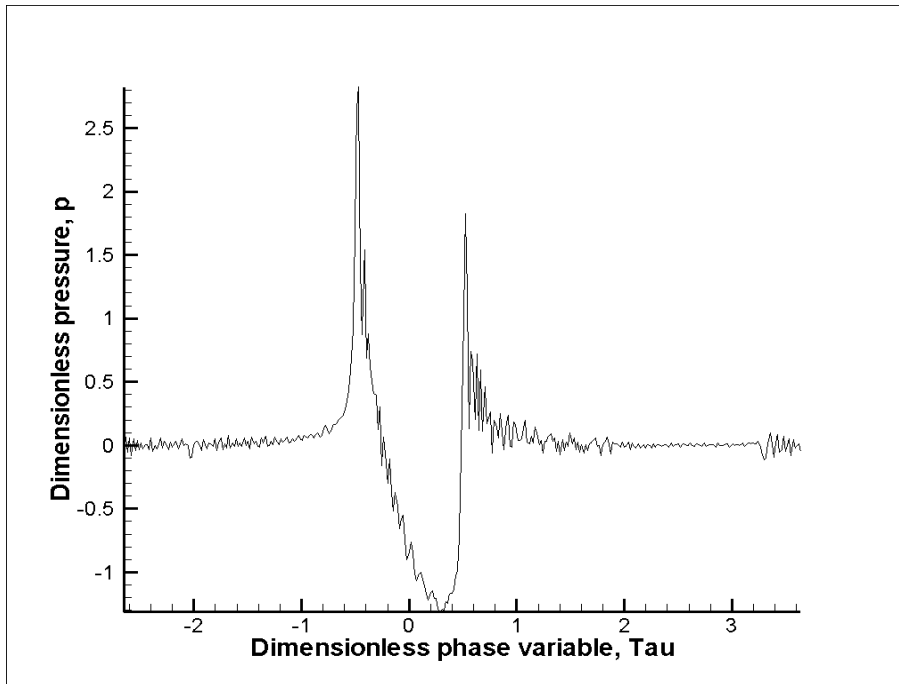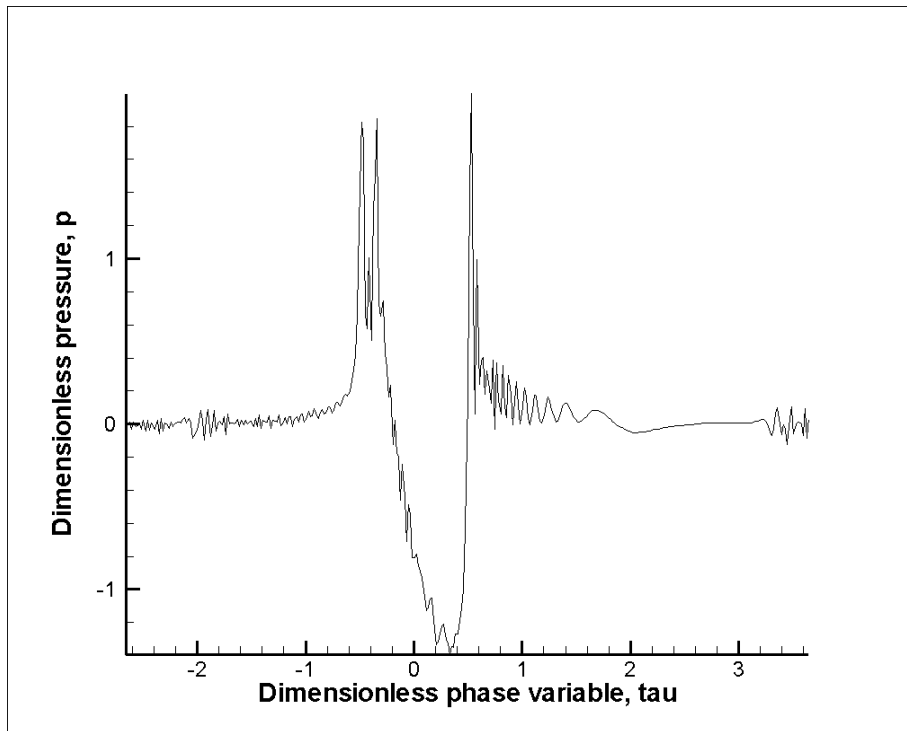
Figure 12. Pressure variation for an incoming N-wave (fig. 10-1 case) at the caustic surface (z = 0) and nt = 20,000 steps.
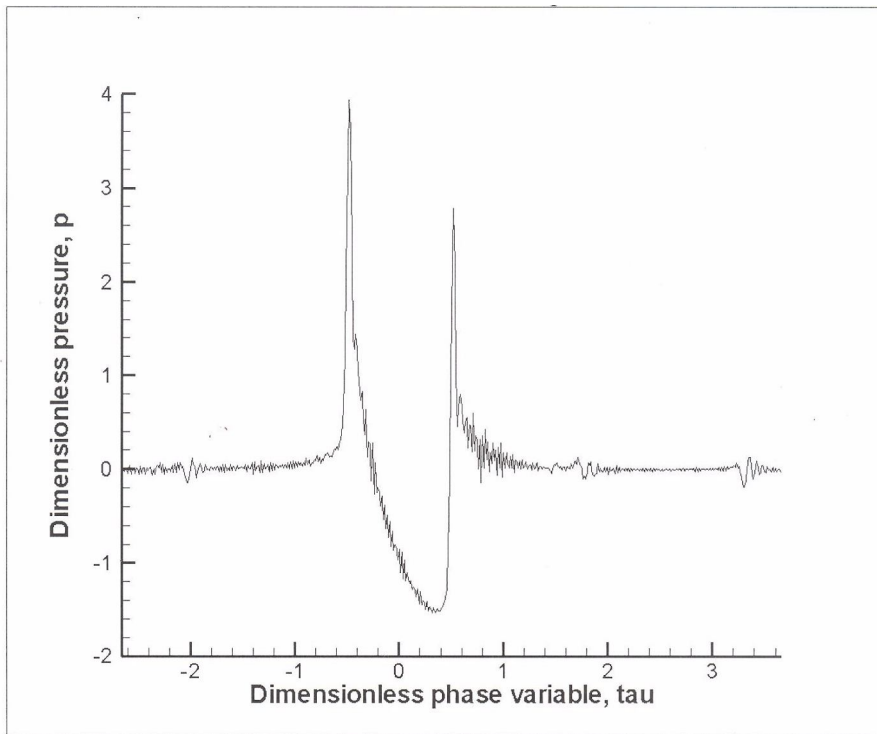
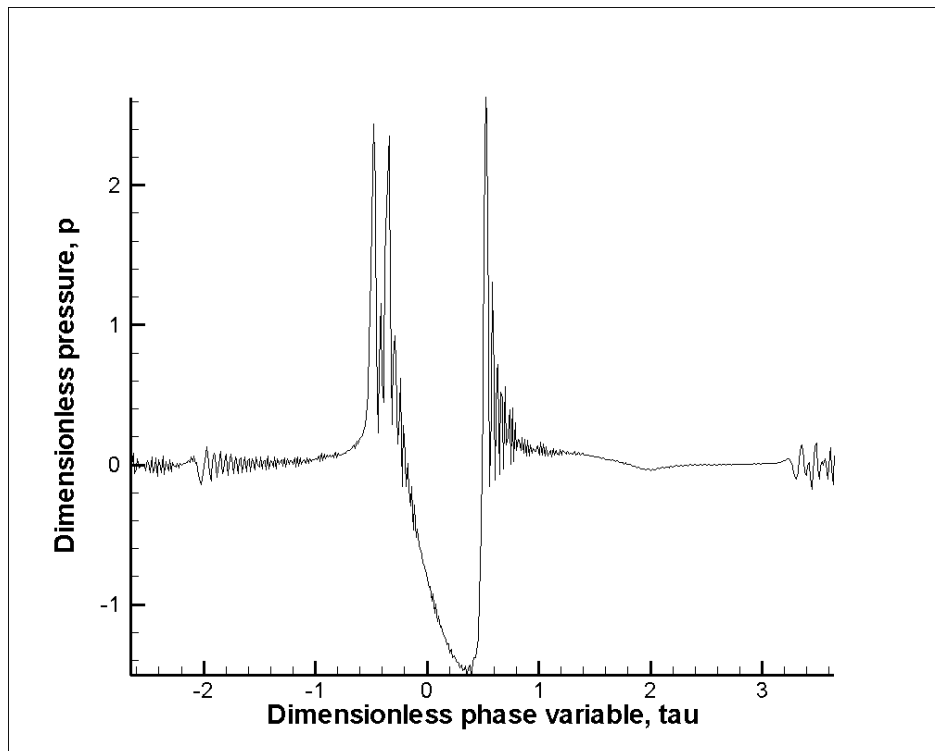Figure 13. – Pressure variation for an incoming N-wave (fig. 10-1 case) at z of maximum pressure, z = 0.0845 and nt = 20,000 steps.
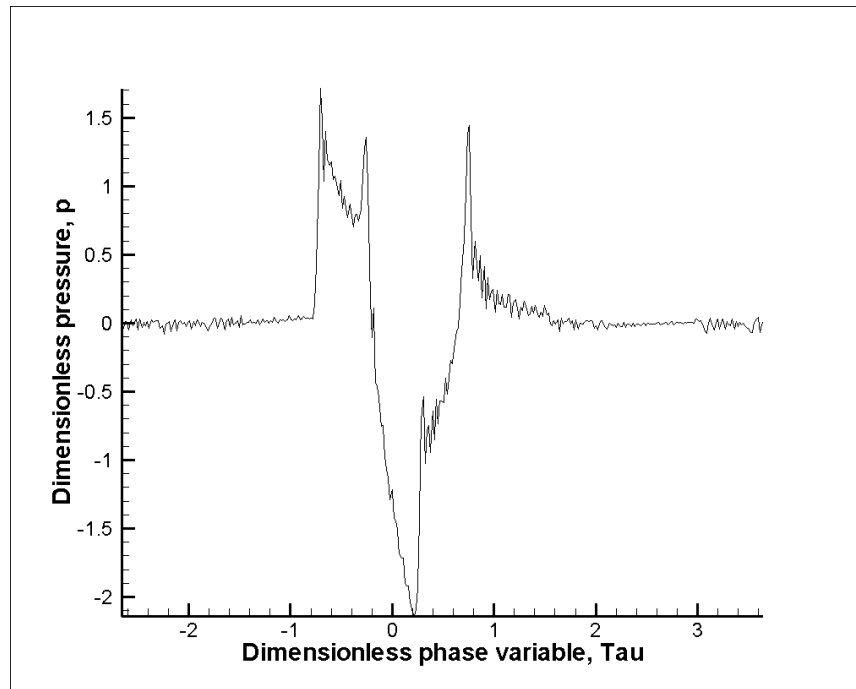
Figure 14. Pressure variation for an incoming N-wave (fig. 10-1 case) at z = 0.5
and nt = 20,000 steps.
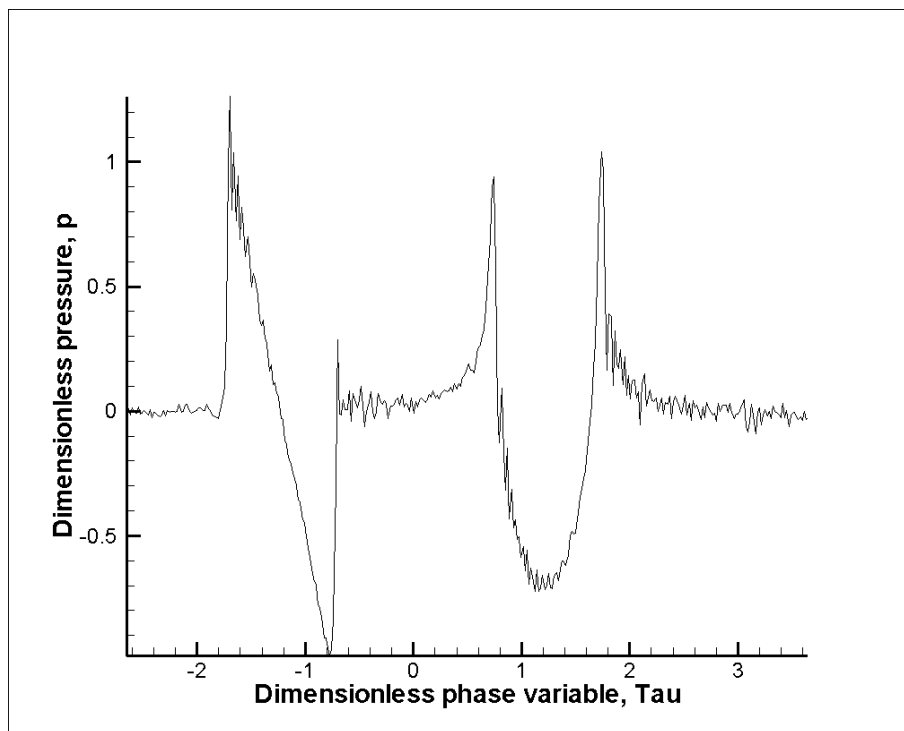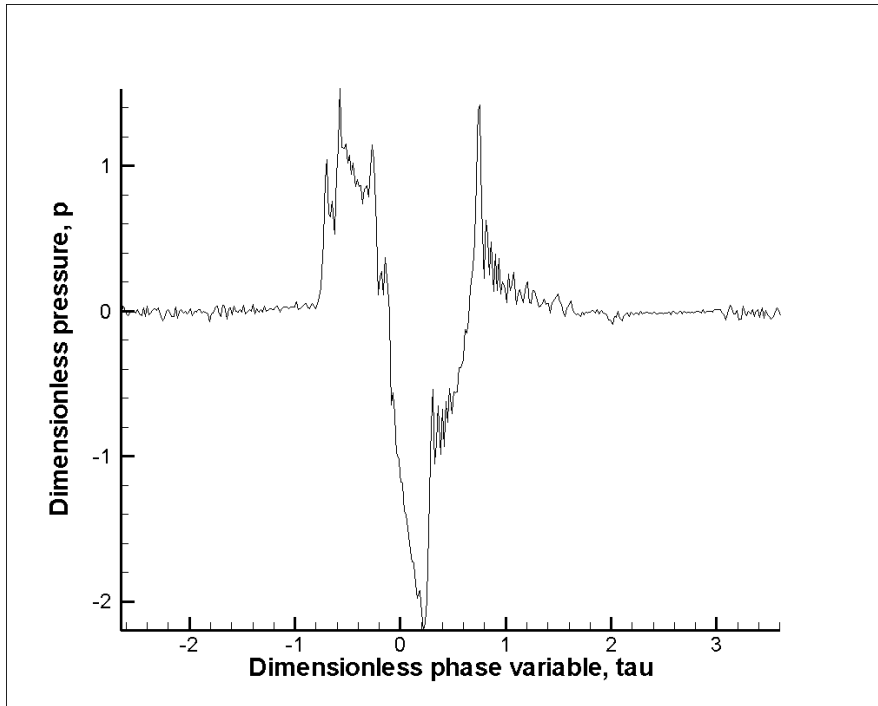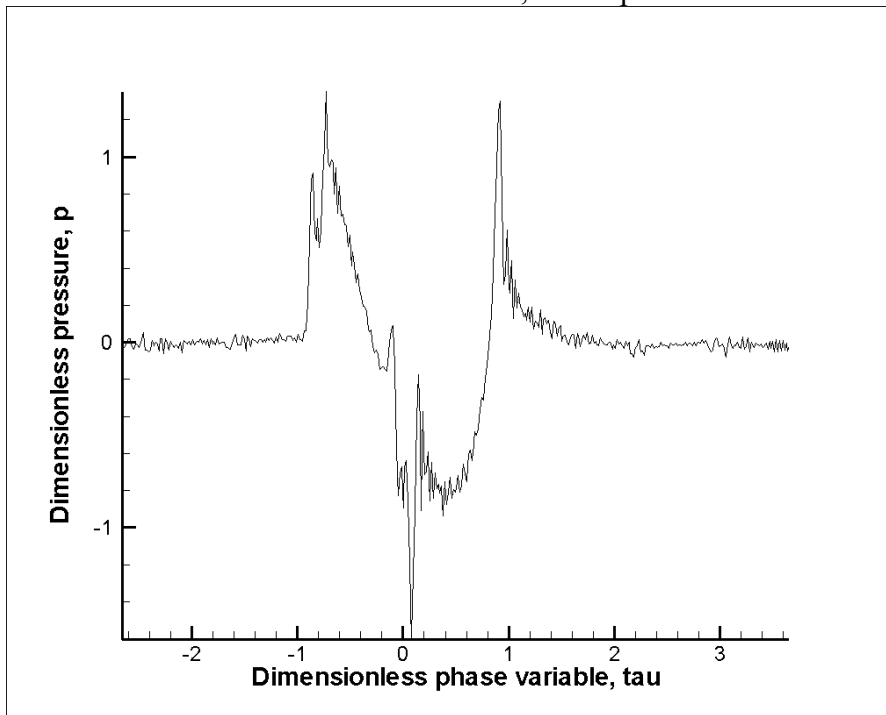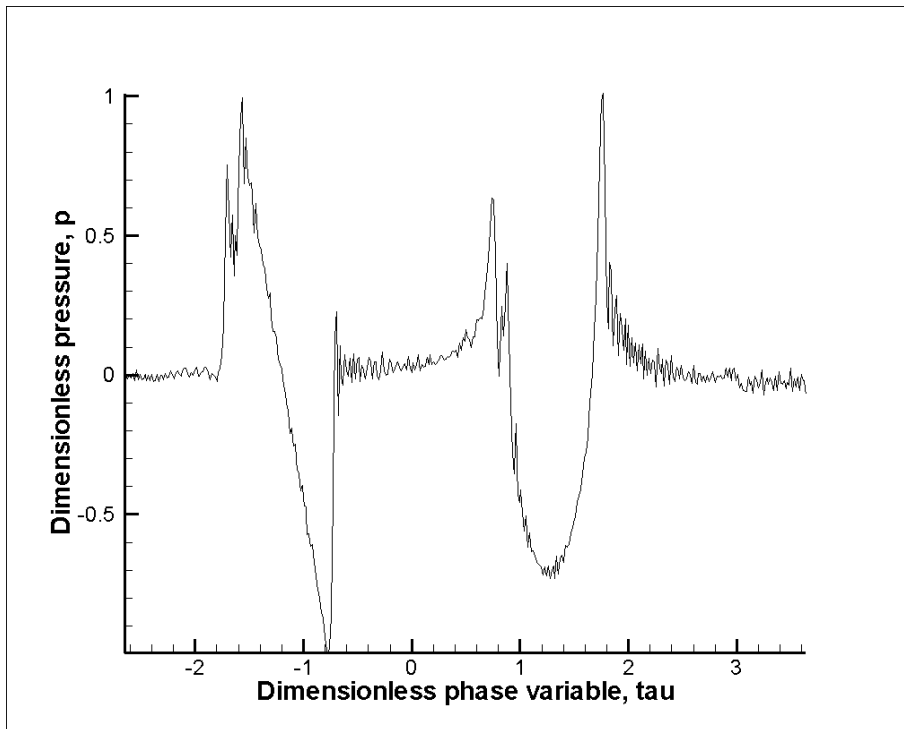

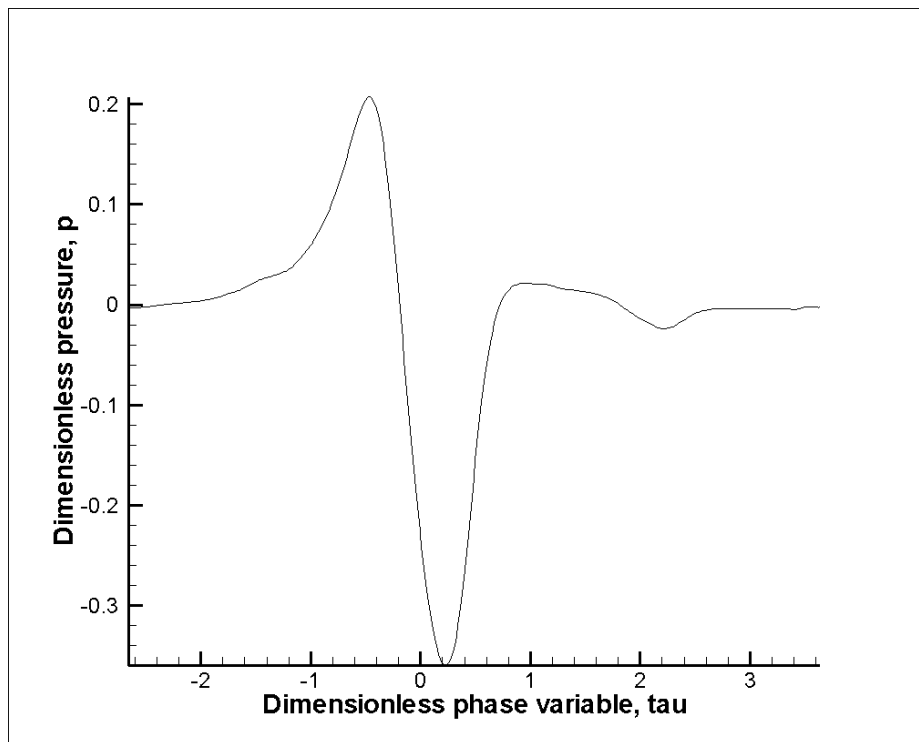Figure 15. Pressure variation for an incoming N-wave (fig. 10-1 case) at z = 1.5
and nt = 20,000 steps.
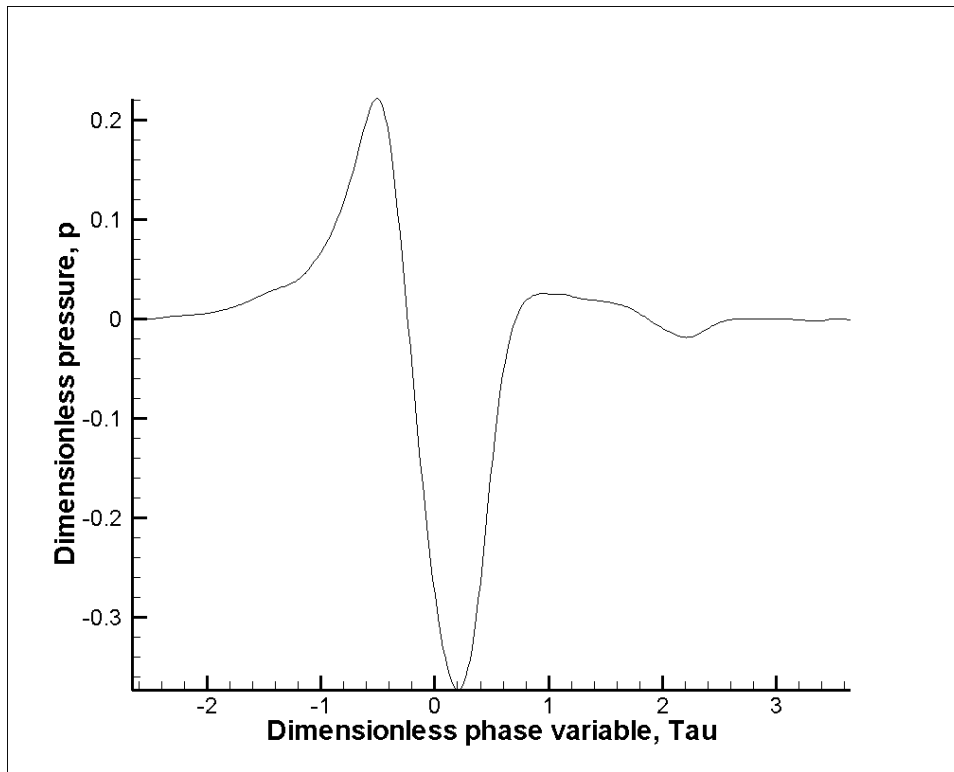
Figure 16. Pressure variation for an incoming N-wave (fig. 10-1 case) at z = -0.5 (shadow zone) and nt = 20,000 steps

Solution for an Incoming Concorde Aircraft Wave (Fig. 10-2 case):

Computational domain and grid:

We choose a rectangular domain with $z \in [-2., 2.]$ and $\tau \in [-2.67, 3.67]$ dimensionless units, and the number of grid points in the Z direction is 1000 and in the τ direction is 02048 points when using the time-domain scheme, or frequencies when using the frequency-domain scheme.

The F- function of Eq. (11) on the upper boundary z = 2.0 is used as an incoming Concorde aircraft wave (see Figure 10-2) which extends from τ = -1.386 to τ = – 2.836 (duration of 1) with p_{max} = 0.689 and 1.0, and p_{min} = -1.1378 (τ and p are dimensionless). With these dimensionless pressure and duration, p = 1 is equivalent to 2.25 psf and τ = 1 is equivalent to 230 ms. The dimensionless time step for the pseudo time integration is taken as 0.001. The case has been run for 20,000 time steps until the total error of the pseudo unsteady time term was reduced to 10^{-7}.

Results and Discussion:

Figure 17 shows the pressure contours of the incoming wave as it progresses in the domain toward the caustic surface at z = 0 and the outgoing wave as it originates from the caustic surface. In Fig. 18, it is noticed that the predicted wave at the caustic surface shows pressure peaks of 1.85, 2.0 and -1.4(equivalent to 4.1625 psf, 4.5 psf and – 3.15 psf, respectively). These results conclusively show that the superboom response from dimensionless pressure peaks of 0.689, and -1.1378 is predicted. It is also consistent with the results of Ref. 6. Figure 19 shows a dimensionless pressure peak, p_{max} of 2.8 which is equivalent to 6.3 psf at z = 0.07.   Figures 20 and 21 show the interaction of the incoming wave with the outgoing wave at z = 0.5 and 0.7.

Figure 22 shows the pressure at z = 1.5, before the interaction starts. These figures show the growth of the pressure peaks as it proceeds toward the caustic surface. Figure 23 shows the pressure wave in the shadow zone, which is fading away.

Again, the small-amplitude high-frequency waves shown on the pressure curves are due to the frequency domain resolution and it can be removed using an additive numerical dissipation in the computational scheme.
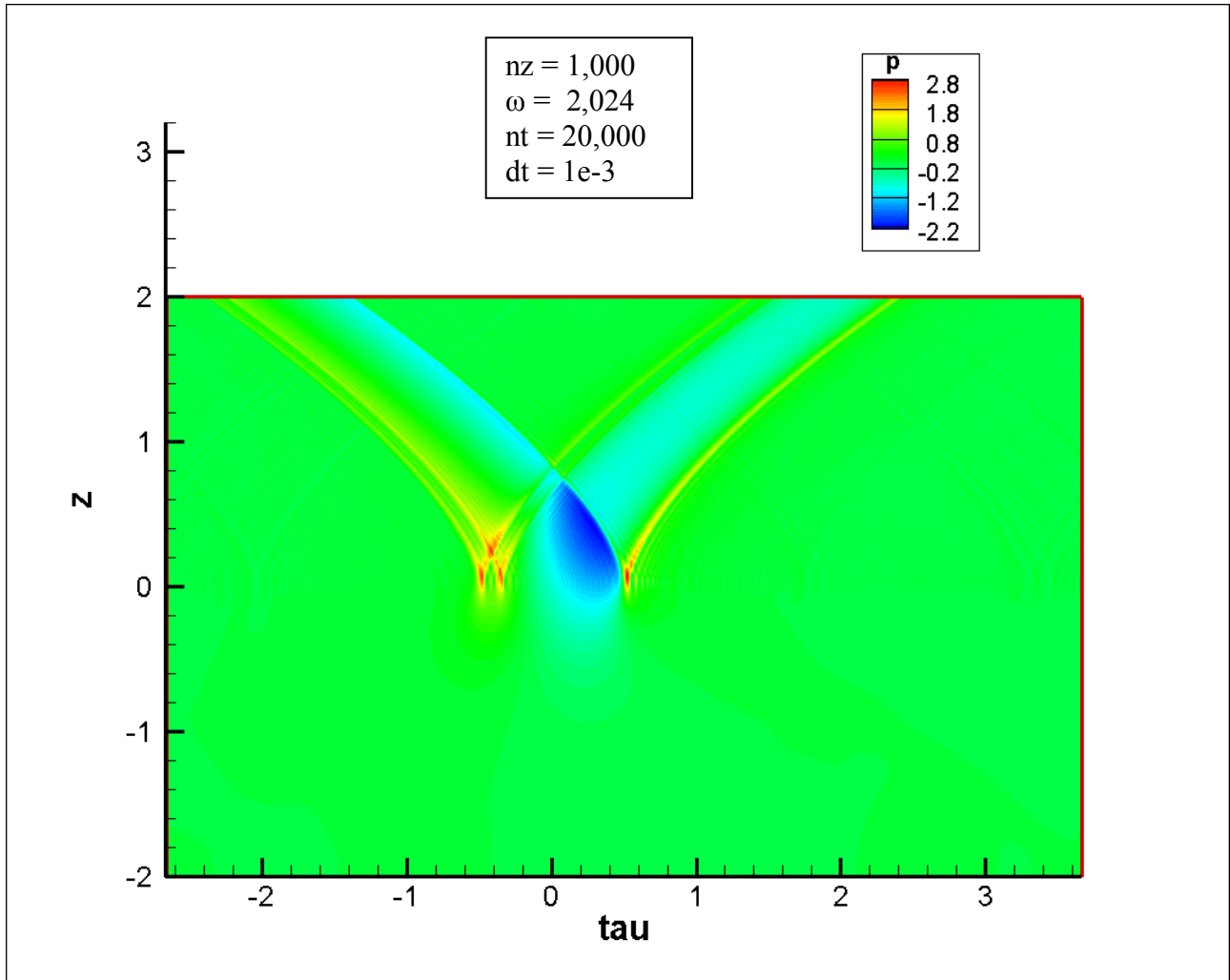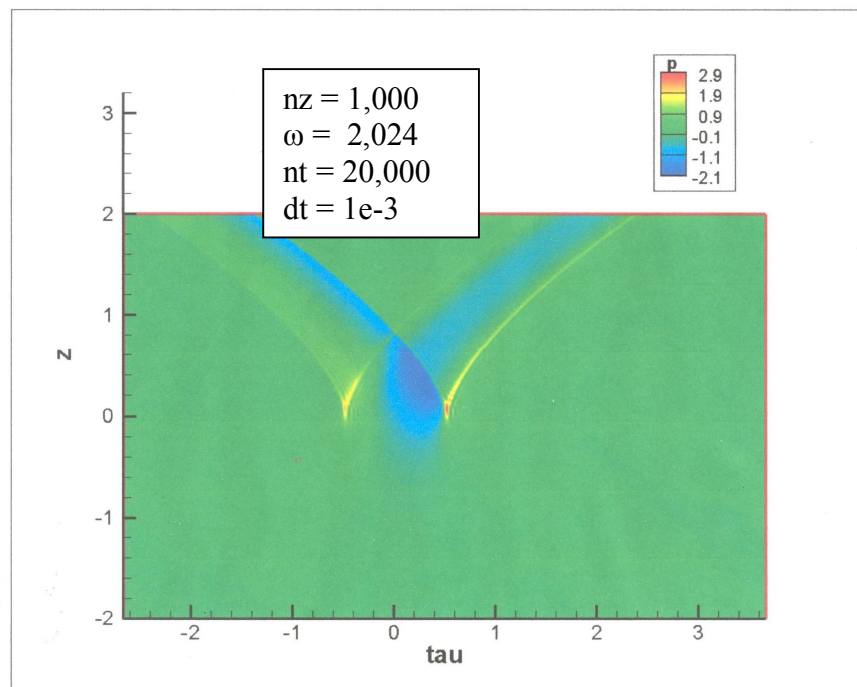

Figure 17. Pressure contours for an incoming Concorde aircraft wave (fig. 10-2 case) at nt = 20,000 time steps. The outgoing wave is clearly predicted.
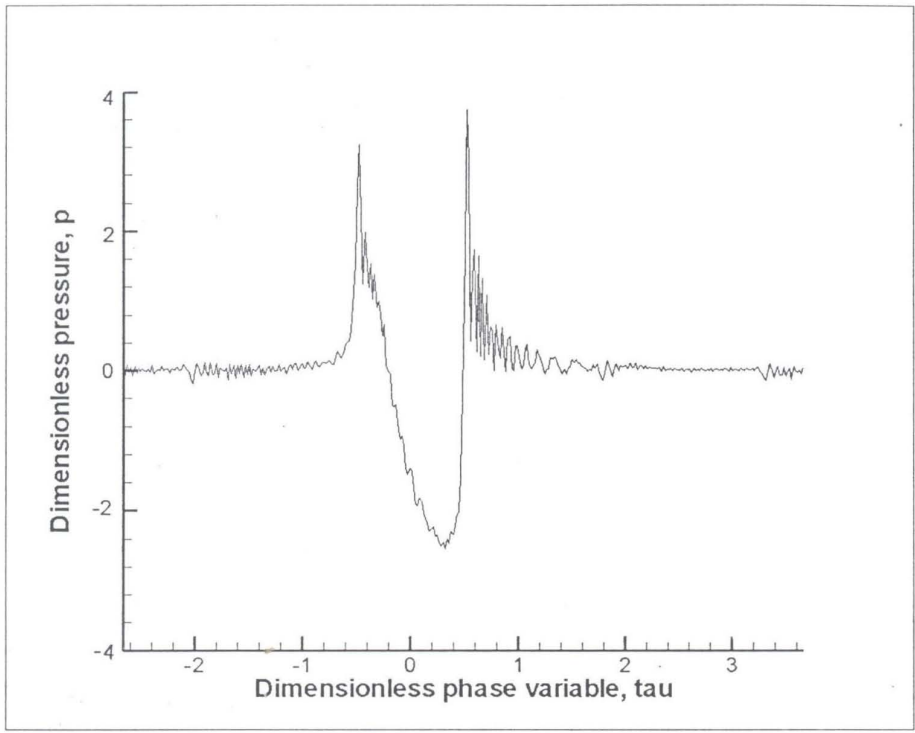
Figure 18. Pressure variation for an incoming Concorde aircraft wave (fig. 10-2 case)
at the caustic surface (z = 0) and nt = 20,000 steps
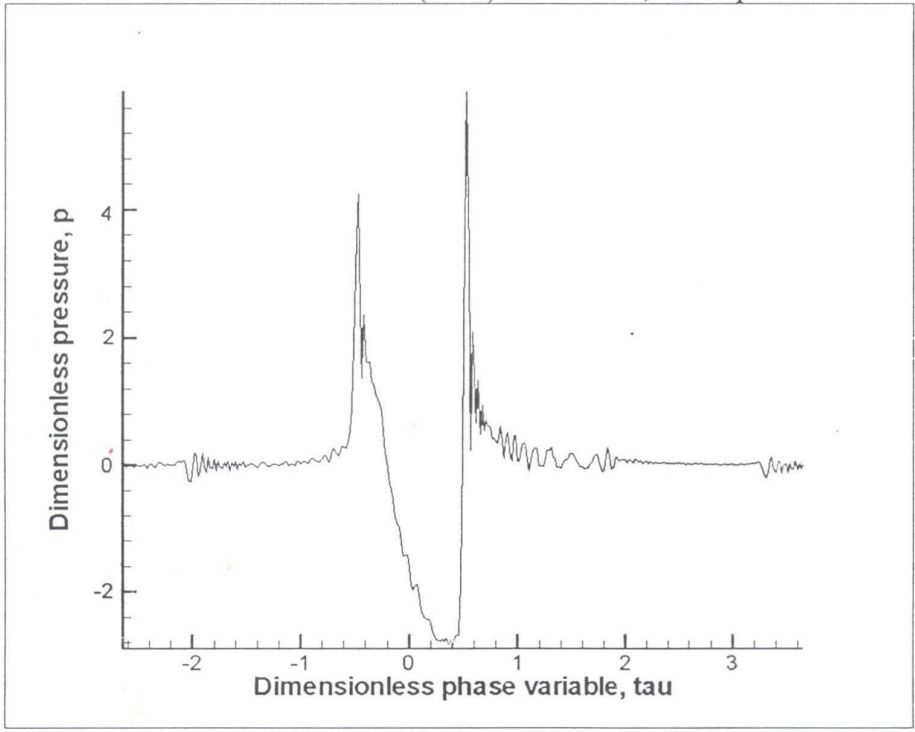

Figure 19. Pressure variation for an incoming Concorde aircraft wave(fig. 10-2 case)
at z of maximum pressure, z = 0.07, and nt = 20,000 steps

Figure 20. Pressure variation for an incoming Concorde aircraft wave (fig. 10-2 case) at z = 0.5 and nt = 20,000 steps.

Figure 21. Pressure variation for an incoming Concorde aircraft wave (fig. 10-2 case) at z = 0.7 and nt = 20,000 steps.

Figure 22. Pressure variation for an incoming Concorde aircraft wave (fig. 10-2 case)
At z = 1.5 and nt = 20,000 steps

Figure 23. Pressure variation for an incoming Concorde aircraft wave (fig. 10-2 case)
at z = - 0.5 (shadow zone) and nt = 20,000 steps.

Solution for an Incoming Flat-Top 1 Wave (Fig.10-3):

Computational domain and grid:

We choose a rectangular domain with $z \in [-2., 2.]$ and $\tau \in [-2.67, 3.67]$ dimensionless units, and the number of grid points in the Z direction is 1000 and in the τ direction is 2048 points when using the time-domain scheme, or frequencies when using the frequency-domain scheme.

The F- function of Eq. (11) on the upper boundary z = 2.0 is used as an incoming flat-top 1 wave (see Figure 10-3), which extends from τ = -1.386 to τ = – 2.836 (duration of 1) with p_{max} = 1 and p_{min} = -1.0 (τ and p are dimensionless). With these dimensionless pressure and duration, p = 1 is equivalent to 0.5 psf and τ = 1 is equivalent to 150 ms. The dimensionless time step for the pseudo time integration is taken as 0.001. The case has been run for 20,000 time steps until the total error of the pseudo unsteady time term was reduced to 10^{-7}.

Results and Discussion:

Figure 24 shows the pressure contours of the incoming wave as it progresses in the domain toward the caustic surface at z = 0 and the outgoing wave as it originates from the caustic surface. In Fig. 25, it is noticed that the predicted wave at the caustic surface shows pressure peaks of 3.2, 3.7 and -2.5 (equivalent to 1.6 psf, 1.85 psf and – 1.25 psf, respectively). Figure 26 shows p_{max} of 5.9, which is equivalent to 2.95 psf at z = 0.0672. These results conclusively show that the superboom response from dimensionless pressure peaks of ±1.0 and -2.0 is predicted. It is noticed that the superboom of this case of a flat-top signature would behave in the same manner as the N-wave of figure 10.1   Figures 27 and 28 show the interaction of the incoming wave with the outgoing wave at z = 0.5 and 1.5. These figures show the growth of the pressure peaks as it proceeds toward the caustic surface. Figure 29 shows the pressure wave in the shadow zone, which is fading away.

Figure 24. Pressure contours for an incoming flat-top 1 wave (Fig. 10-3 Case) at nt = 20,000 time steps. The outgoing wave is clearly predicted.

Figure 25. Pressure variation for an incoming flat-top 1 wave (Fig.10-3 case) at the caustic surface (z = 0) and nt = 20,000 steps

Figure 26. Pressure variation for an incoming flat-top 1 wave (Fig.10-3 case) at z of maximum pressure, z = 0.0672 and nt = 20,000 steps
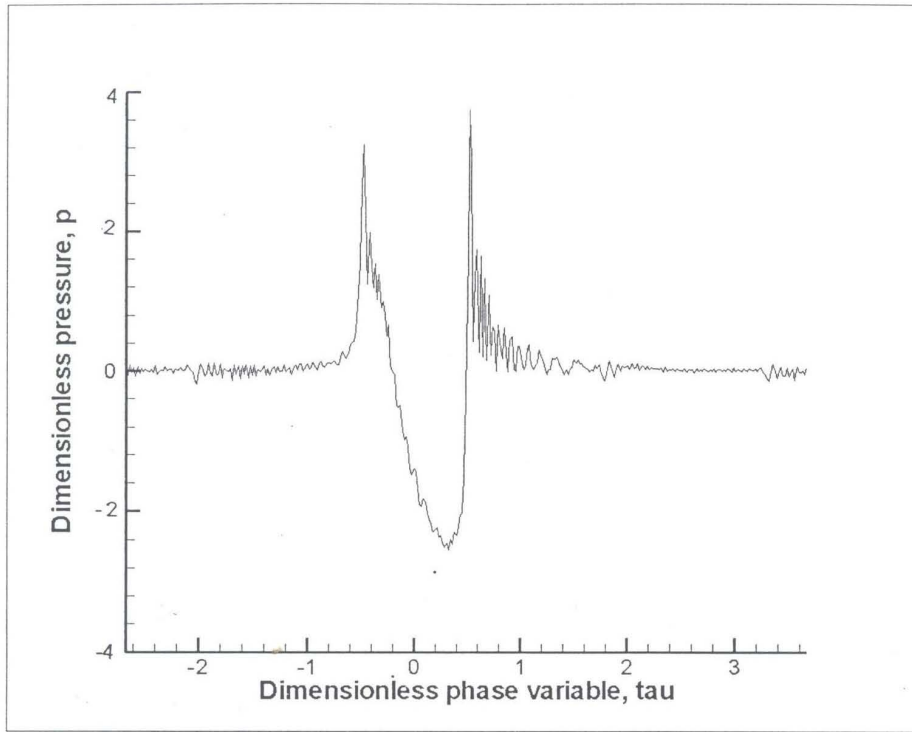
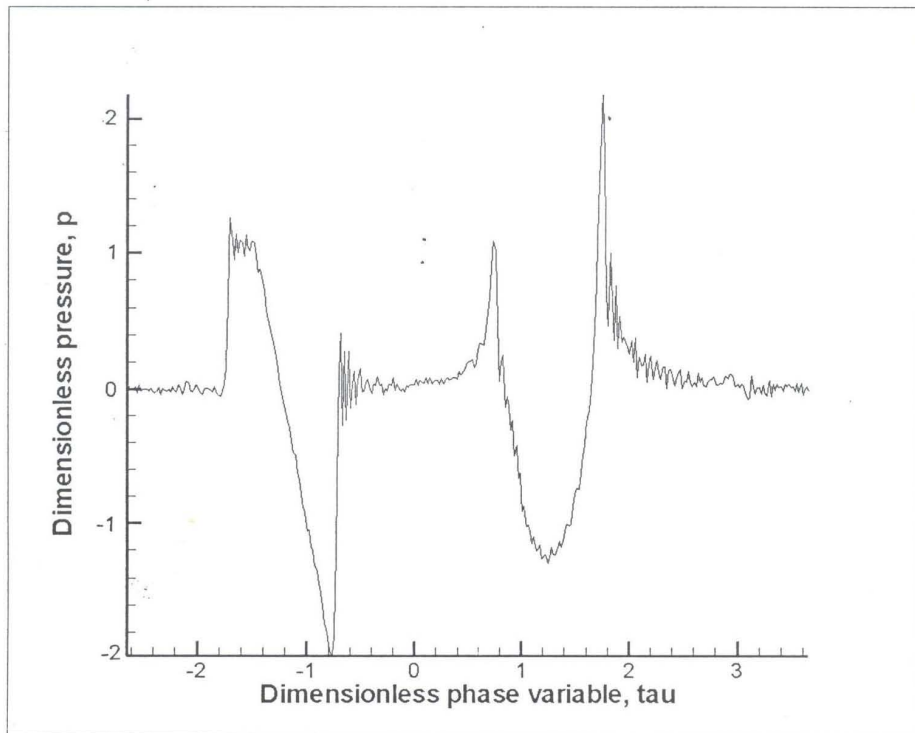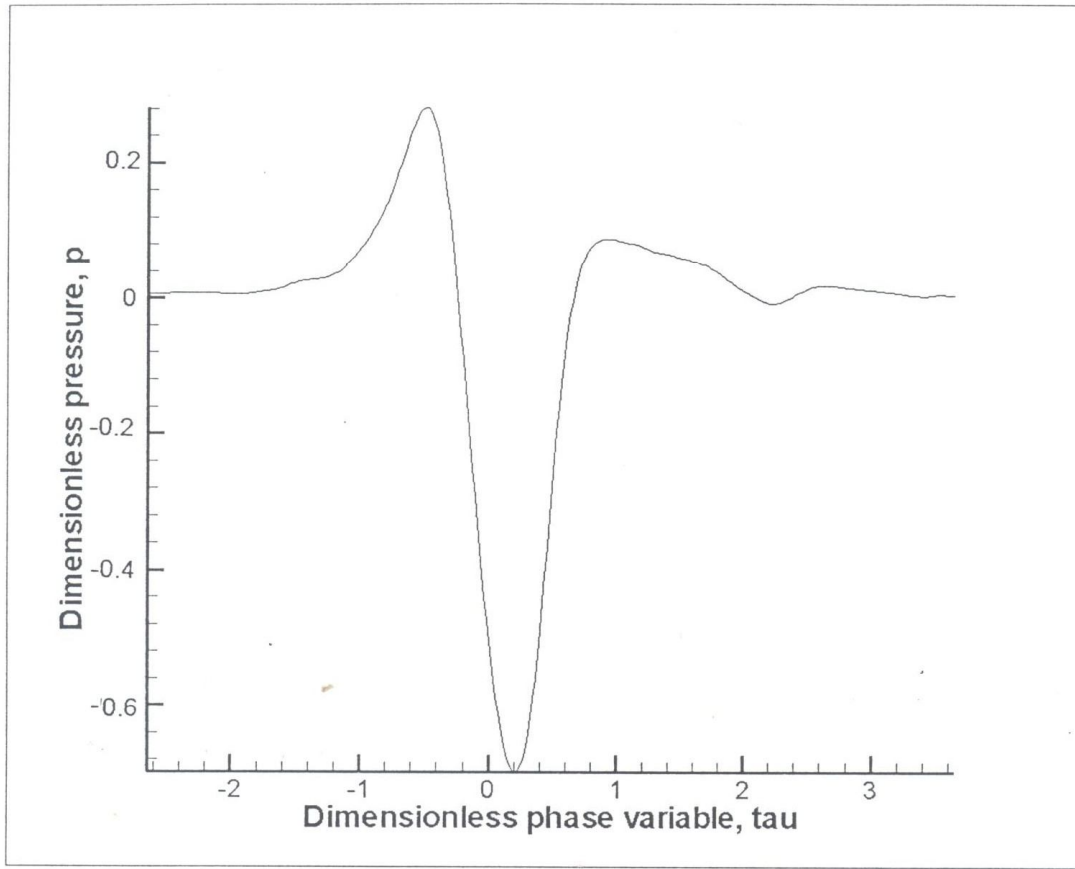Figure 27. Pressure variation for an incoming flat-top 1 wave (Fig.10-3 case) at z = 0.5 and nt = 20,000 steps

Figure 28. Pressure variation for an incoming flat-top 1 wave (Fig.10-3 case) at z = 1.5 and nt = 20,000 step

D-35

Figure 29. Pressure variation for an incoming flat-top 1 wave (Fig. 10.3 case) at z = -0.5
(shadow zone) and nt = 20,000 steps.
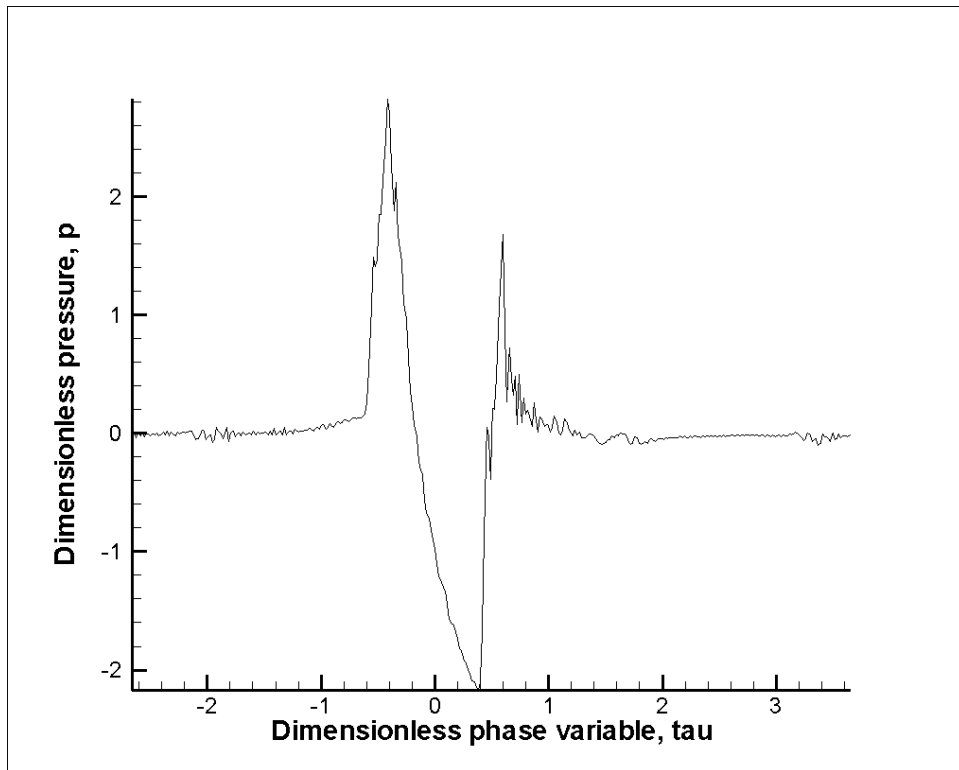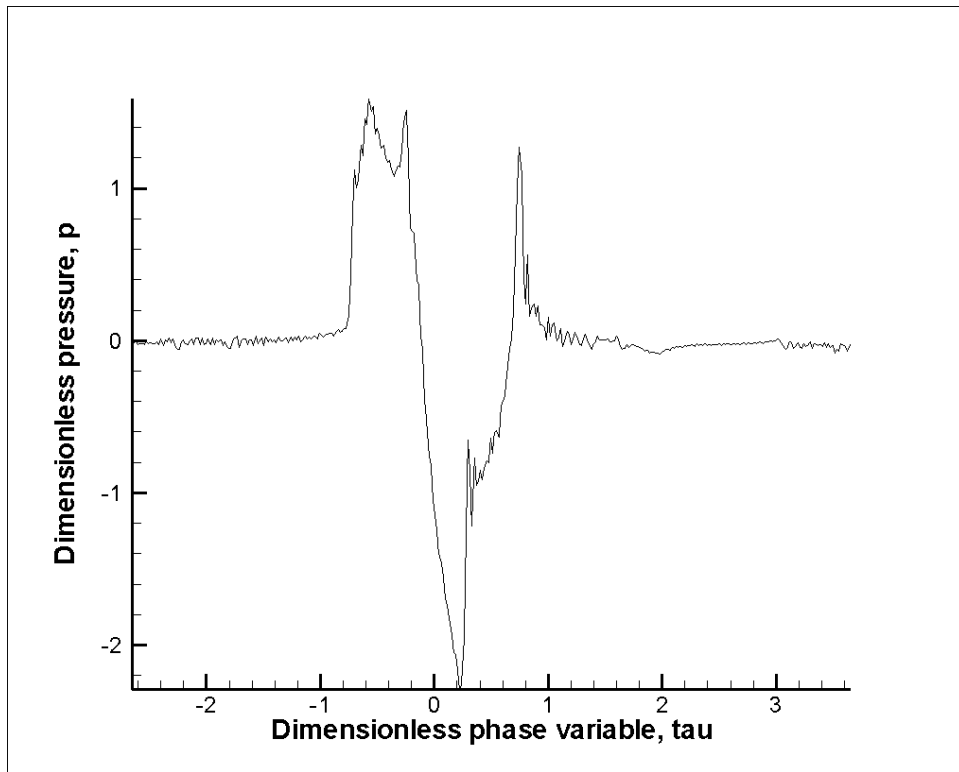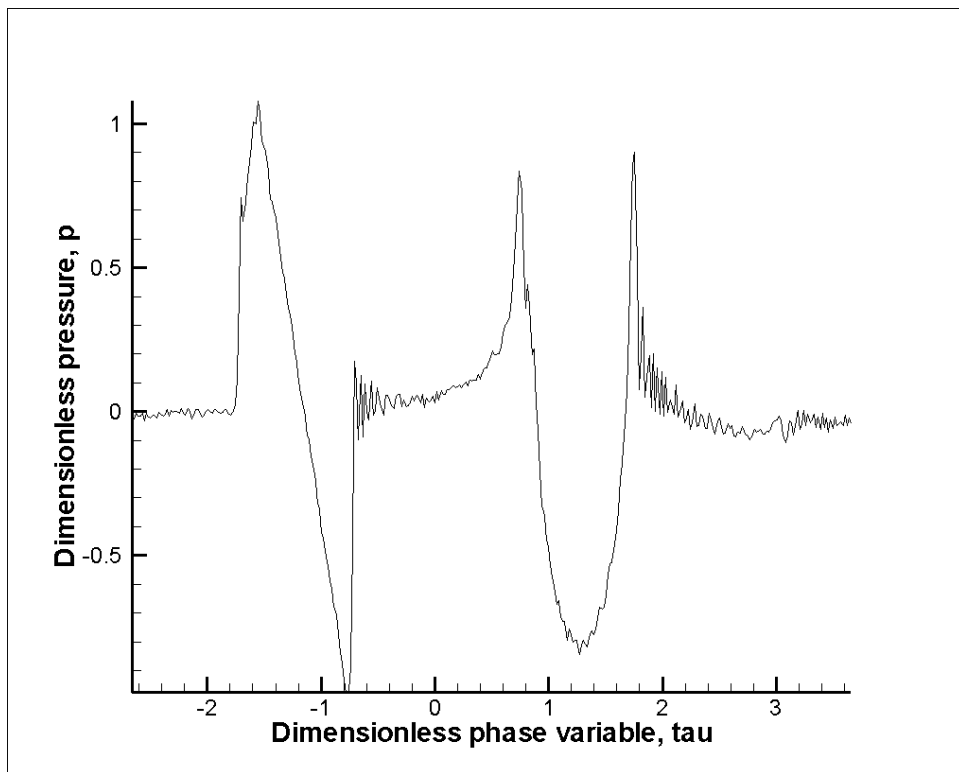
Solution for an Incoming Ramp-Top 1 Wave (Fig.10-4):

Computational domain and grid:

We choose a rectangular domain with $z \in [-2.,2.]$ and $\tau \in [-2.67,3.67]$ dimensionless units, and the number of grid points in the Z direction is 1000 and in the τ direction is 2048 points when using the time-domain scheme, or frequencies when using the frequency-domain scheme.

The F- function of Eq. (11) on the upper boundary z = 2.0 is used as an incoming ramp-top wave (see Figure 10-4), which extends from τ = -1.386 to τ = $-$ 2.836 (duration of 1) with p_{max} = 1 and p_{min} = -1.0 (τ and p are dimensionless). With these dimensionless pressure and duration, p = 1 is equivalent to 1 psf and $\tau = 1$ is equivalent to 150 ms. The dimensionless time step for the pseudo time integration is taken as 0.001. The case has been run for 20,000 time steps until the total error of the pseudo unsteady time term was reduced to 10^{-7}.

Results and Discussion:

Figure 30 shows the pressure contours of the incoming wave as it progresses in the domain toward the caustic surface at z = 0 and the outgoing wave as it originates from the caustic surface. In Fig. 31, it is noticed that the predicted wave at the caustic surface shows pressure

D-36

peaks of 2, 1.6 and -1.4(equivalent to 2 psf, 1.6 psf and – 1.4 psf, respectively). Figure 32 shows p_{max} of 2.8, which is equivalent to 2.8 psf at z = 0.242, and p_{min} of -2.2 and is equivalent to -2.2 psf. These results conclusively show that the superbooom response from dimensionless pressure peaks of ±1.0 is predicted. It is noticed that the superboom of this case is about 33 percent lower relative to the front shock than that of the flat-top case. The recompression shocks are similar in magnitude. Figures 33 and 34 show the interaction of the incoming wave with the outgoing wave at z = 0.5 and 1.5. These figures show the growth of the pressure peaks as it proceeds toward the caustic surface. Figure 35 shows the pressure wave in the shadow zone, which is fading away.
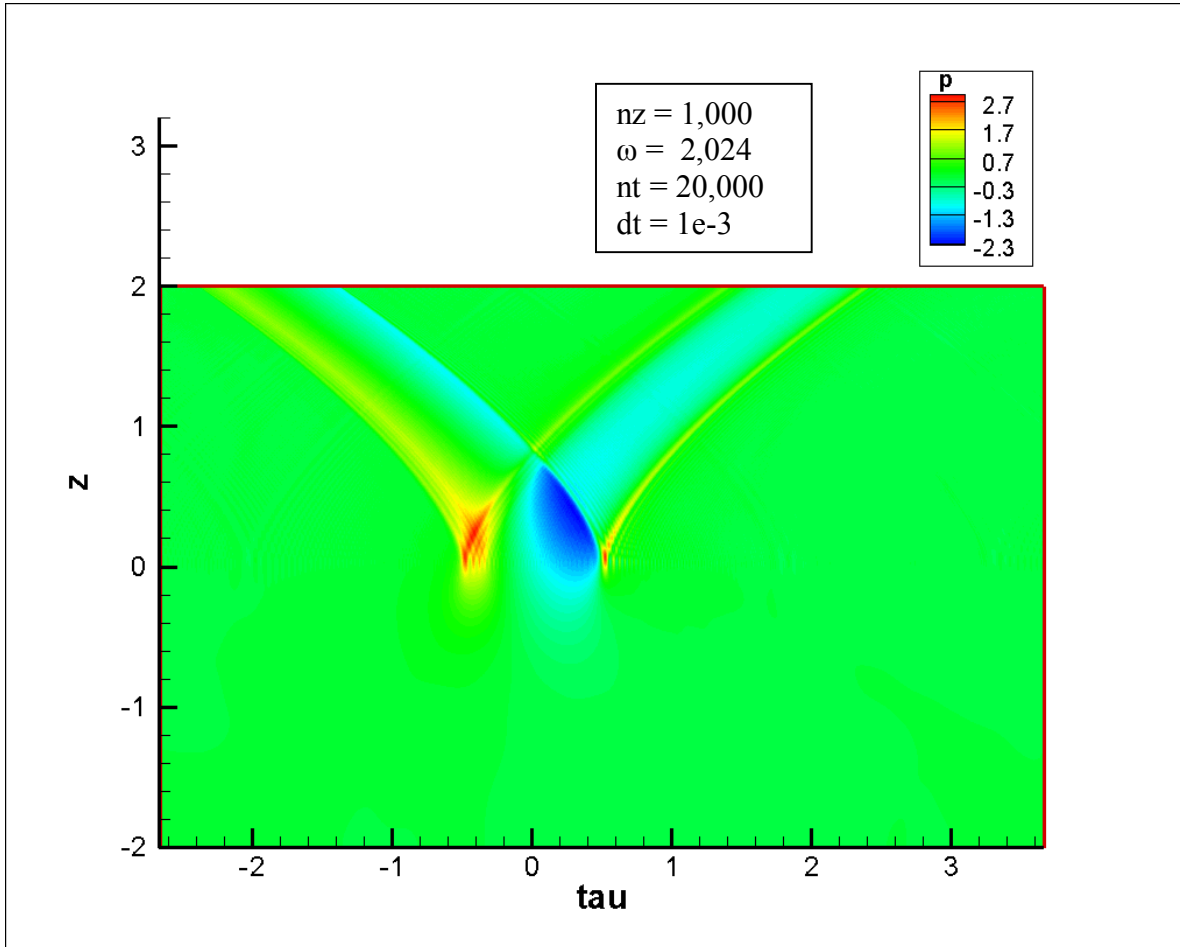
Figure 30. Pressure contours for an incoming ramp-top 1 wave (Fig. 10-4 Case) at nt = 20,000 time steps. The outgoing wave is clearly predicted.

D-37
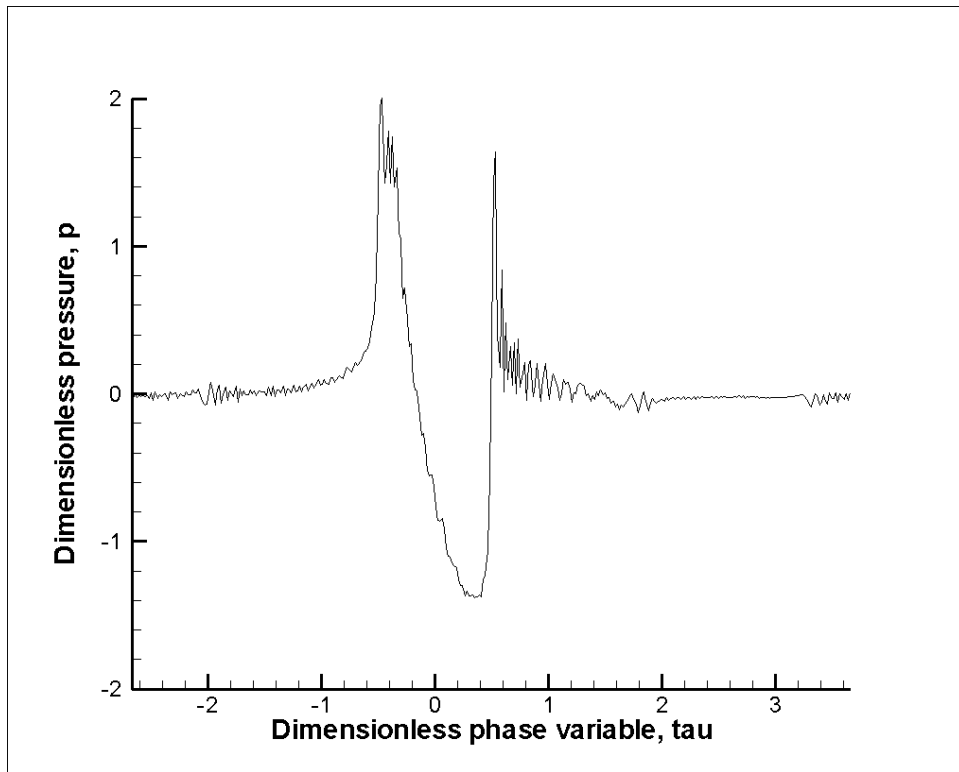
Figure 31. Pressure variation for an incoming ramp-top 1 wave (Fig.10-4 case)
at the caustic surface (z = 0) and nt = 20,000 steps.

Figure 32. Pressure variation for an incoming ramp-top 1 wave (Fig.10-4 case)
at z of maximum pressure, z = 0.242 and nt = 20,000 steps.

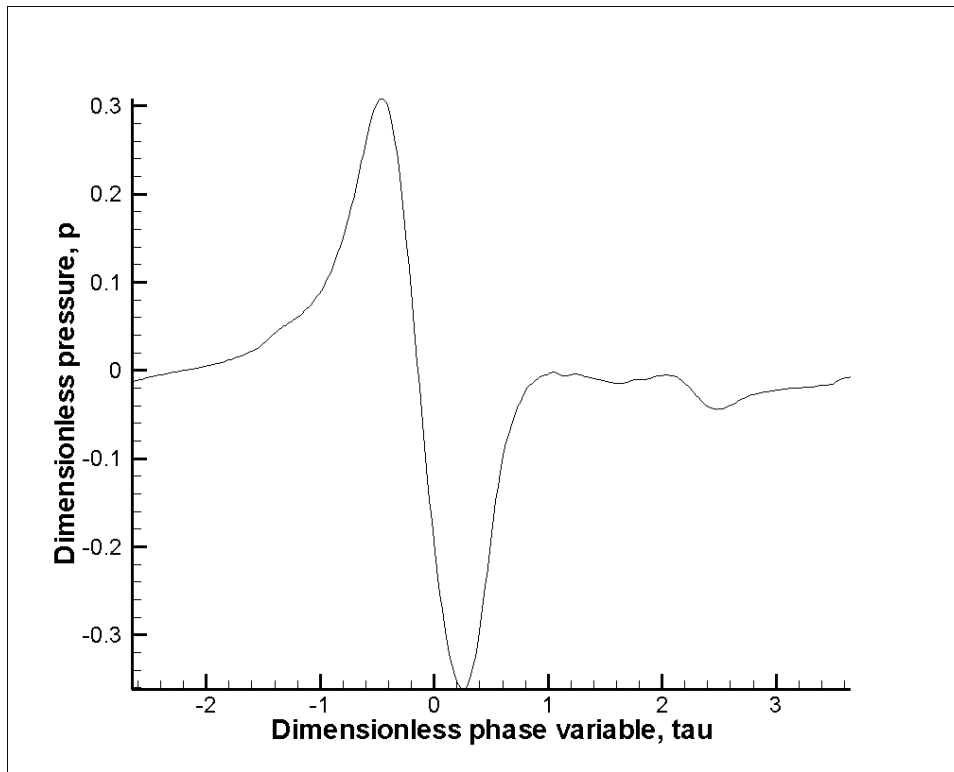Figure 33. Pressure variation for an incoming ramp-top 1 wave (Fig.10-4 case) at z = 0.5 and nt = 20,000 steps.

Figure 34. Pressure variation for an incoming ramp-top 1 wave (Fig.10-4 case) at z = 1.5 and nt = 20,000 steps.

Figure 35. Pressure variation for an incoming ramp-top 1 wave (Fig.10-4 case)
at z = -0.5 (shadow zone) and nt = 20,000 steps

Solution for an Incoming Flat-Top 2 Wave (Fig.10-5):

Computational domain and grid:

We choose a rectangular domain with $z \in [-2., 2.]$ and $\tau \in [-2.67, 3.67]$ dimensionless units, and the number of grid points in the Z direction is 1000 and in the τ direction is 2048 points when using the time-domain scheme, or frequencies when using the frequency-domain scheme.

The F- function of Eq. (11) on the upper boundary z = 2.0 is used as an incoming flat-top 2 wave (see Figure 10-5), which extends from τ = -1.386 to τ = $-$ 2.386 (duration of 1) with p_{max} = 1 and p_{min} = -1.0 (τ and p are dimensionless). With these dimensionless pressure and duration, p = 1 is equivalent to 0.5 psf and τ = 1 is equivalent to 150 ms. The dimensionless time step for the pseudo time integration is taken as 0.001. The case has been run for 20,000 time steps until the total error of the pseudo unsteady time term was reduced to 10^{-7}.

Results and Discussion:

Figure 36 shows the pressure contours of the incoming wave as it progresses in the domain toward the caustic surface at z = 0 and the outgoing wave as it originates from the caustic surface. In Fig. 37, it is noticed that the predicted wave at the caustic surface shows pressure peaks of 3.0, 2.0 and -2.12 (equivalent to 1.5 psf, 1.0 psf and -1.06 psf, respectively). Figure 38 shows p $_{max}$ of 4.2, which is equivalent to 2.1 psf at z = 0.0657. These results conclusively show that the superboom response from dimensionless pressure peaks of $\pm$ 1.0 is predicted. It is noticed that the superboom of this case, as compared to the flat-top case (Fig. 10.3), results in

similar bow-shock pressure values but results in a larger recompression shock pressure level. Figures 39 and 40 show the interaction of the incoming wave with the outgoing wave at z = 0.5 and 1.5. These figures show the growth of the pressure peaks as it proceeds toward the caustic surface. Figure 41 shows the pressure wave in the shadow zone, which is fading away.
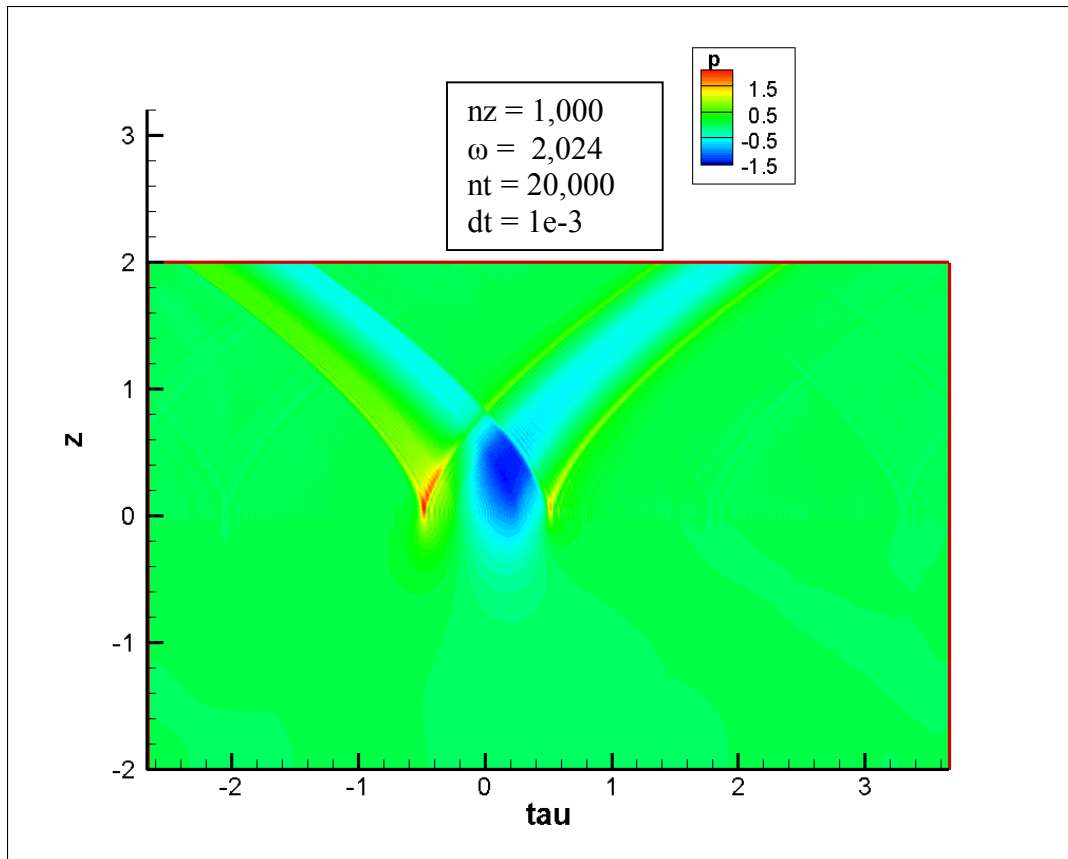

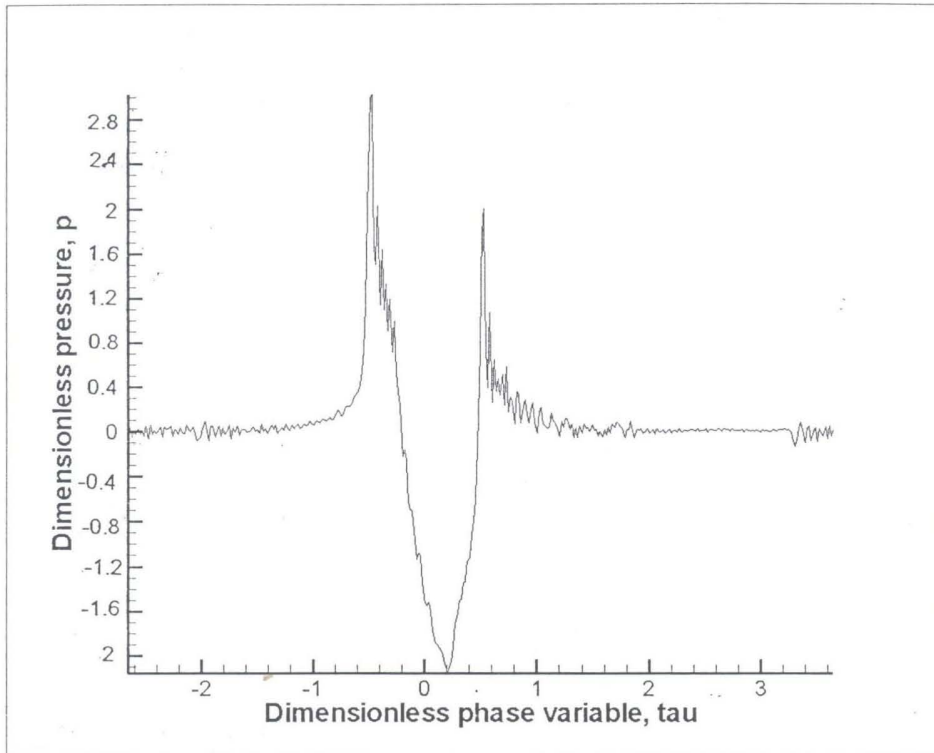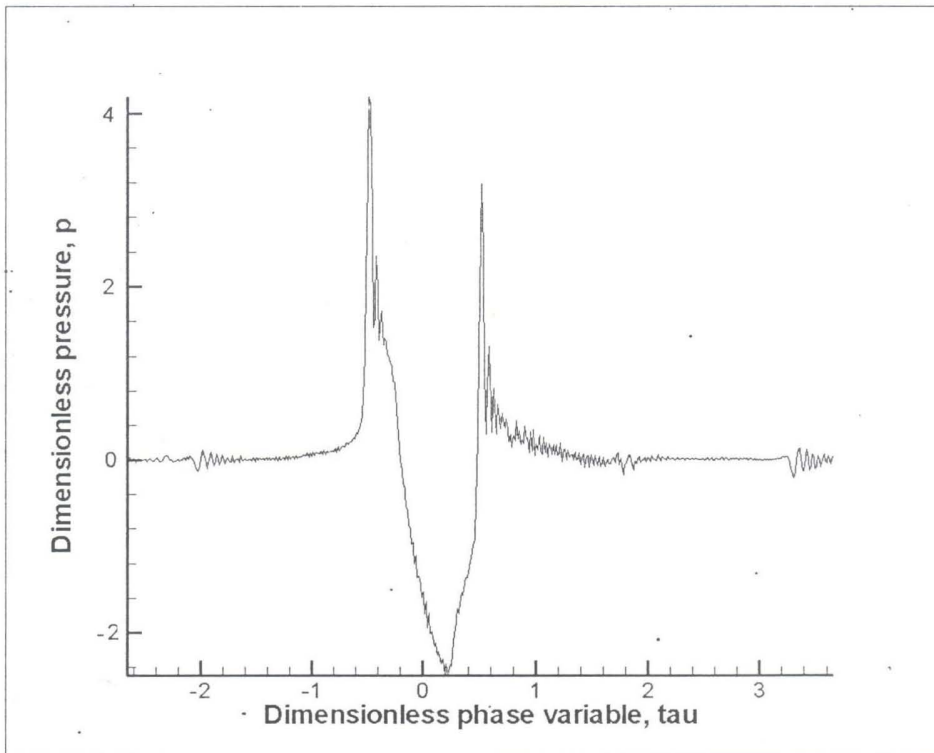Figure 36. Pressure contours for an incoming flat-top 2 wave (Fig. 10-5 Case) at nt = 20,000 time steps. The outgoing wave is clearly predicted.

Figure 37. Pressure variation for an incoming flat-top 2 wave (Fig.10-5 case)
at the caustic surface (z = 0) and nt = 20,000 steps

Figure 38. Pressure variation for an incoming flat-top 2 wave (Fig.10-5 case)
at z of maximum pressure, z = 0.0657 and nt = 20,000 steps
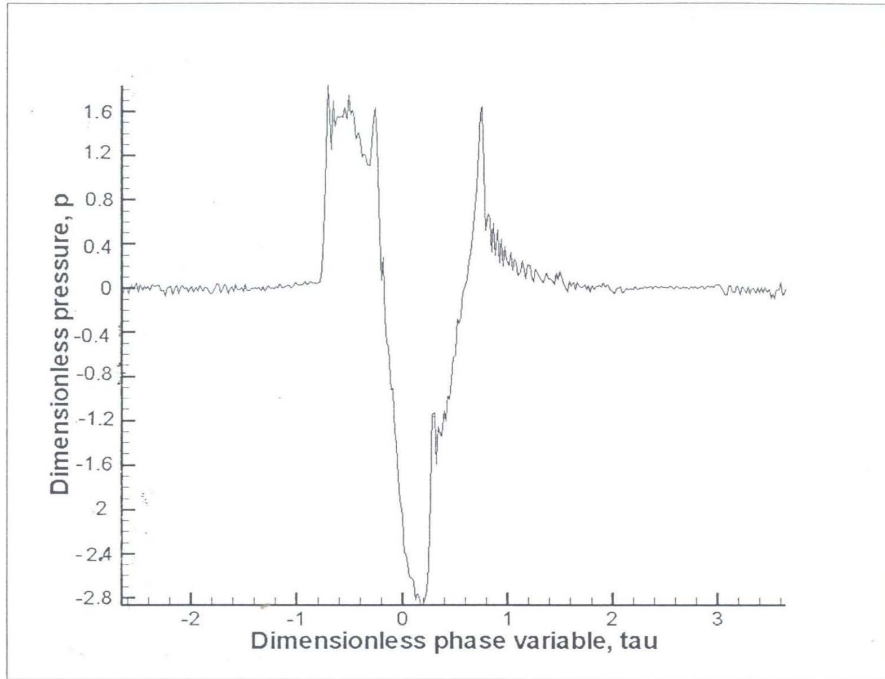
Figure 39. Pressure variation for an incoming flat-top 2 wave (Fig.10-5 case)
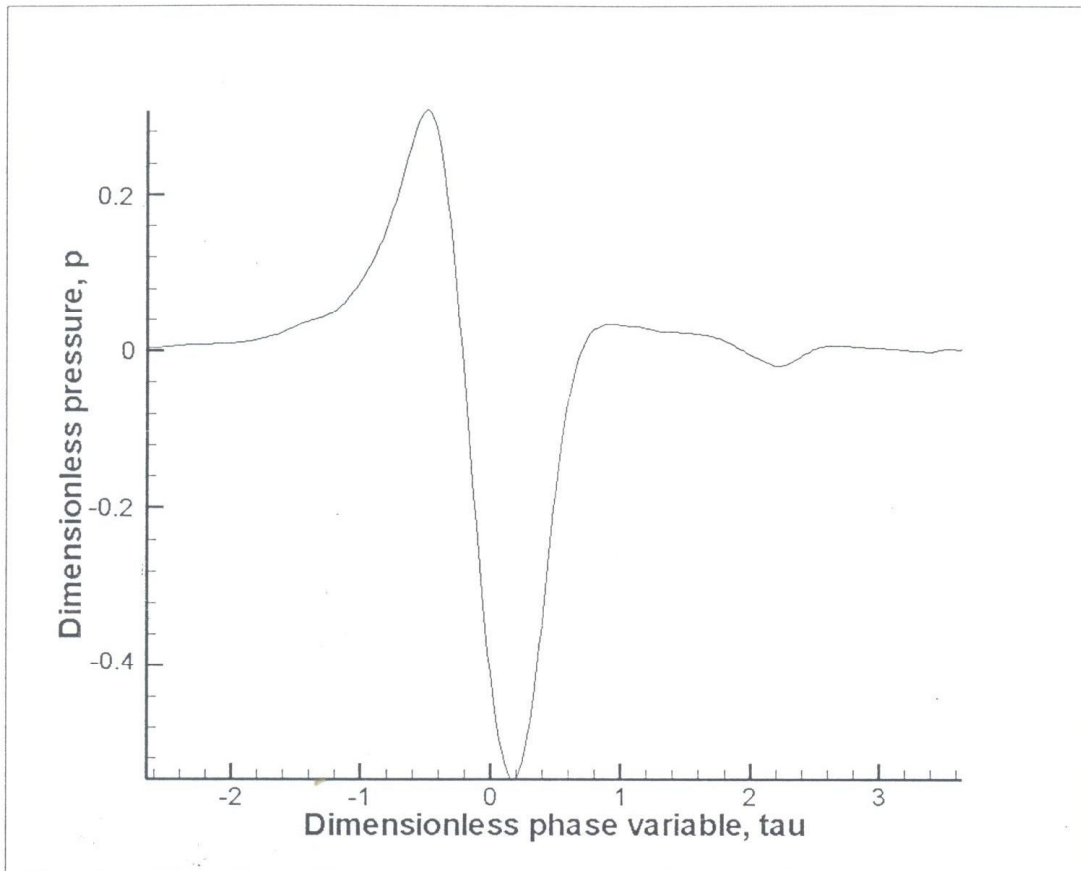at z = 0.5 and nt = 20,000 steps
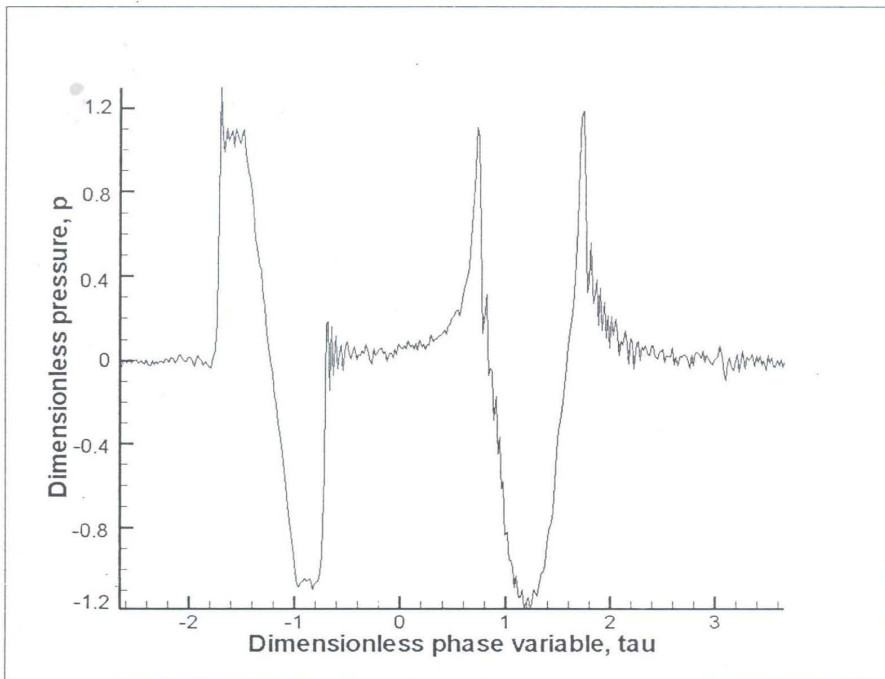
Figure 40. Pressure variation for an incoming flat-top 2 wave (Fig.10-5 case)
at z = 1.5 and nt = 20,000 step

Figure 41. Pressure variation for an incoming flat-top 2 wave (Fig.10-5 case) at z = -0.5 (shadow zone) and nt = 20,000 steps

Solution for an Incoming Ramp-Top 2 Wave (Fig.10-6):

Computational domain and grid:

We choose a rectangular domain with $z \in [-2.,2.]$ and $\tau \in [-2.67, 3.67]$ dimensionless units, and the number of grid points in the Z direction is 1000 and in the τ direction is 2048 points when using the time-domain scheme, or frequencies when using the frequency-domain scheme.

The F- function of Eq. (11) on the upper boundary z = 2.0 is used as an incoming ramp-top 2 wave (see Figure 10-6), which extends from τ = -1.386 to τ = – 2.386 (duration of 1) with p_{max} = 1 and p_{min} = -1.0 (τ and p are dimensionless). With these dimensionless pressure and duration, p = 1 is equivalent to 1 psf and τ = 1 is equivalent to 150 ms. The dimensionless time step for the pseudo time integration is taken as 0.001. The case has been run for 20,000 time steps until the total error of the pseudo unsteady time term was reduced to 10^{-7}.

Results and Discussion:

Figure 42 shows the pressure contours of the incoming wave as it progresses in the domain toward the caustic surface at z = 0 and the outgoing wave as it originates from the caustic

surface. In Fig. 43, it is noticed that the predicted wave at the caustic surface shows pressure peaks of 1.95, 1.3 and -1.7(equivalent to 1.95 psf, 1.3 psf and – 1.7 psf, respectively). Figure 44 shows p_{max} of 2.8, which is equivalent to 2.8 psf at $z = 0.24$, and p_{min} of - 2.5 which is equivalent to -2.5 psf. These results conclusively show that the superboom response from dimensionless pressure peaks of ±1.0 is predicted. It is noticed that the superboom of this case is higher than that of the flat-top case. Figures 45 and 46 show the interaction of the incoming wave with the outgoing wave at $z = 0.5$ and 1.5. These figures show the growth of the pressure peaks as it proceeds toward the caustic surface. Figure 47 shows the pressure wave in the shadow zone, which is fading away.
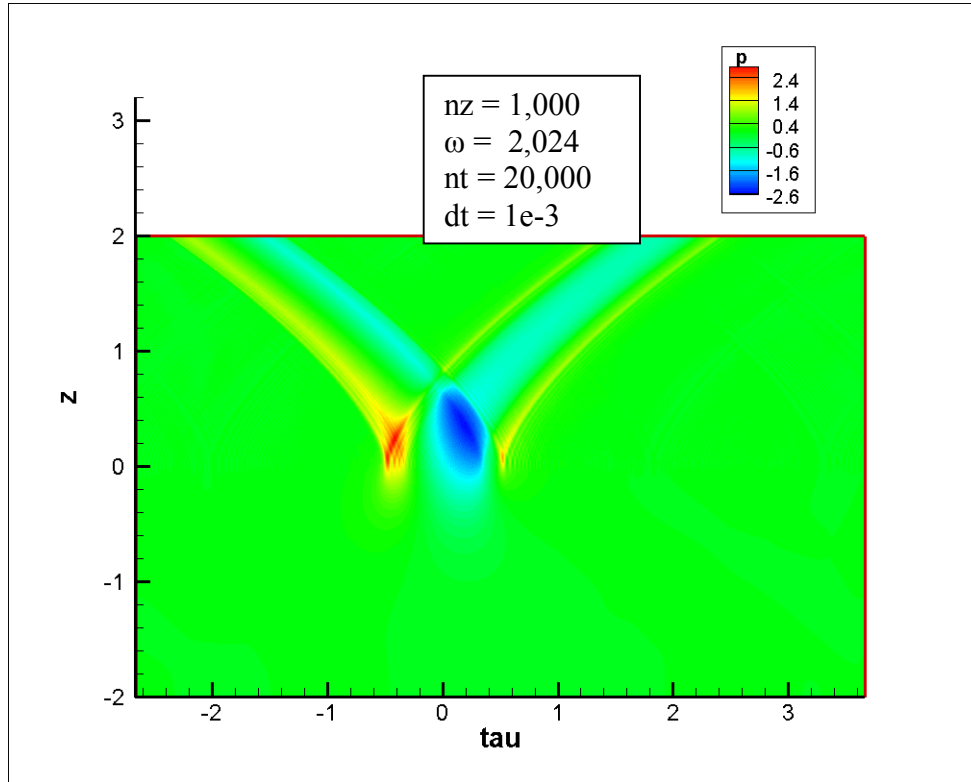
Figure 42. Pressure contours for an incoming ramp-top 2 wave (Fig. 10-6 Case) at nt = 20,000 time steps. The outgoing wave is clearly predicted.
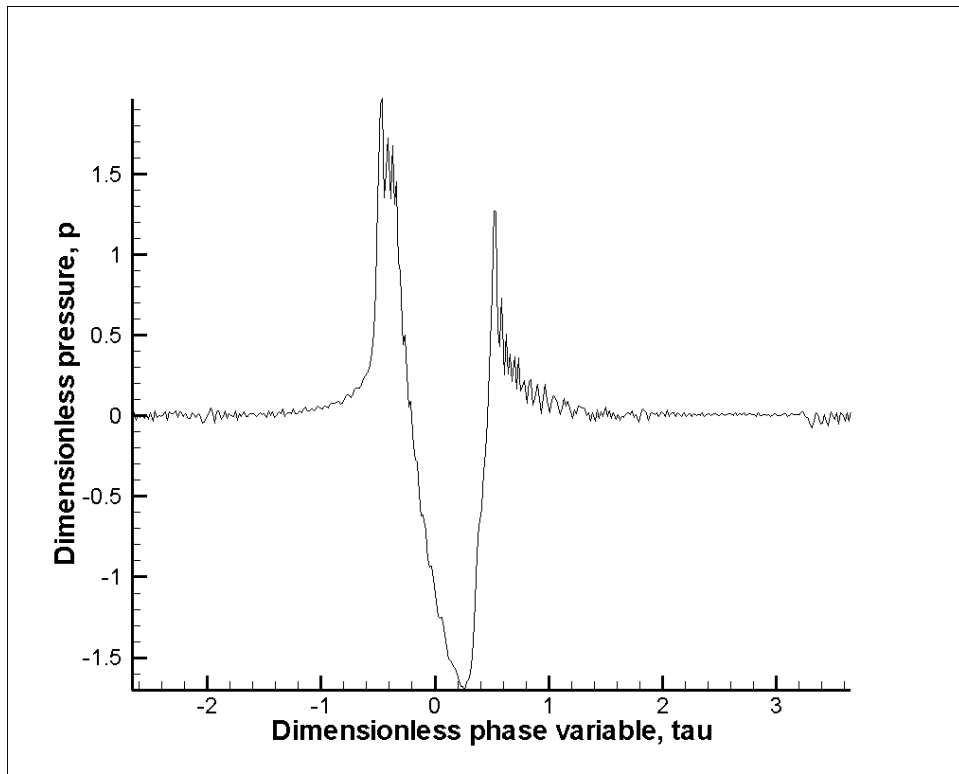
Figure 43. Pressure variation for an incoming ramp-top 2 wave (Fig.10-6 case)
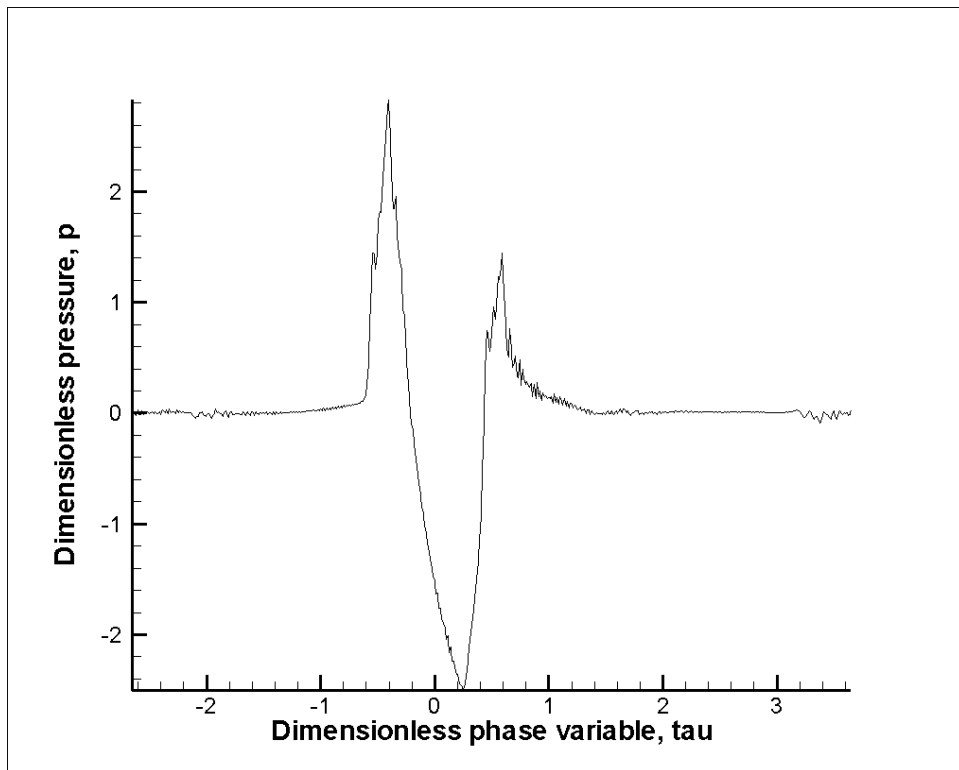at the caustic surface (z = 0) and nt = 20,000 steps

Figure 44. Pressure variation for an incoming ramp-top 2 wave (Fig.10-6 case)
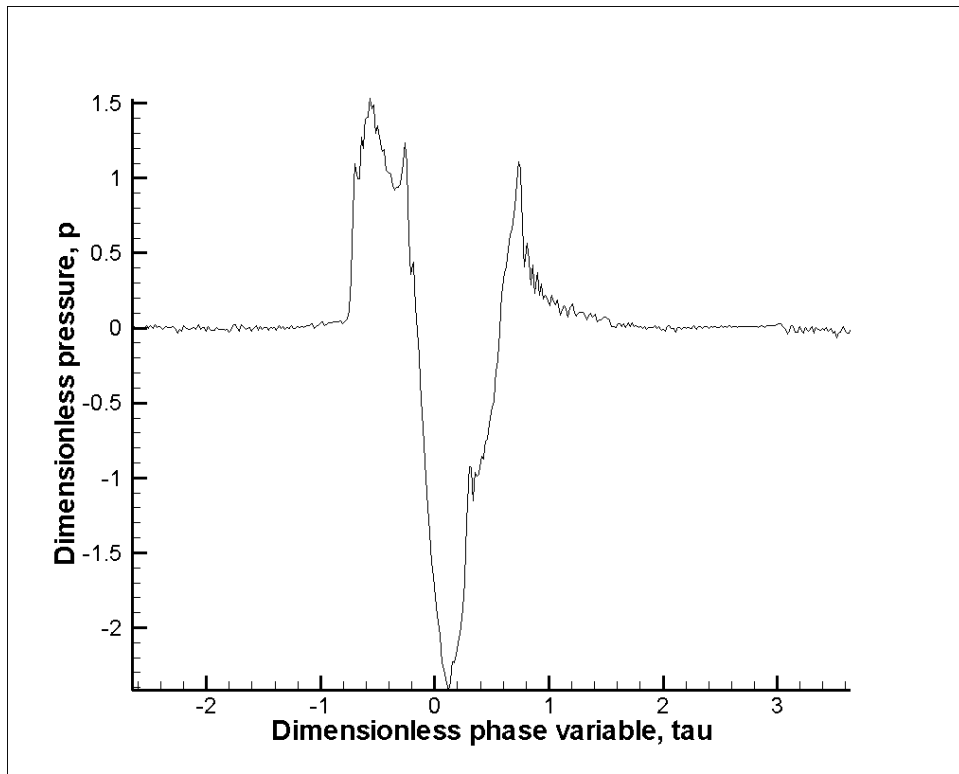at z of maximum pressure, z = 0.24 and nt = 20,000 steps

Figure 45. Pressure variation for an incoming ramp-top 2 wave (Fig.10-6 case)
at z = 0.5 and nt = 20,000 steps
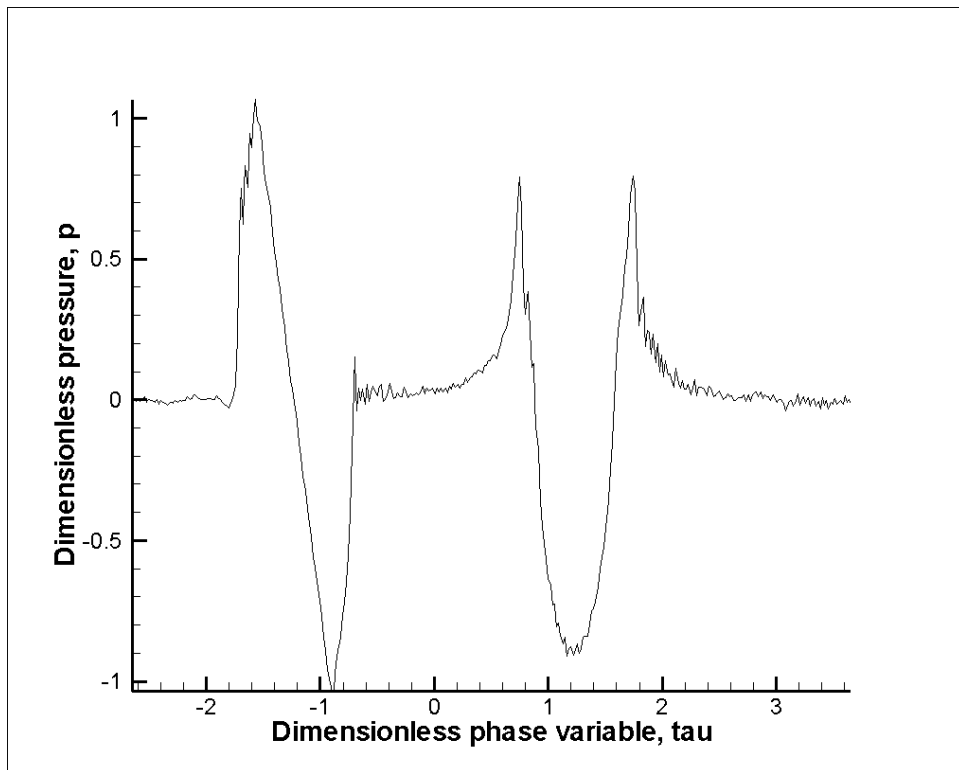

Figure 46. Pressure variation for an incoming ramp-top 2 wave (Fig.10-6 case)
at z = 1.5 and nt = 20,000 steps
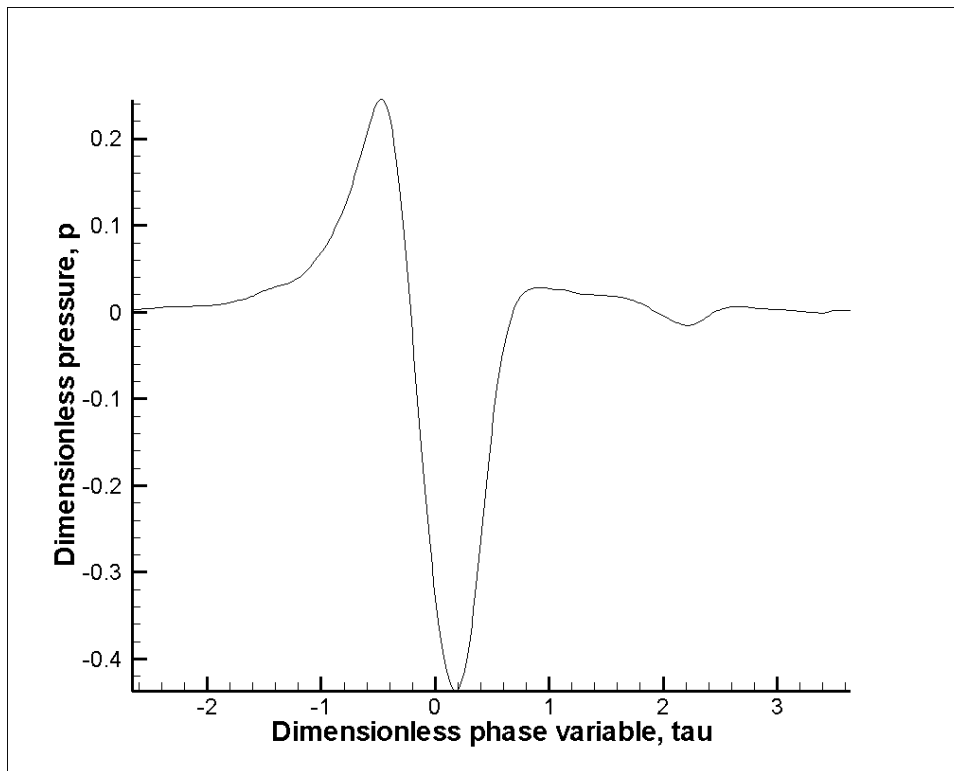
Figure 47. Pressure variation for an incoming ramp-top 2 wave (Fig.10-6 case)
at z = -0.5 (shadow zone) and nt = 20,000 steps.

V.　References:

1. Guiraud, J.-P., "Acoustique geometrique, bruit balistique des avions supersoniques et focalization," J. Mecanique 4, 1965, pp 215-267.

2. Hayes, W. D., "Similarity rules for nonlinear acoustic propagation through a caustic," Proceedings of the Sound Conference on Sonic Boom Research, NASA SP-180, 1968, pp 165-171.

3. Hunter, J. K., "Caustics of Nonlinear Waves," Wave Motion 9, 1987, pp 429-443.

4. Rosales, R. R. and Tabak, E. G., "Caustics of weak shock waves," Phys. Fluids 10, 1997, pp 206-222.

5. Tabak, E. G. and Rosales, R. R., " Focusing of weak shock waves and the von Neumann paradox of oblique shock reflections," Phys. Fluids 6, 1994, pp 1874-1892.

6. Augar, T. and Coulouvrat F., "Numerical Simulation of sonic Boom Focusing," AIAA J., Vol. 40, No. 9, September 2002, pp 1726-1734.

7. Marchiano, R. and Coulouvrat, F., "Numerical simulation of shock wave focusing at fold caustics with application to sonic boom," J. Acoust. Soc. Am. 114, No 4, October 2003, pp 1758-1771.

8. Lee, Y. S. and Hamilton, M. F., "Time-domain modeling of pulsed finite-amplitude sound beams," J. Acoust. Soc. Am. 97, 1995, pp 906-917.

9. McDonald, B. E. and Ambrosiano, J., "High Order upwind flux methods for scalar hyperbolic conservation laws," J. Comput. Phys. 56, 1984, pp 448-460.

10. Hayes, W. D., Haefeli, R. C., and Kulsrud, H. E., "Sonic boom propagation in a stratified atmosphere with computer program," NASA CR-1299, 1969.

REPORT DOCUMENTATION PAGE

1. REPORT DATE *(DD-MM-YYYY)*	2. REPORT TYPE	3. DATES COVERED *(From - To)*
01-06-2011	Contractor Report	

4. TITLE AND SUBTITLE	5a. CONTRACT NUMBER
Focused and Steady-State Characteristics of Shaped Sonic Boom Signatures: Prediction and Analysis	NNL07AE38T
	5b. GRANT NUMBER
	5c. PROGRAM ELEMENT NUMBER

6. AUTHOR(S)	5d. PROJECT NUMBER
Maglieri, Domenic J.; Bobbitt, Percy J.; Massey, Steven J.; Plotkin, Kenneth J.; Kandil, Osama A.; Zheng, Xue	
	5e. TASK NUMBER
	5f. WORK UNIT NUMBER
	984754.02.07.07.11.01

7. PERFORMING ORGANIZATION NAME(S) AND ADDRESS(ES)	8. PERFORMING ORGANIZATION REPORT NUMBER
NASA Langley Research Center Eagle Aeronautics, Inc. Hampton, VA 23681-2199 13 West Mercury Boulevard Hampton, VA 23669-2508	

9. SPONSORING/MONITORING AGENCY NAME(S) AND ADDRESS(ES)	10. SPONSOR/MONITOR'S ACRONYM(S)
National Aeronautics and Space Administration Washington, DC 20546-0001	NASA
	11. SPONSOR/MONITOR'S REPORT NUMBER(S)
	NASA/CR-2011-217156

12. DISTRIBUTION/AVAILABILITY STATEMENT
Unclassified - Unlimited
Subject Category 71
Availability: NASA CASI (443) 757-5802

13. SUPPLEMENTARY NOTES
Maglieri, Bobbitt, Massey: Eagle Aeronautics, Inc. (Steven J. Massey is currently with NASA Langley Research Center); Plotkin: Wyle Laboratories; Khandil and Zheng: Old Dominion University
Langley Technical Monitor: Peter G. Coen

14. ABSTRACT

The objective of this study is to examine the effect of flight, at off-design conditions, on the propagated sonic boom pressure signatures of a small "low-boom" supersonic aircraft. The amplification, or focusing, of the low magnitude "shaped" signatures produced by maneuvers such as the accelerations from transonic to supersonic speeds, climbs, turns, pull-up and pushovers is the concern. To analyze these effects, new and/or improved theoretical tools have been developed, in addition to the use of existing methodology. Several shaped signatures are considered in the application of these tools to the study of selected maneuvers and off-design conditions. The results of these applications are reported in this paper as well as the details of the new analytical tools. Finally, the magnitude of the focused boom problem for "low boom" supersonic aircraft designs has been more accurately quantified and potential "mitigations" suggested. In general, "shaped boom" signatures, designed for cruise flight, such as asymmetric and symmetric flat-top and initial-shock ramp waveforms retain their basic shape during transition flight. Complex and asymmetric and symmetric initial shock ramp waveforms provide lower magnitude focus boom levels than N-waves or asymmetric and symmetric flat-top signatures.

15. SUBJECT TERMS

Sonic boom; Sonic boom signatures; Focused boom; Low boom; Shaped signatures; Shaped sonic boom; Shock ramp waveforms

16. SECURITY CLASSIFICATION OF:			17. LIMITATION OF ABSTRACT	18. NUMBER OF PAGES	19a. NAME OF RESPONSIBLE PERSON
a. REPORT	b. ABSTRACT	c. THIS PAGE			STI Help Desk (email: help@sti.nasa.gov)
					19b. TELEPHONE NUMBER *(Include area code)*
U	U	U	UU	144	(443) 757-5802